

ISSN 2071-4726
2071-0305

Magazine of Civil Engineering

97(5), 2020





ПОЛИТЕХ
Санкт-Петербургский
политехнический университет
Петра Великого

Инженерно-строительный институт
Центр дополнительных профессиональных программ
195251, г. Санкт-Петербург, Политехническая ул., 29,
тел/факс: 552-94-60, www.stroikursi.spbstu.ru,
stroikursi@mail.ru

**Приглашает специалистов организаций, вступающих в СРО,
на курсы повышения квалификации (72 часа)**

Код	Наименование программы	Виды работ*
Курсы по строительству		
БС-01-04	«Безопасность и качество выполнения общестроительных работ»	п.1,2, 3, 5, 6, 7, 9, 10, 11, 12, 13, 14
БС-01	«Безопасность и качество выполнения геодезических, подготовительных и земляных работ, устройства оснований и фундаментов»	1,2,3,5
БС-02	«Безопасность и качество возведения бетонных и железобетонных конструкций»	6,7
БС-03	«Безопасность и качество возведения металлических, каменных и деревянных конструкций»	9,10,11
БС-04	«Безопасность и качество выполнения фасадных работ, устройства кровель, защиты строительных конструкций, трубопроводов и оборудования»	12,13,14
БС-05	«Безопасность и качество устройства инженерных сетей и систем»	15,16,17,18,19
БС-06	«Безопасность и качество устройства электрических сетей и линий связи»	20,21
БС-08	«Безопасность и качество выполнения монтажных и пусконаладочных работ»	23,24
БС-12	«Безопасность и качество устройства мостов, эстакад и путепроводов»	29
БС-13	«Безопасность и качество выполнения гидротехнических, водолазных работ»	30
БС-14	«Безопасность и качество устройства промышленных печей и дымовых труб»	31
БС-15	«Осуществление строительного контроля»	32
БС-16	«Организация строительства, реконструкции и капитального ремонта. Выполнение функций технического заказчика и генерального подрядчика»	33
Курсы по проектированию		
БП-01	«Разработка схемы планировочной организации земельного участка, архитектурных решений, мероприятий по обеспечению доступа маломобильных групп населения»	1,2,11
БП-02	«Разработка конструктивных и объемно-планировочных решений зданий и сооружений»	3
БП-03	«Проектирование внутренних сетей инженерно-технического обеспечения»	4
БП-04	«Проектирование наружных сетей инженерно-технического обеспечения»	5
БП-05	«Разработка технологических решений при проектировании зданий и сооружений»	6
БП-06	«Разработка специальных разделов проектной документации»	7
БП-07	«Разработка проектов организации строительства»	8
БП-08	«Проектные решения по охране окружающей среды»	9
БП-09	«Проектные решения по обеспечению пожарной безопасности»	10
БП-10	«Обследование строительных конструкций и грунтов основания зданий и сооружений»	12
БП-11	«Организация проектных работ. Выполнение функций генерального проектировщика»	13
Э-01	«Проведение энергетических обследований с целью повышения энергетической эффективности и энергосбережения»	
Курсы по инженерным изысканиям		
И-01	«Инженерно-геодезические изыскания в строительстве»	1
И-02	«Инженерно-геологические изыскания в строительстве»	2,5
И-03	«Инженерно-гидрометеорологические изыскания в строительстве»	3
И-04	«Инженерно-экологические изыскания в строительстве»	4
И-05	«Организация работ по инженерным изысканиям»	7

*(согласно приказам Минрегионразвития РФ N 624 от 30 декабря 2009 г.)

**По окончании курса слушателю выдается удостоверение о краткосрочном повышении
квалификации установленного образца (72 ак. часа)**

Для регистрации на курс необходимо выслать заявку на участие, и копию диплома об образовании по телефону/факсу: 8(812) 552-94-60, 535-79-92, , e-mail: stroikursi@mail.ru.

Magazine of Civil Engineering

SCHOLAR JOURNAL

ISSN 2071-0305

Свидетельство о государственной регистрации:
Эл № ФС77-77906 от 19.02.2020,
выдано Роскомнадзором

Специализированный научный журнал. Выходит с
09.2008.

Включен в Перечень ВАК РФ

Индексируется в БД Scopus

Периодичность: 8 раз в год

Учредитель и издатель:

Санкт-Петербургский политехнический университет
Петра Великого

Адрес редакции:

195251, СПб, ул. Политехническая, д. 29

Главный редактор:

Екатерина Александровна Линник

Научный редактор:

Виталий Владимирович Сергеев

Заместитель главного научного редактора:

Галина Леонидовна Козинец

Редакционная коллегия:

PhD, проф. Т. Аввад;
д.т.н., проф. М.И. Бальзанников
д.т.н., проф. А.И. Белостоцкий;
к.т.н., проф. А.И. Боровков;
д.т.н., проф. А. Бородинец;
PhD, проф. М. Велькович;
PhD, проф. Р.Д. Гарг;
PhD, М.Р. Гарифуллин;
Dr.-Ing, проф. Т. Грис;
д.т.н., проф. Т.А. Дацюк;
д.т.н., проф. В.В. Елистратов;
Dr.-Ing., проф. Т. Кэрки;
д.т.н., проф. Д.В. Козлов;
д.т.н., доцент С.В. Корниенко;
д.т.н., проф. Ю.Г. Лазарев;
д.т.н., проф. М.М. Мухаммадиев;
Dr.-Ing. Habil., проф. Х. Пастернак;
Dr.-Ing., проф. Ф. Рёгинер;
д.т.н., проф. Т.З. Султанов;
д.т.н., проф. М.Г. Тягунов;
акад. РАН, д.т.н., проф. М.П. Федоров;
Dr.-Ing., проф. Д. Хецк;
д.г.-м.н. А.Г. Шашкин;
д.т.н. В.Б. Штильман

Дата выхода: 25.09.2020

© ФГАОУ ВО СПбПУ, 2020
© Иллюстрация на обложке: Илья Смагин

Magazine of Civil Engineering

SCHOLAR JOURNAL

ISSN 2071-0305

Peer-reviewed scientific journal

Start date: 2008/09

8 issues per year

Publisher:

Peter the Great St. Petersburg Polytechnic University

Indexing:

Scopus, Russian Science Citation Index (WoS),
Compendex, EBSCO, Google Academia, Index
Copernicus, ProQuest, Ulrich's Serials Analysis System,
CNKI

Corresponding address:

29 Polytechnicheskaya st., Saint-Petersburg, 195251,
Russia

Editor-in-chief:

Ekaterina A. Linnik

Science editor:

Vitaly V. Sergeev

Deputy chief science editor:

Galina L. Kozinetc

Editorial board:

T. Awwad, PhD, professor
M.I. Balzannikov, D.Sc., professor
A.I. Belostotsky, D.Sc., professor
A.I. Borovkov, PhD, professor
A. Borodinets, Dr.Sc.Ing., professor
M. Veljkovic, PhD, professor
R.D. Garg, PhD, professor
M. Garifullin, PhD, postdoctorant
T. Gries, Dr.-Ing., professor
T.A. Datsyuk, D.Sc., professor
V.V. Elistratov, D.Sc., professor
T. Kärki, Dr.-Ing., professor
D.V. Kozlov, D.Sc., professor
S.V. Korniyenko, D.Sc., professor
Yu.G. Lazarev, D.Sc., professor
M.M. Muhammadiev, D.Sc., professor
H. Pasternak, Dr.-Ing.habil., professor
F. Rögener, Dr.-Ing., professor
T.Z. Sultanov, D.Sc., professor
M.G. Tyagunov, D.Sc., professor
M.P. Fedorov, D.Sc., professor
D. Heck, Dr.-Ing., professor
A.G. Shashkin, D.Sc.
V.B. Shtilman, D.Sc.

Date of issue: 25.09.2020

© Peter the Great St. Petersburg Polytechnic University.
All rights reserved.
© Coverpicture – Ilya Smagin

Contacts:

E-mail: mce@spbstu.ru

Web: <http://www.engstroy.spbstu.ru>

Contents

Nuguzhinov, Zh., Vatin, N., Bakirov, Zh., Khabidolda, O., Zholmagambetov, S., Kurokhtina, I. Stress-strain state of bending reinforced beams with cracks	9701
Begich, Y.E., Klyuev, S.V., Jos, V.A., Cherkashin, A.V. Fine-grained concrete with various types of fibers	9702
Molodtsov, M.V., Vshivkov, E.P., Molodtsova, V.E. Behavior of concrete beams reinforced with fiberglass composite rebar under load	9703
Sychkina, E.N., Ofrikhter, I.V., Ponomaryov, A.B. Bearing capacity equations of piles in weathered claystone and sandstone	9704
Serpik, I.N., Tarasova, N.V. Optimisation of steel trusses with a choice of multi-stage prestressing conditions	9705
Koyankin, A.A., Mitasov, V.M. Stress-strain state of the precast monolithic bent element	9706
Akhavan Salmassi, M., Kheyroddin, A., Hemmati, A. Seismic behavior of end walls in RC tall buildings with torsional irregularity	9707
Al-Rousan, R. Behavior of CFRP strengthened columns damaged by thermal shock	9708
Egorov, D., Galyamichev, A., Gerasimova, E., Serdjuks, D. Stress-strain state of fiber cement cladding within curtain wall system	9709
Prozuments, A, Borodinecs, A.B, Zemitis, J., Strelets, K.I. The effect of the air duct tightness on the stability of the indoor air parameters	9710
Perelmuter, A.V. Assessment of the tornado impact on the Chernobyl new safe confinement	9711
Slavcheva, G.S, Artamonova, O.V., Shvedova, M.A., Khan, M.A. Clinkerless slag-silica binder: hydration process and hardening kinetics (part 2)	9712



DOI: 10.18720/MCE.97.1

Stress-strain state of bending reinforced beams with cracks

Zh. Nuguzhinov^{a*}, N. Vatin^b, Zh. Bakirov^c, O. Khabidolda^d, S. Zholmagambetov^c, I. Kurokhtina^c

^a Kazakhstan Multidisciplinary Institute of Reconstruction and Development Republican State Enterprise on the Right of Economic Use, Karaganda, Republic of Kazakhstan

^b Peter the Great St. Petersburg Polytechnic University, St. Petersburg, Russia

^c Karaganda State Technical University, Karaganda, Republic of Kazakhstan

^d al-Farabi Kazakh National University, Almaty, Republic of Kazakhstan

* E-mail: kazmirr@mail.ru

Keywords: reinforced concrete, beam, bending, stress state, crack, pre-stressing, physical nonlinearity, reinforcement, bearing capacity, ultimate state

Abstract. The work is dealing with studying the stress-strain state of bending pre-stressed concrete beams with cracks. The problems of determining preliminary stresses in a reinforced concrete element, determining the moment of crack formation, and determining the stress in a section with a crack are successively solved. The problems were solved for a general section with the vertical axis of symmetry, taking into account the non-linear relationship between strain and stress in concrete. The resolving system of two transcendental algebraic equations is obtained from the equilibrium conditions of a part of the beam on one side of the section with a crack. Analytical expressions have been obtained for determining preliminary stresses, the external bending moment at which a crack normal to the axis appears, as well as the stress state parameters in the section with a crack, including the crack height. The results obtained make it possible to predict the bearing capacity of reinforced concrete structures at the design stage by two groups of limiting states, and to evaluate the real technical condition of the structures in operation. These results can be used to determine the parameters of fracture mechanics and evaluate crack resistance of a reinforced concrete beam.

1. Introduction

A very common type of defects and damage to reinforced concrete structures are cracks [1–3]. They appear both at the manufacturing stage and at the operation stage. Causes of cracking may be excessive tension of the reinforcement in pre-stressed structures, an insufficient protective layer of concrete, shrinkage of concrete, a high temperature during welding of mating elements units. In bearing reinforced concrete structures the occurrence and development of cracks take place due to their deformation under the effects of loads, temperature fluctuations, uneven subsidence of buildings and structures.

The appearance of cracks in bending elements does not mean exhaustion of its carrying capacity. It leads to increasing efforts in the sections with a crack, which reduces the element strength. In addition, due to crack opening, the corrosion of reinforcement increases that reduces the structure durability. The norms regulate the extent of crack opening that depends on the stress state in the section with a crack. Since cracks exist in any reinforced concrete structures, determining the stress state in a cross section with a crack is very important for assessing the actual state of the structure being operated.

The emergence of cracks was studied by the NIIZhB, TsNIISK, in the Kharkov Promstroy NII proekt and other leading research and design organizations. A lot of scientists dealt with the conditions of forming cracks and assessing their effect on strength and deformability, a lot of monographs [1–4] and scientific articles were written. They developed analytical and numerical methods for calculating reinforced concrete structures with cracks.

Nuguzhinov, Zh., Vatin, N., Bakirov, Zh., Khabidolda, O., Zholmagambetov, S., Kurokhtina, I. Stress-strain state of bending reinforced beams with cracks. Magazine of Civil Engineering. 2020. 97(5). Article No. 9701.

DOI: 10.18720/MCE.97.1



This work is licensed under a [CC BY-NC 4.0](https://creativecommons.org/licenses/by-nc/4.0/)

Designing reinforced concrete structures with cracks is a complex scientific problem. The issues of substantiating the computational models and defining the stress-strain state of beams with cracks normal to the axis were dealt with in articles [5–7]. One of the main criteria for the limiting state of reinforced concrete structures with cracks is the width of crack opening. Articles [8-14] are dealing with its definition. Studying the influence of the angle of inclination of cracks on the parameters of the stress state in the cross section is described in works [15, 16].

The issues of crack formation are considered in works [17–22]. Work [23] is dealing with the calculation of crack resistance and changing the beam rigidity and deflections during formation of cracks. Some researchers believe that with the help of organized cracks the deflection of a reinforced concrete beam can be reduced. This idea is being dealt with in work [24].

The above problems are dealt with in a number of experimental studies, the results of which are given in [25–30]. A lot of studies were carried out by numerical methods [6, 8, 9, 31–38].

Recently probabilistic methods of designing have been actively introduced into engineering practice. The use of these methods in predicting the parameters of crack formation and calculation of reinforced concrete structures with cracks reliability according to various criteria are described in [5, 34, 35, 39].

In connection with the widespread introducing of computer technologies into computational practice, it became possible to calculate numerically the parameters of fracture mechanics and to use them for assessing the bearing capacity of reinforced concrete structures with cracks. Article [40] is dealing with these approaches.

From this brief review it is clear that a lot of scientific articles are published on calculation of reinforced concrete structures with cracks, which indicate the problem urgency. At the same time, it should be noted that in the last period there are not so many works dealing with the analytical determination of the parameters of reinforced concrete elements with a crack stress state.

At present there is a generally accepted method for determining the moment of crack formation. The numerical calculations carried out by us using the finite element method show a significant difference between the analytical and numerical results. The method proposed in this paper removes these inconsistencies. A review of the works shows that not enough attention has been paid in the studies to determining stresses from the reinforcement pre-stressing. This operation is considered only as a way to increase crack resistance. In addition, these stresses affect the stress state of the element and through it the limiting state of the structure in use. In this regard we need computational dependencies that allow determining pre-stresses and taking them into account when assessing the real state of the structures.

The authors have been studying the problems of designing reinforced concrete structures with cracks for many years [2, 41].

2. Methods

To determine stresses in the beam, the section method is used. The beam is cut along the considered section and the equilibrium conditions of the cut-off part of the beam are made. For bending beams, these conditions are reduced to the equality to zero of the sum of the projection of all the forces on the axis of the beam and the equality to zero of the sum of the moments of all the forces relative to the transverse axis of the section.

When determining pre-stresses from the tension of the reinforcement and determining the moment of the crack formation, the hypothesis of flat sections is adopted. In the case of cracks, this hypothesis is applied to the average cross section between the cracks. In the section with a crack, the linear deformation diagram is transformed taking into account the uneven deformation along the length of the beam.

An exponential law is used to describe the nonlinear relationship between stress and strain in concrete.

$$\sigma = 1.1R_b [1 - \exp(-0.9\varepsilon E_b / R_b)]. \quad (1)$$

where E_b and R_b are the elasticity modulus and the concrete strength limit.

This law is one of the frequently used expressions for describing the deformation diagram [2, 42].

The main unknown tasks are the height of the compression zone of concrete and the length of the tension zone above the crack. In the absence of a crack, the maximum (regional) tensile stress in concrete is taken as the second unknown. These unknowns are found from two equilibrium equations. Through these parameters, using the hypothesis of flat sections and the law of deformation, all the parameters of the stress state are determined: maximum compressive stress in concrete, stress in reinforcement, crack length or maximum tensile stress in concrete, crack opening width.

The results of the study are determining pre-stresses in a reinforced concrete element, determining the bending moment of the crack formation, determining the stress state of a section with a crack during bending with determining the length of operational cracks.

2.1. Determining pre-stresses

Sometimes in reinforced concrete structures in the process of manufacturing the are especially developed significant compressive stresses in concrete by tension of high-strength reinforcement. The initial compressive stresses are developed in those areas of concrete that will subsequently experience tensile stress. Therefore, in a pre-stressed beam under load the concrete experiences tensile stresses only after the initial compressive stresses are extinguished. At the same time, the load that causes the appearance of cracks or their opening limited in width is much higher than the corresponding load in the beam without pre-stressing. In such beams the structure rigidity is higher, therefore, deflections will be less, and the stochastic nature of forming cracks will not have such a "destructive" effect of cracks, as it happens in beams without pre-stressing.

The magnitude of the pre-stress significantly affects the subsequent work of the elements under load. With small pre-stresses in the reinforcement and low compression of concrete the effect of pre-stress over time will be lost due to relaxation of stresses in the reinforcement, shrinkage and creep of concrete and other factors. At high pre-stresses in the reinforcement close to the standard resistance, there is a danger of rupture and the risk of significant residual deformations. Therefore, it is necessary to know pre-stresses in the section of the reinforced concrete element from the reinforcement stress in order to establish the rational controlled reinforcement stress when manufacturing.

At present, to determine these stresses, a linear calculation of the reduced concrete section is performed, in which the reinforcement area is replaced with the equivalent concrete area. A linear calculation of reinforced concrete elements can be performed at low stress levels, when they do not exceed 70 % of the calculated ones. If a crack does not occur in the section of the element, then you can be sure that this condition is satisfied for the compression zone. This situation is characteristic of determining the compression stresses. At the same time, inelastic deformations can occur in concrete of the tension zone. Therefore, for the deformation diagram in this zone, we adopt the exponential law (1).

In calculations we will proceed from the following aspects:

1. the cross sections remain flat during flattening;
2. in concrete of the compressed zone deformations are only elastic, the stress diagram is triangular;
3. in concrete of the tension zone the relationship between stress and strain is described by the exponential law (1).

Let us consider an I-section with a vertical axis of symmetry (Fig. 1, a). We will introduce the notation:

A_{ct}, A_c are the flanges overhangs areas in the tension and compressed zones;

h_t, h_c are the flanges thicknesses in the tension and compressed zones;

a, a' are the thicknesses of the concrete protective layer in the tension and compressed zones;

A_s, A'_s are the reinforcement areas in the tension and compressed zones;

N_a, N'_a are internal efforts in the reinforcement in the tension and compressed zones.

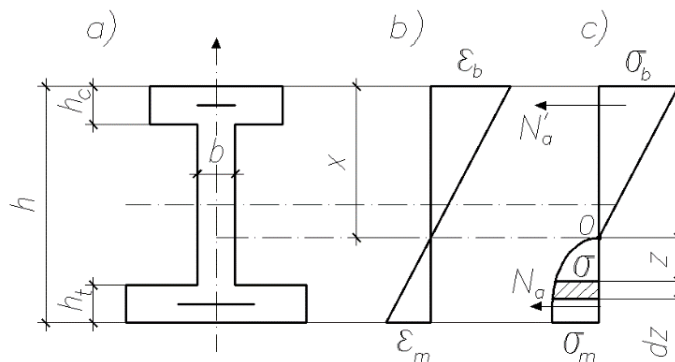


Figure 1. The beam cross section (a), deformation curves (b) and stress curves (c).

The basic unknown values of the problem the compressed zone height x and maximum tensile stress in concrete σ_m . According to the deformation diagram we will find the corresponding deformation

$$\varepsilon_m = -(R_{bt}/0.9E_b) \ln \left[(1 - \sigma_m) / 1.1R_{bt} \right].$$

Let us introduce the notation

$$c = \sigma_m / 1.1R_{bt}, \quad y = -\ln(1 - c).$$

Then the boundary deformations will be equal

$$\varepsilon_m = 1.1yR_{bt}/E_b, \quad \varepsilon_b = \varepsilon_m x / (h - x).$$

The maximum shearing stress in concrete

$$\sigma_b = E_b \varepsilon_b = 1.1yR_{bt}x / (h - x). \quad (2)$$

The mean stress on the compressed zone flange will be taken equal to the value at the level of the overhangs center of gravity:

$$\sigma_{bc} = 1.1yR_{bt} (x - h/2) / (h - x).$$

Due to the curvilinear nature of the curve, stress within the limits of the tension flange changes but little, and can be accepted as equal to the boundary value:

$$\sigma_{bct} = \sigma_m.$$

Due to the concrete pre-stress in the reinforcement there appear compressing stresses

$$\Delta\sigma_s = E_s \varepsilon_s = E_s \varepsilon_{b,s} = \alpha \sigma_{b,s},$$

where $\varepsilon_{b,s}$, $\sigma_{b,s}$ are deformation and stress in concrete at the level of the reinforcement center; $\alpha = E_s / E_b$ is the ratio of the elasticity modules of steel and concrete.

Taking into account this, we will determine stress in the reinforcement of the tension and compressed zones after the concrete pre-stressing

$$\sigma_s = \sigma_{sp} + \alpha \sigma_m, \quad \sigma'_s = \sigma'_{sp} - 1.1y\alpha R_{bt} (x - a') / (h - x), \quad (3)$$

where σ_{sp} , σ'_{sp} are pre-stresses in the reinforcement before pre-stress.

The height of the tension zone is designated as $z_p = h - x$, and the deformation of the layer at the distance of z from the zero line (Fig. 1,b) will be

$$\varepsilon = \varepsilon_m z / z_p.$$

Then the deformation diagram can be re-written as follows

$$\sigma = 1.1R_{bt} \left[1 - \exp(-yz/z_p) \right].$$

Let us find the internal forces resultant in the tension zone of concrete (Fig. 1,c).

$$N_p = b \int_0^{z_p} \sigma dz = 1.1R_{bt}b \int_0^{z_p} \left[1 - \exp(-yz/z_p) \right] dz.$$

After integrating we will obtain

$$N_p = 1.1bR_{bt} (h - x) (1 - c / y). \quad (4)$$

Let us determine the moment of these forces relative to the zero line (Fig. 1, c)

$$M_{po} = b \int_0^{z_p} \sigma z dz = 1.1R_{bt}b \int_0^{z_p} z \left[1 - \exp(-yz/z_p) \right] dz.$$

After integrating we will obtain

$$M_{po} = 1.1R_{bt}bz_p^2 \left[0.5 + (1-c)(1+y)/y^2 - y^{-2} \right]. \quad (5)$$

The internal forces in the cross section from the preliminary reinforcement tension are self-balanced. Let us write the equation of the forces equilibrium in the cross section (Fig. 1, c):

$$N_p + A_{ct}\sigma_{bct} + \sigma_s A_s + 0.5\sigma_b bx - A_c \sigma_{bc} + \sigma'_s A'_s = 0.$$

By substituting here the determined above stresses and force (4), we will obtain

$$1.1R_{bt} \left\{ b(h-x)(1-c/y) + A_{ct}c + \alpha A_s c - y \frac{bx^2/2 + A_c(x-h_c/2) + \alpha A'_s(x-a')}{h-x} \right\} + \sigma_{sp} A_s + \sigma'_{sp} A'_s = 0.$$

Let us write the sum of the internal forces moments relative to the zero line:

$$M_{po} + A_{ct}\sigma_{bct}(h-x-h_{ct}/2) + \sigma_s A_s (h-a-x) + \sigma_b bx^2/3 + A_c \sigma_{bc}(x-h_c/2) - \sigma'_s A'_s (x-a') = 0.$$

By substituting here new values of stresses, taking into account (5) we will obtain

$$1.1R_{bt} \left\{ b(h-x)^2 \left[0.5 + (1-c/y) - \frac{c}{y^2} \right] + A_{ct}c(h-x-h_{ct}/2) + c\alpha A_s (h-a-x) + y \frac{bx^3/3 + A_c(x-h_c/2)^2 + \alpha A'_s(x-a')^2}{h-x} \right\} + \sigma_{sp} A_s (h-a-x) + \sigma'_{sp} A'_s (x-a') = 0.$$

Let us introduce dimensionless parameters:

$$\xi = x/h, \quad a_0 = a/h, \quad a'_0 = a'/h, \quad m_{ct} = A_{ct}/bh, \\ m_c = A_c/bh, \quad \mu = A_s/bh, \quad \mu' = A'_s/bh$$

and re-write these equations in the dimensionless form

$$(1-\xi) \left(1 - \frac{c}{y} \right) + c(m_{ct} + \alpha\mu) - y \frac{\xi^2/2 + m_c(\xi - h_c/2h) + \alpha\mu'(\xi - a'_0)}{1-\xi} + \frac{\mu\sigma_{sp} + \mu'\sigma'_{sp}}{1.1R_{bt}} = 0, \quad (6)$$

$$(1-\xi)^2 \left[0.5 + \left(\frac{1-c}{y} \right) - \frac{c}{y^2} \right] + cm_{ct} \left(1 - \xi - \frac{h_{ct}}{2h} \right) + c\alpha\mu(1-\xi - a_0) + \frac{\xi^3/3 + m_c(\xi - h_c/2h)^2 + \alpha\mu'(\xi - a'_0)^2}{1-\xi} + \frac{\mu\sigma_{sp}(1-\xi - a_0) - \mu'\sigma'_{sp}(\xi - a'_0)}{1.1R_{bt}} = 0. \quad (7)$$

We have obtained the system of two transcendent equations relative to two unknown values ξ , $y(c)$. The solution of the system gives the possibility to determine the height of the compressed zone $x = \xi h$ and the maximum tension stress in concrete $\sigma_m = 1.1R_{bt}c$. Through these parameters there is determined the maximum compressing stress in concrete by formula (2) and stresses in the reinforcement by formulas (3).

Equations (6) and (7) are common for all the reinforced elements with pre-stress and without it, with different forms of cross section: I-shaped, T-shaped, rectangular. For the T-shaped cross section A_c or A_{ct}

is equal to zero. For the rectangular cross section the area of both overhangs are equal to zero. So, for the rectangular cross section with stressed reinforcement in the compressed zone we will obtain

$$(1-\xi)\left(1-\frac{c}{y}\right)-y\frac{\xi^2/2+\alpha\mu'(\xi-a_0')}{1-\xi}+\frac{\mu'\sigma_{sp}'}{1.1R_{bt}}=0,$$

$$(1-\xi)^2\left[0.5+\left(\frac{1-c}{y}\right)-\frac{c}{y^2}\right]+y\frac{\xi^3/3+\alpha\mu'(\xi-a_0')^2}{1-\xi}-\frac{\mu'\sigma_{sp}'(\xi-a_0')}{1.1R_{bt}}=0.$$

There are a lot of ways to solve the system of nonlinear algebraic equations and the corresponding algorithms and programs for their implementation. In our case of two variables, the solution can be found graphically: to construct curves $\phi_1(\xi, y) = 0$ and $\phi_2(\xi, y) = 0$ on the plane ξ, y and to find their intersection points.

This method of calculation is valid till there is no crack in the section of the element. Therefore, we find the pre-stressing value in the reinforcement at which a crack appears. A crack is formed when the maximum tensile stress in concrete reaches the tensile strength, i.e. $\sigma_m = R_{bt}$.

According to deformation diagram (1) we find the ultimate tensile deformation of concrete

$$\varepsilon_{ubt} = 2.667R_{bt} / E_b. \quad (8)$$

Using formulas (2) and (9) we will find stress at the boundary of the compressed zone

$$\sigma_b = 2.667R_{bt}x / (h-x).$$

Mean compression stresses on the flanges will be equal

$$\sigma_{bc} = 2.667R_{bt}(x-h_c/2)/(h-x), \quad \sigma_{bct} = R_{bt}.$$

Taking into account the limiting deformation (8) we will write stresses in the reinforcement

$$\sigma_s = \sigma_{sp} + 2.667\alpha R_{bt}, \quad \sigma_s' = \sigma_{sp}' - 2.667\alpha R_{bt}(x-a') / (h-x).$$

Similarly to the above-described distribution of stress on the height of the tension zone, we can write the following

$$\sigma = 1.1R_{bt}\left[1 - \exp\left(-2.4z/z_p\right)\right].$$

Then the internal forces resultant in the tension zone and their moment relative to the zero line can be determined by formulas (4) and (5) accepting $y = 2.4$, $c = 0.909$. As a result we will obtain:

$$N_p = 0.683bR_{bt}(h-x), \quad N_{po} = 0.418R_{bt}b(h-x)^2. \quad (9)$$

Let us write down the equation of the internal forces equilibrium in the cross section and the sum of their moments relative to the zero line (Fig. 1).

$$N_p + A_{ct}R_{bt} + N_a - 0.5\sigma_bxb - A_c\sigma_{bc} + N_a' = 0,$$

$$M_{po} + A_{ct}R_{bt}(h-x-h_{ct}/2) + N_a(h-x-a) + \sigma_bbx^2/3 + A_c\sigma_{bc}(x-h_c/2) - N_a'(x-a') = 0.$$

By substituting here the above-determined stresses, forces and the moment, we will write down

$$R_{bt}\left\{\frac{0.683b(h-x) + A_{ct} + 2.667\alpha A_s - 1.333bx^2 + 2.667A_c(x-h_c/2) + 2.667\alpha A_s'(x-a')}{h-x}\right\} + \sigma_{sp}A_s + \sigma_{sp}'A_s' = 0, \quad (10)$$

$$R_{bt} \left\{ \begin{aligned} &0.4188b(h-x)^2 + A_{ct}(h-x-h_{ct}/2) + 2.667\alpha A_s(h-x-a) + \\ &\frac{0.889bx^3 + 2.667A_c(x-h_c/2)^2 + 2.667A_s'(x-a')^2}{h-x} \end{aligned} \right\} + \quad (11)$$

$$+\sigma_{sp}A_s(h-x-a) - \sigma_{sp}'A_s'(x-a') = 0.$$

These equations allow determining the limiting value of the pre-stress. Usually pre-stressed reinforcement is placed only in zones of tensile stresses under operational loads. Then $\sigma_{sp}' = 0$ and from equation (10) we can express the force $\sigma_{sp}A_{sp}$ in terms of x . Substituting this expression into (11), we obtain a cubic equation for determining the height of the compressed zone before the formation of a crack. Further, from (10), when x is known, the limiting pre-stressing is determined.

For the rectangular section with pre-stressed reinforcement in the compressed zone, the resolving equations are written as follows:

$$R_{bt} \left\{ 0.683b(h-x) - \left[1.333bx^2 + 2.667\alpha A_s'(x-a') \right] / (h-x) \right\} + \sigma_{sp}'A_s' = 0,$$

$$R_{bt} \left\{ 0.4188b(h-x)^2 + \left[0.889bx^3 + 2.667\alpha A_s'(x-a')^2 \right] / (h-x) \right\} \sigma_{sp}'A_s'(x-a') = 0.$$

From here for determining the height of the compressed zone we will obtain the following cubic equation:

$$x^3 + (0.626h - 3.63a')x^2 + (3.19h^2 - 7.63ha')x + 3.816h^2a' - 2.335h^3 = 0$$

2.2. Determining the ultimate moment of crack formation

Through this ultimate moment, the first category of requirements of the second group of the limit state is written. Therefore, such calculations are normative. They assume that stress in the tension zone of concrete is constant and equal to the tensile strength of concrete, R_{bt} . In this work the calculations have a real stress profile in this zone: the boundary stress is equal to R_{bt} , and in the other fibers they are determined according to the deformation diagram in accordance with the strain curve.

Let us consider the cross section of a general form, shown in Fig. 1, in which the boundary stress $\sigma_m = R_{bt}$. We consider fair the assumptions made in determining pre-stressing stress. Then all the arguments and calculations given in determination the maximum pre-stress in the reinforcement remain valid.

In contrast to the case considered here, an external load is added: the bending moment or an eccentrically applied force. If earlier the internal forces were self-balanced, here they are balanced by external load.

Therefore, an external force P is added to equilibrium equation (10):

$$R_{bt} \left\{ \begin{aligned} &0.683b(h-x) + A_{ct} + 2.667\alpha A_s - \\ &\frac{1.333bx^2 + 2.667A_c(x-h_c/2) + 2.667\alpha A_s'(x-a')}{h-x} \end{aligned} \right\} + \quad (12)$$

$$+\sigma_{sp}A_s + \sigma_{sp}'A_s' \pm P = 0.$$

Here the force P is taken with the plus sign under the eccentric compression and the minus sign under the eccentric tension and during bending it is zero.

The sum of the moments of internal forces (11) is now equal to the external moment and determines the ultimate moment of the crack formation. The external moment is convenient to be determined relative to the center of gravity of the section. With respect to this axis, the moment of internal forces will be equal to:

$$M_m = R_{bt} \left\{ \begin{aligned} & b(h-x)(0.076h+0.265x) + A_{ct}(h-h_{ct}/2) + 2.667\alpha A_s(h/2-a) + \\ & \frac{0.222bx^2(3h-2x) + 1.333A_c(x-h_c)(x-h_c/2) + 2.667\alpha A_s'(x-a')(h/2-a')}{h-x} + \\ & \frac{\sigma_{sp}A_s(h/2-a) - \sigma_{sp}'A_s'(h/2-a')}{R_{bt}} \end{aligned} \right\} = \quad (13)$$

$$= W_{pe}R_{bt},$$

where W_{pe} is the elastic-plastic moment of resistance of the pre-stressed section.

To determine the limiting moment from (12) by solving the quadratic equation there is determined the height of the compressed zone x . Substituting it into expression (13) we find the ultimate moment of the crack formation.

Equations (12) and (13) are universal: they are applicable for various forms of sections for different types of reinforcement. For special cases they are simplified. So, for a bending rectangular section with pre-stressed reinforcement in the tension zone, we obtain

$$0.683b(h-x)^2 + 2.667\alpha A_s(h-x) - 1.333bx^2 + \sigma_{sp}A_s(h-x)/R_{bt} = 0,$$

$$M_m = R_{bt} \left\{ b(h-x)(0.076h+0.265x) + 2.667\alpha A_s \left(\frac{h}{2} - a \right) + \frac{0.222bx^2(3h-2x)}{h-x} + \sigma_{sp}A_s \left(\frac{h}{2} - a \right) \right\}.$$

Introducing dimensionless parameters:

$$\xi = x/h, \quad \mu = A_s/bh, \quad a_0 = a/h, \quad S = \mu\sigma_{sp}/R_{bt} \quad (14)$$

We will re-write these equations in the following form:

$$\xi^2 + 2(1.05 + 2.05\alpha\mu + S/1.3)\xi - 1.05 - 2.05\alpha\mu - 1.54S = 0,$$

$$\frac{M_t}{bh^2R_{bt}} = (1-\xi)(0.076 + 0.265\xi) + 2.667\alpha\mu(0.5 - a_0) + \frac{0.222\xi^2(3-2\xi)}{1-\xi} + S(0.5 - a_0).$$

For non-reinforced rectangular section according to these equations, we obtain $\xi = 0.417$, $W_{pe} = 0.252bh^2$, that coincides with the known formula of material resistance $W_{pe} = bh^2/4$.

2.3. Designing the stress state of a section with a crack

The first cracks along the length of the element appear in the most loaded section or due to the non-uniform strength of concrete in the weakest section. With the distance from the edges of the crack, due to adhesion with concrete, stress in the reinforcement decreases, and tensile stresses in concrete increase and where they reach the limit value, an adjacent crack appears located at the h_m distance from the first one. In the section with a crack the adhesion of the reinforcement to the concrete is broken, the tensile forces are generally taken up by the reinforcement. In the sections between the cracks both reinforcement and concrete take up tensile forces. Deformations and stresses in the reinforcement and concrete, as well as the height of the compressed zone between cracks vary. As it was noted above, for reinforced concrete structures without pre-stressing, the diagram-energy calculation method has been developed, but for pre-stressed reinforced concrete we will use below the classical formulation, when this unevenness in the calculations is taken into account by introducing special coefficients that are equal to the ratios of average values in the section between the cracks and values in the section with a crack.

$$\psi_s = \varepsilon_{sm}/\varepsilon_s, \quad \psi_b = \varepsilon_{bm}/\varepsilon_b.$$

All the existing analytical methods for calculating stress in sections with a crack suggest the known crack length. It is believed that it exists initially, regardless of the actual loads, and its length is determined by measurement. The actual crack length depends on the applied load. Therefore, we must be able to predict it.

The proposed designing method is based on the following assumptions:

the middle sections located between the cracks remain flat after bending;

in the part of the tension zone of concrete, where stresses have reached the tensile strength, a crack is formed and it does not take the loads;

in concrete of the tension zone over a crack the relationship between stress and strain is described by exponential law (1);

the concrete of the compressed zone does not work elastically, the stress diagram is replaced by a rectangle here taking into account the coefficient of completeness of the curve ω .

Let us consider the section of a general form shown in Fig. 2,a. The deformation curve in the middle section and the stress curve in the section with a crack are shown in Fig. 2,b and 2,c.

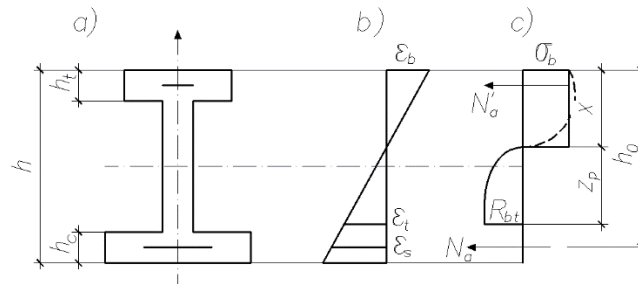


Figure 2. Towards designing a section with a crack.

By the deformation diagram, the strain at the tip of a crack will be equal

$$\varepsilon_t = 2.667 R_{bt} / E_b.$$

The strain at the boundary of the compressed zone is

$$\varepsilon_b = \varepsilon_t x / z_p = 2.66 (R_{bt} / E_b) x / z_p,$$

where $z_p = h - x - l_m$ is the height of the tension zone of concrete above the crack; l_m is the crack length.

Stresses at the boundary of the compressed zone will be

$$\sigma_b = E_b' \varepsilon_b = 2.667 R_{bt} \nu x / z_p, \quad \nu = E_b' / E_b.$$

Stresses on the reinforcement of the compressed zone

$$\sigma_s' = \sigma_{sp}' - \varepsilon_t E_s (x - a') / z_p = \sigma_{sp}' - 2.667 \alpha R_{bt} (x - a') / z_p.$$

Let us find stress in the reinforcement of the tension zone. In the middle section deformations at the level of the crack and the reinforcement are equal

$$\varepsilon_{tm} = \psi_b \varepsilon_t, \quad \varepsilon_{sm} = \varepsilon_{tm} (h_0 - x) / z_p, \quad h_0 = h - a.$$

Deformation at the level of the reinforcement in the section with a crack

$$\varepsilon_s = \varepsilon_{sm} / \psi_s = \varepsilon_t \psi_b / \psi_s \cdot (h_0 - x) / z_p.$$

Then stress in the reinforcement is equal

$$\sigma_s = E_s \varepsilon_s = 2.667 \alpha R_{bt} (\psi_b / \psi_s) (h_0 - x) / z_p. \quad (15)$$

The internal forces resultant in the tension zone and their moment relative to the zero line are determined by formulas (9) with substituting $(h - x)$ by z_p . These forces moment relative to the concrete center of gravity will be

$$M_{pc} = M_{po} - N (h/2 - x) = R_{bt} b z_p [0.418 z_p - 0.683 (h/2 - x)].$$

Let us write down the equation of the forces equilibrium in the section with a crack

$$\sigma_s A_s + N_p + \sigma_{sp}' A_s' - 2.667 \alpha R_{bt}' A_s' (x - a') / z_p - \omega \sigma_b (bx + A_c) \pm P = 0.$$

Substituting here the above-determined forces and stresses, after transformations we will write

$$0.256 b z_p^2 + \alpha A_s \frac{\psi_b}{\psi_s} (h_0 - x) + \frac{0.375 z_p \sigma_{sp}' A_s'}{R_{bt}'} - \alpha A_s' (x - a') - \omega \nu x (bx + A_c) \pm \frac{P z_p}{2.667 R_{bt}'} = 0 \quad (16)$$

In this equation the product $\omega \nu$ weakly depends on the shape of the normal stress field of the compressed zone. For example, with a rectangular curve $\omega = 1$, the coefficient ν can be taken 0.5 in connection with the appearance of significant inelastic deformations; consequently, $\omega \nu = 0.5$. With a triangular curve (elastic deformations) $\omega = 0.5$, and $\nu = 1$; therefore, in this case $\omega \nu = 0.5$. The real curvilinear diagram in this zone is replaced by a rectangular diagram for convenience of calculation.

We will write the sum of moments of all forces relative to the center of gravity of the section with a crack.

$$M_{pc} + \sigma_s A_s \left(\frac{h}{2} - a \right) + \sigma_b \omega b x \frac{h-x}{2} + \sigma_b \omega A_c \frac{h-h_c}{2} + 2.667 \alpha R_{bt}' A_s' \frac{(x-a') \left(\frac{h}{2} - a' \right)}{z_p} - \sigma_{sp}' A_s' \left(\frac{h}{2} - a' \right) = M_{bn}.$$

Since stress σ_s in the reinforcement of the tension zone occurs after the moment of the external forces M exceeds the moment of the pre-stress force M_{pr} , in this equation the total external moment is

$$M_{bn} = M - M_{pr} = M - \sigma_{sp}' A_s' (h/2 - a),$$

where the bending moment M is taken from the external forces relative to the concrete center of gravity.

By substituting in the equation of the moment the above-determined stresses, after transformations we will obtain

$$0.157 b z_p^3 - 0.256 b z_p^2 (h/2 - x) + \alpha A_s (\psi_b / \psi_s) (h_0 - x) (h/2 - a) + \nu \omega x [bx(h-x) + A_s (h - h_c)] / 2 + \alpha A_s' (x - a') (h/2 - a') - 0.375 z_p [\sigma_{sp}' A_s' (h/2 - a') + M_{bn}] / R_{bt}' = 0. \quad (17)$$

Equations (16) and (17) form a system of two nonlinear algebraic equations relative to two unknown values (x, z_p) . After solving this system, stress in the reinforcement is determined by expression (15). The boundary stress in the compressed zone concrete is determined by the deformation diagram by substituting deformation ε_b :

$$\sigma_b = 1.1 R_{bn} \left[1 - \exp(-2.4 x R_{bt}' / R_{bn} z_p) \right].$$

The crack length is determined by the formula

$$l_m = h - x - z_p.$$

To make the calculations it is necessary to determine preliminarily the irregularity ratios. The norms [2, 3] recommend $\psi_b = 0.9$, a

$$\psi_s = 1.25 - \varphi_{es} \varphi_m - \frac{1 - \varphi_m^2}{(3.5 - 1.8 \varphi_m) M / N_t e_{op}}, \quad (18)$$

where the total axial force

$$N_t = \pm P + P_0;$$

$P_0 = \sigma_{sp} A_s$ is the force of pre-stress; e_{op} is the eccentricity of the total force relative to the concrete center of gravity.

The φ_{es} coefficient characterizes the duration of the load action and the profile of the reinforcement bars. It is selected in the following way [3]: under short-term load for corrugated bars $\varphi_{es} = 1.1$; for plain bars and wire binders $\varphi_{es} = 1$; under long-term load independent on the reinforcement profile $\varphi_{es} = 0.8$.

The coefficient

$$\varphi_m = M_{b,m} / M_{bn} \leq 1,$$

where $M_{b,m}$ is the moment taken up by the concrete non-reinforced section prior to the crack formation determined from equations (12) and (13). For the rectangular section $\xi = 0.417$, and $M_{b,m} = 0.252bh^2 R_{bt}$.

For binding elements without pre-stress formula (18) is simplified

$$\psi_s = 1.25 - \varphi_{es} \varphi_m.$$

The norms also allow using the simplified expression [2, 9]:

$$\psi_s = 1 - 0.85 \varphi_m.$$

Let us write down resolving equations (16) and (17) for the rectangular section with the unilateral reinforcement in the tension zone with bending

$$0.256\lambda^2 - 0.5\xi + \alpha\mu(\bar{h} - \xi)\psi_b / \psi_s = 0, \quad (19)$$

$$0.157\lambda^3 - 0.256\lambda^2(0.5 - \xi) + \alpha\mu(\bar{h} - \xi)(\bar{h} - 0.5)\psi_b / \psi_s + \xi^2(1 - \xi)/4 - 0.357\lambda M_{bn} / R_{bt}bh^2 = 0.$$

Here there are used dimensionless parameters (14) and added

$$\lambda = z_p / h, \quad \bar{h} = h_0 / h.$$

From the first equation of this system

$$\lambda = \sqrt{1.95\xi^2 - 3.9\alpha\mu(\bar{h} - \xi)\psi_b / \psi_s}. \quad (a)$$

The integrand must be larger than zero:

$$\xi \geq -\alpha\mu\psi_b / \psi_s + \sqrt{(\alpha\mu\psi_b / \psi_s)^2 + 2\alpha\mu\bar{h}\psi_b / \psi_s}. \quad (b)$$

From the second equation of the system we will write

$$y = \frac{M_{bn}}{R_{bt}bh^2} = 0.418\lambda^2 - 0.683\lambda(0.5 - \xi) + \frac{2.667\alpha\mu(\bar{h} - \xi)(\bar{h} - 0.5)\psi_b / \psi_s + 0.667\xi^2(1 - \xi)}{\lambda}. \quad (c)$$

The system of equations (a), (c) is convenient to be solved graphically. We will take ξ according condition (b), according to (a) we determine λ ; then we find y from expression (c). Repeating these procedures, we build the function graph $y = f(\xi)$. The graph crossing with horizontal $y = M_{bn} / R_{bt}bh^2$

gives the ξ value that satisfies the system being solved. Then from (a) we obtain λ . The further determining of the stress state parameters is carried out according to the above-described methodology.

3. Results and Discussion

At present pre-stresses are determined by the elastic model for the transformed concrete section. Replacing the real section with the transformed one is, in our opinion, not entirely justified. The modeling of pre-stressing using the finite element method shows that the linear relationship between stress and strain is confirmed only for the compressed zone of concrete; in the tension zone the stress profile is not linear.

To estimate the error of the existing designing method, a calculation was performed using the LIRA program for the rectangular cross section with dimensions of $b = 15.3 \text{ cm}$, $h = 30.1 \text{ cm}$ with pre-stressed single reinforcement in the compressed zone: $A_s = 4 \text{ cm}^2$, $a' = 2.8 \text{ cm}$, $\sigma'_{sp} = 112 \text{ MPa}$. The material characteristics are as follows: B40 class concrete, grade TB ($R_{bt} = 2.1 \text{ MPa}$, $E_b = 3.2 \cdot 10^4 \text{ MPa}$); A-III class reinforcement ($R_s = 370 \text{ MPa}$, $E_s = 2.1 \cdot 10^5 \text{ MPa}$). The difference between the numerical results and the results of the linear calculation was 37 % for tensile stresses and 7.5 % for compressive stresses. This was the basis for developing a nonlinear method for calculating pre-stress, which reduced the indicated error to 5 % for tensile stresses and to 2.8 % for compressive stresses.

In addition, of independent significance is determining pre-stress in the formation of a crack σ_{pr} . This allows reasonable selecting the value of the controlled pre-stressing of the reinforcement σ_{con} in manufacturing pre-stressed concrete structures. At present the norms recommend that $\sigma_{con} \leq 0.8R_s$. We believe that this stress should be limited to 80 % of the stress in the formation of cracks ($\sigma_{con} \leq 0.8\sigma_{pr}$).

Determining the moment for the crack formation refers to regulatory calculations. In the normative model it is assumed that in the tension zone of concrete, stress is constant and equal to the tensile strength R_{bt} . But logic dictates that in order for the crack appearance it is enough for the maximum tensile stress to reach the limit value. It follows that the normative calculations give overestimated values of the moment for the crack formation. These arguments confirmed the numerical calculations by the finite element method. Therefore, the problem of determining the moment of the crack formation was set and solved on the basis of the actual strain diagram of the tension zone of concrete. According to the developed method, the moment of the crack formation is much smaller than that in the existing method. So, for the above section with non-stressed reinforcement by our method it has been obtained

$$\xi = 0.53, M_m = 0.318R_{bt}bh^2 = 0.318 \cdot 2100 \cdot 0.153 \cdot 0.301^2 = 9.24 \text{ kNm}.$$

According to the existing methodology

$$\xi = 0.526, M_m = 0.68R_{bt}bh^2 = 19.4 \text{ kNm}.$$

To check the proposed model, a nonlinear calculation of the stress state of the reinforced concrete element considered above for pure bending was performed using the finite element method using the ANSYS program. The bending moment was increased with a certain step and the appearance of a crack controlled. It appeared at $M = 10.8 \text{ kNm}$, which exceeds the moment calculated by us by 8.3 %, and the position of the zero line almost coincides. Taking this into account, the proposed model should be recognized as adequate and suitable for engineering calculations.

An important result of the work is the developed analytical method for designing the stress state in the cross section with a crack, which makes it possible to determine the crack length. According to this method, the stress state of the previously considered rectangular section without pre-stressing from the bending moment $M = 18 \text{ kNm}$ has been calculated and there has been obtained

$$\sigma_s = 189.8 \text{ MPa}, \sigma_b = 9.2 \text{ MPa}, l_m = 15.8 \text{ cm}.$$

To assess the accuracy of the method this problem was solved by the numerical method using the numerical method using the ANSYS program. There were obtained the following results (in brackets there is indicated % of the results discrepancy):

$$\sigma_s = 184.1 \text{ MPa (3 \%)}, \sigma_b = 9.2 \text{ MPa (5.4 \%)}, l_m = 16.5 \text{ cm (4.2 \%)}$$

Comparing the calculation results indicates good accuracy of the proposed method of designing the stress state of reinforced concrete beams with cracks.

Resolution equation (19) gives the relationship between the dimensionless parameters of the compression zone height and the length of the crack. A plot of the experimental relationship between these parameters is given in [1] (Fig. 8.11). For comparison, we built this graph according to equation (19) with $\alpha\mu = 0.038$, $\psi_b/\psi_s = 1.2$, $\bar{h} = 0.907$. In Fig. 3 it is shown by the solid line. In the same place, a dashed line shows this dependence obtained by the finite element method. In addition, the experimental points from the aforementioned graph are plotted with a cross (the other points are absent). The maximum deviation of our results from the numerical experiment is 9.1 %, and from the full-scale experiment 9.2 %. This discrepancy in results can be considered satisfactory.

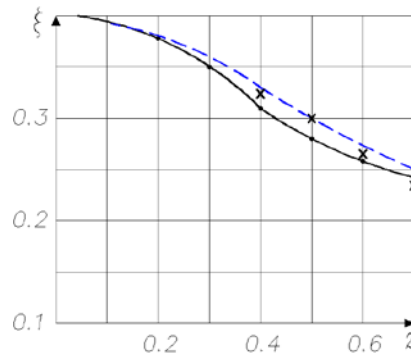


Figure 3. Compression zone height dependence on the crack length.

In [27] experimental values of the maximum compressive deformations in a bent reinforced concrete beam of rectangular cross section under various external loads are given. For comparison with the experimental value, we performed a calculation with the force $F = 400 \text{ kg}$ using the described methodology. In this case

$$y = \frac{Fl}{4R_{bt}bh^2} = \frac{400 \cdot 9.8 \cdot 0.9}{4 \cdot 1.4 \cdot 10^6 (7 \cdot 14^2) 10^{-6}} = 0.459;$$

$$\alpha\mu\psi_b/\psi_s = (20/2.05)0.005 \cdot 0.9/0.68 = 0.065; \quad \bar{h} = 0.9.$$

Solution of system (19) gives $\xi = 0.307$, $\lambda = 0.182$. The maximum strain in concrete

$$\varepsilon_b = 2.667(R_{bt}/E_b)\xi/\lambda = 2.667(1.4/20500)0.307/0.182 = 3.07 \cdot 10^{-4}.$$

The strain experimental value is 2.96×10^{-4} . The results discrepancy makes 3.6 %.

This calculation method allows determining all the parameters of the stress state in the section with a crack. These parameters can be used to determine the step and width of the crack opening (critical parameter) according to the normative method [1–3].

4. Conclusion

The paper proposes an analytical method for determining stresses in reinforced concrete elements when mounting reinforcement with preliminary stress. From the obtained dependences, the value of the ultimate stress of the reinforcement is determined at which a crack appears in the element. This allows reasonable selecting the value of the controlled pre-stressing of the reinforcement.

In the proposed method of assessing the bearing capacity of bent reinforced concrete beams determining the stress-strain state of these beams taking into account operational cracks is of great importance. The proposed method of calculating reinforced concrete beams with a crack, in contrast to the existing analytical calculation methods, allows determining the length of a crack in a section. This is very important for determining the parameters of fracture mechanics in the future and assessing on this basis the crack resistance of the structures by the force criterion.

Based on the results of the work, the following conclusions can be made.

1. A methodology for nonlinear analytical calculation of the stress state of reinforced concrete elements with pre-stressing of reinforcement has been developed.
2. The limiting value of the preliminary stress of the reinforcement is determined, at which a crack appears at the manufacturing stage.
3. A new technique is proposed for determining the external moment from crack formation.
4. A new analytical method has been developed for calculating bending reinforced concrete beams with a crack, which allows determining all the parameters of the stress state: maximum compressive stress in concrete, stresses in reinforcing bars, crack length and height of the compression zone.

The method is qualitatively confirmed by comparing with experimental data of determining the relationship between the crack length and the height of the compression zone [1] and determining the maximum compressive deformations in a bending reinforced concrete beam with a crack [27]. In addition, the proposed analytical method agrees well quantitatively with numerical calculations by the finite element method. The maximum deviation in the calculations to determine pre-stresses in rectangular elements and the stress state parameters in cross sections with a crack did not exceed 5.4 %.

The calculation method is valid for bending reinforced concrete beams of arbitrary section with working rod reinforcement.

References

1. Zaytsev, Yu.V. Mekhanika razrusheniya dlya stroiteley [Destruction mechanics for builders]. Moscow: Higher school, 1991. 288 p. (rus)
2. Nuguzhinov, Zh.S. Teoriya rascheta zhelezobetonnykh konstruksiy s povrezhdeniyami [Theory of calculating reinforced concrete structures with damage]. Karaganda: KSTU Publishing house, 2012. 203 p. (rus)
3. Baykov, V.N., Sigalov, E.Ye. Zhelezobetonnyye konstruksii: Obshchiy kurs [Reinforced concrete structures: General course]. Moscow: Stroyizdat, 1991. 767 p. (rus)
4. Travush, V.I., Konin, D.V., Krylov, A.S. Strength of reinforced concrete beams of high-performance concrete and fiber reinforced concrete. Magazine of Civil Engineering. 2018. 77(1). Pp. 90–100. DOI: 10.18720/MCE.77.8
5. Desnerck, P., Lees, J., Morley, C. Bond behaviour of reinforcing bars in cracked concrete. Construction and Building Materials. 2015. Vol. 94. Pp. 126–136. DOI: 10.1016/j.conbuildmat.2015.06.043
6. Chernin, L., Val, D.V. Prediction of corrosion-induced cover cracking in reinforced concrete structures. Construction and Building Materials. 2011. 25 (4). 1854–1869. DOI: 10.1016/j.conbuildmat.2010.11.074
7. Kolchunov, V.I., Dem'yanov, A.I. The modeling method of discrete cracks in reinforced concrete under the torsion with bending. Magazine of Civil Engineering. 2018. 81 (5). Pp. 160–173. DOI: 10.18720/MCE.81.16
8. Kwan, A.K.H., Ma, F.J. Crack width analysis of reinforced concrete under direct tension by finite element method and crack queuing algorithm. Engineering Structures. 2016. Vol. 126. Pp. 618–627. DOI: 10.1016/j.engstruct.2016.08.027
9. Ma, F.J., Kwan, A.K.H. Crack width analysis of reinforced concrete members under flexure by finite element method and crack queuing algorithm. Engineering Structures. 2015. Vol. 105. Pp. 209–219. DOI: 10.1016/j.engstruct.2015.10.012
10. Ng, P, Ma, F, Kwan, A. Crack analysis of reinforced concrete members with and without crack queuing algorithm. Structural Engineering and Mechanics. 2019. 70 (1). Pp. 43–54. DOI: 10.12989/sem.2019.70.1.043
11. Oliver-Leblond, C., Delaplace, A., Ragueneau, F. Modelling of three-dimensional crack patterns in deep reinforced concrete structures. Engineering Structures. 2015. Vol. 83. Pp. 176–186. DOI: 10.1016/j.engstruct.2014.10.040
12. Tan, R., Eileraas, K., Whispers, O., Zirgulis, G., Hendriks, M.A.N., Geiker, M., Brekke, D.-E., Kanstad, T. Experimental and theoretical investigation of crack width calculation methods for RC ties. Structural Concrete. 2018. 19 (5). Pp. 1436–1447. DOI: 10.1002/suco.201700237
13. Yang, S.T., Li, K.F., Li, C.Q. Numerical determination of concrete crack width for corrosion-affected concrete structures. Computers & Structures. 2018. Vol. 207. Pp. 75–82. DOI: 10.1016/j.compstruc.2017.07.016
14. Amin, A., Gilbert, R.I. Instantaneous Crack Width Calculation for Steel Fiber-Reinforced Concrete Flexural Members. ACI Structural Journal. 2018. 115 (2). Pp. 535–543. DOI: 10.14359/51701116
15. Bashirov, Kh.Z., Chernov, K.M. Razrusheniye zhelezobetonnykh sostavnykh konstruksiy ot poteri stsepleniya v zone zaankerivaniya po naklonnym treshchinam tretyego tipa [Tangential section failure of anchorage zone in composite reinforced concrete elements]. Stroitel'naya mekhanika i raschet sooruzheniy. 2013. 1 (246). Pp. 02–06.
16. Travush, V.I., Krylov, S.B., Konin, D.V., Krylov, A.S. Ultimate state of the support zone of reinforced concrete beams. Magazine of Civil Engineering. 2018. 83 (7). Pp. 165–174. DOI: 10.18720/MCE.83.15
17. Hua, Zhu. Crack formation of steel reinforced concrete structure under stress in construction period. Frattura ed Integrità Strutturale. 2016. No. 36. Rp. 191–200. DOI: 10.3221/IGF-ESIS.36.19
18. Salnikov, A., Kolchunov, V.I., Yakovenko, I. The computational model of spatial formation of cracks in reinforced concrete constructions in torsion with bending. Applied Mechanics and Materials. 2015. Vol. 725-726. Pp. 784–789. DOI.org/10.4028/www.scientific.net/AMM.725-726.784
19. Dem'yanov, A., Salnikov, A. The estimation of spatial cracks formation in reinforced concrete structures under the action torsion with bending. IOP Conference Series: Materials Science and Engineering. 2018. 365 (5). DOI: 10.1088/1757-899X/365/5/052019
20. Visintin, P., Sturm, A., Oehlers, D. Long- and short-term serviceability behavior of reinforced concrete beams: Mechanics models for deflections and crack widths. Structural Concrete. 2018. 19 (2). Pp. 489–507. DOI: 10.1002/suco.201700022
21. Deng, Zh., Wang, Y., Yang, H., Qian, J. Research on Crack Behavior of Recycled Concrete Beams under Short-term Loading. KSCE Journal of Civil Engineering. 2018. 22 (5). Pp. 1763–1770. DOI: 10.1007/s12205-017-0678-7
22. Shafigullin, L.N., Treschev, A.A., Telichko, V.G., Erofeev, V.T. Calculation of reinforced concrete shell of positive Gaussian curvature, given different resistance of concrete and cracking. Astra Salvensis. 2017. Pp. 77–91.

23. Sheng, J., Yin, S.P., Xu, S.L., Jin, Z.Y. Experimental and theoretical investigations on crack spacing and stiffness of textile-reinforced concrete-strengthened reinforced concrete beams. *Advances in Structural Engineering*. 2018. 21 (11). Pp. 1696–1707. DOI: 10.1177/1369433218754333
24. Mitasov, V.M., Logunova, M.A., Statsenko, N.V. Novyye podkhody k resheniyu zadach deformirovaniya zhelezobetonnykh konstruksiy s treshchinami [New approaches to the solution of the tasks of deformation of reinforced framings with cracks]. *Izvestiya vuzov. Investitsii. Stroitelstvo. Nedvizhimost*. 2017. Vol. 7, No. 1. Pp. 77–82.
25. Koyankin, A.A., Mitasov, V.M., Deordiev, S.V. The compatibility of deformation of the hollow-core slab with beams. *Magazine of Civil Engineering*. 2019. 87 (3). Pp. 93–102. DOI: 10.18720/MCE.87.8
26. Travush, V.I., Konin, D.V., Krylov, A.S. Strength of composite steel and concrete beams of high-performance concrete. *Magazine of Civil Engineering*. 2018. 79 (3). Pp. 36–44. DOI: 10.18720/MCE.79.4
27. Mikhaylova, N.S. Eksperimentalnyye issledovaniya zhelezobetonnykh balok bez treshchin i zaraneye namechennoy treshchiny [Experimental Investigation of Reinforced Concrete Beams without Cracks and with Previously Intended Crack]. *Izvestiya vuzov*. 2007. Stroitelstvo. No. 4. Pp. 110–113. (rus)
28. Shardakov, I., Bykov, A., Shestakov, A. et al. Crack control in concrete using shock wave techniques. *Procedia Structural Integrity*. 2017. Vol. 5. Pp. 210–216. DOI: 10.1016/j.prostr.2017.07.114
29. Fantilli, A.P., Chiaia, B. Golden Ratio in the Crack Pattern of Reinforced Concrete Structures. *Journal of Engineering Mechanics*. 2013. Vol. 139. Pp. 1178–1184. DOI: 10.1061/(ASCE)EM.1943-7889.0000548
30. Bykov, A.A., Matveenko, V.P., Shardakov, I.N., Shestakov, A.P. Shock wave method for monitoring crack repair processes in reinforced concrete structures. *Mechanics of Solids*. 2017. Vol. 52. Pp. 378–383. DOI: 10.3103/S0025654417040033
31. Bílý, P., Kohoutková, A., Jedlinský, P. FEM simulation of static loading test of the Omega beam. *IOP Conference Series: Materials Science and Engineering*. 2017. 236 (1). Art. No. 012066, DOI: 10.1088/1757-899X/236/1/012066
32. Morozov, V.I., Pukhareno, Yu.V., Yushin, A.V. The numerical investigations of double-span concrete beams strengthened with fiber reinforced plastics across the oblique section. *Materials Physics and Mechanics*. 2017. 31 (1–2). Pp. 40–43.
33. Ma, F.J., Kwan, A.K.H. Finite element analysis of concrete shrinkage cracks. *Advances in Structural Engineering*. 2018. 21 (10). Pp. 1454–1468. DOI: 10.1177/1369433217746346
34. Rossi, P., Daviau-Desnoyers, D., Tailhan, J.L. Analysis of cracking in steel fibre-reinforced concrete (SFRC) structures in bending using probabilistic modeling. *Structural Concrete*. 2015. Vol. 16. Pp. 381–388. DOI: 10.1002/suco.201400081
35. Cohen, M., Monteleone, A., Potapenko, S. Finite element analysis of intermediate crack debonding in fibre reinforced polymer strengthened reinforced concrete beams. *Canadian Journal of Civil Engineering*. 2018. 45 (10). Pp. 840–851. DOI: 10.1139/cjce-2017-0439
36. Nagy, N., Mohamed, M., Boot, J. Nonlinear numerical modelling for the effects of surface explosions on buried reinforced concrete structures. *Geomechanics and Engineering*. 2010. 2 (1). Pp. 1–18. DOI: 10.12989/gae.2010.2.1.001
37. Sainov, M.P., Kotov, F.V., Nazarov, N.V. Serviceability of rockfill dam with reinforced concrete face and grout curtain. *Magazine of Civil Engineering*. 2018. 79 (3). Pp. 77–85. DOI: 10.18720/MCE.79.8.18720/MCE.79.8
38. Chen, G., Teng, J., Chen, J. Finite-element modeling of intermediate crack debonding in FRP-plated RC beams. *Journal of Composites for Construction*. 2011. 15 (3) Pp. 339–353. DOI: 10.1061/(ASCE)CC.1943-5614.0000157
39. Utkin, V.S., Solovyev, S.A. Raschet nadezhnosti zhelezobetonnoy balki po kriteriyu dliny treshchiny [Calculation of reinforced concrete beam reliability on the crack length criterion]. *Stroitel'naya mekhanika inzhenernykh konstruksiy i sooruzheniy*. 2016. No. 5. Pp. 24–33.
40. Klyuyeva, N.V., Kolchunov, V.I., Yakovenko, I.A. Problemnyye zadachi razvitiya gipotez mekhaniki razrusheniya primenitelno k raschetu zhelezobetonnykh konstruksiy [Problem tasks of development of hypotheses of mechanics of destruction in relation to calculation of ferroconcrete designs]. *Izvestiya KGASU*. 2014. No. 3 (29) Pp. 41–45. (rus)
41. Korsun, V., Vatin, N., Franchi, A., Korsun, A., Crespi, P., Mashtaler, S. The strength and strain of high-strength concrete elements with confinement and steel fiber reinforcement including the conditions of the effect of elevated temperatures. *Procedia Engineering*. 2015. 117 (1). Pp. 970–979. DOI: 10.1016/j.proeng.2015.08.192
42. Almazov, V.O. *Proyektirovaniye zhelezobetonnykh konstruksiy po yevronormam* [Designing reinforced concrete structures according to Euro-norms]. Moscow: ACB Publ. House, 2011. 216 p. (rus)

Contacts:

Zhmagul Nuguzhinov, kazmirr@mail.ru

Nikolai Vatin, vatin@mail.ru

Zhetpisbai Bakirov, bakirov_50@mail.ru

Omirkhan Khabidolda, oka-kargtu@mail.ru

Syrlybek Zholmagambetov, syrlybekzh@mail.ru

Irina Kurokhtina, kurokhtina.ira@mail.ru

© Nuguzhinov, Zh., Vatin, N., Bakirov, Zh., Khabidolda, O., Zholmagambetov, S., Kurokhtina, I., 2020



DOI: 10.18720/MCE.97.2

Fine-grained concrete with various types of fibers

Y.E. Begich^{a*}, S.V. Klyuev^b, V.A. Jos^a, A.V. Cherkashin^a

^a Peter the Great St. Petersburg Polytechnic University, St. Petersburg, Russia

^b Belgorod State Technological University named after V.G. Shukhov, Belgorod, Russia

* E-mail: yasmin1010@yandex.ru

Keywords: fiber, fine-grained concrete, amorphous fiber, strength properties, fiber reinforced materials, fiber-reinforced concrete cements, binders concretes, cementitious concrete, mechanical activation

Abstract. This paper investigates the strength properties of the fine-grained concrete reinforced with the amorphous fiber based on the Fe-B-C system and obtained by the "spinning" method, and concretes reinforced with commercially available types of fibers: fiber based on mineral wool, basalt fiber, fiberglass, steel and polypropylene fibers. The flexural and compressive strength tests with the fiber-reinforced concrete specimens were carried out in accordance with the standard method corresponding to the Russian State Standard. The analysis of results was made by comparison with the characteristics of the control specimens without reinforcement. The best flexural strength characteristics were shown by specimens with the amorphous fiber, while the highest compressive strength was demonstrated with the steel fiber. The addition of the amorphous fibers leads to an increase of 56 % in the flexural strength, but decreases the compressive strength by 30 % compared to the control specimens, which proves the efficiency of this fiber working in bending. The addition of the steel fiber shows an increase of 20 % in flexural strength and an increase of 14 % in compressive strength, which confirms the positive effect of adding a commercially available fiber to the fine-grained concrete. The compounds of the fiber concrete with the compression strength limit up to 38 MPa and tensile strength in bending up to 12 MPa were developed, which allows to use amorphous fiber as a compound of fine-grained concrete in the construction industry.

1. Introduction

Nowadays, the actual direction of the development of high-quality cement concretes, characterized by a wider range of functional capabilities, is the use of complex additives that combine components with various functional purposes. Such additives allow to effectively manage the processes of structure formation at all stages of the technology of concrete preparation and, as a result, allow to obtain the concrete with various high-performance properties [1–3].

To increase the strength characteristics of modern concrete, various technical and technological solutions are used, including dispersed reinforcement with fibers. This type of building material is called fiber-reinforced concrete. The industry of modern building materials demonstrates various types of fibers used in the manufacture of the fiber-reinforced concrete. Fibers of both artificial and natural origin are used.

Every year the application field of the fiber-reinforced concrete is becoming wider. The use of various types of fibers is determined by their purpose: the amorphous and the steel fibers are used in new construction to increase the bearing capacity of the structure. It is generally recommended to use these fibers in floor slabs or walls experiencing strong bending loads. In the reconstruction of buildings and structures, the amorphous and the steel fibers are used to strengthen the load-bearing structures. It is proposed to use a layer of the fiber-reinforced concrete as a reinforcement for damaged vertical structures due to its increased bending strength compared to the ordinary concrete [4, 5]. The other types of fibers are mainly used to unweight construction and increase crack resistance. These fibers are added to various blocks (autoclaved aerated concrete, foam concrete and others) to reduce their weight and to the floor screed construction.



Besides the new properties of the fiber-reinforced concrete, this material suggests a new technology for the manufacturing of reinforced concrete products. This technology allows preparing a reinforced concrete mixture in concrete mixers due to the possibility of adding fibers with other aggregates directly into the mixers. In this case the time of the manufacturing is reduced and the labor costs for reinforcing works are becoming unnecessary.

Moreover, the fiber-reinforced concrete opens up great opportunities for the use of recycled materials, and, as a result, for the improvement of the environmental situation in the world through the efficient disposal of material debris. The use of fibers from the plastic PET (polyethylene terephthalate) waste in the fiber-reinforced concrete showed the comparable efficiency with using the commercial synthetic fiber specimens [6]. The authors of [7] investigate the efficiency of using recycled steel fibers obtained from machining process discards.

The widely used and most studied artificial types of fibers are steel ones, as well as fibers based on polymers, for example, polypropylene fiber.

The articles [8, 9] present the results of the study of the steel fiber for dispersed concrete reinforcement. The experimental studies of the deformation characteristics of the steel fiber concrete specimens are described. It was obtained that reinforcement with the steel fiber increases the compressive strength of concrete by 15 % and the flexural strength by 50 % compared to concrete without reinforcement. In contrast to the previous studies, where the cement was a binder in the fiber-reinforced concrete mix, the papers [10–12] deal with the steel-fiber-reinforced concrete specimens based on the fine ground cement and the low water demand binder. It was established that the use of composite binders and the high-density packing of aggregate grains significantly increases strength characteristics. The compressive strength of the specimens ranged from 84.8 MPa to 160.2 MPa, when the flexural strength was in the range from 19.8 MPa to 31.2 MPa.

The issues of using the polymer fiber for the concrete reinforcement are considered in [13, 14]. The results of determining the strength characteristics are presented. The studies show that the adding of the polymer fibers increases the flexural strength of the concrete specimens by 18–32 %. The simultaneous use of the steel and the polypropylene fibers for the reinforcement shows a positive synergistic effect [15]. These specimens show the higher flexural strength compared with the studied specimens, where the steel and the polypropylene fibers were used separately from each other. The steel-fiber-reinforced concrete mixtures and the concrete mixtures reinforced with the polymer fibers were studied in detail in [16], where the features and recommendations for the preparation of these mixtures are described.

In the article [17] the authors use waste in the production of mineral wool as an additive to concrete. The compressive strength of the obtained materials reaches 80 MPa. Moreover, these specimens are characterized by high water resistance.

Also, some fibers of organic origin are used for the dispersed reinforcement. The jute fibers have a positive effect on the flexural and compressive strengths [18]. The authors of articles [13, 19] consider sisal fiber as dispersed reinforcement. The results demonstrate that the sisal fiber reinforcement could provide the same level of residual strength for concrete as the polypropylene fiber reinforcement.

The main issue of optimizing the geometric parameters and the physical properties of the fiber is the need to ensure reliable adhesion of the fiber to the cement matrix under loads, as well as resistance to withstand tensile forces [20–22]. The interfacial connection of the fiber and the matrix is very important – it helps to counteract the shear stress transmitted from the cement matrix to the fibers at the interface. As the adhesion increases, the resulting cement composites become more durable and elastic due to the transmission of the arising tangential stresses from the concrete to the fibers. The results of experimental studies of the influence of the type, length, and amount of reinforcing fibers on the structure and strength of the fiber-reinforced concrete are presented in [12, 23].

The paper [24] investigates the numerical model for predicting the diffusion of chloride ions in fiber-reinforced concrete. Moreover, the results demonstrate that four factors, including the fiber diameter, the volume fraction of fibers, the aggregate diameter and the volume fraction of aggregates, significantly affect the diffusion of chloride in fiber concrete.

In addition, one of the most important characteristics of fiber-reinforced concrete is the increased crack resistance. This characteristic was investigated during the bending tensile tests by constructing and analyzing stress-strain curves of the specimens [25], as well as crack growth resistance curves [26].

The goal of the present work is to study the effect of the dispersed reinforcement of the fine-grained concrete with the amorphous fiber based on the Fe-B-C system, and to compare the strength characteristics of the fine-grained concrete specimens reinforced with the amorphous fiber with reinforcement with the following types of fibers: polypropylene fiber (Fig. 1), basalt fiber (Fig. 2), fiberglass (Fig. 3), mineral wool fiber (Fig. 4), steel fiber (Fig. 5).



Figure 1. Polypropylene fiber.



Figure 2. Basalt fiber.



Figure 3. Fiberglass.



Figure 4. Mineral wool fiber.



Figure 5. Steel fiber.



Figure 6. Amorphous fiber (Fe-B-C system).

The field of application of the fine-grained concrete and its characteristics depend on the properties of the fiber material. Currently three main types of dispersed micro-reinforcement are used abroad: fibers as short cuts of steel thin wire, glass and polypropylene fibers. Authors of this paper suggest using six different types of dispersed reinforcement: polypropylene, basalt, glass-fiber, mineral wool, steel and amorphous (Table 1).

Table 1. Technical characteristics of different fibers.

Indicator	Polypropylene fiber	Basalt fiber	Fiber-glass fiber	Mineral wool fiber	Steel fiber	Amorphous fiber
Material	Polypropylene	Basalt fiber	Glass fiber	Mineral wool	Carbon steel wire	Fe-B-C alloy
Fiber diameter	10–25 μm	13–17 μm	13–15 μm	15–30 μm	0,5–1,2 mm	30 μm
Fiber length	6–18 mm	3.2–15.7 mm	4.5–18 mm	0.5–1 mm	30–50 mm	35 mm
Melting temperature, $^{\circ}\text{C}$	160	1450	860	1110	1550	1700
Corrosion and alkali resistance	Low	High	Medium	High	Medium	Medium

2. Methods

To obtain the amorphous fiber the multicomponent amorphous metal alloy (metallic glass) was used. This alloy of the Fe-B-C system consisting of Mo (up to 20 %), Cr (up to 17 %), and V (6 %) was obtained at the “Material Science and Technology” department of «Institute of Metallurgy, Mechanical Engineering and Transport» of Peter the Great St. Petersburg Polytechnic University.

The initial ingots (40–50 g) of multicomponent alloys were made in quartz crucibles using high frequency currents (HFC). Melting was carried out in stages. At the first stage, the components of the Fe-B-C alloy in a certain weight ratio were melted in vacuum. Secondly the crucible was filled with an inert gas, after which

sparingly soluble alloying additives were introduced into the melt in the order of their reaction activity (Cr, Mo, V). Overheating at 200–500 °C above the melting temperature ensured complete dissolution of the components and a fairly uniform alloy structure.

In the following stage after melting, the necessary gas pressure in the crucible (Δp) is created and the melt is squeezed out in the form of a thin (fraction of a millimeter) jet onto a drum rotating at a speed of V_d . The drum is made of copper and rotates at a speed that provides a linear surface speed, and, consequently, provides a linear speed of the tape up to 50 m/s. The jet of melt drops at a speed V_m at an angle α to the surface, as a result, a stationary pool of melt is formed on the surface of the refrigerator drum [27].

This method of producing amorphous metal alloys in the form of thin tapes by means of ultrafast cooling of the melt on the surface of a rotating cold drum is called «spinning».

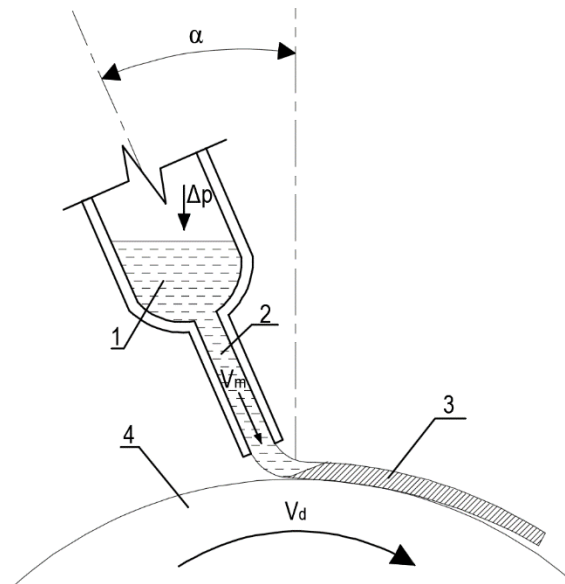


Figure 7. Scheme of the spinning process.

1 – molten metal, 2 – jet of melt, 3 – amorphous metal fiber, 4 – cold drum

The melt spinning method has been particularly investigated by many authors. Various modifications of this method can be used both for research purposes and for an industrial production of amorphous tapes of various alloys.

Cement PJSC “Evrocement group” (Joint stock company) Cement I 42,5N D0 and aggregate were used in the work in order to get high quality fiber concrete compounds. Their main physical-mechanical properties were studied for the estimation of the quality of the applied aggregate (Table 2).

Table 2. Physical-mechanical properties of the aggregate.

Indicator	Sand of Sestrinskii origin
Fraction module	1.38
Bulk density, kg/m ³	1448
True density, kg/m ³	2630
Voidness, %	44.9
Water demand, %	7

The compounds of the disperse-reinforced fine-grained concretes are presented in Table 3.

Table 3. Compounds of the disperse-reinforced fine-grained concretes.

No	Compound	Unit of measurement	Control
1	Cement	kg	650
2	Sand	kg	1500
3	Water	liters	210
4	Water/Cement Ratio		0.32

To obtain the beam specimens with the dimensions of 40×40×160 mm, the mortar mixture prepared according to the method, which was described above, was placed in a three-section mold. To consolidate the concrete by vibration the mold was fixed on a standard vibrating. Finally, this molds with the concrete specimens were stored for the first 24 hours in the high humidity space, then the beams freed from the molds were stored in water at a temperature of (20 ± 2) °C.

To obtain the comparable results, the described method of preparing a mortar mixture was also used in the process of manufacture of the test specimens with fibers. The fibers were added to the dry mixture of sand and cement in the amount of 1 % (21.8 kg), 2 % (43.7 kg) and 3 % (65.5 kg) of the mass of the concrete grout (2240 g). Then, after achieving a uniform distribution of the fibers in the mixture, water was added. The polypropylene fiber was added in the amount of 0.1, 0.5 and 1 % because of the low density.

Thereby the volume of this fiber is very significant, which violates the rheological properties of the concrete grout due to an increase of the overall specific surface. It is significant to note that during the process of adding water and the further process of preparing the mixture, the so-called “hedgehogs” (fiber clumping) were not observed, which proves the correctness of the fiber percentage in the concrete grout.

The flexural and compressive strength tests were carried out in accordance with the standard method corresponding to the Russian State Standard 310.4-81 at the age of 3, 7, 28 days.

3. Results and Discussion

The flexural and compressive strengths test results of the prismatic specimens from fiber-reinforced concrete are presented in the diagram form in Fig. 8 and Fig. 9 respectively.

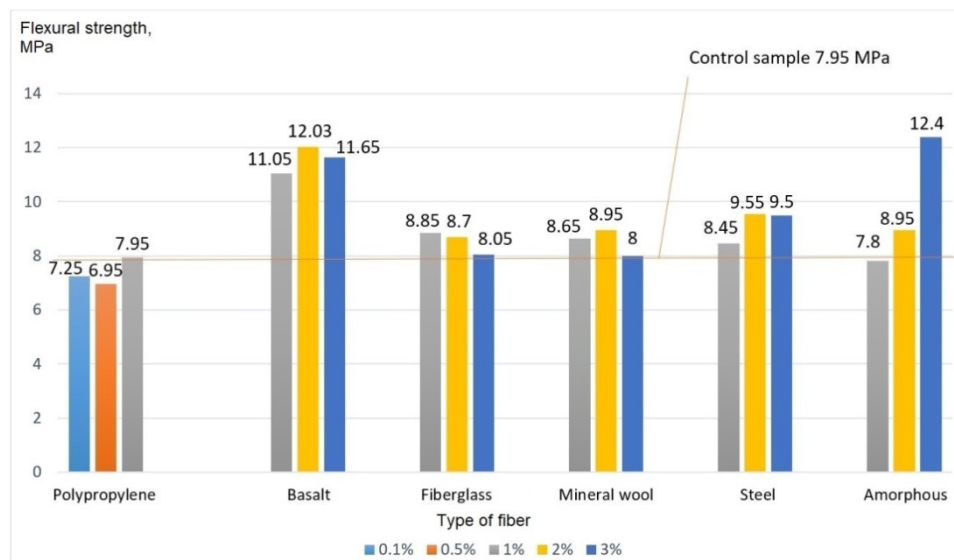


Figure 8. Flexural strength test results of fiber-reinforced concrete specimens.

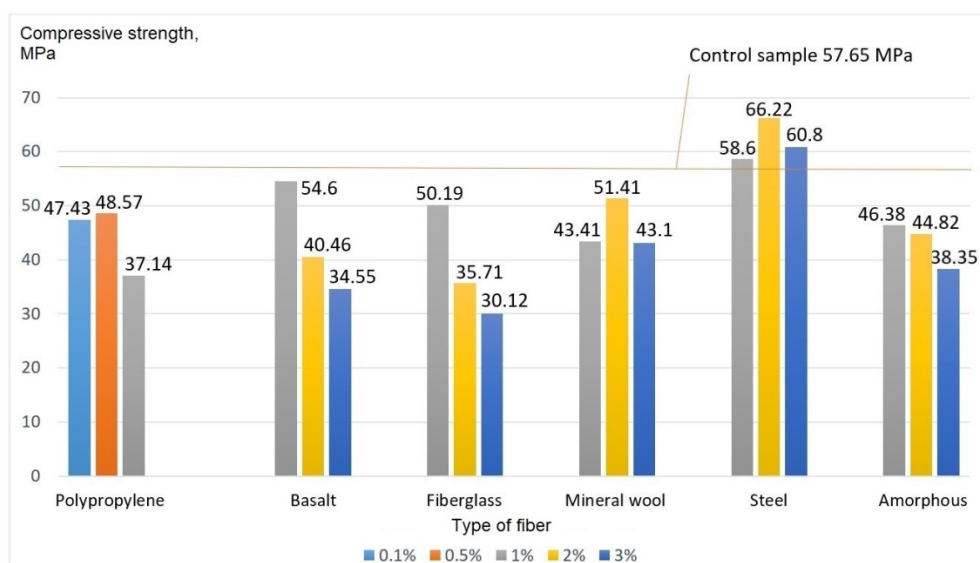


Figure 9. Compressive strength test results of fiber-reinforced concrete specimens.

The bar chart on Fig. 8 illustrates that the best flexural strength characteristics were shown by specimens with a content of 3 % amorphous fiber. This fact proves that the amorphous fiber works well together with the concrete matrix in bending. The specimens with basalt fiber demonstrate comparable results with the specimens reinforced with amorphous fiber. While the amorphous fiber shows an increase in flexural strength with increasing percentage concentration, the basalt fiber values remains nearly constant. All the others specimens show worse results, but an increase in flexural strength is still observed. The exception is only the specimens with polypropylene fiber demonstrating lower values compared to the control specimens.

The Fig. 9 represents that the sample with the steel fiber in 2 % concentration has the best compressive strength characteristic. It can be seen that the addition all the others fibers to the specimens led to a fall in compressive strength values. The main cause for such result is that the geometrical parameters of the steel fiber are smaller compared to the others (the length is about 10–12 mm). Such dimensions make the beam wall works in bending, which increases the compressive strength. It is important to note that the rise of percentage concentration of the fiberglass, basalt and amorphous fibers decreases the compressive strength.

The flexural and compressive tests of concrete specimens reinforced with different fibers were also carried out by the other authors. M.G. Gabidullin et al. found that the single-level dispersed concrete reinforcement with the steel fiber allows to increase the compressive strength of concrete by 15 % and the flexural strength by 50 % compared to concrete without reinforcement [8]. The authors of the paper [9] conducted experiments with concrete specimens reinforced by steel fiber to determine the compressive strength. The results show a growth in the range of 18.6–21 % compared with the specimens without reinforcement. The percentage value of the compressive strength increase in the present work is approximately 15 % (Fig. 9) which is very similar to the results obtained by the authors mentioned above.

The flexural strength of the steel fiber-reinforced fine-grained concrete is equal to 9.55 MPa and the compressive strength is equal to 66.22 MPa accordingly to the Fig. 8 and Fig. 9 respectively.

However, there are studies which demonstrates very high values (approximately 2 times higher) for the flexural and compressive strengths for the same type of fiber-concrete. The compressive strength of the specimens ranges from 84.8 MPa to 160.2 MPa, when the flexural strength is equal to 19.8–31.2 MPa [10–12]. Such high values of these strength characteristics were obtained because of special types of cement and aggregates used in the concrete mixture. These studies investigate the fine-grained concrete based on the fine ground cement and the low water demand binder. Moreover, the special type of technogenic sand was used. The sand was mined in Kursk Magnetic Anomaly. Technogenic sands comparing with natural ones have fundamental differences concerning the shape of grains, main properties and composition. The most obvious distinction is the rough, irregular and nonspherical shape of technogenic sand grains in contrast to the round and smooth shape of the natural sand structure. It is significant for comparative analysis to take into account the characteristics and of all the components in concrete mixture. In addition to this, the shape of fiber itself is quite important. For instance, the highest test results in [11] were demonstrated by the specimens with the wave-shaped fibers compared with other shapes. Authors of this research claim that the wave-shaped fibers as a reinforcing compound in steel fiber-reinforced fine-grained concrete have the best strength characteristics. The same wave-shaped fibers were used in [10, 12].

Polypropylene fiber is another commercially available type of fiber that demonstrates the decrease of strength values in experiments (Fig. 8, Fig. 9). Nevertheless, the papers [13–15] provide the positive conclusions about using the polymer fibers. D.N. Petrov observed the growth of the flexural strength in the range of 18–32 % with the addition of the polymer fiber to the concrete. This controversial fact may be explained by the use of fibers with different technical parameters and characteristics of material.

4. Conclusion

At this stage of the studies of the amorphous fiber of the Fe-B-C system and the comparison of its effect on the mechanical-and-physical properties of the fine-grained concrete with other types of fibers, the following conclusions may be highlighted:

1. The addition of the amorphous fibers in various concentrations to the cement composite leads to an increase of 56 % in the flexural strength, but decreases the compressive strength by 30 % compared to the control specimens.
2. The steel fiber showed an increase of 20 % in flexural strength and an increase of 14 % in compressive strength, which confirms the positive effect of adding a commercially available fiber to the fine-grained concrete.
3. The selected percentages (1, 2, 3 % of the weight of the control concrete grout) for all the above-mentioned fibers, except the polypropylene fiber, are optimal because of absence of the "hedgehogs" (fiber clumping).

4. The compressive strength decreases for all the observed fiber-reinforced concrete specimens (except the specimens with the steel fiber) compared to the control specimens. This fact proves that fibers, like dispersed inclusions in a concrete, adversely affect the compressive strength.

References

1. Subbotin, O.S. Osobennosti ispolzovaniya stroitelnykh materialov v restavratsii arkhitekurno-gradostroitel'nogo naslediya [Features of using building materials in the restoration of architectural and town-planning heritage]. *Construction Materials and Products*. 2019. 3 (2). Pp. 85–89. URL: <https://www.elibrary.ru/item.asp?id=39144982>
2. Elistratkin, M.Yu., Minakov, S.V., Shatalova, S. Vliyaniye mineralnoy dobavki v sostave kompozitsionnogo vyazhushchego na effektivnost raboty plastifikatora [Composite binding mineral additive influence on the plasticizer efficiency]. *Construction Materials and Products*. 2019. 2 (2). Pp. 10–16. URL: <http://bstu-journals.ru/wp-content/uploads/2019/07/elistratkin-2.pdf>
3. Strokova, V.V., Babayev, V.B., Markov, A.Yu., Sobolev, K.G., Nelyubova V.V. Cravnitel'naya otsenka konstruksiy dorozhnoy odezhdyy s ispolzovaniyem tsementobetona [Comparative evaluation of road pavement structures using cement concrete]. *Construction Materials and Products*. 2019. 2 (4). Pp. 56–63.
4. Vavruš, M., Koteš, P. Numerical comparison of concrete columns strengthened with layer of fiber concrete and reinforced concrete. *Transportation Research Procedia*. 2019. 40 (August). Pp. 920–926. DOI: 10.1016/j.trpro.2019.07.129. URL: <https://doi.org/10.1016/j.trpro.2019.07.129>
5. Gholampour, A., Hassanli, R., Mills, J.E., Vincent, T., Kunieda, M. Experimental investigation of the performance of concrete columns strengthened with fiber reinforced concrete jacket. *Construction and Building Materials*. 2019. 194. Pp. 51–61. DOI: 10.1016/j.conbuildmat.2018.10.236 URL: <https://doi.org/10.1016/j.conbuildmat.2018.10.236>
6. Khalid, F.S., Irwan, J.M., Ibrahim, M.H.W., Othman, N., Shahidan, S. Performance of plastic wastes in fiber-reinforced concrete beams. *Construction and Building Materials*. 2018. 183. Pp. 451–464. DOI: 10.1016/j.conbuildmat.2018.06.122 URL: <https://doi.org/10.1016/j.conbuildmat.2018.06.122>
7. Grzymiski, F., Musiał, M., Trapko, T. Mechanical properties of fibre reinforced concrete with recycled fibres. *Construction and Building Materials*. 2019. 198. Pp. 323–331. DOI: 10.1016/j.conbuildmat.2018.11.183 URL: <https://doi.org/10.1016/j.conbuildmat.2018.11.183>
8. Fládr, J., Bílý, P. Specimen size effect on compressive and flexural strength of high-strength fibre-reinforced concrete containing coarse aggregate. *Composites Part B: Engineering*. 2018. 138 (January 2018). Pp. 77–86. DOI: 10.1016/j.compositesb.2017.11.032 URL: <https://doi.org/10.1016/j.compositesb.2017.11.032>
9. Borisyuk, A.P., Zyatuk, Yu.Yu. Issledovaniye deformatsionnykh kharakteristik fibrobetona so stalnoy fibroy [The study of the deformation characteristics of fiber reinforced concrete with steel fiber]. *Vestnik Belorussko-Rossiyskogo universiteta*. 2016. 3 (52). Pp. 160–168.
10. Klyuev, S.V., Klyuev, A.V., Khezhev, T.A., Pukharenko, Y.V. Technogenic sands as effective filler for fine-grained fibre concrete. *Journal of Physics: Conference Series*. 2018. 1118 (1). DOI: 10.1088/1742-6596/1118/1/012020
11. Klyuev, S., Klyuev, A., Vatin, N. Fine-grained concrete with combined reinforcement by different types of fibers. *MATEC Web of Conferences*. 2018. 245. DOI: 10.1051/mateconf/201824503006
12. Klyuev, S.V., Klyuev, A.V., Abakarov, A.D., Shorstova, E.S., Gafarova, N.G. The effect of particulate reinforcement on strength and deformation characteristics of fine-grained concrete. *Magazine of Civil Engineering*. 2017. 75 (7). Pp. 66–75. DOI: 10.18720/MCE.75.6
13. Castoldi, R. de S., Souza, L.M.S. de, de Andrade Silva, F. Comparative study on the mechanical behavior and durability of polypropylene and sisal fiber reinforced concretes. *Construction and Building Materials*. 2019. 211. Pp. 617–628. DOI: 10.1016/j.conbuildmat.2019.03.282 URL: <https://doi.org/10.1016/j.conbuildmat.2019.03.282>
14. Petrov, D.N. Opredeleniye prochnostnykh pokazateley betonov s polimernoy fibroy [Determination of strength indicators of concrete with polymer fiber]. *Zapiski Gornogo instituta*. 2013. 204. Pp. 236–239.
15. Sukontasukkul, P., Jamsawang, P. Use of steel and polypropylene fibers to improve flexural performance of deep soil-cement column. *Construction and Building Materials*. 2012. 29. Pp. 201–205. DOI: 10.1016/j.conbuildmat.2011.10.040 URL: <http://dx.doi.org/10.1016/j.conbuildmat.2011.10.040>
16. Klyuev, S.V., Klyuev, A.V., Khezhev, T.A., Pucharenko, Y.V. High-Strength Fine-Grained Fiber Concrete with Combined Reinforcement by Fiber. *Journal of Engineering and Applied Sciences*. 2018. 13 (SI 8). Pp. 6407–6412. DOI: 10.3923/jeasci.2018.6407.6412 URL: <http://docsdrive.com/pdfs/medwelljournals/jeasci/2018/6407-6412.pdf>
17. Erofeev, V.T., Rodin, A.I., Yakunin, V.V., Tuvín, M.N. Structure, composition and properties of geopolymers from mineral wool waste. *Magazine of Civil Engineering*. 2019. 90 (6). Pp. 3–14. DOI: 10.18720/MCE.90.1
18. Fediuk, R. Reducing permeability of fiber concrete using composite binders. *Special Topics & Reviews in Porous Media: An International Journal*. 2018. 9. Pp. 79–89. DOI: 10.1615/SpecialTopicsRevPorousMedia.v9.i1.100
19. Sabarish, K.V., Paul, P., Bhuvaneshwari, Jones, J. An experimental investigation on properties of sisal fiber used in the concrete. *Materials Today: Proceedings*. 2019. DOI: 10.1016/j.matpr.2019.07.686 URL: <https://doi.org/10.1016/j.matpr.2019.07.686>
20. Bentur, A., Mindess, S. *Fibre Reinforced Cementitious Composites*. Second. CRC Press. London and New York, 2006.
21. Travush, V.I., Konin, D. V., Krylov, A.S. Strength of composite steel and concrete beams of high-performance concrete. *Magazine of Civil Engineering*. 2018. 79 (3). Pp. 36–44. DOI: 10.18720/MCE.79.4
22. Fediuk, R.S., Mochalov, A.V. Composite Binders for Concretes With Improved Shock Resistance. *University News. North-Caucasian Region. Technical Sciences Series*. 2018. (4). Pp. 85–91. DOI: 10.17213/0321-2653-2018-4-85-91
23. Pukharenko, Yu.V. Printsipy formirovaniya struktury i prognozirovaniye prochnosti fibrobetonov [Principles of structure formation and fiber concrete strength prediction]. *Vestnik grazhdanskikh inzhenerov*. 2004. (1). Pp. 98–103.
24. Liu, J., Jia, Y., Wang, J. Calculation of chloride ion diffusion in glass and polypropylene fiber-reinforced concrete. *Construction and Building Materials*. 2019. 215. Pp. 875–885. DOI: 10.1016/j.conbuildmat.2019.04.246 URL: <https://doi.org/10.1016/j.conbuildmat.2019.04.246>
25. Klyuev, S.V., Khezhev, T.A., Pukharenko, Y.V., Klyuev, A.V. The fiber-reinforced concrete constructions experimental research. *Materials Science Forum*. 2018. 931. Pp. 598–602.
26. Fediuk, R.S., Mochalov, A. V., Pezin, D.N., Liseitsev, Y.L. Composite Binders for Concretes with Improved Impact Endurance. *Inorganic Materials: Applied Research*. 2019. 10 (5). Pp. 1177–1184. DOI: 10.1134/S207511331905006X

27. Goykhenberg, Yu.N., Gamov, P.A., Dudorov, M.V., Roshchin, V.Ye. Struktura amorfiziruyushchegosya splava 5bdsr, ispolzuyemogo dlya proizvodstva nanokristallicheskoj lenty [The structure of the amorphizing alloy 5bdsr used for the production of nanocrystalline tape]. Vestnik YuUrGU. 2012. (39). Pp. 128–133.

Contacts:

Yasmin Begich, yasmin1010@yandex.ru

Sergey Klyuev, Klyuyev@yandex.ru

Vladislav Jos, jos_vlad@mail.ru

Artemiy Cherkashin, jizm@mail.ru

© Begich, Y.E., Klyuev, S.V., Jos, V.A., Cherkashin, A.V., 2020



DOI: 10.18720/MCE.97.3

Behavior of concrete beams reinforced with fiberglass composite rebar under load

M.V. Molodtsov*, E.P. Vshivkov, V.E. Molodtsova

South Ural State University, Chelyabinsk, Russia

* E-mail: molodtsovmv@susu.ru

Keywords: concrete, beam, fiberglass composite reinforcement, deflection, crack, cracking formation onset, bearing capacity

Abstract. Fiberglass composite reinforcement has been used in Russia for a long time, but there is still not enough research and necessary related data. Therefore this paper focuses on how exposure to loads affects concrete beams with fiberglass composite and metal reinforcement. The concrete beams samples (80×160×1400) were tested for bending as single-span hinged-supported elements. The load was applied within 20 seconds intervals in order to prevent relaxation of the concrete. All samples collapsed along the cross-section having maximum crack opening in the area of pure bending. The experiments show that the nature of beam collapsing and cracking does not depend on the type of reinforcement. However, the maximum crack opening width for beams with fiberglass composite reinforcement is 28.8 % greater than for beams with metal reinforcement. The value of the maximum deflection for fiberglass is 43.3 % greater. In addition, despite the initial experimental condition of equal loading onset time, the value of the crack formation for beams with fiberglass composite reinforcement is 15.5 % less. The average value of the breaking moment for beams with fiberglass composite reinforcement is 18.06 % less. Taken together, the data obtained in the course of the experiments suggest that the bearing capacity of the elements with fiberglass composite reinforcement, bent along the cross-section, decreases due to the low stiffness of the element itself. Therefore, this type of reinforcement is likely to be applicable for concrete structures on the elastic foundation.

1. Introduction

The construction of reinforced concrete buildings and structures plays a significant part of the overall construction works [1–3]. There is a need to increase - bearing capacity of reinforced concrete structures while reducing their size. In addition, the past decade has seen the rapid development of environmentally friendly construction processes. New safety requirements for construction have appeared and the cost of metal products has risen. All of the above has led to the introduction of new building materials. For example, V.A. Rybakov and K.G. Kozinetc suggested the lightweight steel concrete structures with foam and fiber-cement sheets [4], O.N. Stolyarov and A.S. Gorshkov proposed the use of high-strength textile materials as a component of concrete [5], and R.V. Lesovik and S.V. Klyuyev suggested using composite binders [6, 7].

The use of composite materials is one of the methods of strengthening concrete structures. Composite materials are made of polypropylene, carbon, basalt and glass fiber. The researches in this area have been carried out by D.V. Kyrlapov, A.S. Kyvaeva [8], F.N. Rabinovich [9]. A.I. Kirsanov and O.N. Stolyarov [10], T.S. Morozova and T.S. Kyznetsov [11].

Many researchers have also dealt with the problem of using new polymeric materials for reinforcing various types of concrete. For example, Z. Pehlivanli and his associates investigated the possibilities of using such materials in autoclaved aerated concrete [12], Wenjie Ge and Jiwen Zhang studied flexural behaviors of hybrid concrete beams reinforced with Basalt Fiber Reinforced Plastic (BFRP) bars [13], H. Ahmed experimented with geopolymers concrete (GPC) reinforced with glass fibre-reinforced polymer (GFRP) bars and carbon fibre-reinforced polymer (CFRP) bars [14] etc.

Fiberglass is one of the most promising composite materials [15, 16]. Fiberglass is a composite which contains continuous reinforcing compound made of glass fiber [17, 18]. A lot of Russian researchers, such as



A.R. Gizdatullin, V.G. Khozin, A.N. Kuklin, A.M. Khusnutdinov, E.A. Nekliudova, A.S. Semenov, B.E. Melnikov, S.G. Semenov, N.V. Begunova have proved the positive properties of glass composite reinforcement. It possesses a considerable number of advantages in lightness, high tensile strength, low thermal conductivity, adaptability and resistance to aggressive environments over traditional metal [19–23]. But all of the above researchers mainly aimed at studying the properties of the reinforcement itself, and despite the fact that fiberglass composite reinforcement has been used in Russia for a long time, it has not received wide application due to the considerable lack of the proper research and the regulatory reference data for engineering design.

The overseas studies of fiberglass reinforcement application have been carried out since long ago. The article "Flexural behavior of concrete beams reinforced with GFRP bars" was published in 1998. This study presents the results of the comparison made between the predicted and the actual load-deflection relationships for 12 concrete beams reinforced either with steel or GFRP bars [24]. In the case of GFRP reinforced beams, the service load deflection predicted by the ACI model is in error by 70 %, while that predicted by the modified model is in error by less than 15 %. The structural behavior of tested GFRP beams is validated by developing FE models using the ANSYS software in further research. This simulation showed a very small error [25].

Moreover, several researchers studied the flexural behavior and serviceability performance of GFRP-reinforced concrete beams under static and impact loading [26], fabricated with geopolymer concrete [27], or with regular and high-strength concretes [28, 29].

A lot of research has also been done on the behavior of GFRP-reinforced concrete elements such as columns [30], slabs [31], panels [32] and beams [26, 28, 29, 33–36].

One of the latest publications on this subject, written by Xiangjie Ruan and Chunhua Lu is quite significant. The researchers showed that the ultimate flexural capacity of GFRP concrete beams was nearly 91–97 % of that of steel-reinforced concrete beams [35]. The other results showed that the ultimate load of the beams reinforced with pultruded GFRP grating mesh ranged between 19 % and 38 % higher than the ultimate load of the beams reinforced with steel bars [36].

However, the above mentioned researches paid little to no attention to crack formation processes. This study aims to focus on the crack formation in concrete beams with fiberglass reinforcement in comparison with concrete beams with the traditional steel reinforcement. The experiments have been carried out keeping the same conditions.

2. Methods

In the experiments we used the following materials: Portland cement 500 made at Korkinsky cement plant (density – 3.15 g/cm³, bulk density – 1.20 g/cm³), 5-20 mm crushed stone from Novo-Smolinsky quarry (density – 2.55 g/cm³, bulk density – 1.44 g/cm³, compressive strength – 89 MPa, sand from Fedorovsky quarry (density – 2.60 g/cm³, bulk density – 1.70 g/cm³, sand contamination with dust and clay particles – 3 %, sand size modulus – 2.0) and tap water from Chelyabinsk water supply system.

The studies were conducted with concrete (class B25) of the following composition: cement – 298 kg; water – 190 kg; sand – 578 kg; crushed stone – 1257 kg. The composition of concrete based on the large number of previous studies [37–39]. The beams selected for the experiment had a cross section of 80×160 mm and a length of 1400 mm.

For the first series of samples we used metal reinforcement with a diameter of 12 mm, class AIII (A400), tensile strength – 350 MPa according to Russian State Standard GOST 5781-82 [40]. Technical conditions made into a single framework by spot welding. This reinforcement framework had a form of the grid with a spacing of 80 mm (Fig. 1) and increased reinforcement in the left and right thirds of the beam, which contributed to its destruction along its cross-section.

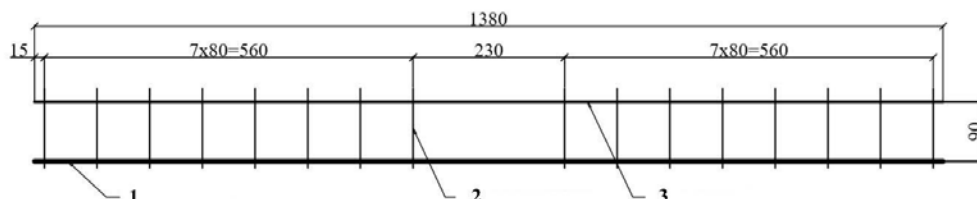


Figure 1. Reinforcement framework:
1 – bearing rod, 2 – wiring bar, 3 – structural bar.

For the second series of samples we used fiber glass composite reinforcement with a diameter of 10 mm, tensile strength of 1000 MPa according to Russian State Standard GOST 31938-2012 [41–43],

assembled with plastic clamps in a framework similar to the above. The diameter of the reinforcement was determined in compliance with the physical-mechanical properties of the reinforcement itself and based on of the previous studies [44–46].

A series of cube samples with sides of 100×100×100 mm was made to verify the conformity of concrete to B25 class. All series of samples were stored under the same temperature and humidity conditions for 28 days during hardening. The difference in the masses between the lightest and the heaviest samples did not exceed 50 kg/m³, which meets the requirements of [47]. According to the results of cubic samples tests, the average cubic strength corresponds to 31.30 MPa, the concrete class for the experimental composition was estimated as 24.37, with the coefficient of variation equal to 13.5 %.

The geometric features of the beam sections are shown in Fig. 2, and the theoretical design features of the beams in Table 1. As it can be seen from Table 1, the reinforcement of the beams is chosen in a way that the supposed (design) time of the of crack formation is the same in both sample series.

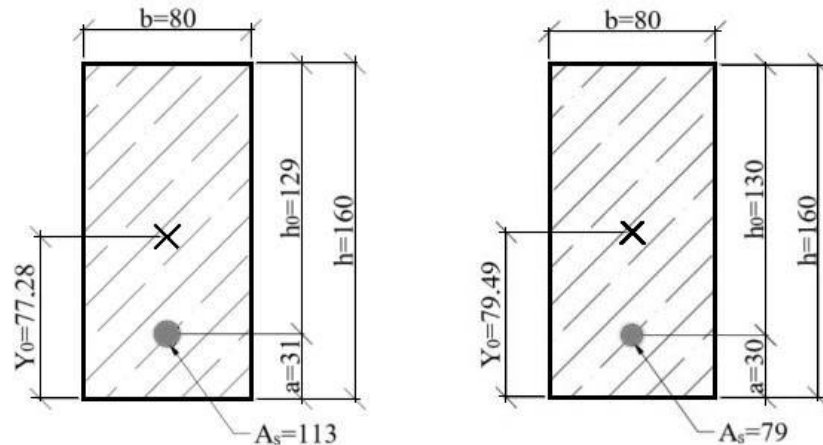


Figure 2. The geometric characteristics of the beam sections.

Table 1. The design features of the beams.

Feature	Value for a beam with metal reinforcement	Value for a beam with fiber glass composite reinforcement
R_b is calculated concrete compressive strength, MPa	14.5	14.5
R_{bt} is calculated concrete tensile strength, MPa	1.05	1.05
E_b is modulus of concrete elasticity, MPa	30 000	30 000
R_s is reinforcement tensile strength, MPa	350	1000
E_s is modulus of reinforcement elasticity, MPa	200 000	50 000
γ_b is bulk weight of the beam, kg/m ³	2423.4	2412.6
A_{red} is area of the reduced section, mm ²	13553.33	12931.67
S_{red} is static moment of modified sectional area relative to the lower edge, mm ²	1047353.33	1027950.00
I_{red} is moment of inertia of the reduced section relative to the center of gravity of the section, mm ⁴	29014884.28	27632481.85
W_{red} is moment of resistance of the reduced section relative to the bottom edge, mm ³	375468.70	347618.12
W_{pl} is elasto-plastic moment of resistance relative to the lower edge, mm ³	657070.23	608331.71
$F_{cr,cal}$ is Load corresponding to the theoretical moment of crack formation, kN	3.09	2.89
$M_{cr,cal}$ is supposed moment of crack formation, kN·m	0.68	0.68

The samples were tested for bending as single-span hinged-supported beams. The load was applied with a delay of 20 seconds in order to prevent the relaxation of concrete. In the course of the test, the following indices were taken: the behavior of the supports, deflections of the beam and reinforcement in the area of pure bending, and the width of crack opening.

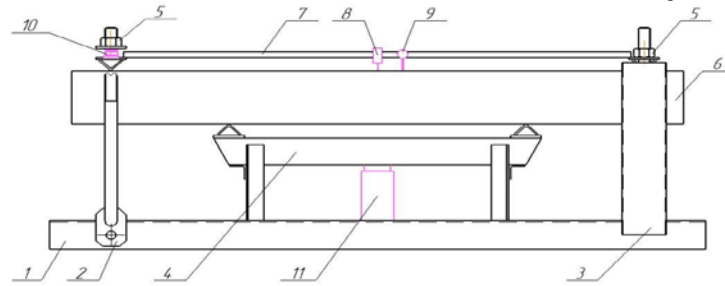


Figure 3. Installation setup for the experiment:
 1 – stand base, 2 – mobile support, 3 – rigid support, 4 – traverse, 5 – adjusting nut,
 6 – test sample, 7 – instrument rail, 8 – Huguenberger strain gauge, 9 – dial gauge,
 10 – strain gauge LPA-4.7t-TOKBEC, 11 – jack.

A schematic diagram of a test bench with two concentrated loads is presented in Fig. 3. The jack 11 mounted on the base 1 creates pressure on the traverse 4, which slides along the guides in the vertical plane and creates pressure on the test beam at two points. Supports 2 and 3 due to the adjusting nuts do not let the beam move in the plane of the load application. Sensor 8 (Huguenberger strain gauge) relieves the deflection of the reinforcement in the area of pure bending. In order to install the Huguenberger strain gauge, the concrete in the samples was excavated until the reinforcement was exposed. Sensor 9 (dial gauge) reads the deflection of the beam. Sensor 10 (strain gauge LPA-4.7t-TOKBEC) reads the behavior of the support during the loading of the beam. The general view of the installation setup is shown in Fig. 4.



Figure 4. Installation setup for the experiment.

3. Results and Discussion

The diagrams of the forces arising in the beam in the course of the test were made based on the received data. It was determined that the onset of cracking occurred under the load $F_{crc,exp} = 3.06$ kN, which corresponds to the moment $M_{crc,exp} = 0.67$ kN·m, while the calculated value was $M_{crc,exp} = 0.68$ kN·m. The discrepancy between the calculated and experimental values is 1.5 %.

The results of the laboratory tests for a series of beams with metal reinforcement were used to create the diagrams of bending deflections starting from the loading moment for all series of samples (Fig. 5).

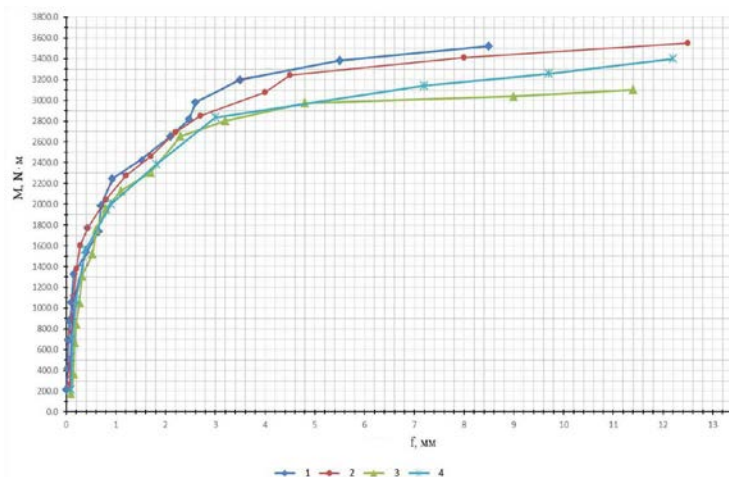


Figure 5. Deflection diagram of beams with metal reinforcement subject to the loading moment:
 1, 2, 3, 4 – number of the sample series.

The destruction of the beams with metal reinforcement took place along the cross-section. The averaged out value of the breaking load is $F_{ult,exp} = 13.096$ kN, which corresponds to the moment $M_{ult,exp} = 3.536$ kN·m. The calculated value is $M_{ult,exp} = 3.67$ kN·m. The discrepancy between the calculated and experimental values is 13.4 %. The first crack appeared in the area of pure bending. The deflection value in the area of pure bending increased with the increase in load. New cracks were formed in the area of pure bending; as well as inclined cracks appeared in the left and right thirds of the beam span (Fig. 6). Among all samples of the series, the maximum crack opening width in the area of pure bending is 3.2 mm. The maximum deflection value of the beam in the center is 12.5 mm among all samples of the series. The crack formation pattern is shown in Fig. 6, and the cracks themselves are shown in Fig. 7.

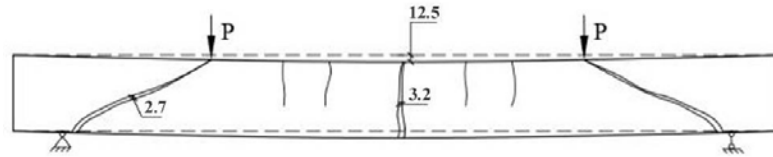


Figure 6. The crack formation pattern for the beam with metal reinforcement.



Figure 7. Cracking in the beam with metal reinforcement.

The results of the laboratory tests for a series of beams with fiber glass composite reinforcement were also used to create the diagrams of bending deflections starting from the loading moment for all series of samples (Fig. 8).

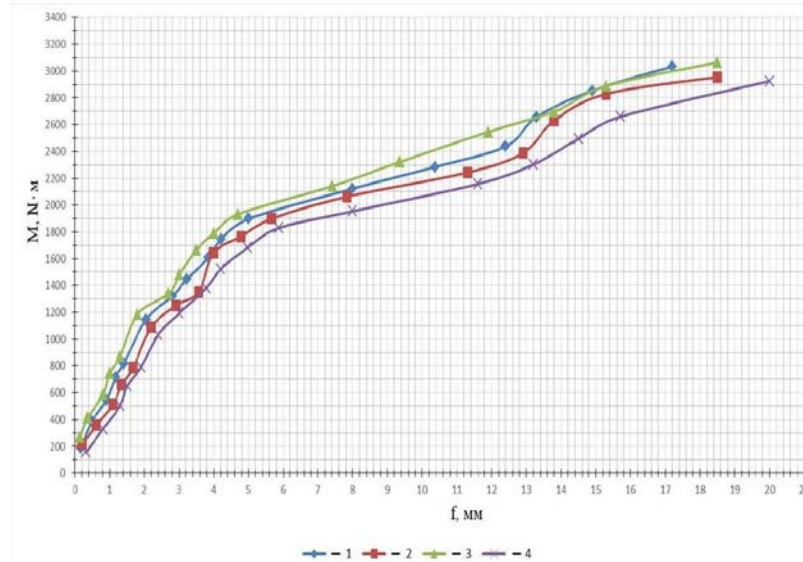


Figure 8. Deflection diagram of beams with fiber glass composite reinforcement subject to the loading moment: 1, 2, 3, 4 – number of the sample series.

The diagrams of the arising in the beam forces in the course of the test were made based on the received data. It was determined that the onset of cracking in the beams with fiber glass composite reinforcement occurred under the load $F_{cr,exp} = 2.57$ kN, which corresponds to the moment $M_{cr,exp} = 0.58$ kN·m, while the calculated value was $M_{cr,exp} = 0.68$ kN·m. The discrepancy between the calculated and experimental values is 17.2 %.

In general, the destruction of beams with fiber glass composite reinforcement was of the same nature as the destruction of the beams with metal reinforcement. The averaged out value of breaking load is $F_{ult,exp} = 11.092$ kN, which corresponds to the moment $M_{ult,exp} = 2.995$ kN·m.

The ultimate flexural capacity of GFRP concrete beams is 85 % of steel-reinforced concrete beams. Other researchers show the capacity nearly 91 % [35].

Among all samples of the series, the maximum crack opening width in the area of pure bending is 4.5 mm. The maximum deflection value of the beam in the center is 20 mm among all samples of the series. The crack formation pattern is shown in Fig. 9, and the cracks themselves are shown in Fig. 10.

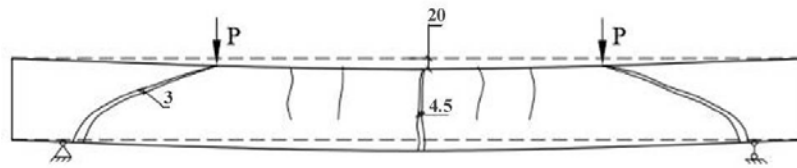


Figure 9. The crack formation pattern for the beam with fiber glass composite reinforcement.



Figure 10. Cracking in the beam with fiber glass composite reinforcement.

The summarized data of the test results for all series of samples are presented in Fig. 11. The graph clearly indicates that the moment value for the onset of crack formation is smaller by 15.5 % for a beam with fiber glass reinforcement compared to a beam with metal reinforcement. For the beams with metal reinforcement, the onset of the crack formation the moment $M_{cr,exp}$ corresponds to 0.67 kN·m, while for the beams reinforced with glass-composite reinforcement the moment $M_{cr,exp}$ equals to 0.58 kN·m.

Overall, the destruction of all the beams was of the same nature and did not depend on the type of reinforcement. However, for the beams with fiber glass composite reinforcement the averaged value of the breaking load $F_{ult,exp}$ was 11.092 kN, which corresponded to the moment $M_{ult,exp} = 2.995$ kN·m. The averaged value of breaking load for beams with metal reinforcement $F_{ult,exp}$ was 13.096 kN, which corresponded to the moment $M_{ult,exp} = 3.536$ kN·m. So, the value of the breaking load for the beams with fiber glass composite reinforcement was by 18.06 % less compared to the beams with metal reinforcement.

Another anticipated finding was that the value of the maximum deflection for the beams with fiber glass composite reinforcement amounted to 18.55 mm. While the maximum deflection of the beams with metal reinforcement was as much as 10.5 mm. Thus, the maximum deflection for the beams with fiber glass composite reinforcement was 43.3 % more than the maximum deflections of the beams with metal reinforcement. Other researchers show the same deflection for the GFRP beams [23, 35].

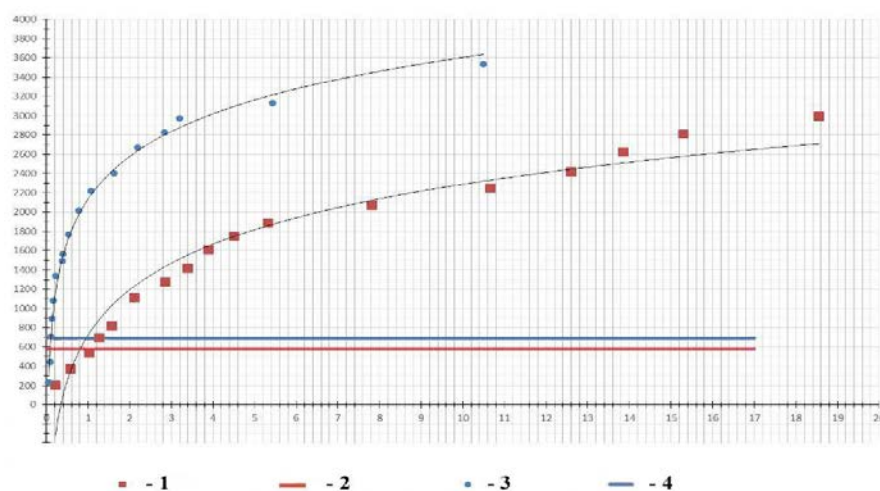


Figure 11. A generalized diagram of the beam deflection with reference to the loading onset: 1 – beams with fiber glass composite reinforcement, 2 – moment of crack formation in beams with fiber glass composite reinforcement, 3 – beams with metal reinforcement, 4 – moment of crack formation in beams with metal reinforcement.

The further analysis of the data showed that the cracks in the beams with fiber glass composite reinforcement began to open at the lower values of the loading moments and the larger deflections of the beams by an average of 40 ... 60 %, especially in the initial loading period, if compared to the same characteristics of the beams with metal reinforcement. The maximum crack opening for beams with fiber glass composite reinforcement was also 28.8 % larger. The results clearly demonstrate lower rigidity of concrete structures with fiber glass composite reinforcement and, as a consequence, a reduction in the entire bearing capacity of such elements. It is possible to increase the bearing capacity of fiber glass composite elements by either increasing the percentage of reinforcement or the elasticity modulus of fiber glass composite reinforcement. Both methods will lead to large additional costs, and therefore, the use of fiber glass composite in the reinforcement of simple flexible elements is not economically feasible. This type of reinforcement is likely to be applicable for concrete structures on the elastic foundation. However, it is clearly understood that further research should be done on this matter further before.

4. Conclusion

1. The destruction of the beams has taken place along their cross-section; the nature of the destruction and cracking in general has been of the same nature with no dependence on the reinforcement type.

2. The averaged value of the breaking moment $M_{ult,exp}$ is 2.995 kN·m for beams with fiber glass composite reinforcement, and 3.536 kN·m for beams with metal reinforcement, which makes a considerable discrepancy of 18.06 %.

3. Despite the initial experimental condition of equal loading onset moment, the moment $M_{cr,exp}$ is 0.67 kN·m for beams with metal reinforcement, and 0.58 kN·m for beams with metal reinforcement. Thus, the value of the crack formation for beams with fiber glass composite reinforcement is 15.5 % less compared to the same value for beams with metal reinforcement.

4. The cracks in the beams with fiber glass composite reinforcement began to open at the lower values of the loading moments and the larger deflections of the beams by an average of 40 ... 60 %, especially in the initial loading period, if compared to the same characteristics of the beams with metal reinforcement.

5. The value of the maximum deflection for beams with fiber glass composite reinforcement (18.55 mm) is 43.3 % more than the maximum deflection for beams with metal reinforcement (10.5 mm). The maximum crack opening for beams with fiber glass composite reinforcement is also 28.8 % greater than the maximum crack width for beams with metal reinforcement.

References

1. Sychova, A.M., Svatovskaya, L.B., Starchukov, D.S., Soloviova, V.Y., Gravit, M. V. The improving of the concrete quality in a monolithic clip. Magazine of Civil Engineering. 2018. 80(4). Pp. 3–14. DOI: 10.18720/MCE.80.1
2. Pakravan, H.R., Latifi, M., Jamshidi, M. Hybrid short fiber reinforcement system in concrete: A review. Construction and Building Materials. 2017. 142. Pp. 280–294. DOI: 10.1016/j.conbuildmat.2017.03.059 URL: <https://linkinghub.elsevier.com/retrieve/pii/S0950061817304361>.
3. Yoo, D.-Y., Yoon, Y.-S. A Review on Structural Behavior, Design, and Application of Ultra-High-Performance Fiber-Reinforced Concrete. International Journal of Concrete Structures and Materials. 2016. 10 (2). Pp. 125–142. DOI: 10.1007/s40069-016-0143-x URL: <http://link.springer.com/10.1007/s40069-016-0143-x>
4. Rybakov, V.A., Kozinets, K.G., Vatin, N.I., Velichkin, V.Z., Korsun, V.I. Lightweight steel concrete structures technology with foam fiber-cement sheets. Magazine of Civil Engineering. 2018. 82 (6). Pp. 103–111. DOI: 10.18720/MCE.82.10
5. Stolyarov, O.N., Gorshkov, A.S. Application of extra-strong textile materials in construction. Magazine of Civil Engineering. 2009. 6(4). Pp. 21–25. (rus). DOI: 10.18720/MCE.6.3
6. Lesovik, R.V., Klyuyev, S.V. Fiber concrete containing composite binders and technogenic sands of Kursk magnetic anomaly for flexural structures. Magazine of Civil Engineering. 2012. 29 (3). Pp. 41–47. DOI: 10.5862/MCE.29.5
7. Yoo, D.-Y., Banthia, N. Mechanical and structural behaviors of ultra-high-performance fiber-reinforced concrete subjected to impact and blast. Construction and Building Materials. 2017. 149. Pp. 416–431. DOI: 10.1016/j.conbuildmat.2017.05.136
8. Kurlapov, D.V., Kuvayev, A.S., Rodionov, A.V., Valeyev, R.M. Usileniye zhelezobetonnykh konstruksiy s primeneniym polimernykh kompozitov [Strengthening of reinforced concrete structures using polymer compounds]. Magazine of Civil Engineering. 2009. 5 (3). Pp. 22–24. (rus)
9. Rabinovich, F.N. Kompozity na osnove dispersno armirovannykh betonov. Voprosy teorii i proektirovaniya [Composites based on dispersed reinforced concrete. Questions of theory and design, technology, design]. Moscow: ASV, 2011. 643 p. (rus)
10. Kirsanov, A.I., Stolyarov, O.N. Mechanical properties of synthetic fibers applied to concrete reinforcement. Magazine of Civil Engineering. 2018. No. 80(4). Pp. 15–23. DOI: 10.18720/MCE.80.2
11. Morozova, T.S., Kuznetsov, V.D. External reinforcement of reinforced concrete column by composite coal-plastic material. Magazine of Civil Engineering. 2010. 13(3). Pp. 35–38. (rus). DOI: 10.18720/MCE.13.4
12. Pehlivanli, Z.O., Uzun, İ., Demir, İ. Mechanical and microstructural features of autoclaved aerated concrete reinforced with autoclaved polypropylene, carbon, basalt and glass fiber. Construction and Building Materials. 2015. 96. Pp. 428–433. DOI: 10.1016/j.conbuildmat.2015.08.104 URL: <https://linkinghub.elsevier.com/retrieve/pii/S0950061815303196>
13. Ge, W., Zhang, J., Cao, D., Tu, Y. Flexural behaviors of hybrid concrete beams reinforced with BFRP bars and steel bars. Construction and Building Materials. 2015. 87. Pp. 28–37. DOI: 10.1016/j.conbuildmat.2015.03.113

14. Ahmed, H.Q., Jaf, D.K., Yaseen, S.A. Comparison of the Flexural Performance and Behaviour of Fly-Ash-Based Geopolymer Concrete Beams Reinforced with CFRP and GFRP Bars. *Advances in Materials Science and Engineering*. 2020. DOI: 10.1155/2020/3495276
15. Jia, D., Guo, Q., Mao, J., Lv, J., Yang, Z. Durability of glass fibre-reinforced polymer (GFRP) bars embedded in concrete under various environments. I: Experiments and analysis. *Composite Structures*. 2020. 234. DOI: 10.1016/j.compstruct.2019.111687
16. Kluev, S.V., Lesovik, R.V. Dispersno-armirovannyi melkozernisty beton steklovoloknom [Dispersive - reinforced fine-grained concrete with fiberglass]. *Concrete and reinforced concrete*. 2011. 6. Pp. 4–6. (rus)
17. Mu, B. and Meyer, C. Flexural Behavior of Fiber Mesh-reinforced Concrete with Glass Aggregate. *Aci Materials Journal*. 2002. 99(5). Pp. 425–434.
18. Alsayed, S.H., Al-Salloum, Y.A., Almusallam, T.H. Performance of glass fiber reinforced plastic bars as a reinforcing material for concrete structures. *Composites Part B: Engineering*. 2000. 31 (6–7). Pp. 555–567. DOI: 10.1016/S1359-8368(99)00049-9 URL: <https://linkinghub.elsevier.com/retrieve/pii/S1359836899000499>
19. Gizdatullin, A.R., Khozin, V.G., Kuklin, A.N., Khusnutdinov, A.M. Specifics of testing and fracture behavior of fibre-reinforced polymer bars. *Magazine of Civil Engineering*. 2014. 47 (3). Pp. 40–47. (rus). DOI: 10.5862/MCE.47.4
20. Nekliudova, E.A., Semenov, A.S., Melnikov, B.E., Semenov, S.G. Experimental research and finite element analysis of elastic and strength properties of fiberglass composite material. *Magazine of Civil Engineering*. 2014. 47(3). Pp. 25–39. DOI: 10.5862/MCE.47.3
21. Lamy, F., Godbout, S., Marquis, A. Feasibility of composite structures in slats of reinforced-concrete. *Canadian Agricultural Engineering*. 1994. 36(3). Pp. 151–154.
22. Rajput, A.S., Sharma, U.K. Seismic upgrade of corroded confined reinforced concrete columns using composite materials. *ACI Materials Journal*. 2019. 116(5). Pp. 37–48. DOI:10.14359/51716825
23. Begunova, N.V., Grahov, V.P., Vozmishchev, V.N., Kislyakova, I.G. Comparative Evaluation of Results on Test of Concrete Beams with Fiberglass Rebar and Calculated Data. *Science & Technique*. 2019. 18(2). Pp. 155–163. DOI: 10.21122/2227-1031-2019-18-2-155-163
24. Alsayed, S.H. Flexural behaviour of concrete beams reinforced with GFRP bars. *Cement and Concrete Composites*. 1998. 20(1). Pp. 1–11. DOI: 10.1016/S0958-9465(97)00061-9 URL: <https://www.sciencedirect.com/science/article/abs/pii/S0958946597000619?via%3Dihub> (date of application: 12.02.2020).
25. Kalpana, V.G., Subramanian, K. Behavior of concrete beams reinforced with GFRP BARS. *Journal of Reinforced Plastics and Composites*. 2011. 30 (23). Pp. 1915–1922. DOI: 10.1177/0731684411431119
26. Goldston, M., Remennikov, A., Sheikh, M.N. Experimental investigation of the behaviour of concrete beams reinforced with GFRP bars under static and impact loading. *Engineering Structures*. 2016. 113. Pp. 220–232. DOI: 10.1016/j.engstruct.2016.01.044 URL: <https://www.sciencedirect.com/science/article/pii/S0141029616000602?via%3Dihub> (date of application: 12.02.2020).
27. Shrikant, H., Sarang, D. Comparison of glass fiber reinforced concrete & geopolymer concrete with glass fiber reinforcement. *International Journal of Research in Engineering and Technology*. 2014. 03 (01). Pp. 263–265. DOI: 10.15623/ijret.2014.0301045 URL: <https://ijret.org/volumes/2014v03/i01/IJRET20140301045.pdf>
28. El-Nemr, A., Ahmed, E.A., Benmokrane, B. Flexural Behavior and Serviceability of Normal- and High-Strength Concrete Beams Reinforced with Glass Fiber-Reinforced Polymer Bars. *ACI Structural Journal*. 2013. 110 (6). Pp. 1077–1087.
29. Abdelkarim, O.I., Ahmed, E.A., Mohamed, H.M., Benmokrane, B. Flexural strength and serviceability evaluation of concrete beams reinforced with deformed GFRP bars. *Engineering Structures*. 2019. 186. Pp. 282–296. DOI: 10.1016/j.engstruct.2019.02.024 URL: <https://www.sciencedirect.com/science/article/pii/S0141029618317590?via%3Dihub> (date of application: 15.02.2020).
30. Hadhood, A., Mohamed, H.M., Ghrib, F., Benmokrane, B. Efficiency of glass-fiber reinforced-polymer (GFRP) discrete hoops and bars in concrete columns under combined axial and flexural loads. *Composites Part B: Engineering*. 2017. 114. Pp. 223–236. DOI: 10.1016/j.compositesb.2017.01.063 URL: <https://www.sciencedirect.com/science/article/abs/pii/S1359836816323745?via%3Dihub> (date of application: 17.02.2020).
31. Al-Rubaye, M., Manalo, A., Alajarmeh, O., Ferdous, W., Lokuge, W., Benmokrane, B., Edo, A. Flexural behaviour of concrete slabs reinforced with GFRP bars and hollow composite reinforcing systems. *Composite Structures*. 2020. 236. Pp. 111836. DOI: 10.1016/j.compstruct.2019.111836. URL: <https://www.sciencedirect.com/science/article/pii/S0263822318341060?via%3Dihub> (date of application: 17.02.2020).
32. Qiao, P., Liu, Q., Lu, Z., Wang, Z. Flexural behaviour of GFRP-encased concrete panels. *Magazine of Concrete Research*. 2018. 70(24). Pp. 1265–1279. DOI:10.1680/jmacr.17.00423
33. Mohamed, H.M., Benmokrane, B. Torsion Behavior of Concrete Beams Reinforced with Glass Fiber-Reinforced Polymer Bars and Stirrups. *ACI Structural Journal*. 2015. 112(5) Pp. 543–552.
34. Toutanji, H.A., Saafi, M. Flexural Behavior of Concrete Beams Reinforced with Glass Fiber-Reinforced Polymer (GFRP) Bars. *ACI Structural Journal*. 2000. 97(5). Pp. 712–719. DOI:10.14359/8806 URL: <http://www.concrete.org/Publications/ACIMaterialsJournal/ACIJournalSearch.aspx?m=details&ID=8806>
35. Ruan, X., Lu, C., Xu, K., Xuan, G., Ni, M. Flexural behavior and serviceability of concrete beams hybrid-reinforced with GFRP bars and steel bars. *Composite Structures*. 2020. 235. Pp. 111772. DOI: 10.1016/j.compstruct.2019.111772 URL: <https://www.sciencedirect.com/science/article/pii/S0263822319317027> (date of application: 12.02.2020).
36. Hadi, M.N.S., Almalome, M.H.A., Yu, T., Rickards, W.A. Flexural behavior of beams reinforced with either steel bars, molded or pultruded GFRP grating. *So steel and composite structures*. 2020. 31 (01). Pp. 17–34.
37. Zyablikov, D.P. Tekhnologicheskie osobennosti primeneniya betona, armirovannogo smes'yu stal'nyh volokon [Technological characteristics of reinforced concrete application]. Omsk, 1998. 22 p. (rus)
38. Klyuyev, S.V. High-strength fiber concrete for industrial and civil construction. *Magazine of Civil Engineering*. 2012. 34(8). Pp. 61–66. (rus). DOI: 10.5862/MCE.34.9
39. Posobiye po proyektirovaniyu betonnykh i zhelezobetonnykh konstruktsiy iz tyazhelogo betona bez predvaritel'nogo napryazheniya armatury (k SP 52-101-2003) [Manual for the design of concrete and reinforced concrete structures of heavy concrete without prestressing of reinforcement] (for SP 52-101-2003)]. TSNIIPromzdaniy, NIIGB. Moscow: OAO TSNIIPromzdaniy, 2005. 214 p. (rus)
40. Russian Stat Standard GOST 5781-82 Stal goryachekatanaya dlya armirovaniya zhelezobetonnykh konstruktsiy. Tekhnicheskiye usloviya [Hot-rolled steel for reinforced concrete structures. Technical conditions]. Moscow: Standards Publishing House, 1993. 31 p. (rus)

41. Russian Stat Standard GOST 31938-2012 Armatura kompozitnaya polimernaya dlya armirovaniya betonnykh konstruksiy. Obshchiye tekhnicheskiye usloviya [Composite composite reinforcement for reinforcement of concrete structures. General specifications]. Moscow: Standartinform, 2014. 34 p. (rus)
42. Russian Stat Standard GOST 32492-2015 Armatura kompozitnaya polimernaya dlya armirovaniya betonnykh konstruksiy. Metody opredeleniya fiziko-mekhanicheskikh kharakteristik [Composite composite reinforcement for reinforcement of concrete structures. Methods for determining the physicochemical characteristics]. Moscow: Standartinform, 2016. 16 p. (rus)
43. Russian construction code SP 295.1325800.2017 Konstruksii betonnyye, armirovannyye polimernoy kompozitnoy armaturoy. Pravila proyektirovaniya [Concrete structures reinforced with polymer composite reinforcement. Design rules]. Moscow: Standartinform, 2017. 48 p. (rus)
44. Vlasenko, F.S., Raskutin, A.E. Primeneniye polimernykh kompozitsionnykh materialov v stroitelnykh konstruksiyakh [Applying FRP in building structures]. Trudy VIAM. 2013. No. 8. Pp. 24–37. (rus)
45. Gil, A.I., Badalova, Ye.N., Lazovskiy, Ye.D. Stekloplastikovaya i ugleplastikovaya armatura v stroitelstve: preimushchestva, nedostatki, perspektivy primeneniya [Glass fiber and carbon fiber reinforcement in construction: Advantages, disadvantages, prospects of application]. Vestnik polotskogo gosudarstvennogo universiteta. Seriya f: Stroitelstvo. Prikladnyye nauki [Bulletin of Polotsk State University. Series f: Construction. Applied Science]. 2015. No. 16. Pp. 48–53. (rus)
46. Blaznov A.N., Volkov Yu.P., Lugovoy A.N., Savin V.F. Ispytaniya na dlitelnuyu prochnost sterzhney iz kompozitsionnykh materialov [Tests of long-term strength of composite cores]. Zavodskaya Laboratoriya. Diagnostika Materialov [Factory laboratory. Diagnostics of materials]. 2006. 72(2). Pp. 44–52. (rus)
47. Russian Stat Standard GOST 10180-2012 Betony. Metody opredeleniya prochnosti po kontrolnym obraztsam [Concrete. Methods for determining the strength of the control samples]. Moscow: Standartinform, 2013. 30 p. (rus)

Contacts:

Maxim Molodtsov, molodtcovmv@susu.ru

Evgeniy Vshivkov, laito174@gmail.com

Valeriya Molodtsova, molodtcovave@susu.ru

© Molodtsov, M.V., Vshivkov, E.P., Molodtsova, V.E., 2020



DOI: 10.18720/MCE.97.4

Bearing capacity equations of piles in weathered claystone and sandstone

E.N. Sychkina, I.V. Ofrikhter*, A.B. Ponomaryov

Perm National Research Polytechnic University, Perm, Russia

* E-mail: ian.ofrikhter@gmail.com

Keywords: bearing capacity, cast-in-place piles, design, claystone, sandstone, mechanical properties

Abstract. The article proposes models of nonlinear estimation of the bearing capacity of piles on weathered claystone and sandstone. These soils are often used as the foundation for deep foundations for critical structures such as bridges, transport structures, dams. Often, laboratory tests of such soils give underestimated values of the characteristics. As a result, the bearing capacity of the designed pile foundations is much more than necessary. The main goal of this study is to develop equations that allow us to evaluate the bearing capacity of the pile foundation in these soils by a non-destructive method. The authors propose semi-empirical equations based on analytical solutions and empirical data, obtained from plate-bearing tests. These equations can be used for an estimation of the bearing capacity of piles of various diameters without conducting expensive field tests. Assessment of the obtained equations reliability showed that the determination coefficient is 0.90 for claystone, and 0.96 for sandstone. This allows us to characterize the obtained approximating functions as theoretical models of good quality. Proposed equations was compared with other methods and static load test results.

1. Introduction

Pile bearing capacity is one of the most important factor in deep foundations design. Over the years, the bearing capacity of the deep foundation in a weathered and fissured rock base has been the subject of many studies in the field of geotechnics [1–22]. As a result, the researchers proposed a number of theoretical and experimental solutions for predicting the bearing capacity of piles. However, an accurate estimation of the pile bearing capacity and a reliable interpretation of the mechanism of load transfer from the pile to the ground are still far from perfect due to the complexity of the problem. In addition, many factors must be taken into account: the shape and size of the foundation, the laying depth, the load, and the characteristics of the weathered rocky soil.

The calculation methods given in the Russian Federation standards are developed primary for quaternary sandy-clay soils of sedimentary origin and rocky unripe soils and do not always allow obtaining the correct values of the bearing capacity of End-bearing pile in argillite-like clays and sandstones. Weathered argillite-like clays and sandstones of Permian age cannot be classified as low-compressible rocky soils [23, 25], since they have a deformation modulus much less than 50 MPa. Due to the lack of reliable methods for calculating the bearing capacity of piles on weathered claystone and sandstone, it is often necessary to use expensive and time-consuming static tests and plate-bearing tests. Calculation methods implemented in world design practice [2, 13–17, 25–29] require the use of additional soil parameters that are not always determined in practice of engineering and geological surveys. In addition, the proposed theoretical models require correlation by comparing the results of calculations with the field tests data.

As follows from the foregoing, the goal of this work is the development of a methodology for calculating the bearing capacity of piles in weathered claystone and sandstone of Permian age. To achieve this goal, the following issues were solved:

1. An analysis of the existing calculation methods for determining the bearing capacity of piles.



2. Soil resistance under the pile toe was determined from the plate-bearing tests results. The technique of experimental studies is described. The results of field tests are analyzed.
3. Equations for calculating the bearing capacity of cast-in-place piles in weathered claystone and sandstones of Permian age have been developed.

It has been proven that rock masses have fracture, anisotropy, nonlinearity of properties, etc. Therefore, a simple theoretical approach to determining the bearing capacity for the case of a homogeneous isotropic continuous medium with a linear fracture law does not reflect the real properties of the rock mass at the base of the foundation [4, 6, 7, 11, 13, 26, 30]. In the case when the rock mass is highly weathered and fractured, loads from the foundation can lead to the appearance of both elastic and plastic deformations. The most widely used methods for determining the bearing capacity of foundations can be divided into four groups: analytical methods, numerical methods, semi-empirical methods and field tests of piles. Numerical methods, such as the finite element method (FEM) and the limit equilibrium method (LEM), predict the pile bearing capacity using geometry and the soil properties of the foundation as input. [17, 31, 33]. Semi-empirical methods are based on a correlation between the bearing capacity and soil properties based on empirical observations and the results of experimental tests [4, 11, 28, 33–41].

The existing semi-empirical equations (1, 2) for calculating the bearing capacity of piles use data from laboratory soil tests.

$$F_d = \gamma_c \frac{R_{c,m,n}}{\gamma_g} \left(1 + 0.4 \frac{l_d}{d_f} \right) A \quad (1)$$

where γ_c is coefficient of pile working conditions in the soil, taken equal to 1; $R_{c,m,n}$ is the value of the uniaxial compression strength of rocky soil in a water-saturated state in the field; γ_g is the soil reliability coefficient equal to 1.4; A is the cross section area of the pile toe, m²; l_d is the calculated depth of embedment of the pile into claystone, m; d_f is the outer diameter of the pile, m.

$$Q_p = A_p \cdot q_p = A_p \cdot (c' N_c + q' N_q) \quad (2)$$

where A_p is the cross section area of the pile toe, m²; q_p is the soil resistance characteristic under the tip of the pile; c' is the cohesion of the soil surrounding the pile; q_p is the soil resistance under the tip of the pile; q' is the effective vertical stress at the depth of the tip of the pile; N_c , N_q is the coefficients taken according to Eurocode tables.

Determination of the tensile strength of weathered claystone and sandstones under laboratory conditions often shows underestimated results in relation to field tests [13]. As a result, the application of the uniaxial compression strength results obtained in laboratory conditions gives underestimated values of the bearing capacity of the end-bearing pile. In addition, for calculations it is often necessary to use special coefficients that take into account the fracture of weathered rocky soils. However, in the standard engineering and geological surveys, this coefficient is not determined.

The calculation of the bearing capacity of piles on hard clay, presented in [19], showed that the bearing capacity of piles is significantly underestimated in comparison with the results of piles field tests. Often, instead of plate-bearing tests, cone penetration test and pile with static and dynamic load tests are used. However, cone penetration test has limited application in dense claystone and sandstone with cementation bonds and static load testing can be quite expensive especially for heavily loaded cast-in-place piles. High strain dynamic pile testing may be a good solution, but most standards require a large safety factor for the results of these tests. A description of existing methods for calculating the bearing capacity of piles and some issues encountered in their application can be found in [10, 14–18, 28, 31, 34, 35, 37, 39, 40]. When drilling piles are used in soft soils, the bearing capacity is mainly limited by the stability of the piles [40, 41]. But for pile less than 40 m in length capacity is still majorly limited by soil resistance.

Based on the results of the analysis, it can be concluded that it is necessary to adjust existing solutions in the field of calculating the bearing capacity of piles on weathered claystone and sandstone. The development of analytical and semi-empirical solutions that can be used to calculate the foundations at the pre-design stages is of particular interest.

2. Methods

In this study, the results of plate-bearing tests of the early Permian age claystone and sandstone are analyzed. The geological and lithological structure of the plate-bearing test sites is represented by fill-up soils, loam from a hard-plastic to a fluid-plastic consistency, gravel-pebble soils with clay aggregate, which overlap claystone below (Fig. 1a) and Permian sandstone (Fig. 1b).



a) Claystone b) Sandstone

Figure 1. Claystone (a) and Sandstone (b) samples.

The claystone is dark brown. It consists of clay material (60–70 %), silt material (10–20 %), admixture of carbonates (10–15 %) and iron oxides. The sandstone is greenish-gray and grayish-brown, fine and fine-grained (rarely medium-grained), layered (from thin-layered to unclear-layered), polymictic, with carbonate-clay, clay-carbonate and carbonate cement. The content of clastic material in sandstones is 50–90 %, cement is 12–30 %. The values of the physical and mechanical properties of claystone and sandstone are given in Table 1. The properties were determined according to Russian State Standard GOST 12248-2010.

Cohesion and friction angle were defined from the direct shear test. In most cases modules are defined from oedometer soil test. The RQD parameter was not determined. Usually, during geological surveys it is impossible to take cores of the considered soil with a height of more than 10 cm.

Table 1. Average values of physical characteristics of claystone and sandstone.

Typical borehole	Physical and mechanical properties	Claystone (4)	Sandstone (5)
	Bulk density, g / cm ³	2.02	2.07
	Humidity	0.19	0.16
	Liquid limit	0.33	-
	Plasticity Limit	0.23	-
	Plasticity Index	0.16	-
	Liquidity Index	<0	-
	Saturation	0.84	0.83
	Coefficient of weathering	0.76	0.76
	Elastic modulus, MPa	11.6	12.8
	Coefficient of cohesion, kPa	30	11
	Friction angle	26	33

The plate-bearing was conducted in the well. A type III plate with a sole area of 600 cm² was used. Drilling the test well was carried out with casing. The embossing of plate in claystone ranged from 1.0 to 11.0 m, in sandstone – from 0.5 to 6.0 m. A hydraulic jack DU100P150 with a manual hydraulic station NRG 7036 was used as a loading device (Fig. 2).



Figure 2. Plate-bearing test.

The pressure in the system was controlled using a trusted pressure gauge with a division price of 1 kgf/cm^2 . Reactive efforts were perceived by a custom manufacturing anchor system. The design of the stand was previously designed for a load of 1.5 times the required load during the test. The set was recorded using 6PAO deflection meters, the temperature deformations of the steel wire were taken into account using the compensation deflection meter. The plate was loaded in steps of 0.2 MPa . Each pressure stage was maintained until the plate was conditionally stabilized. It was believed that the plate was stabilized if the stamp settling speed did not exceed 0.1 mm per 0.5 hours . The final value of pressure p_n was determined as follows: if, at pressure p_i , the pressure increment is twice as large as for the previous pressure step p_{i-1} , and at the next pressure step p_{i+1} , the pressure increment will be equal to or greater than the pressure increment at p_i , for the final value p_n should take p_{i-1} . In the absence of a criterion for achieving pressure p_n , the test was terminated when the ultimate load bearing capacity of the stand was reached. In total, in this study, 11 stamp tests of claystone and 5 stamp tests of sandstone were considered.

3. Results and Discussion

In order to identify the probabilistic relationships between the uniaxial compression strength in the field ($R_{c,m,n}$) and the plate embedment depth (l_d), an analytical function was searched that best describes the dependence of $R_{c,m,n}$ on l_d . The results of plate-bearing test presented in diagrams of the characteristics $R_{c,m,n}$ and l_d for claystone and sandstone in Fig. 3 and Fig. 4, respectively.

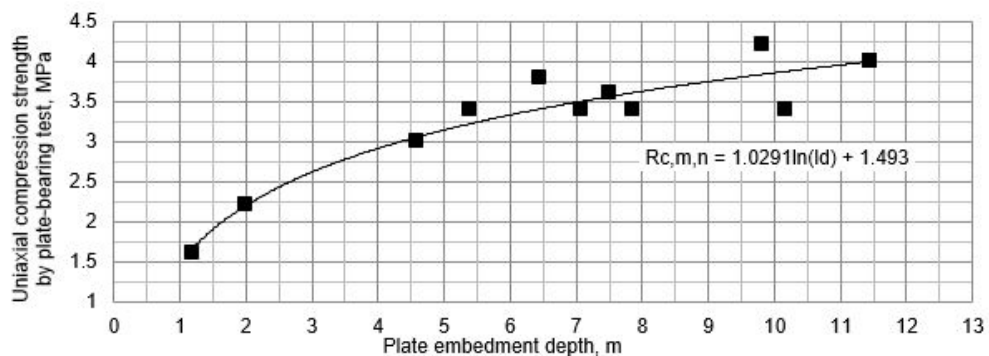


Figure 3. The relationship between the tensile strength of uniaxial compression plate in the field ($R_{c, m, n}$) from the depth of the punch (l_d) for argillite-like clay.

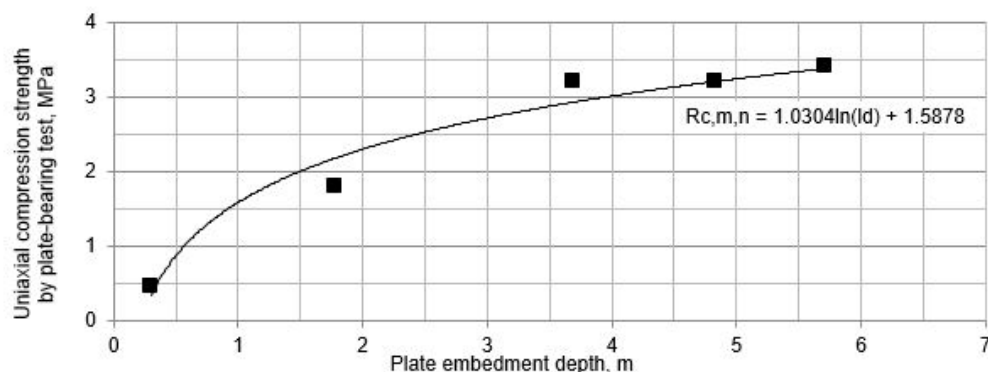


Figure 4. The relationship between the tensile strength of uniaxial compression stamp in the field ($R_{c, m, n}$) from the depth of the punch (l_d) for sandstone.

Figs. 3 and 4 show that with an increase in the immersion depth of the test plate in claystone and sandstone, the ultimate bearing capacity of soil also increases.

To approximate the experimental data, logarithmic functions were chosen. Assessment of the reliability of the approximation of the obtained equations showed that the determination coefficient is 0.90 for claystone and 0.96 for sandstone. Therefore, it can be said that the obtained approximating equation describes well the relationship between the depth of embedment of the slab and the resulting soil rotation.

Based on the performed theoretical and experimental studies, a technique for calculating the bearing capacity of piles on argillite-like clays and sandstones of Permian age is proposed. The equations presented below make it possible to calculate the bearing capacity of shell pile, filling and bored piles of any diameter with embedment from 1.0 to 11.0 m in claystone and from 0.5 to 6.0 m in sandstones. The pile bearing capacity in claystone can be calculated by the equation (3):

$$F_d = \gamma_c A \cdot (1.0291 \ln(l_d) + 1.493) \cdot (1 + 0.4 \frac{l_d}{d_f}) \quad (3)$$

where γ_c is the coefficient of pile working conditions in the soil, taken equal to 1; A is the cross section area of the pile toe, m²; l_d is the calculated depth of embedment of the pile into claystone, m; d_f is the the outer diameter of the pile, m.

The pile bearing capacity in sandstone can be calculated by the equation (4):

$$F_d = \gamma_c A \cdot (1.0304 \ln(l_d) + 1.5878) \cdot (1 + 0.4 \frac{l_d}{d_f}) \quad (4)$$

Studies [2, 4–6, 9, 11, 14, 18, 20, 39] have repeatedly emphasized the need to take into account a large number of factors affecting the joint work of piles on weathered rocky soils. The equations presented in this study allow one to take into account a number of factors that have a significant impact on the bearing capacity of piles on weathered rocky soils: pile geometry, embedment depth, and soil strength near the pile end. The obtained solutions require additional verification in the case of application for other types of weathered rocky soils – shale, limestone, siltstone, granite, etc. It should be borne in mind that soils formed at different geological times and in different conditions can have different engineering properties.

For piles based on weathered rocky soils with compressive strength exceeding 2 MPa, soil resistance exceeds the strength of the pile material [18, 19, 41]. In such cases, pile set is more critical than bearing capacity. On weathered rocky soils that have rheological properties, great attention must be paid to the speed and degree of development of uneven foundation sets [41]. Uneven sets can lead to additional forces and brittle fracture in structural elements. Thus, the design of piles should be based on the assessment of set under design loads with the use of a safety factor. However, claystone and sandstone often have an uneven degree of weathering and uniaxial compression strength of less than 2.0 MPa. This leads to the need to take into account the bearing capacity of piles along with long-term settlement of piles.

For the soils under consideration, the RQD parameter is usually not determined, since it is usually not possible to drill a core with a height of 10 cm or more. In addition, these soils are highly weathered. According to the requirements of national standards, the load-bearing capacity of piles in highly weathered bases should be determined from static tests. The uniaxial compression strength is typically 1.15–2.15 MPa.

To compare proposed equations with other methods static load test of one cast-in-place pile was conducted. Pile has 22.52 meters in length and 600 mm in diameter. Bearing capacity was calculated according to SP 24.13330 method and finite element method. OCR parameter was obtained Initial stresses were generated using the K0 procedure using OCR = 1.8 coefficients for argillite-like clay to take into account the state of overconsolidation. Comparison of obtained results with static load test presented in Table 2.

Table 2. Comparison between proposed equations and standard equations.

Bearing capacity according to SP 24.13330 analytical method, kN	Proposed equations, kN	Finite element method (Plaxis)	Static load test, kN
3688	4975	4530	5400

As can be seen from the comparison results, the standard method significantly underestimates the bearing capacity of piles. The finite element method shows somewhat better convergence with SLT, however, the results are also lower. This may be due to incorrectly defined characteristics. All characteristics used in the calculations are determined in laboratory conditions. However, there is no guarantee that the sample does not lose strength at the time of sampling. Existing standards should be revised to ensure the design of piles on weathered claystone and sandstone using the correct equations and reliability factors to predict not only bearing capacity, but also long-term settlement.

4. Conclusion

1. This article addresses the issue of predicting the bearing capacity of piles on weathered rocky soils. The authors analyzed the results of determining the uniaxial compression strength of claystone and sandstone by plate-bearing test. Various relationships were revealed between the uniaxial compression tensile strength and the plate embedment depth for.

2. A semi-empirical technique is proposed for a preliminary assessment of the bearing capacity of a pile foundation, based on weathered claystone and sandstones of the early Permian age. The presented equations make it possible to calculate the bearing capacity of various types of piles of any diameter with embedment from 1.0 to 11.0 m in claystone and from 0.5 to 6.0 m in sandstones.

3. Assessment of the reliability of the obtained equations showed that the determination coefficient is 0.90 for claystone and 0.96 for sandstone. It should be noted that only claystone and sandstone of the early Permian age were considered in this paper. Soils, which are formed at a different geological time, and having a different loading history may have different engineering properties. Therefore, the resulting equations should be used with caution for other types of weathered rocky soils.

4. When designing pile foundations on weathered rocky soils, it is necessary to take into account both the bearing capacity of the pile and long-term set increase. This is because for piles based on soils with a compressive strength of more than 2 MPa, the bearing capacity of the soil exceeds the strength of the piles. Existing standards should be revised to ensure the design of piles on weathered claystone and sandstone using the correct equations and reliability factors to predict not only bearing capacity, but also long-term settlement.

5. Acknowledgments

The authors are grateful to the Russian Science Foundation. This study was carried out with a grant from the Russian Science Foundation – project No. 18-79-00042.

References

- Skempton, A.W. Cast in-situ bored piles in London clay. *Geotechnique*. 1959. 9 (4). Pp. 153–173. DOI: 10.1680/geot.1959.9.4.153
- Meigh, A.C., Wolski, W. Design parameters for weak rocks. *Design parameters in geotechnical engineering. Proc. 7th European conference on soil mechanics and foundation engineering Brighton, 1979. Vol. 5, (British Geotechnical Society; distributed by T. Telford Ltd., London). 1981. Pp. 59–79.*
- Fellenius, B.H. Analysis of results from routine pile load tests. *Ground Engineering*. 1980. 13 (6). Pp. 19–31.
- Hoek, E., Brown, E.T. Empirical strength criterion for rock masses. *Journal of the Geotechnical Engineering Division, ASCE*. 1980. 106 (GT9, Proc. Paper, 15715). Pp. 1013–1035.
- Horvath, R.G., Kenney, T.C., Kozicki, P. Methods of improving the performance of drilled piers in weak rock. *Canadian geotechnical journal*. 1983. 20 (4). Pp. 758–772. DOI: 10.1139/t83-081
- Jaeger, J.C. Shear Failure of Anisotropic Rocks. *Geological Magazine*. 1960. 97 (1). Pp. 65–72. DOI: 10.1017/S00167-56800061100
- Haberfield, C.M., Lochaden, A.L.E. Analysis and design of axially loaded piles in rock. *Journal of Rock Mechanics and Geotechnical Engineering*. 2019. 11 (3). Pp. 535–548. DOI: 10.1016/j.jrmge.2018.10.001
- Reese, L.C., O'Neill, M.W. New design method for drilled shafts from common soil and rock tests. Publ by ASCE, 1989. Pp. 1026–1039.
- Poulos, H.G. Pile behaviour-theory. *Geotechnique*. 1989. 39 (3). Pp. 365–415.
- Kodikara, J.K., Johnston, I.W. Analysis of compressible axially loaded piles in rock. *International Journal for Numerical and Analytical Methods in Geomechanics*. 1994. 18 (6). Pp. 427–437. DOI: 10.1002/nag.1610180606
- Hoek, E., Brown, E.T. Practical estimates of rock mass strength. *International Journal of Rock Mechanics and Mining Sciences*. 1997. 34 (8). Pp. 1165–1186. DOI: 10.1016/S1365-1609(97)80069-X
- Carrubba, P. Skin friction of large-diameter piles socketed into rock. *Canadian Geotechnical Journal*. 1997. 34 (2). Pp. 230–240. DOI: 10.1139/t96-104
- Dinc Gogus, O., Sonmez, H., Tunusluoglu, M., Kasapoglu, K. A new general empirical approach for the prediction of rock mass strengths of soft to hard rock masses. *International Journal of Rock Mechanics and Mining Sciences – INT J ROCK MECH MINING SCI*. 2011. 48. Pp. 650–665. DOI: 10.1016/j.ijrmms.2011.03.001
- Wrana, B. Pile Load Capacity – Calculation Methods. *Studia Geotechnica et Mechanica*. 2016. 37 (4). Pp. 83–93. DOI: 10.1515/-sgem-2015-0048
- Vardanega, P.J., Kolody, E., Pennington, S.H., Morrison, P.R.J., Simpson, B. Bored pile design in stiff clay I: Codes of practice. *Proceedings of the Institution of Civil Engineers: Geotechnical Engineering*. 2012. DOI: 10.1680/geng.11.00062
- Vardanega, P.J., Williamson, M.G., Bolton, M.D. Bored pile design in stiff clay II: Mechanisms and uncertainty. *Proceedings of the Institution of Civil Engineers: Geotechnical Engineering*. 2012. DOI: 10.1680/geng.11.00063
- Alavi, A.H., Sadrossadat, E. New design equations for estimation of ultimate bearing capacity of shallow foundations resting on rock masses. *Geoscience Frontiers*. 2016. 7 (1). Pp. 91–99. DOI:10.1016/j.gsf.2014.12.005
- Haberfield, C.M., Lochaden, A.L.E. Analysis and design of axially loaded piles in rock. *Journal of Rock Mechanics and Geotechnical Engineering*. 2019. 11 (3). Pp. 535–548. DOI: 10.1016/j.jrmge.2018.10.001

19. Kolodiy, E., Vardanega, P.J., Patel, D.C. Settlement prediction of bored piles in stiff clay at a site in the Moscow region. Geotechnical Engineering for Infrastructure and Development - Proceedings of the XVI European Conference on Soil Mechanics and Geotechnical Engineering, ECSMGE 2015. 6. ICE Publishing, 2015. Pp. 3619–3624.
20. Ivanova, T.V., Albert, I.U., Kaufman, B.D., Shulman, S.G. The load-bearing capacity of hanging piles by the strength criterion of a pile or soil material. Magazine of Civil Engineering. 2016. 67 (7). Pp. 3–12. DOI: 10.5862/MCE.67.1
21. Perlei E.M., Rayuk V.F., Belenka V.V., Almazov A.N. Pile foundations and buried structures during reconstruction of existing enterprises. Stroizdat. 1989. – 176 p. (rus)
22. Bartolomey, A.A., Omelchak, I.M., Yushkov, B.S. Prognoz osadok svaynykh fundamentov [Settlement forecast of pile foundations]. Moscow: Stroyizdat, 1994. 384 p. (rus)
23. Ponomaryov, A., Sychkina, E. Analysis of strain anisotropy and hygroscopic property of clay and claystone. Applied Clay Science. 2015. 114. Pp. 161–169. DOI: 10.1016/j.clay.2015.05.023
24. Ponomarev, A.B., Sychkina, E.N. On the Stress-Strain State and Load-Bearing Strength of Argillite-Like Clays and Sandstones. Soil Mechanics and Foundation Engineering. 2018. 55 (3). Pp. 141–145. DOI: 10.1007/s11204-018-9517-1
25. Bond, A.J., Simpson, B. Pile design to Eurocode 7 and the UK National Annex Part 2: UK National Annex. Ground Engineering. 2010. 43 (1). Pp. 28–31.
26. Toh, C.T., Ooi, T.A., Chiu, H.K., Chee, S.K., Ting, W.H. Design parameters for bored piles in a weathered sedimentary formation. Proceedings of the International Conference on Soil Mechanics and Foundation Engineering. 2. Publ by A.A. Balkema, 1989. Pp. 1073–1078.
27. Zhang, L., Einstein, H.H. Using RQD to estimate the deformation modulus of rock masses. International Journal of Rock Mechanics and Mining Sciences. 2004. 41 (2). Pp. 337–341. DOI: 10.1016/S1365-1609(03)00100-X
28. Rezazadeh, S., Eslami, A. Empirical methods for determining shaft bearing capacity of semi-deep foundations socketed in rocks. Journal of Rock Mechanics and Geotechnical Engineering. 2017. 9 (6). Pp. 1140–1151. DOI: 10.1016/j.jrmge.2017.06.003
29. Skels, P., Bondars, K. Applicability of Small Strain Stiffness Parameters for Pile Settlement Calculation. Procedia Engineering. 172. Elsevier Ltd, 2017. Pp. 999–1006.
30. Zhao, Y., Shi, Y., Yang, J. Cracking of tunnel bottom structure influenced by carbonaceous slate stratum. Magazine of Civil Engineering. 2019. 86 (2). Pp. 83–91. DOI: 10.18720/MCE.86.8
31. Józefiak, K., Zbiciak, A., Maślakowski, M., Piotrowski, T. Numerical modelling and bearing capacity analysis of pile foundation. Procedia Engineering. 111. Elsevier Ltd, 2015. Pp. 356–363.
32. Chaudhary, M.T.A. FEM modelling of a large piled raft for settlement control in weak rock. Engineering Structures. 2007. 29 (11). Pp. 2901–2907. DOI: 10.1016/j.engstruct.2007.02.001
33. Rosenberg, P., Journeaux, N.L. Friction and end bearing tests on bedrock for high capacity socket design: Reply. Canadian Geotechnical Journal. 1977. 14 (2). Pp. 272–272. DOI: 10.1139/t77-029
34. Williams, A.F., Pells, P.J.N. SIDE RESISTANCE ROCK SOCKETS IN SANDSTONE, MUDSTONE, AND SHALE. Canadian geotechnical journal. 1981. 18 (4). Pp. 502–513. DOI: 10.1139/t81-061
35. Lianyang Zhang, Einstein, H.H. End bearing capacity of drilled shafts in rock. Journal of Geotechnical and Geoenvironmental Engineering. 1998. 124 (7). Pp. 574–584. DOI: 10.1061/(ASCE)1090-0241(1998)124:7(574)
36. Reul, O., Randolph, M.F. Piled rafts in overconsolidated clay: Comparison of in situ measurements and numerical analyses. Geotechnique. 2003. 53 (3). Pp. 301–315. DOI: 10.1680/geot.2003.53.3.301
37. Serrano, A., Olalla, C. Shaft resistance of a pile embedded in rock. International Journal of Rock Mechanics and Mining Sciences. 2004. 41 (1). Pp. 21–35. DOI: 10.1016/S1365-1609(03)00070-4
38. Zhussupbekov, A., Omarov, A. Modern Advances in the Field Geotechnical Testing Investigations of Pile Foundations. Procedia Engineering. 165. Elsevier Ltd, 2016. Pp. 88–95.
39. Cai, G., Liu, S., Tong, L., Du, G. Assessment of direct CPT and CPTU methods for predicting the ultimate bearing capacity of single piles. Engineering Geology. 2009. 104 (3–4). Pp. 211–222. DOI: 10.1016/j.enggeo.2008.10.010
40. Niazi, F.S., Mayne, P.W. Cone Penetration Test Based Direct Methods for Evaluating Static Axial Capacity of Single Piles. Geotechnical and Geological Engineering. 2013. 31 (4). Pp. 979–1009.
41. Bartolomei, A.A., Ponomarev, A.B. Experimental investigations and prediction of settlements of conical-pile foundations. Soil Mechanics and Foundation Engineering. 2001. 38 (2). Pp. 42–50. DOI: 10.1023/A:1010422029681
42. Prygunov M.A. Stability of injection piles. Kazan. 2004. 136 p. (rus)
43. Lalin, V.V., Yavarov, A.V., Orlova, E.S., Gulov, A.R. Application of the Finite Element Method for the Solution of Stability Problems of the Timoshenko Beam with Exact Shape Functions. Power Technology and Engineering. 2019. 53 (4). Pp. 449–454. DOI: 10.1007/s10749-019-01098-6

Contacts:

Evgeniya Sychkina, aspirant123@mail.ru

Ian Ofrikhter, ian.ofrikhter@gmail.com

Andrey Ponomaryov, andreypab@mail.ru



DOI: 10.18720/MCE.97.5

Optimisation of steel trusses with a choice of multi-stage prestressing conditions

I.N. Serpik*, N.V. Tarasova

Bryansk State University of Engineering and Technology, Bryansk, Russia

* E-mail: inserpik@gmail.com

Keywords: steel trusses, multiple pre-stresses, optimisation, genetic algorithm, strength, stiffness, stability

Abstract. This paper presents a methodology for optimisation of flat steel trusses with a system of high-strength tie bars, for each of which the possibility of multiple pre-stresses is provided. Pre-stress is one of the most effective ways to increase the carrying capacity of steel trusses with minimum material costs. Besides, a significant effect, according to the literature data, can be achieved by alternating stages of pre-stresses and payloads. At the same time, algorithms for designing such objects while choosing a sequence of force actions still need to be worked out. The problem of minimising the truss cost is considered taking into account strength, stiffness, and stability constraints. A search has been specified for the sequence of alternating the stages of pre-stress and the application of portions of useful loads, pre-stress forces, bar profiles, and cable cross-section area values. Multiple allowable scenarios of force impacts on a redundant template are used. It is acceptable to indicate the load absence condition in such template in some positions. A possibility has been implemented for the cable system to set a redundant topology which is controlled by including the ability to select negligible cross-section areas. As a result, the mathematical statement of the problem is reduced to discrete parametrical optimisation. A scheme of genetic algorithm is implemented with a mixed approach to the mutation operator in order to find efficient solutions. A methodology has been developed to calculate the stress-strain state of steel frameworks pre-stressed using high-strength cables in a single computational process to efficiently check for compliance with the problem constraints. The performance of the suggested procedure of the optimum search has been illustrated by the example of a steel arch truss. A possibility to use bars made of round pipes together with high-strength tie bars was provided. The efficient parameters of the framework and force impact modes have been determined. The expediency of alternating impacts caused by pre-stresses of cables and application of useful load parts is confirmed. The approach proposed will significantly increase the possibility of obtaining cost-effective design solutions for steel trusses.

1. Introduction

Today attention is being increasingly focused on the development of unique structures, including various types of long span constructions. It is often required to use a pre-stress for strained systems of this kind so as to increase their load-carrying capacity while minimising the material costs. Such structure types can be designed efficiently on the basis of an optimum search. Herewith, it is expedient to vary their parameters and topologies on discrete sets of admissible variants determined via existing standards and construction conditions.

Classical approaches to the optimisation of pre-stressed steel structures are well-known [1–4]. These algorithms specify, first of all, the application of mathematical programming methods, and the optimum design process is divided into several stages. Work [1], on the basis of such methodology types, considers the issues of selecting rational structural layouts for pre-stressed systems, determination of rational pre-stress forces, and optimum distribution of material in the structure, unification of framework cross-section area values, and selection of the sequence of pre-stress operations. Article [2] presents stage-by-stage optimisation of pre-stressed flat steel trusses made of tubular profiles. Topological optimisation of the design and selection of bar cross-section areas from the regulatory requirements are performed during the first and second stages, respectively, without regard to pre-stress. At the third stage, the influence of pre-stress of a truss by means of cables built into its lower flange on the structure's load-carrying capacity is assessed, and the structure's



parameters are adjusted. Work [3] covers the optimum design of steel cable trusses in which the cable pre-stress is provided. The truss weight is minimised at restrictions on stresses. The structure topology, pre-stress forces, and cable cross-section area values vary. Initially a uniform-strength system is used. Then the truss topology is corrected by providing an opportunity of selecting “zero” element cross-section area values. In [4] a procedure for minimising the weight of a flat framed structure subjected to pre-stress with restrictions on stresses and displacements is given. At the first stage, the pre-stress force and geometric characteristics of bars are determined. At the second stage, topological optimisation is implemented on the basis of exclusion of the least-loaded structural elements from the structure.

Stage-by-stage optimisation allows to simplify the problem, but, in some cases, it results in a loss of efficient design solutions. This problem can be solved on the basis of up-to-date achievements in the development of the optimum design of different complex engineering systems using metaheuristic iteration methods [5, 6]. Such approaches are efficient in finding global extrema, they do not require that derivatives of functions are considered, while ensuring the possibility of searching for variable parameters on discrete sets. Evolutionary metaheuristic procedures have gained fairly wide popularity for optimisation of deformable objects. They are usually implemented as genetic algorithms [7–11]. Some other metaheuristic methods were also used for this purpose: Particle Swarm Optimization [12], Simulated Annealing [13], Tabu Search [14], Harmony Search [15], Ant Colony Optimization [16], Big Bang – Big Crunch Algorithm [17], Imperialist Competitive Algorithm [18], Ray Optimization [19], Mine Blast Algorithm [20], Cuckoo Search Algorithm [21], Firefly Algorithm [22], Dolphin Echolocation [23], Teaching-Learning-Based Optimization [24], Chaotic Swarming of Particles [25], Bat-Inspired Algorithm [26], Colliding Bodies Optimization [27], Search Group Algorithm [28], etc. Quite detailed information on the use of metaheuristic procedures for optimisation of load-bearing systems is given in the reviews [29–31].

The research [32–35] uses metaheuristic schemes that allow to solve optimal search problems for pre-stressed frames according to all design parameters in a single computation process. Work [32] presents the procedure for optimisation using a genetic algorithm of pre-stressed reinforced concrete multi-span bridges. The selected parameters are the number of object spans, the bridge cross-section area, and the principal reinforcement parameters. Article [33] considers the optimum design of pre-stressed, pre-cast reinforced concrete bridges for pedestrians. A bridge structure with a framework, that includes a pre-stressed reinforced concrete beam with a U-shaped cross-section and a reinforced concrete slab, is examined. The bridge's cost is minimised in variation of beam and slab dimensions, material grades, as well as parameters of principal and design reinforcement. Herewith, a metaheuristic procedure based on a Simulated Annealing algorithm is used. Works [34, 35] describe the development of an evolutionary algorithm for the optimum design of pre-stressed steel flat trusses with system of tie bars consisting of high-strength cables. The truss minimisation problem is solved taking into account the strength, stiffness, and stability limitations. Simultaneously the search is performed both for bar profiles and for the cross-section area of tie bars and their pre-tension. Herewith, in article [34] the possibility of excluding tie-bars from the redundant cable system topology is considered.

Work [36] presents an optimisation algorithm using an ANSYS v12 software system for an innovative suspended structure with the main load-carrying elements as pre-stressed cable trusses. The flooring panels in such a framework are made of perpendicularly glued board layers and are located over the lower truss flange. The optimisation goal is to obtain the values of the design parameters while ensuring minimum material consumption. The stress and displacement limitations were taken into account. The cable cross-section areas and pre-stress forces were considered as variable parameters.

It should be noted that one of the important methods of using the possibilities of pre-stress is the implementation of alternating pre-stresses and useful load applications [1, 37]. At the same time, the methodology of the efficient design of objects in a single iteration procedure for such tasks is still to be adjusted as applied to various framework classes.

The aim of the present work is to develop of an algorithm to ensure the possibility of discrete optimisation on the basis of an evolutionary approach to pre-stressed steel flat trusses with a comprehensive selection of rational alternation of the stages of pre-stress and useful load application, cable structure, pre-stress forces, bar profiles, and cable cross-section areas.

2. Methods

2.1. Problem statement

Let us assume that the truss is fastened from its plane in nodes. We should take into account the tension-compression and flexure strains when dealing with bars, and tensile strain when dealing with cables. We provide for setting a redundant structure for the cable system in general case, and a redundant number of force impacts of different types. The control of these redundant possibilities is provided by taking into account parameters of conditional tie bar variants with negligible cross section areas and zero pre-stress forces and useful load portions in sets of permissible values. Then the topology and parametric optimisation is reduced to parametric one.

Let us minimise the design cost C :

$$C\left(\{V\}_1, \{V\}_2, \dots, \{V\}_{k_o}, \{A\}, \{H\}\right) \Rightarrow \min, \quad (1)$$

where

$$\{V\}_k = \left\{ K_{g(k)} \left(n_{1(k)}, \beta_{1(k)} \right) \left(n_{2(k)}, \beta_{1(k)} \right) \dots \left(n_{m(k)}, \beta_{m(k)} \right) K_{p1(k)} K_{p2(k)} \dots K_{ps_o(k)} \right\}^T$$

$(k = 1, 2, \dots, k_o)$ is the vector determining the action group k ; k_o is the total number of possible impact groups; $K_{g(k)}$ is the portion of design gravity forces related to group k ; $(n_{j(k)}, \beta_{j(k)})$ ($j = 1, 2, \dots, m$) is a pair of numbers determining for group k the number $n_{j(k)}$ of tie bar T_j in the general numbering system of load-carrying elements and share $\beta_{j(k)}$ of the tension force increment at this stage of its total pre-stress; m is the maximum number of tie bars which may be used in the truss according to the problem statement; $K_{ps(k)}$ is the share of the useful load s for group k ($s = 1, 2, \dots, s_o$); s_o is the number of useful loads; $\{A\} = \{A_1 A_2 \dots A_r\}^T$ is a vector of independently variable areas A_l of cross sections for bar groups ($l = 1, 2, \dots, r$); $\{H\} = \left\{ (D_{T1}, \alpha_{T1}) (D_{T2}, \alpha_{T2}) \dots (D_{Tm}, \alpha_{Tm}) \right\}^T$ is a vector of number pairs, each of which determines for tie bar T_j ($j = 1, 2, \dots, m$) diameter D_{Tj} and share α_{Tj} of force S_j of its total pre-stress of the breaking load R_{Tj} ($S_j = \alpha_{Tj} R_{Tj}$).

Let us take into account the following limitations the compliance with which is checked with consideration the requirements of standard "SP 16.13330.2017. Steel structures. The updated edition of SNiP II-23-81*" on each of the considered force impact stages:

1. Limitation on stresses in the truss bars:

$$|\sigma_M| \leq R_y, \quad (2)$$

where σ_M is von Mises stress; R_y is the design steel resistance assigned on the basis of the yield strength.

2. Limitation on forces in the tie bars:

$$N_T \leq R_T / k_T, \quad (3)$$

where N_T is the longitudinal force in any tie bar; R_T is the breaking load for the tie bar; k_T is the safety margin.

3. Limitation on stiffness:

$$|\delta| \leq f, \quad (4)$$

where δ is a projection of the truss node displacement vector to any Cartesian coordinate system axes; f is the permissible value of the modulus of such displacement.

4. The bar stability condition.
5. Design and technological requirements.

2.2. Algorithm for calculating stress-strain state of a truss during multiple pre-stresses

Let us assume that each tie bar can be pre-stressed to the structure in several stages. We take into account the design non-linearity expressed by change of the framework structure as each new tie bar is included into it. n impacts are considered as tie bar pre-stresses and components of design loads. Let us discretise the object using the finite element method according to displacement method [38]. For each impact the calculation will be performed in a linear setting by solving the following linear algebraic equation system:

$$\left([K] + \sum_{j=1}^{J_i} [K_T]_j \right) \{\Delta_i\} = \{R_i\}, \quad (5)$$

where $[K]$ is the global stiffness matrix for a truss without tie bars; J_i is a number of tie bars which shall be included into the design diagram of the i th impact; $[K_T]_j$ is an addition to the global stiffness matrix taking into account tie bar T_j ; $\{\Delta_i\}$ is a vector of nodal displacement increments caused by impact i ; $\{R_i\}$ is a vector of statically equivalent nodal forces for the i th impact.

After that the nodal displacement values are adjusted:

$$\{\delta\}^{(i)} = \{\delta\}^{(i-1)} + \{\Delta_i\}, \quad (6)$$

where $\{\delta\}^{(i)}$, $\{\delta\}^{(i-1)}$ are the nodal displacement vectors obtained on the basis of the results of impacts i and $i-1$ ($\{\delta\}^{(0)} = 0$).

Calculation of the structure pre-stress using tie bar T_j is taken into consideration in two stages using conditional temperature strains. Let us assume that with due allowance for losses, the tie bar shall get the positive increment ΔS_{jA} of the tension force. At the 1st stage we set the test change of temperature Δt in the tie bar resulting in the appearance of auxiliary nodal forces $F_{Oj}^{(1)}$ (Fig. 1), the modulus of which is

$$|F_{Oj}^{(1)}| = \alpha_T |\Delta t| E_T A_T, \quad (7)$$

where α_T , E_T , A_T are the linear temperature expansion coefficient, elasticity modulus, and cross section area of the cable.

The object is calculated taking into consideration only such forces with computation of longitudinal force $N_{Fj}^{(1)}$ in the tie bar which will work in compression conditionally. Then the actual increment of the longitudinal force in the tie bar is determined:

$$\Delta N_j^{(1)} = |F_{Oj}^{(1)}| + N_{Fj}^{(1)}, \quad (8)$$

where longitudinal forces are considered as algebraic values.

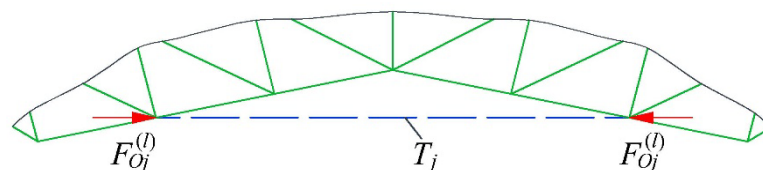


Figure 1. Auxiliary forces caused by conditional temperature effect on tie bar T_j

at stage l ($l = 1, 2$).

At stage 2 the value of auxiliary forces is adjusted:

$$|F_{Oj}^{(2)}| = \frac{|F_{Oj}^{(1)}| \Delta S_{jA}}{\Delta N_j^{(1)}}, \quad (9)$$

the truss calculation is repeated, and the increment of longitudinal force $\Delta N_j^{(2)}$ for this stage is determined.

Since the calculations within one impact are performed in a linear setting, we will have $\Delta N_j^{(2)} = \Delta S_{jA}$, fulfilling the condition of modelling the stress-strain state of the structure caused by pre-stress. If the tensioning

is carried out to stops, then by setting force $F_{Oj}^{(1)} = \Delta S_{jA}$ we ensure modelling of the object state caused by the considered impact after only one calculation stage.

During each subsequent impact i force in tie bar T_j is re-calculated as follows:

$$N_{j(i)} = N_{j(i-1)} + \Delta N_{j(i)}, \quad (10)$$

where $N_{j(i)}$, $N_{j(i-1)}$ are tension forces in tie bar T_j before and after impact i ; $\Delta N_{j(i)}$ is change of tension force in tie bar T_j , obtained due to impact i .

2.3. Optimum search procedure

Limitation 5 is taken into account when the permissible values of variable parameters are set. All other limitations are considered during optimisation as active ones. To achieve an optimum design, we use an approach to evolutionary modelling of frameworks in the form of a genetic algorithm the basic provisions of which are detailed in [39, 40]. Let us consider the main population Π_A with length L of chromosome and auxiliary population Π_B of elite individuals, the size of which depends on the results of operation of genetic algorithm, but does not exceed L . Population Π_B is used for keeping the efficient genetic material taken into account during replenishment of population Π_A . The limitations are considered by simple rejection of non-operable structure variants. A single-point crossover is implemented. We apply a mixed procedures ensuring random change of parameter values with alternation of selection from variants with the nearest number in the chromosome and from the elements which are randomly located in the chromosome. Table 1 explains the parameter value variation scheme, where p_a, p_b are numbers randomly generated on numeric line segment $[0, 1]$ at uniform distribution law, r_j is the current position number in a set of its permissible values, w_j is the number of elements in such set, $m_a, m_{b1}, m_{b2}, m_{b3}$ are the specified values. During optimisation of truss structures it is expedient to assume $m_a = 0.9, m_{b1} = 0.5, m_{b2} = 0.75, m_{b3} = 0.9$ [40].

Table 1. Scheme of parameter value change during mutation.

Condition on p_a	Condition on p_b	Condition on r_j	Parameter value selection method
$p_a \leq m_a$	$p_b < m_{b1}$	$r_j \geq 3$	$r_j = r_j - 2$
		$r_j = 2$	$r_j = r_j - 1$
	$m_{b1} \leq p_b < m_{b2}$	$r_j \geq 2$	$r_j = r_j + 1$
	$m_{b2} \leq p_b < m_{b3}$	$r_j \leq w_j - 1$	
	$p_b \geq m_{b3}$	$r_j = w_j - 1$	
		$r_j \leq w_j - 2$	$r_j = r_j + 2$
$p_a > m_a$	is not taken into consideration	is not taken into consideration	The value is randomly selected from a set of permissible values

It is assumed in this task that the chromosome can contain the following information in the general case:

$$[G] = [\zeta \ A_1 \ A_2 \ \dots \ A_r \ (D_{T1}, \alpha_{T1}) \ (D_{T2}, \alpha_{T2}) \ \dots \ (D_{Tm}, \alpha_{Tm})], \quad (11)$$

where ζ is the number of scenario of impact on the truss.

It should be noted that for exhaustive type problems, the only reliable criteria for achieving the global optimum is usually the complete exhaustion of all possible variants associated with a significant number of calculations. Numerical experiments show that at the optimum synthesis of pre-stressed steel trusses on the basis of the approach presented herein, the absence of changes in the group of elite projects for 500–600 iterations indicates the expediency of completion of the evolutionary search. Usually the continuation of such process does not result in any significant change to the objective function.

3. Results and Discussion

Let us provide the results of designing the steel flat truss shown in Fig. 2. It was assumed that the bars are made of round pipes in accordance with Russian State Standard GOST 32931-2015 "Steel shaped tubes for steel structures. Specifications." The truss bar material is steel S245 (SP 16.13330.2017). A provision was made to introduce up to two high-strength cable-type tie bars in accordance with GOST 3081-80 "Two lay rope of LK-O type, design 6 19 (1+9+9)+7×7 (1+6)." In accordance with SP 16.13330.2017, the elasticity modulus for the bar material was assumed as $E = 2.06 \cdot 10^5$ MPa, the elasticity modulus of rope material was assumed as $E_T = 1.47 \cdot 10^5$ MPa. In accordance with SP 20.13330.2016 "Loads and impacts. Updated edition of SNiP 2.01.07-85*," the maximum permissible deflection for 1/300 of the truss span was set. The cost of rolled metal products was calculated using the cost of metal pipes of Metallokonstruksii LLC (<http://www.metalconstr.ru/09.html>), the cost of tie bars manufactured by Optimist LLC (<http://optimist-32.ru/produksiya/kanaty-i-veryovki/kanat-stalnoj/>). The prices taken into account were current as of May 2019.

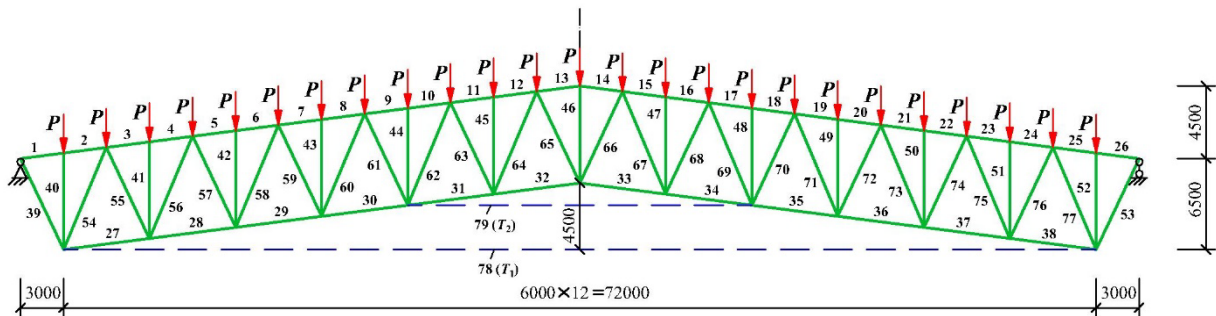


Figure 2. Long-span truss: 1–77 are bars, 78 (T_1), 79 (T_2) are tie bars.

Permitted possibilities included using two tie bars T_1 , T_2 during tensioning on the structure, and the absence of one or both ropes. Weights of bars and ropes depend on the parameter values and useful load as a system of concentrated forces applied to the upper truss flange, where $P = 30$ kN were taken into consideration. The impact sequence was considered at $k_o = 2$, $s_o = 1$ based on the following template:

$$\begin{aligned} \{V\}_1 &= \left\{ 1 \begin{pmatrix} n_{1(1)}, \beta_{1(1)} \\ n_{2(1)}, \beta_{2(1)} \end{pmatrix} K_{p1(1)} \right\}^T, \\ \{V\}_2 &= \left\{ 0 \begin{pmatrix} n_{1(2)}, \beta_{1(2)} \\ n_{2(2)}, \beta_{2(2)} \end{pmatrix} K_{p1(2)} \right\}^T. \end{aligned} \quad (12)$$

This template shows that initially the object gravity forces are taken into account, then the consecutive rope tensioning and useful load application can be performed. Then a provision is made to finally tension the ropes and take into consideration the remaining portion of the useful load.

The set of permissible impact scenarios was specified (Table 2). The bar grouping is detailed in Table 3. For each group a possibility was specified to use the following values of the pipe outer diameter and thickness ($D \times t$): 70×4, 89×5.5, 127×5.5, 159×6, 177.8×8, 219×8, 219×9, 219×10, 219×12, 219×13, 219×14, 273×12, 273×14, 325×13, 325×14, 355.6×14, and 377×14 (mm). Couples of numbers ($D_{Tj} \times \alpha_{Tj}$) for ropes were chosen from these options: (33, 0.6), (33, 0.5), (33, 0.4), (33, 0.3), (33, 0.2), (33, 0.1), (33, 0), (31, 0.6), (31, 0.5), (31, 0.4), (31, 0.3), (31, 0.2), (31, 0.1), (31, 0), (29.5, 0.6), (29.5, 0.5), (29.5, 0.4), (29.5, 0.3), (29.5, 0.2), (29.5, 0.1), (29.5, 0), (27, 0.6), (27, 0.5), (27, 0.4), (27, 0.3), (27, 0.2), (27, 0.1), (27, 0), (25, 0.6), (25, 0.5), (25, 0.4), (25, 0.3), (25, 0.2), (25, 0.1), (25, 0), and (0, 0) (mm, -). Condition $D_{Tj} = 0$ corresponds to absence of rope. Case $\alpha_{Tj} = 0$ and/or $\beta_{j(i)} = 0$ indicates that the rope was only subjected to small technological tensioning. If $D_{Tj} = 0$ is considered for a tie bar, then its pre-stress order set in scenarios is not taken into consideration. Thus, the specified possibilities include both one-time and two-time rope tensioning, setting ropes without any significant tensioning, exclusion of ropes from the redundant topology of the framework.

Table 2. Scenarios of impact on truss.

Scenario	$n_{1(1)}$	$\beta_{1(1)}$	$n_{2(1)}$	$\beta_{2(1)}$	$K_{p1(1)}$	$n_{1(2)}$	$\beta_{1(2)}$	$n_{2(2)}$	$\beta_{2(2)}$	$K_{p1(2)}$
1	78	0.7	79	0.7	0.7	78	0.3	79	0.3	0.3
2	78	0.7	79	0.7	0.5	78	0.3	79	0.3	0.5
3	78	0.7	79	0.7	0.3	78	0.3	79	0.3	0.7
4	78	0.7	79	0.7	0.1	78	0.3	79	0.3	0.9
5	78	0.5	79	0.5	0.7	78	0.5	79	0.5	0.3
6	78	0.5	79	0.5	0.5	78	0.5	79	0.5	0.5
7	78	0.5	79	0.5	0.3	78	0.5	79	0.5	0.7
8	78	0.5	79	0.5	0.1	78	0.5	79	0.5	0.9
9	78	0.3	79	0.3	0.7	78	0.7	79	0.7	0.3
10	78	0.3	79	0.3	0.5	78	0.7	79	0.7	0.5
11	78	0.3	79	0.3	0.3	78	0.7	79	0.7	0.7
12	78	0.3	79	0.3	0.1	78	0.7	79	0.7	0.9
13	78	0.1	79	0.1	0.7	78	0.9	79	0.9	0.3
14	78	0.1	79	0.1	0.5	78	0.9	79	0.9	0.5
15	78	0.1	79	0.1	0.3	78	0.9	79	0.9	0.7
16	78	0.1	79	0.1	0.1	78	0.9	79	0.9	0.9
17	78	0	79	0	0.7	78	1	79	1	0.3
18	78	0	79	0	0.5	78	1	79	1	0.5
19	78	0	79	0	0.3	78	1	79	1	0.7
20	78	0	79	0	0.1	78	1	79	1	0.9
21	78	0	79	0	0	78	1	79	1	1
22	79	0.7	78	0.7	0.7	79	0.3	78	0.3	0.3
23	79	0.7	78	0.7	0.5	79	0.3	78	0.3	0.5
24	79	0.7	78	0.7	0.3	79	0.3	78	0.3	0.7
25	79	0.7	78	0.7	0.1	79	0.3	78	0.3	0.9
26	79	0.5	78	0.5	0.7	79	0.5	78	0.5	0.3
27	79	0.5	78	0.5	0.5	79	0.5	78	0.5	0.5
28	79	0.5	78	0.5	0.3	79	0.5	78	0.5	0.7
29	79	0.5	78	0.5	0.1	79	0.5	78	0.5	0.9
30	79	0.3	78	0.3	0.7	79	0.7	78	0.7	0.3
31	79	0.3	78	0.3	0.5	79	0.7	78	0.7	0.5
32	79	0.3	78	0.3	0.3	79	0.7	78	0.7	0.7
33	79	0.3	78	0.3	0.1	79	0.7	78	0.7	0.9
34	79	0.1	78	0.1	0.7	79	0.9	78	0.9	0.3
35	79	0.1	78	0.1	0.5	79	0.9	78	0.9	0.5
36	79	0.1	78	0.1	0.3	79	0.9	78	0.9	0.7
37	79	0.1	78	0.1	0.1	79	0.9	78	0.9	0.9
38	79	0	78	0	0.7	79	1	78	1	0.3
39	79	0	78	0	0.5	79	1	78	1	0.5
40	79	0	78	0	0.3	79	1	78	1	0.7
41	79	0	78	0	0.1	79	1	78	1	0.9
42	79	0	78	0	0	79	1	78	1	1

Table 3. Bar grouping.

Group	Numbers of bars in the group	Group	Numbers of bars in the group
1	1, 26	10	41, 42, 50, 51
2	2, 3, 4, 5, 22, 23, 24, 25	11	43, 44, 48, 49
3	6, 7, 8, 9, 18, 19, 20, 21	12	45, 47
4	10, 11, 12, 13, 14, 15, 16, 17	13	46
5	27, 28, 37, 38	14	54, 56, 58, 73, 75, 77
6	29, 30, 35, 36	15	60, 62, 64, 67, 69, 71
7	31, 32, 33, 34	16	55, 57, 59, 72, 74, 76
8	39, 53	17	61, 63, 65, 66, 68, 70
9	40, 52	–	–

30 independent optimisation process runs were carried out with implementation of 15,000 iterations of evolutionary algorithm in one run. Based on the results of the search, 3 different structure variants were found, in each of which the algorithm left one rope. The information about obtained results is provided in Tables 4 and 5. As Table 4 shows, the lowest cost is achieved in the 1st structure variant obtained in 2 runs. Herewith, the lower tie bar T_1 is left at $D_{T1} = 33$ mm, and two possible impact scenarios are selected, each of which stipulates two-stage application of useful load (see Table 2). At the same time, scenario 22 stipulates the two-time pre-stress of the rope, and scenario 39 stipulates initial introduction of the rope without any significant pre-stress and actual one-time pre-stress between stages of impact by useful load. The second structure variant achieved in 26 runs is associated with ten impact scenarios and stipulates the use of only tie-bar T_1 , but at $D_{T1} = 31$ mm. In the third variant which was implemented in two runs with identical impacts, only the upper tie bar T_2 is left at $D_{T2} = 25$ mm.

Table 4. Results of optimisation on objective function, ropes and impact conditions.

Structure variant number	C , thous. RUB.	Remaining tie bar	D_{Tj} , mm	α_{Tj}	S_j , kN	Scenario number	Number of runs
1	689.7	T_1	33	0.4	248.6	22	1
						39	1
2	721.1	T_1	31	0.4	168.45	34	7
						39	3
						38	4
						36	4
						26	1
						27	2
						23	1
						35	1
						22	2
						30	1
3	870.6	T_2	25	0.5	174.0	17	2

Table 5. Results for bar profiles.

Bar group	$D \times t$, mm for structure variants		
	Variant 1	Variant 2	Variant 3
1	127×5.5	127×5.5	127×5.5
2	177.8×8	177.8×8	219×8
3	219×8	219×9	219×12
4	219×8	219×9	219×12
5	127×5.5	127×5.5	177.8×8
6	159×6	177.8×8	219×9
7	177.8×8	177.8×8	219×8
8	127×5.5	127×5.5	159×6
9	89×5.5	89×5.5	89×5.5
10	89×5.5	89×5.5	89×5.5
11	89×5.5	89×5.5	70×4
12	89×5.5	89×5.5	89×5.5
13	159×6	127×5.5	89×5.5
14	219×8	219×8	219×8
15	159×6	159×6	177.8×8
16	89×5.5	127×5.5	127×5.5
17	89×5.5	70×4	70×4

The behaviour of decrease of the objective function in the developed computational scheme is illustrated in Fig. 3 by examples of runs with the best and the worst convergence for each of the obtained structure variants. As a whole, for all 30 runs in the best case, in terms of convergence, the considered result was achieved by iteration 154, in the worst case – by iteration 10,012.

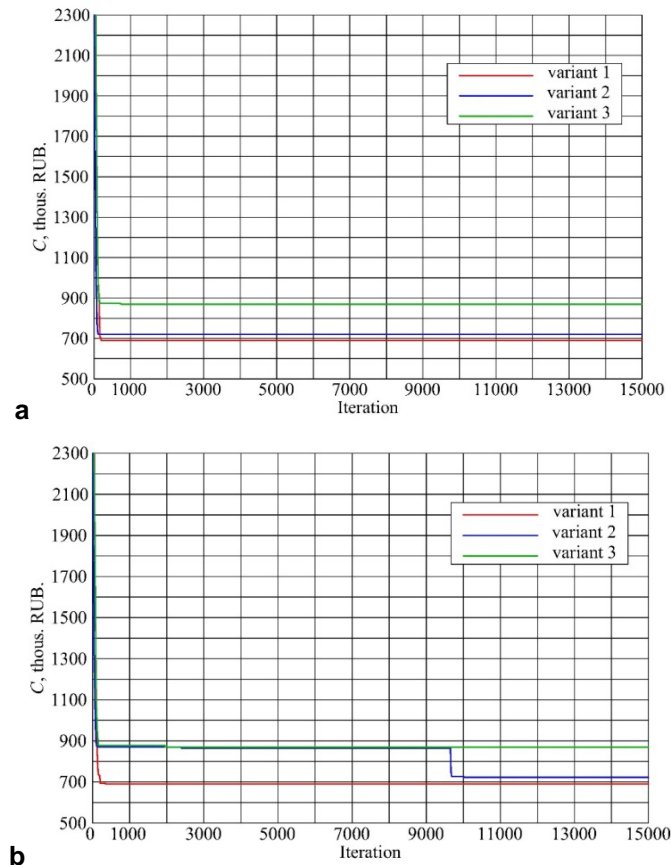


**Figure 3. Change of the objective function during optimisation:
a – best convergences, b – worst convergences.**

In none of 30 runs impact scenario 42 was accepted, stipulating one-time pre-stress of tie bars and subsequent application of all useful load. At the same time, this scenario, according to its position in the set of permissible impact combinations, was accepted by us for all individuals of the initial population. This result corresponds to the provision of principal efficiency of alternating impacts caused by the application of useful load portions and shares of tie bar pre-stresses [1, 37].

It should be noted that the optimum search organisation variant with the setting of permissible scenarios suggested herein allows the designer to significantly take into consideration the peculiarities of real civil construction conditions. The developed methodology may become the basis for expanding the use of multi-stage pre-stresses in building structures, because it permits automation of the framework development process with such control of force impacts.

4. Conclusions

1. We have suggested a computational scheme for the evolutionary optimisation of pre-stressed steel truss structures with the possibility to vary the system of high-strength tie bars, pre-stress sequence and application of useful loads, pre-stress forces, bar profiles and tie bar cross section areas on discrete topology sets. The active limitations in terms of strength, stiffness, and stability are taken into consideration. Design and process requirements are taken into account during the creation of sets of permissible parameter values.

2. A methodology has been developed for calculation of the stress-strain state of steel trusses subjected to pre-stress using a rope system in a single computational process. The design's non-linearity associated with the change of the framework structure during inclusion of each new tie bar is taken into consideration.

3. The operability of the suggested computational scheme of optimum design has been confirmed by the example of a pre-stressed steel truss with 78 m span tie bars. As a result of the performed optimisation processes, three structure variants have been obtained which stipulate alternating tie bar pre-stresses and the application of useful load shares.

4. The research results may be used for the design and reconstruction of pre-stressed structure systems in civil construction and primarily for unique structures. It is expedient to implement the basic provisions of the developed algorithms in finite element analysis software application packages.

5. Acknowledgement

The reported study was funded by RFBR according to the research project No. 18-08-00567.

References

- Olkov, Ya.I., Holopov, I.S. Optimal'noye proyektirovaniye metallicheskih predvaritel'no napryazhennykh ferm [Optimal design of metal prestressed trusses]. STROYIZDAT. Moscow, 1985. 155 p. (rus)
- Gkantou, M., Theofanous, M., Baniotopoulos, C. Optimisation of high strength steel prestressed trusses. Proceedings of 8th GRACM international congress on computational mechanics. Volos, Greece. 2015 [Online]. System requirements: Adobe Acrobat Reader. https://www.researchgate.net/publication/319204483_Optimisation_of_high_strength_steel_prestressed_trusses (date of application: 10.09.2019)
- Yang, H.J., Zhang, A.L., Yao, L. Topology optimization design of prestressed cable-truss structures. Journal of Beijing Polytechnic University. 2011. 37 (9). Pp. 1360–1366.
- Yao, L. Topology optimization design of pre-stressed plane entity steel structure with the constrains of stress and displacement. Advanced Materials Research. 2014. No. 945–949. Pp. 1216–1222. DOI: 10.4028/www.scientific.net/AMR.945-949.1216
- Yang, X.-S. Engineering Optimization: An Introduction with Metaheuristic Applications. Wiley. Hoboken, 2010. 376 p.
- Du, K.-L., Swamy, M.N.S. Search and Optimization by Metaheuristics: Techniques and Algorithms Inspired by Nature. Birkhäuser. Basel, 2016. 434 p.
- Toğan, V., Daloğu, A.T. An improved genetic algorithm with initial population strategy and self-adaptive member grouping. Computers and Structures. 2008. 86 (11–12). Pp. 1204–1218. DOI: 10.1016/j.compstruc.2007.11.006
- Grygierek, K. Optimization of trusses with self-adaptive approach in genetic algorithms. Architecture Civil Engineering Environment. 2016. 9 (4). Pp. 67–72. DOI: 10.21307/acee-2016-053
- Kirsanov, M.N. Geneticheskiy algoritm optimizatsii sterzhnevnykh sistem [Genetic algorithm for optimizing of rod systems]. Structural Mechanics and Analysis of Constructions. 2010. 229 (2). Pp. 60–63. (rus)
- Alekhin, V.N., Hanina, A.B. Razrabotka modeli geneticheskogo algoritma dlya optimizatsii stal'nykh mnogoetazhnykh ram [Development of a genetic algorithm model for optimizing steel multi-story frames]. International Journal for Computational Civil and Structural Engineering. 2008. 4 (2). Pp. 16–18.
- Serpik, I.N., Alekseytsev, A.V., Balabin, P.Y., Kurchenko, N.S. Flat rod systems: optimization with overall stability control. Magazine of Civil Engineering. 2017. 76 (8). Pp. 181–192. DOI: 10.18720/MCE.76.16
- Zhengdong, H., Zhengqi, G., Xiaokui, M., Wanglin, C. Multimaterial layout optimization of truss structures via an improved particle swarm optimization algorithm. Computers & Structures. 2019. No. 222. Pp. 10–24. DOI: 10.1016/j.compstruc.2019.06.004
- Millán-Páramo, C. Modified simulated annealing algorithm for discrete sizing optimization of truss structure. Jordan Journal of Civil Engineering. 2018. 12 (4). Pp. 683–697.
- Degertekin, S.O., Hayalioglu, M.S. Optimum design of steel space frames: tabu search vs. simulated annealing and genetic algorithms. International Journal of Engineering and Applied Sciences. 2009. 1 (2). Pp. 34–45.
- Degertekin, S.O. Improved harmony search algorithms for sizing optimization of truss structures. Computers and Structures. 2012. No. 92–93. Pp. 229–241. DOI: 10.1016/j.compstruc.2011.10.022
- Kaveh, A., Talatahari, S. Particle swarm optimizer, ant colony strategy and harmony search scheme hybridized for optimization of truss structures. Computers and Structures. 2009. 87 (5–6). Pp. 267–283. DOI: 10.1016/j.compstruc.2009.01.003
- Toklu, Y.C. Application of big bang - big crunch optimization to resource constrained scheduling problems. KSCE Journal of Civil Engineering. 2018. 22 (12). Pp. 4760–4770. DOI: 10.1007/s12205-017-1549-y
- Kaveh, A., Talatahari, S. Optimum design of skeletal structures using imperialist competitive algorithm. Computers and Structures. 2010. 88 (21–22). Pp. 1220–1229. DOI: 10.1016/j.compstruc.2010.06.011
- Kaveh, A., Khayatizad, M. A new meta-metaheuristic method: ray optimization. Computers and Structures. 2012. 112–113. Pp. 283–294. DOI: 10.1016/j.compstruc.2012.09.003
- Sadollah, A., Bahreininejad, A., Eskandar, H., Hamdi, M. Mine blast algorithm for optimization of truss structures with discrete variables. Computers and Structures. 2012. No. 102–103. Pp. 49–63. DOI: 10.1016/j.compstruc.2012.03.013
- Gandomi, A.H., Talatahari, S., Yang, X.S., Deb, S. Design optimization of truss structures using cuckoo search algorithm. The Structural Design of Tall and Special Buildings. 2012. 22 (17). Pp. 1330–1349. DOI: 10.1002/tal.1033
- Miguel, L.F.F., Lopez, R.H. Multimodal size, shape and topology optimization of truss structures using the firefly algorithm. Advances in Engineering Software. 2013. No. 56. Pp. 23–37. DOI: 10.1016/j.advengsoft.2012.11.006
- Arjmand, M., Sheikhi Azqandi, M., Delavar, M. Hybrid improved dolphin echolocation and ant colony optimization for optimal discrete sizing of truss structures. Journal of Rehabilitation in Civil Engineering. 2018. 6 (1). Pp. 72–87. DOI: 10.22075/jrce.20-17.11367.1186
- Degertekin, S.O., Hayalioglu, M.S. Sizing truss structures using teaching-learning-based optimization. Computers and Structures. 2013. No. 119. Pp. 177–188. DOI: 10.1016/j.compstruc.2012.12.011
- Kaveh, A., Sheikholeslami, R., Talatahari, S., Keshvari-Ilkhichi, M. Chaotic swarming of particles: a new method for size optimization of truss structures. Advances in Engineering Software. 2014. No. 67. Pp. 136–147. DOI: 10.1016/j.advengsoft.20-13.09.006
- Hasancebi, O.A., Teke, T., Pekcan, O. Bat-inspired algorithm for structural optimization. Computers and Structures. 2013. No. 128. Pp. 77–90. DOI: 10.1016/j.compstruc.2013.07.006
- Kaveh, A., Mahdavi, V.R. Colliding bodies optimization method for optimum design of truss structures with continuous variables. Advances in Engineering Software. 2014. No. 70. Pp. 1–12. DOI: 10.1016/j.advengsoft.2014.01.002
- Goncalves, M.S., Lopez, R.H., Miguel, L.F.F. Search group algorithm: A new metaheuristic method for the optimization of truss structures. Computers and Structures. 2015. No. 153. Pp. 165–184. DOI: 10.1016/j.compstruc.2015.03.003
- Lamberti, L., Pappalettere, C. Metaheuristic design optimization of skeletal structures: A review. Computational Technology Reviews. 2011. No. 4. Pp. 1–32. DOI: 10.4203/ctr.4.1
- Saka, M.P., Geem, Z.W. Mathematical and metaheuristic applications in design optimization of steel frame structures: An extensive review. Mathematical Problems in Engineering. 2013. Pp. 1–33. DOI: 10.1155/2013/271031
- Stolpe, M. Truss optimization with discrete design variables: A critical review. Structural and Multidisciplinary Optimization. 2016. 53 (2). Pp. 349–374. DOI: 10.1007/s00158-015-1333-x

32. Ayd, Z., Ayvaz, Y. Overall cost optimization of prestressed concrete bridge using genetic algorithm. *KSCE Journal of Civil Engineering*. 2013. 17 (4). Pp. 769–776. DOI: 10.1007/s12205-013-0355-4
33. Martí, J.V., González-Vidosa, F., Alcalá, J. Heuristic optimization of prestressed concrete precast pedestrian bridges. *Advances in Engineering Software*. 2010. 41 (7–8). Pp. 916–922. DOI: 10.1016/j.advengsoft.2010.05.003
34. Serpik, I.N., Tarasova, N.V. Optimizatsiya predvaritel'no napryazhennykh stal'nykh ferm s ispol'zovaniyem evolyutsionnogo poiska [Optimization of pre-stressed steel trusses with using the evolutionary search]. *Structural Mechanics and Analysis of Constructions*. 2019. 282 (1). Pp. 58–64. (rus)
35. Serpik, I.N., Tarasova, N.V. Poisk effektivnykh parametrov predvaritel'no napryazhennykh stal'nykh bol'sheproletnykh ferm s neskol'kimi zatyazhkami [Search for effective parameters of prestressed steel long-span trusses with several tie bars]. *Innovation in construction-2017: Materials of the international scientific-practical conference*. BGITU. Bryansk, 2017. Pp. 285–290. (rus)
36. Buka-Vaivade, K., Serdjuks, D., Goremikins, V., Pakrastins, L., Vatin, N.I. Suspension structure with cross-laminated timber deck panels. *Magazine of Civil Engineering*. 2018. 83 (7). Pp. 126–135. DOI: 10.18720/MCE.83.12
37. Belenya, E.I. *Prestressed load-bearing metal structures*. 2nd edn. Moscow: Mir. 1977. 463 p.
38. Zienkiewicz, O.C., Taylor, R.L., Fox, D. *The Finite Element Method for Solid and Structural Mechanics*. Elsevier. Oxford, 2014. 672 p.
39. Serpik, I.N., Miroshnikov, V.V., Serpik, M.I., Tyutyunnikov A.I. Geneticheskaya protsedura sinteza nesushchikh konstruktsiy vagonov [Genetic procedure of wagons bearing structures synthesis]. *Kachestvo mashin: Sbornik trudov 4-y mezhdunarodnoy nauchno-tekhnicheskoy konferentsii. V dvukh tomakh. T.1.* [Quality of machines: Proceedings of the IV international scientific and technical conference. In two volumes. No. 1]. Bryansk, 2001. Pp. 75–77. (rus)
40. Serpik, I.N., Alekseytsev, A.V., Balabin, P.Y. Mixed approaches to handle limitations and execute mutation in the genetic algorithm for truss size, shape and topology optimization. *Periodica Polytechnica Civil Engineering*. 2017. 61 (3). Pp. 471–482. DOI: 10.3311/PPci.8125

Contacts:

Igor Serpik, insepik@gmail.com

Natalya Tarasova, tarasova_natalie@mail.ru

© Serpik, I.N., Tarasova, N.V., 2020



DOI: 10.18720/MCE.97.6

Stress-strain state of the precast monolithic bent element

A.A. Koyankin^{a*}, V.M. Mitasov^b^a Siberian Federal University, Krasnoyarsk, Russia^b Novosibirsk state University of architecture and construction, Novosibirsk, Russia* E-mail: KoyankinAA@mail.ru

Keywords: reinforced concrete, compressive strength, cracks, tensile strength, reinforcement, experimental investigations, precast monolithic structures

Abstract. The features of the stress-strain state of a precast monolithic bent element (beam) arising as a result of its phased installation and loading are considered and experimentally investigated. At the first stage, the load is perceived only by the precast part of the beam made of heavy concrete, and at the second stage, monolithic lightweight concrete (expanded clay concrete) is included in the process of deformation and perception of the external load. There were two factors that served as motivation for these experimental studies: – Real precast monolithic structure, mounted on the construction site, in the absence of special structural measures (temporary mounting racks, brackets, etc.) is included in the deformation process in stages, first being the prefabricated part, followed by the monolithic one. This point is in no way reflected in the regulatory documents for design; – Insufficient study of the influence of the phased installation on the stress-strain state of the precast monolithic bent element leads to a biased assessment of its performance. Experimental studies of the stress-strain state of the precast monolithic bent element are performed, taking into account the installation process and the stepwise inclusion of the precast and then monolithic parts in the deformation process. At that, the precast part is made of heavy concrete, and monolithic-of light concrete (expanded clay concrete). The influence of the following factors on the stress-strain state of precast monolithic structures is investigated and studied: the value of pre-loading of the precast part at the first stage; the stages of installation and loading; the height of the monolithic part of the concrete. As a result of conducted research, the new data concerning features of formation of the stress-strain state of the precast monolithic element are received. The positive influence of phase loading and higher height of the monolithic part on the stress-strain state of the precast monolithic structure is revealed. In this case, the insignificant influence of the value of pre-loading of the precast part is determined.

1. Introduction

Ever increasing interest of builders [1–4] has caused the need for a more detailed study of the issues related to the features of the formation of the stress-strain state of precast-monolithic bent elements. Engineers and scientists conduct various studies aimed at identifying the degree of influence of various aspects on the deformation process of composite structures, including structures made of precast-monolithic concrete. For example, in [5, 6] various studies of individual junctions of hollow core slabs with precast-monolithic beams are carried out, as well as the peculiarities of the deformation of junctions of precast beams with columns are studied. As a result, a number of design drawbacks have been revealed that require technical improvements in the structural systems of prefabricated monolithic buildings used in modern construction practice. In [8, 9, 18, 19] the research devoted to studying of joints of plates with beams and beams with columns has also been carried out.

The results of experimental study of the research of precast-monolithic and monolithic slabs are studied in [7]. The data on the bearing capacity, deformability and crack resistance of the slabs are obtained, and the analysis of their stress-strain state is performed.

In addition, one should mention the contributions devoted to the study of individual structural elements, allowing a qualitative assessment of their design features. In [3, 10, 11, 25] experimental studies of precast-



monolithic slabs are carried out, and in some publications the issue of deformation of multilayer structures [12] is considered, including the issues of deformation of structures with external sheet reinforcement [13, 14] or separate types of impact [15–17].

In [20, 21, 24] the issues of structural reliability of building frames on the whole are shown, with the identification of deformation features of precast-monolithic structures taking into account the stages of their construction.

Along with consideration of questions of constructive reliability both of buildings from precast-monolithic reinforced concrete, and separate constructive elements, questions of feature of technology of their construction are actively considered [22, 23].

Despite the increasing experience of precast-monolithic housing construction and the increasing volume of research materials on this type of construction system, the authors of the article have identified two factors that, in our opinion, are insufficiently studied and require additional research. In particular, a more extensive study of the structural features of the stress-strain state of bent precast-monolithic structures is required, taking into account that:

- The real precast-monolithic structure, mounted on the construction site, in the absence of special structural measures (temporary mounting racks, brackets, etc.) will be included in the deformation process in stages, first the prefabricated part, and then the monolithic one;

- Insufficient study of the influence of the phased installation on the stress-strain state of the precast-monolithic bent element leads to a biased assessment of its performance.

It is these two factors that have prompted the authors of this article to perform experimental studies of the stress-strain state (the subject of research) of precast-monolithic gradually erected and loaded bent elements (the object of research).

The aim of conducted experimental studies is to study the features of forming the stress-strain state of the precast-monolithic bent element, taking into account its phased installation and loading.

2. Methods

In order to conduct experimental studies, 6 different series (B1...B6) of samples of hinged beams were manufactured and tested (Fig. 1).

The experimental models were carried out in 2 stages:

- 1st stage. At the plant of reinforced concrete products, precast parts of prototypes made of heavy concrete class B25 with 1700×80×80 (h) mm dimensions were manufactured and reinforced: longitudinal reinforcement-1Ø10A240; transverse reinforcement in the support zone-Ø4B500 with a step of 50 mm in the support zone; transverse reinforcement in the central zone was missing (Fig. 1,a,b);

- 2nd stage. In laboratory conditions, the precast parts were concreted with light concrete (structural expanded clay concrete of class B12. 5). The height of the grouted part was 60 mm in the samples of series B1...B3, B5 and 100 mm in the samples of series B4 and B6, i.e. the total dimensions of the precast-monolithic experimental samples were 1,700×80×140 (h) mm and 1,700×80×180 (h), respectively ((Fig. 1,a,c).

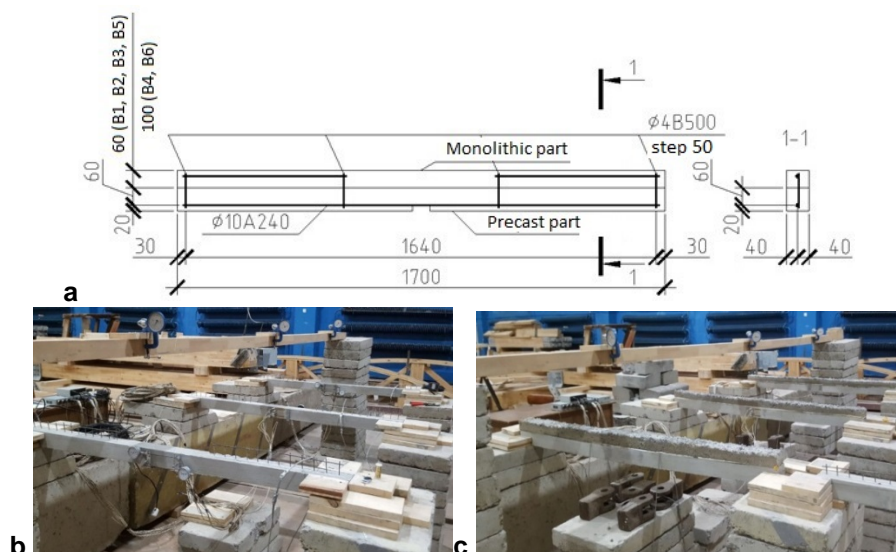


Figure 1. Experimental samples: a – drawing; b – precast parts (photo); c – precast-monolithic samples (photo).

In total, 15 samples were produced and tested: 3 samples in series B1...B3 and 2 samples in series B4...B6.

Series B1...B3 structurally did not differ from each other, the difference between them being in the value of the preload applied to the precast part, which was: B1 – $P = 0.83$ kN; B2 – $P = 1.18$ kN; B3 – $P = 1.56$ kN. The purpose of testing samples of series B1...B3 is to identify the influence of the preload value on the stress-strain state of the precast-monolithic bending element.

The B4 series differed from the B2 series samples in the height of the monolithic part, which was 100 mm. The value of the load previously applied to the precast part was $P = 1.18$ kN (similar to B2 series samples). The purpose of testing B4 series samples and subsequent comparison with the results of testing B2 series samples is to identify the influence of the height of the monolithic part on the stress-strain state of the precast – monolithic bent element.

Series B5 and B6 are structurally similar to the samples of series B2 and B4, respectively, but with the difference that the monolithic part was arranged without pre-loading of the precast part. Thus, the samples of the B5 and B6 series were loaded in a ready-assembled monolithic execution. The purpose of testing samples of series B5 and B6 and subsequent comparison with the test results of samples of series B2 and B4, respectively-to identify the impact of the fact of phased installation and loading on the stress-strain state of the precast-monolithic bent element.

The experimental setup (Fig. 2) is provided by 2 concrete blocks on which the single-span beam with its subsequent loading by the concrete and metal blocks suspended on flexible cables hinges leans.

Loading of samples B1...B4 was carried out in 2 stages:

– 1st stage (Fig. 2,a). Loading of the precast part with a preliminary load simulating the loading of precast elements with a mounting load in real construction (the own weight of the precast element itself and other elements supported on it, the weight of monolithic concrete);

– 2nd stage (Fig. 2,b). After the required strength of monolithic concrete, loading of precast monolithic structure took place by the load, simulating additional mounting load (floor structures weight, partitions, curtain walls) and operational load.

Samples of B5 and B6 series were loaded, being in a ready-precast monolithic version.

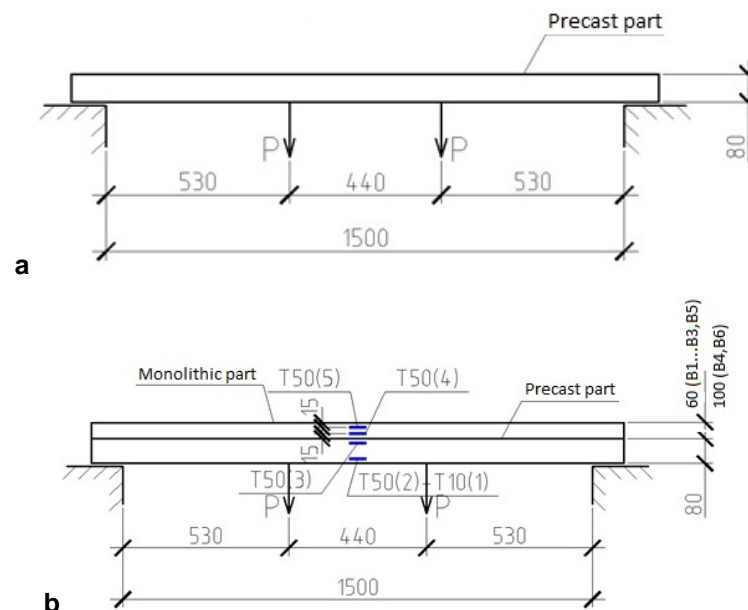


Figure 2. Test scheme:
a – 1st loading stage; b – 2nd loading stage.

Strains in concrete and reinforcement were recorded using strain gauges of 10 mm (T10) and 50 mm (T50), respectively. Readings from strain gauges were duplicated (for confirmation) with the help of hour-type indicators (not shown in the Fig.). Deflections were fixed by deflection meters placed in the center of the beam (not shown in the Fig.).

3. Results and Discussion

During the tests, the following points were noted, common to all experimental samples:

– mutual displacement of monolithic and precast parts relative to each other did not happen;

– exhaustion of the bearing capacity of the beams occurred as a result of reaching the flow limit in the longitudinal reinforcement.

The analysis of the obtained deflection values showed the following (Fig. 3):

– at the end of the 2nd stage of loading in the samples of series B1...B3, the greatest deflection is recorded in the sample B3 and, first of all, this difference is caused by the larger value of the deflection accumulated within the 1st stage of loading (in Fig. 3 a red square means the end of the 1st stage of loading). In particular, at load $P = 5.1$ kN average deflections in samples of series B1 were 8.88 mm, B2-10.17 mm and B3-11.35 mm. At that the difference of deflections after the 1st stage of loading was 4.15 mm between samples of series B1 and B3, and 2.86 mm between samples of series B2 and B3;

– Gradual involvement in the deformation process of precast and monolithic concrete in the result is more profitable than their simultaneous deformation from the first step of loading. This is indicated by the fact that the values of the average deflections at the 2nd stage at a load of $P = 4.0$ kN in the samples of the B2 series were 8.23 mm, against 9.60 mm in the samples of B5 series. And this is despite the fact that after the 1st stage of loading, i.e. before the inclusion of monolithic concrete in the deformation process, the deflections in B2 series samples are on the contrary greater than the deflections in B5 series samples. Thus, at a certain point in time, the deflections of the simultaneously deformed B5 series samples "overtake" the deflections of B2 series samples gradually involved in the deformation process. Similar results were shown by samples (B4 and B6) with a larger height of the monolithic concrete zone;

– The larger height of the monolithic zone naturally increases the bending stiffness, and at a load of $P = 5.1$ kN, the average deflection of samples of B2 series was 10.17 mm, and in samples of B4 series – 6.18 mm. A similar pattern is observed in samples with one-stage loading, where the average deflection at a load of $P = 3.71$ kN in B5 was 8.30 mm, and in B6 – 4.39 mm.

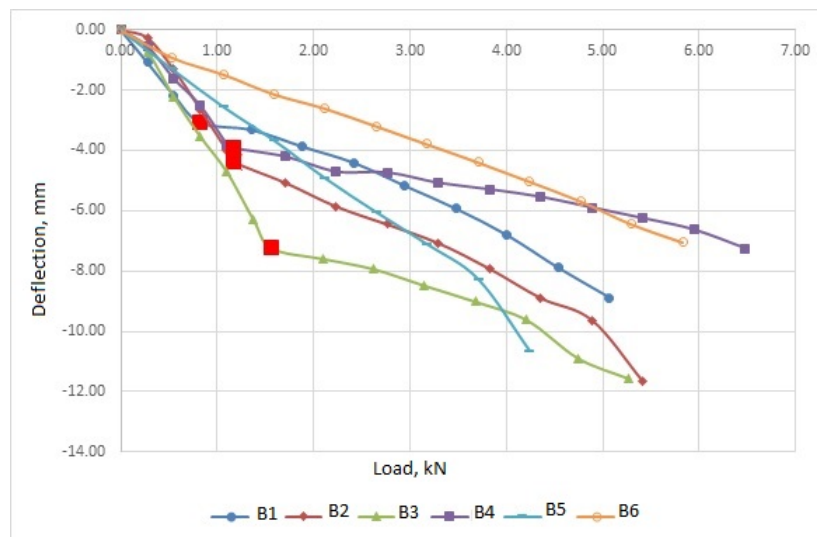


Figure 3. Graphs of averaged deflection values of experimental samples.

In phased loaded samples of series B1...B4 in the middle of the beam span at the 1st stage of loading normal cracks were formed at a load of $P = 0.55...0.83$ kN. By the end of the first loading stage in all samples recorded cracks had a height of 30...50 mm and a width of disclosure of not more than 0.1 mm.

Within the 2nd stage of loading in samples of series B1...B3 (height of monolithic concrete 60 mm) cracks were formed and developed only in the precast part without transition to monolithic one. In the samples of series B4 (height of in-situ concrete 100 mm) with increasing load the crack from precast concrete penetrated into monolithic concrete at a depth of 50 mm.

The formation of cracks in the samples of series B5 and B6 begins at later loads (1.06...1.59 kN in the samples of series B5 and 2.65 kN-B6) due to the greater bending stiffness of the element. As the load increased, the critical crack completely crossed the precast part; however, it did not pass into monolithic concrete, stopping at the border.

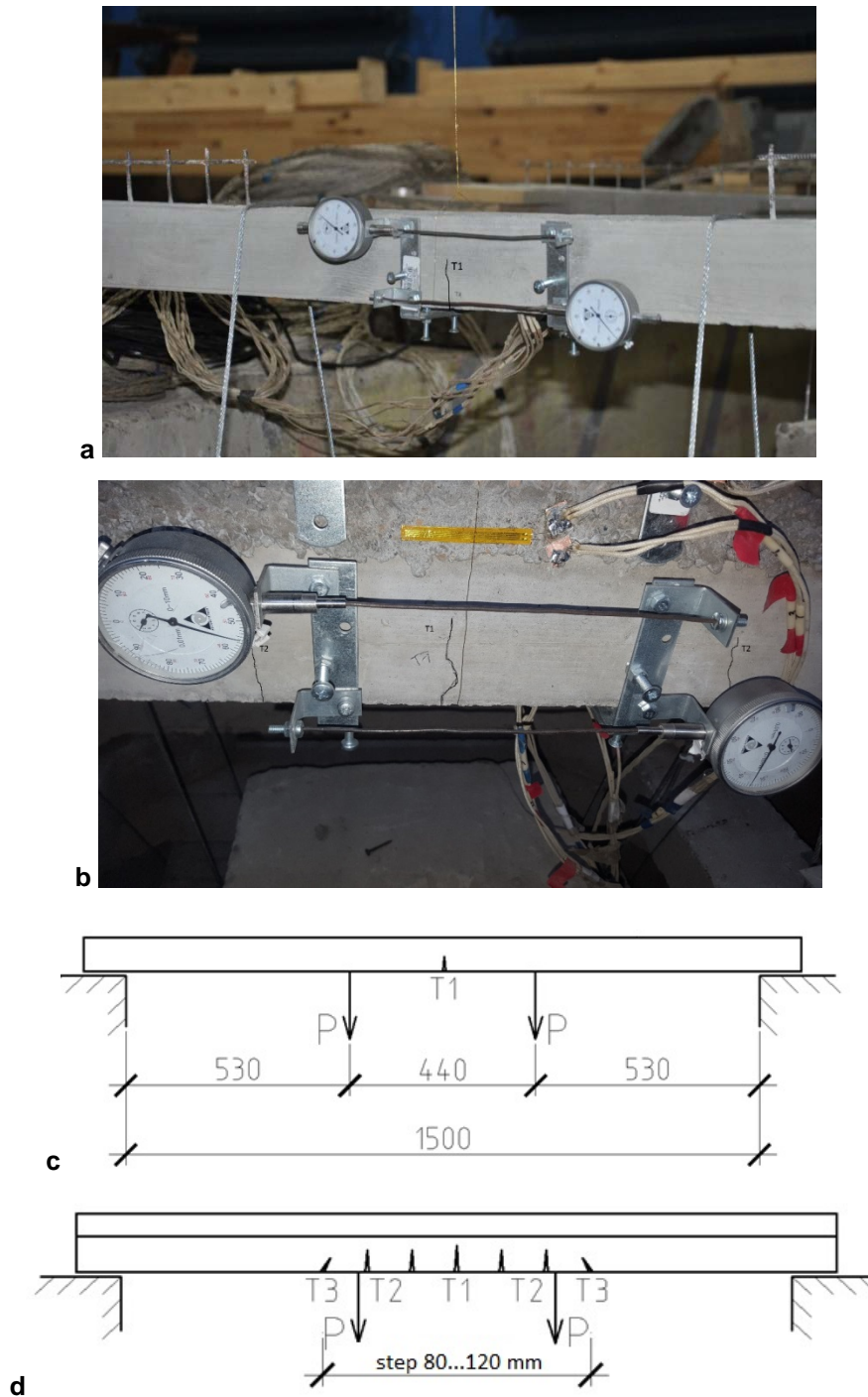


Figure 4. Cracking: a – photo of the beam series B1 after the 1st stage of loading; b – photo of the beam series B1 at the loading step prior to destruction; c – scheme of cracks in samples of series B1...B4 at the 1st stage of loading; d – scheme of cracks in samples of series B1...B4 at the 2nd stage of loading.

The analysis of the data obtained by measuring the deformation of the longitudinal reinforcement showed the following (Fig. 5):

– At the end of the 1st stage of loading, the strain of the longitudinal reinforcement was the greater, the higher the value of the applied load. In particular, in the samples of the B1 series, the average strains were 0.000616, B2 – 0.000796, B3 – 0.001079. However, at the end of the 2nd stage of loading with the force preceding the destruction ($M = 2.7 \text{ kN}\cdot\text{m}$), the values of the strains in the same samples were in the range from 0.001728 to 0.001766, i.e. the values were almost equal;

– Phased inclusion of monolithic concrete in the deformation process eventually led to lower values of reinforcement strains than simultaneous deformation of precast and monolithic concrete from the first loading step. In particular, with the force $M = 2.1 \text{ kN}\cdot\text{m}$, the average value of strains of sample B5 was 0.002212, which is more than the values in the samples of series B2 that are equal to 0.001433. Similar results were

obtained in samples of series B4 and B6, where at $M = 2.7 \text{ kN}\cdot\text{m}$ the average values of strains of longitudinal reinforcement of samples were 0.001287 and 0.001247, respectively;

– The greater height of the monolithic zone leads to a decrease in the values of strains in the longitudinal reinforcement. In particular, the value of strains in the samples of series B2 and B4, approximately equal after the 1st stage (0.000796 and 0.000834, respectively), within the deformation at the 2nd stage (after inclusion in the deformation process of monolithic concrete) becomes significantly different (when the force $M = 2.7 \text{ kN}\cdot\text{m}$ 0.001758 and 0.001287, respectively). A similar pattern is observed in the one-stage loading of the structure, where with the force of $M = 1.97 \text{ kN}\cdot\text{m}$, the average value of strains in the longitudinal reinforcement of samples of B5 series was 0.002141, and in samples of the B6 series – 0.000860;

– The exhaustion of the bearing capacity of the experimental samples occurred as a result of reaching the yield strength in the longitudinal reinforcement as evidenced by the non-stabilizing growth of deformation of the reinforcement and deflections of the beams at the last step of loading. At the same time, there were no visible signs of destruction and limit values of relative compression strains of concrete.

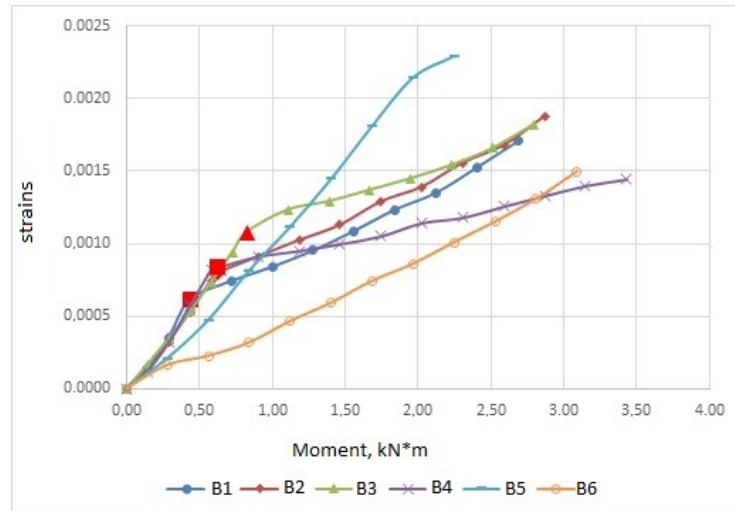


Figure 5. The reinforcement strain average values.

The data obtained from strain gauges located on the concrete are shown in Fig. 6:

– In samples of series B1...B3, an increase in the average strains occurred approximately identically and at the value of the bending moment $M = 2.7 \text{ kN}\cdot\text{m}$, the compression strains in the samples of series B1 were 0.000499, B2-0.000525 and B3-0.000598. At the same time, within the bending moment equal to $2.5 \text{ kN}\cdot\text{m}$, there is a minimal difference in the values of strains;

– A rise in the height of the monolithic zone increases, in turn, the bending stiffness of the transverse section. As a result, the value of compression strains of monolithic concrete is significantly reduced. In particular, at the value of the bending moment force $M = 2.7 \text{ kN}\cdot\text{m}$, the average strains in the samples of B2 series were 0.000525, and in the samples of the B4 series – 0.000389. Similarly, the samples of series B5 and B6 behave in the same way, where the deformation under the force preceding the destruction amounted to 0.000605 and 0.000265, respectively;

– limiting compressive strains in monolithic and precast concrete have not been achieved.

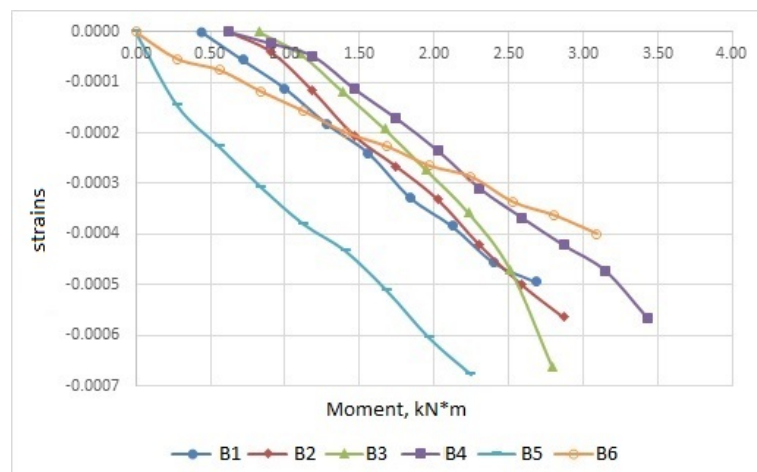


Figure 6. The average values of the monolithic concrete upper part strain.

Tensile strains of precast concrete in the phased loaded samples of series B1...B4 reach the limit values during the 1st stage of loading at the load range of $P = 0.55...0.83$ kN. Approximately at the same values the formation of cracks occurs in the precast parts.

At the 1st stage of loading in the upper zone of the precast part in the samples of series B1...B4 there arise compression strains not exceeding 0.0007. After a set of the required strength by monolithic concrete and subsequent loading of the structure within the 2nd stage, an increase in compression strains stops and in almost all samples, the value of the strain that occurred earlier even decreases. In the samples of series B5 and B6 strains in the upper zone of precast concrete had, as a rule, insignificant tensile values.

The average value of the bending moment at which the load-bearing capacity was exhausted in the samples of different series is shown in Fig. 7. The analysis of the bearing capacity has shown the following:

- The amount of pre-loading of the precast part did not significantly affect the bearing capacity of the precast-monolithic element. The range of the maximum bending moment perceived by the samples of series B1...B3 was 3.00...3.06 kN * m;

- Separation of the deformation process of the precast-monolithic bent element into 2 stages allows to increase the load-bearing capacity. In particular, the average carrying capacity of the B2 series samples was 3.00 kN*m, and in the B5 series samples – 2.53 kN*m. The same situation is with the samples of the B4 and B6 series, where the values were 3.99 kN*m and 3.37 kN*m, respectively;

- The height of the monolithic concrete significantly affects the load-bearing capacity of the precast-monolithic structure. The average carrying capacity of samples with a monolithic part height of 100 mm was higher than that of the samples with a monolithic part height of 60 mm (B4 – 3.99 kN*m vs. B2 – 3.00 kN*m, and B5 – 2.53 kN*m vs. B6 – 3.37 kN*m).

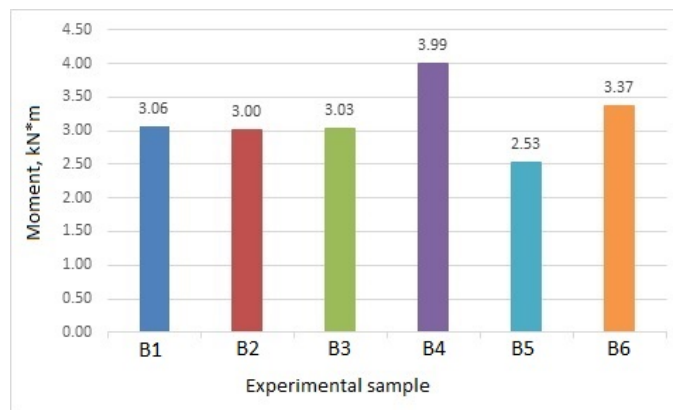


Figure 7. Diagram of the experimental sample carrying capacity averaged values.

The results obtained in the course of experimental studies are quite well correlated with the data defined in other scientific contributions. In particular, the character of stress and strain distribution during the gradual phased involvement of precast and monolithic concrete in the deformation process shown in numerical studies [21] has been confirmed in this experimental research. In addition, similar results are shown in [25], which also confirmed the high shear stiffness of the joint of different-aged concretes performed with transverse reinforcement.

4. Conclusions

On the basis of the conducted research the following conclusions are made:

1. The phased involvement of precast and monolithic concrete in the deformation process significantly changes the picture of stress-strain of precast-monolithic bent element, which makes it mandatory to take this fact into account in design.

2. The value of the pre-loading of the precast part does not significantly affect the subsequent stress-strain state and bearing capacity of the precast-monolithic structure.

3. The gradual inclusion of monolithic concrete in the deformation process has a positive effect on the bearing capacity and the nature of the stress-strain state of the precast monolithic element as a whole, in comparison with the single-staged manufactured and loaded elements. There was a decrease in deflections up to 14 %, a decrease in the strain of longitudinal reinforcement up to 20 % and an increase in the bearing capacity up to 18 %.

4. An increase in the height of monolithic concrete leads to a decrease in deflections up to 40 %, a decrease in the value of strains in concrete and reinforcement and an increase in load-bearing capacity up to 33 %.

References

1. Shmelev, G.D., Fomenko, N.A., Gavrilova, V.N. Comparative analysis of contemporary systems of establishing civil design buildings. Housing and utilities infrastructure. 2018. 3 (6). Pp. 9–19. (rus) https://zhkh.cchgeu.ru/?page_id=216&lang=en
2. Opbul, Eh. K. Perspective structural solutions in fiber-reinforced concrete cast-in-place and precast floors. Bulletin of Civil Engineers. 2014. 5 (46). Pp. 33–38. (rus) <https://elibrary.ru/item.asp?id=22648218>
3. Teplova, Z.S., Vinogradova, N. Combined and monolithic overlappings of "MARKO" system. Construction of Unique Buildings and Structures. 2015. 8 (35). Pp. 48–59. (rus) DOI: 10.18720/CUBS.35.4. <https://unistroy.spbstu.ru/en/article/2015.34.4/>
4. Serbin, S.A., Dedyukhin, P.O., Fomin, N.I. The analysis of technological parameters of precast-monolithic system with permanent formwork walls. 4th International conference on safety problems of civil Engineering critical infrastructures. Safety, 2018. DOI: 10.1088/1757-899X/481/1/012051 <http://hdl.handle.net/10995/75421>
5. Koyankin, A.A., Mitasov, V.M., Deordiev, S.V. The compatibility of deformation of the hollow-core slab with beams. Magazine of Civil Engineering. 2019. 3 (87). Pp. 93–102. DOI: 10.18720/MCE.87.8
6. Koyankin, A.A., Mitasov, V.M. Experimental study of the operation of the bolt joint of a bearer with a column in precast-monolithic ceiling. Vestnik MGSU. 2015. No. 5. Pp. 27–35. (rus) DOI: 10.22227/1997-0935.2015.5.27-35 <http://vestnikmgsu.ru/en/component/sjarchive/issue/article.display/2015/5/27-35>
7. Smoljago, G.A., Krjuchkov, A.A., Dronova, A.V., Drokin, C.V. Results of the experimental studies of bearing capacity, crack resistance and deformability of the precast-monolithic and monolithic overlaps. Izvestiya Yugo-Zapadnogo gosudarstvennogo universiteta. 2011. 5 (38)-2. Pp. 105–109. (rus) https://swsu.ru/izvestiya/journal/5-2_38_2011.pdf
8. Breccolotti, M., Gentile, S., Tommasini, M., Materazzi, A.L., Bonfigli, M.F., Pasqualini, B., Colone, V., Gianesini, M. Beam-column joints in continuous RC frames: Comparison between cast-in-situ and precast solutions. Engineering Structures. 2016. No. 127. Pp. 129–144. DOI: <https://doi.org/10.1016/j.engstruct.2016.08.018>
9. Drakatos, I.S., Muttoni, A., Beyer, K. Internal slab-column connections under monotonic and cyclic imposed rotations. Engineering Structures. 2016. No. 123. Pp. 501–516. DOI: <https://doi.org/10.1016/j.engstruct.2016.05.038>
10. Nedviga, E., Beresneva, N., Gravit, M., Blagodatskaya, A. Fire Resistance of Prefabricated Monolithic Reinforced Concrete Slabs of «Marko» Technology. Advances in Intelligent Systems and Computing. 2018. No. 692. Pp. 739–749.
11. Parashchenko, N.A., Gorshkov, A.S., Vatin, N.I. Partially rib precast and cast-in-situ floors with cellular-concrete blocks. Magazine of Civil Engineering. 2011. 24 (6). Pp. 50–55. (rus) DOI: 10.5862/MCE.24.7 <https://engstroy.spbstu.ru/en/article/2011.24.7/>
12. Chepurnenko, A.S. Stress-strain state of three-layered shallow shells under conditions of nonlinear creep. Magazine of Civil Engineering. 2017. 8 (74). Pp. 156–168. DOI: 10.18720/MCE.76.14
13. Garrido, M. Creep behaviour of sandwich panels with rigid polyurethane foam core and glass-fibre reinforced polymer faces: Experimental tests and analytical modeling. Journal of Composite Materials. 2014. Vol. 48. No. 18. Pp. 2237–2249.
14. Medvedev, V.N., Semeniuk, S.D. Durability and deformability of braced bending elements with external sheet reinforcement. Magazine of Civil Engineering. 2016. No. 3 (63). 2016. Pp. 3–15. DOI: 10.5862/MCE.63.1
15. Olmati, P., Sagaseta, J., Cormie, D., Jones, A.E.K. Simplified reliability analysis of punching in reinforced concrete flat slab buildings under accidental actions. Engineering Structures. 2017. No. 130. Pp. 83–98. DOI: <https://doi.org/10.1016/j.engstruct.2016.09.061>
16. Qian, K., Li, B. Resilience of Flat Slab Structures in Different Phases of Progressive Collapse. ACI Structural Journal. 2016. No. 113. Pp. 537–548.
17. Micallef, K., Sagaseta, J., Fernandez Ruiz, M., Muttoni, A. Assessing Punching Shear Failure in Reinforced Concrete Flat Slabs Subjected to Localized Impact Loading. International Journal of Impact Engineering. No. 71. 2014. Pp. 17–33. DOI: <https://doi.org/10.1016/j.ijimpeng.2014.04.003>
18. Varlamov, A.A., Pivovarov, V.S., Pivovarova, O.V. Variant of keyed joint of precast-monolithic slab. Materials of the international scientific and practical conference: Architecture. Construction. Education. 2014. Pp. 249–255. (rus) <http://ace-journal.ru/wp-content/uploads/2017/04/%E2%84%961-3-2014.pdf>
19. Sursanov, D.N., Sazonova, S.A., Ponomarev, A.B. Analysis of concrete dowel full-scale shearing tests. Vestnik PNIPU. Stroitel'stvo I arhitektura. 2015. No. 2. Pp. 7–23. (rus) DOI: 10.15593/2224-9826/2015.2.01. http://vestnik.pstu.ru/arhit/archives/?id=&folder_id=4845
20. Koyankin, A., Mitasov, V. Assessment of structural reliability of precast concrete buildings. MATEC Web of Conferences. IV International Young Researchers Conference «Youth, Science, Solutions: Ideas and Prospects» (YSSIP-2017). Volume 143, 2018. DOI: <https://doi.org/10.1051/mateconf/201814301001>
21. Koyankin, A.A., Mitasov, V.M. Stress-strain state of precast and cast-in place buildings. Magazine of Civil Engineering. 2017. 6 (74). Pp. 175–184. DOI: 10.18720/MCE.74.14
22. Vatin, N.I., Velichkin, V.Z., Kozinets, G.L., Korsun, V.I., Rybakov, V.A., Zhuvak, O.V. Precast-monolithic reinforced concrete beam-slabs technology with claydit blocks. Construction of Unique Buildings and Structures. 2018. 70 (7). Pp. 43–59. (rus) DOI: 10.18720/CUBS.70.4 <https://unistroy.spbstu.ru/en/article/2018.70.4/>
23. Afanas'ev, A.A. Technology of erection of precast frame buildings at negative temperatures. Vestnik MGSU. 2012. No. 4. Pp. 175–180. (rus) DOI: 10.22227/1997-0935.2012.4.175-180 <http://vestnikmgsu.ru/en/component/sjarchive/issue/article.display/2012/4/175-180>
24. Koyankin, A.A., Mitasov, V.M. Cast-in-place building frame and its features at separate life cycles. Vestnik MGSU. 2015. No. 9. Pp. 28–35. (rus) DOI: 10.22227/1997-0935.2012.4.175-180 <http://vestnikmgsu.ru/en/component/sjarchive/issue/article.display/2012/4/175-180>
25. Kolchunov, V.I., Povetkin, M.S., Merkulov, D.S. Results of the experimental studies of the ferroconcrete constructions of the composite section. Proceedings of the Kursk state technical university. 2009. 3 (28). Pp. 67–74. (rus). https://swsu.ru/izvestiya/journal/28_3_2009.pdf

Contacts:

Alexander Koyankin, KoyankinAA@mail.ru

Valery Mitasov, mitassovv@mail.ru



DOI: 10.18720/MCE.97.7

Seismic behavior of end walls in RC tall buildings with torsional irregularity

M. Akhavan Salmassi^a, A. Kheyroddin^{b*}, A. Hemmati^a

^a Department of Civil Engineering, Semnan Branch, Islamic Azad University, Semnan, Iran

^b Semnan University, Semnan, Iran

* E-mail: kheyroddin@semnan.ac.ir

Keywords: end wall, shear wall, tall buildings, linear static analysis, warping

Abstract. Many factors affect tall buildings under the influence of earthquake forces. According to the conducted studies, more tensions have been observed in the end wings of shear walls. The end shear wall is used to reduce tensions and to improve the performance of shear walls in tall buildings. In this study, 10-story, 30-story and 50-story concrete buildings with square plans were modeled and two cases of the moment-resisting frame with shear wall and moment-resisting frame with end shear wall, which were under the influence of earthquake and linear static analysis have been investigated. In this analysis, the buildings were torsioned and the results of the analysis showed that the values of the drifts, roof displacement and first period in the structure with the end wall are about 50 % percent less than of that of the building without the end wall, also, On the other hand, with the presence of the end wall in structure the ratio ($\Delta_{max}/\Delta_{avg}$) is more than 1.2, so, the use of the end wall led to a more appropriate behavior of warping in comparison to concrete square frames with no end walls.

1. Introduction

One of the examples that can be mentioned by some researcher about the use of the end wall is the Kingdom tower built in the city of Jeddah, Saudi Arabia, in 2013 which has been used end shear walls to withstand lateral forces; on the other hand, due to severe stresses, the shear walls at the end of the shear walls flanges have been used in the vicinity of the fire escape stairs which have improved the hardness and stability of the system. Also, the layout of the core walls caused torsion strength and hardness for the overall structure system, and the extension of the end wall at the corners has limited the deformation of the floor system [1].

In the case of shear walls, a number of studies have been carried out on different results regarding the effects and behavior of shear walls and related parameters.

Other researcher argued the warping analysis of RC cores and concluded that warping should consider in design, because, longitudinal tensions are very significant [2]. Also, some investigators searched for tall building braced by shear walls and thin-walled under seismic load. at this paper applied Galerkin technique and a generalized method proposed at this aim, and the accuracy of this method controlled by numerical example [3]. A research about seismic behavior of composite shear wall systems and smart structures technology indicated that the design of mentioned shear wall systems could be applied by smart structures technology [4]. Some researcher investigated about RC shear wall in Tall building. One result showed the critical demands occurred in the middle height of the tall building [5]. A study indicated that composite shear wall behavior subjected to cyclic loadings caused slope reduction load-displacement curve [6]. On the other hand, investigators examined size effects in RC flanged shear walls, and they could not find a single relationship about the dimension and behavior of the shear wall [7]. An investigation considered asymmetric shear walls and their vibration analysis by transfer matrix method, and realized the proposed method had acceptable result [8]. Also, other researchers noted to the flange thickness and its behavior in shear walls. The results indicated that while flange is in pressure, the global behavior is more than in tension [9]. Some investigators searched for static analysis in non-planar coupled shear walls and using continues connection method indicated the mentioned method is suitable for pre-design purposes of non-planar coupled shear walls

Akhavan Salmassi, M., Kheyroddin, A., Hemmati, A. Seismic behavior of end walls in RC tall buildings with torsional irregularity. Magazine of Civil Engineering. 2020. 97(5). Article No. 9707. DOI: 10.18720/MCE.97.7



This work is licensed under a [CC BY-NC 4.0](https://creativecommons.org/licenses/by-nc/4.0/)

[10]. simplified model for the analysis of free plan buildings investigated by researchers and shear wall core modeled by wide column element and finally a model devised by shear wall, energy dissipation system and inelastic behavior of walls [11]. Also, a conceptual design investigated in coupled shear walls and indicated by comparison performance-based seismic design and conventional design based on linear response spectrum, they realized that PBSB significantly improved [12]. Another study about seismic behavior of steel frames with RC shear walls searched by researchers. Analytical results showed that the ductility and the response modification factor depend on the structure height [13]. Some investigators focused on the warping deformation on thin-walled open section shear walls, and after evaluation an experimental test, proposed formulation [14].

On the other hand, some researchers and their colleagues carried out the seismic behavior of narrow RC walls. Some of the conclusion presented that by reduction of wall thickness, 25 % declines the displacement ductility, capacity and energy dissipation [15]. Other investigators discussed about multi-plastic hinges in tall buildings. The elevation indicated a non-elastic energy loss in walls [16]. Also, in a study published by researchers about the seismic damage in prestressed concrete of the wall connection. And it was concluded that the maximum stresses expand on the shear wall and then extend to the wall connection in the first floor [17]. others determined the shear wall position in RC building by Vertical Irregularities and It is observed by using Response Spectrum method and comparison torsional values in structures with and without shear walls realized the mentioned values in structure with shear wall is greater (for EQX) than other one [18]. Also, by consideration shear force in RC walls and showed due to architectural limitations, the optimized support conditions are impossible, some solutions proposed by using late-cast slabs, transfer girders with increased depth, thicker upper shear walls, and using higher grade concrete in critical regions [19]. Other researchers investigated for effect of lintel beams and floor slabs on natural frequencies in tall buildings core and presented by using Vlasov theory and transfer matrix method achieved suitable agreement in the obtained results with FEM and experimental results [20]. An investigation argued energy dissipation and tall RC core-wall buildings by consideration with numerous plastic hinges and using time history analysis. also the performance subjected to near-fault and far-fault compared. One of the result showed inelastic energy dissipation occurring at the part of high, specially, at the base and above the mid-height of the walls [21].

On the other hand, the shear-walls of the high-rise structural system investigated in two type of Open and closed, in this way, the structure modeled as a single equivalent cantilever. So, the method proposed are indicated by a numerical example [22].

Other researches and their colleagues presented shear lag effect shear wall in of T-shaped and short-leg, Research shows that numerical calculation values of results are acceptable, and parameters effect on shear lag coefficient, differently [23].

On the other hand, some investigators extended this work to include the effect of shear wall on seismic behavior of unsymmetrical RC structure, the results showed when shear walls are located at exterior corners, base shear and torsion declined to 28 % to 35 %, 29 % to 35 %, respectively, for earthquake in of X and Y dimensions [24]. Also, others analyzed about seismic performance of slender C-shaped walls under uni-and bi-directional loading by loads, and the results showed in comparison C-shaped to planar walls, there was a more ductile flexural-tension in the C-shaped specimens, specifically, where wall flanges contribute in pressure loads [25]. An investigation demonstrated about boundary element and their detailing in shear walls. also, results indicated that by testing the boundary elements in axial compression just achieving the minimum ACI 318 requirements and strength and strain capacities are, on meaning, 20 % and 10 % more than unconfined concrete, respectively [26]. on the other hand, an evaluation about drift capacity of RC structural walls and in this study considered boundary elements, the study indicates that deformation capacity in wall has a function of some ratios such as 1) wall neutral axis depth-to-compression zone width (c/b), 2) wall length-to-compression zone width (l_w/b), 3) wall shear stress ratio ($v_{max}/\sqrt{f'_c}$), and 4) the configuration of boundary transverse reinforcement [27]. Some researchers investigated about the headquarters tower in Turin and Structural analysis subjected horizontal loads. One of the consequence showed the proposed algorithm used at this article led to reliable results [28].

A survey of literature review indicates an investigation is needed about the effect of end wall on behavior of RC tall building. end wall connect end of shear walls in all stories in tall buildings, and some parameters such as maximum displacement, maximum drift and torsional effects play a significant role in the behavior of RC tall buildings under seismic forces. So, this paper present study about the effect of end wall by focus on mentioned parameters in RC tall building with torsional irregularities subjected seismic load.

2. Methods

2.1. Mathematical Formulation

Notations:

I_w is warping moment of inertia;

J_1 is torsion constant;

$B(z)$ is second moment;

$\sigma(c, z)$ is vertical tension of the wall at a distance c from the neutral axis;

$T_w(z)$ is the torsion associated with the warping;

$T_v(z)$ is the torsion associated with the shear currents;

$\sigma(s, z)$ is the distribution of tension in height (z);

$\omega(s)$ is field coordinates;

H is the height of the structure;

A is the area of the plan;

μ is poisson coefficient;

f_c is concrete comprehensive strength;

ρ is concrete reinforced ratio;

f_y is yield strength of steel.

In the buildings being studied, the shear wall systems were rigid at base of the core and had torsions at the top. Assuming a simple cross section, I , in which the warping effect is observed, these walls are symmetrical in relation to the axes X and Y , and are under the torsion of the eccentricity ratio 0.05. When the torsion T is applied around the axis Z and above the member, this member is rotated around the shear center and the wings will rotate in their plate around the X axis and rotate around the vertical axis. In the moment effect, the slab sections revolve around the X axis in different directions, and the sections of the plate are exited from the plate or warped. The torsion has been noted by researchers [29]; that is tolerated by the spin of the wings equals to:

$$T_v(z) = GJ_1 \frac{d\theta}{dz}(z) \quad (1)$$

I_w is the geometric property of the section and it called the warping moment of inertia or the warping constant. Also, J_1 is the torsion constant and the torsion equation resulting from the warping is as follows:

$$-EI_w \frac{d^3\theta}{dz^3}(z) + GJ_1 \frac{d\theta}{dz}(z) = T \quad (2)$$

On the other hand, $B(z)$ is an action which is called the second moment.

$$B(z) = M(z)L \quad (3)$$

$\sigma(c, z)$ is the vertical tension of the wall at a distance c from the neutral axis.

$$\sigma(c, z) = \frac{M(z)c}{I} \quad (4)$$

For the rigid warping effect of the uniform cores under the influence of the torsion, we can refer to the theory of Vlasov. In order to study the differential equation, we can assume a core that is rigid at the bottom and free at the top and is under the influence of the extensive torsion $m(z)$. For the analysis of the equation, we can assume that the core has a cross section with uniform dimensions and properties at all altitudes.

The general warping is defined as:

$$T(z) = T_v(z) + T_w(z) \quad (5)$$

The torsion associated with the warping is defined in Eq. (6):

$$T_w(z) = -EI_\omega \frac{d^3\theta}{dz^3}(z) \quad (6)$$

And the torsion associated with the shear currents is as follows:

$$T_v(z) = GJ \frac{d\theta}{dz}(z) \quad (7)$$

The differential equation representing the torsion of the warping of the core is as follows:

$$\frac{d^4\theta}{dz^4}(z) - \alpha^2 \frac{d^2\theta}{dz^2}(z) = \frac{m(z)}{EI_\omega} \quad (8)$$

In which:

$$\alpha^2 = \frac{GJ}{EI_\omega} \quad (9)$$

In a uniform extensive torsion by applying boundary conditions, we will have:

$$\theta(z) = \frac{mH}{EI_\omega} \left\{ \frac{1}{(\alpha H)^4} \int \frac{\alpha H \sinh \alpha H + 1}{\cosh \alpha H} (\cosh \alpha z - 1) - \alpha H \sinh \alpha z + (\alpha H)^2 \left[\frac{z}{H} - \frac{1}{2} \left(\frac{z}{H} \right)^2 \right] \right\} \quad (10)$$

$$\alpha H = H \sqrt{\frac{GJ}{EI_\omega}} \quad (11)$$

$$\alpha z = \alpha H \left(\frac{z}{H} \right) \quad (12)$$

The above equation consists of two independent parts. The parts inside the brackets represents the distribution of rotation in the height, and it is a function of dimensionless structures parameters of αH and Z/H .

On the other hand, investigators [29] mentioned the warping stresses are calculated as follows with respect to the second moment $B(z)$.

$$B(z) = -EI_\omega \frac{d^2\theta}{dz^2}(z) \quad (13)$$

$$\sigma(s, z) = \frac{B(z)\omega(s)}{I_\omega} \quad (14)$$

As it can be seen in Eq. (14), adding an end wall reduces the stresses and consequently reduces the effect of warping and torsion.

2.2. Specifications of structures and materials

Since the behavior of end walls has less been studied, the purpose of this paper is to investigate the effects of end walls in tall buildings with square plan and moment frames subjected to earthquake forces in relation to the torsion effect using Etabs 2016 software for linear static analysis of frames of 30 and 50 stories in two cases of having an end wall and no end wall.

In order to investigate the effects of end walls on tall buildings with square plan under two-dimensional seismic forces, two concrete frames of 10, 30 and 50 stories with moment frames with and without end walls are used. Eccentricity ratio considered 0.05 for torsional effective in all buildings.

Table 1. Concrete frames models.

Label	Description	Rang	
		Name	Stories
CMF ₁	Concrete Moment Frame	High-Rise	50
CMF ₂	Concrete Moment Frame With End Wall	High-Rise	50
CMF ₃	Concrete Moment Frame	Mid-Rise	30
CMF ₄	Concrete Moment Frame With End Wall	Mid-Rise	30
CMF ₅	Concrete Moment Frame	Low-Rise	10
CMF ₆	Concrete Moment Frame With End Wall	Low-Rise	10

In these models, the location of the site is the same and the frames are considered as three-dimensional concrete of moment type with 7 meters' spans and the height of 4 meters. Table 2 to 4 show the specification of sections and materials.

Table 2. Buildings specifications.

Name	H (m)	A (m^2)	Plan Dimensions (m \times m)	Story
Building 1	200	61250	35 \times 35	50
Building 2	200	61250	35 \times 35	50
Building 3	120	36750	35 \times 35	30
Building 4	120	36750	35 \times 35	30
Building 5	40	12250	35 \times 35	10
Building 6	40	12250	35 \times 35	10

Also, the sections of beams and columns and specifications of the materials used are as follows:

Table 3. Sections specifications.

Label	Dimension
50 Story:	
Beams	(0.6)m wide \times (0.8)m deep
Columns	(0.8)m \times (0.8)m
Wall	(35)m long \times (0.8)m thick
End Walls	(11)m long \times (0.8)m thick
Slab	(0.15) m thick
30 Story:	
Beams	(0.4) m wide \times (0.5) m deep
Columns	(0.6) m \times (0.6) m
Walls	(35) m long \times (0.5) m thick
End Walls	(11) m long \times (0.5) m thick
Slabs	(0.15) m thick
10 Story:	
Beams	(0.3) m wide \times (0.3) m deep
Columns	(0.4) m \times (0.4) m
Walls	(35) m long \times (0.2) m thick
End Walls	(11) m long \times (0.2) m thick
Slabs	(0.15)m thick

Table 4. Materials specifications.

Concrete		Steel	
ν	0.15	Type	A ₃
f_c	50 MPa	f_y	400 N/mm ²
ρ	2.5		

In the below plans, the layout of the shear walls has been considered with and without end walls, and on the other hand, the dimensions of opening 1.80 \times 2.40 has been considered in all stories at C and D axesa.

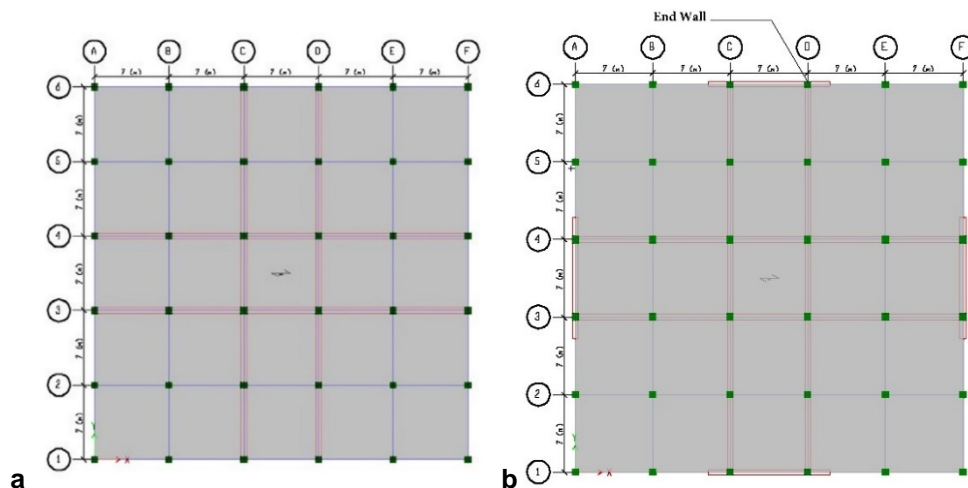


Figure 1. Building plan: (a) Building 1,3,5, (b) Building 2,4,6.

In Fig. 1 (b), the end walls are placed in axes A, F, 1 and 6, and Fig. 1 (a) is a plan without the end wall. CMF1, CMF2 CMF3, CMF4, CMF5 and CMF6 farms are under seismic forces in two directions of x, y.

3. Results and Discussion

In order to investigate the warping effect on CMF1, CMF2, CMF3, CMF4, CMF5 and CMF6 structures, EQX and EQY was applied in them.

Also, for more evaluation used displacement results of the 10 stories,30-stories and 50-stories, Fig. 2 (a), (b) and (c) show the displacements graphs based on the stories in the CMF1, CMF2, CMF3, CMF4, CMF5 and CMF6 structures under EXN. The maximum displacement of frames mentioned at Table 5. In primarily levels the different of displacements are not very much, but they increase at high levels gradually. Reducing the maximum displacement in structure with end wall is observed.

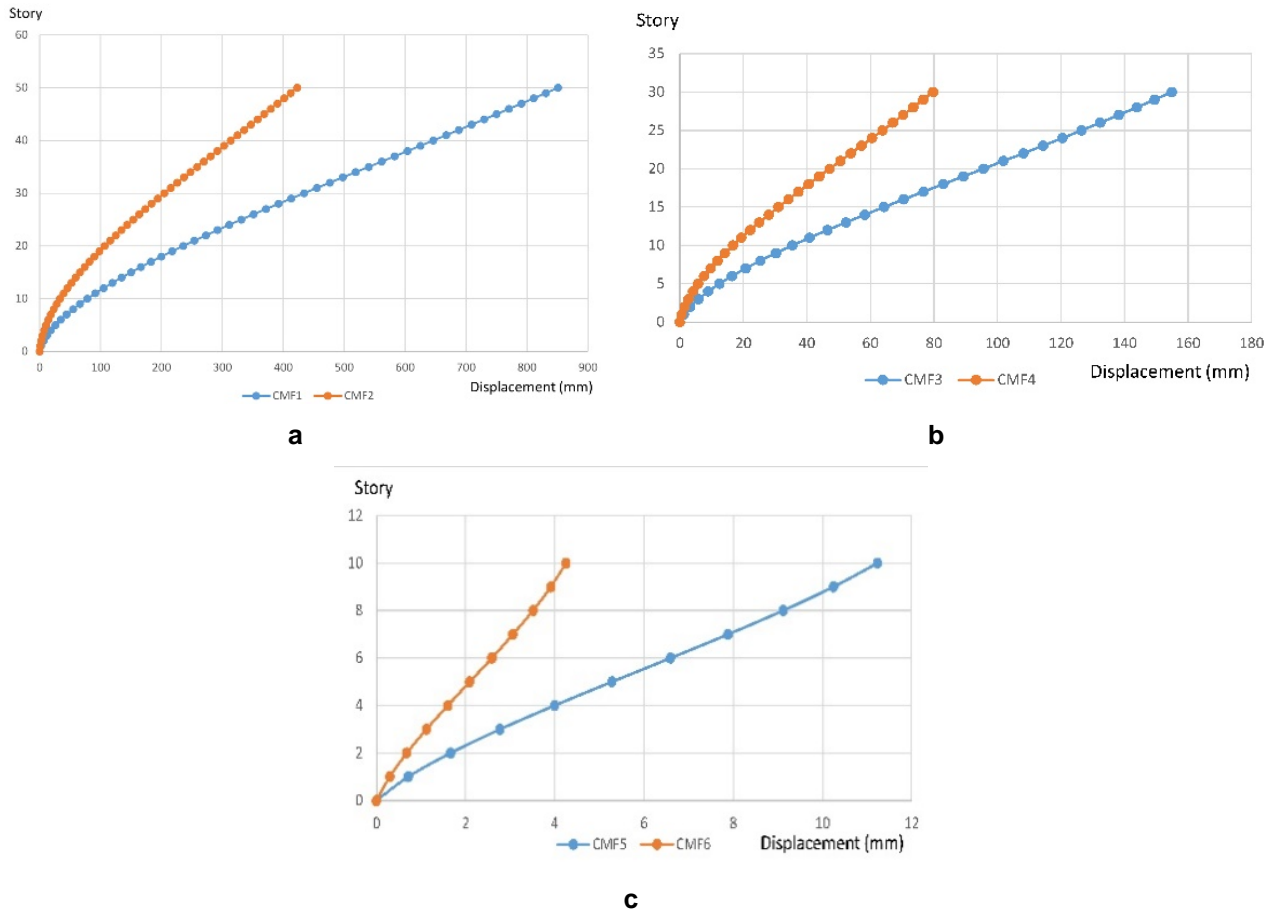


Figure 2. Displacement-Story under EXN (a) CMF1 and CMF2, (b) CMF3 and CMF4, (c) CMF5 and CMF6.

Table 5. Maximum displacement.

Lable	Maximum displacemnet (mm)
CMF1	850
CMF2	422
CMF3	154
CMF4	79
CMF5	11
CMF6	4

Due to the presence of the end wall, a significant reduction from 850 mm, 154 mm, 11 mm to 422 mm, 79 mm, 4 mm in the roof, which indicates the suitable performance of the end wall in all type of structures.

On the other hand, for more comparision,the periods based on modes of CMF1, CMF2, CMF3, CMF4, CMF5 and CMF6 indicated in Fig. 3(a), (b) and (c). For example, first modes are 6.69 and 4.24 (sec) in CMF1 and CMF2, respectivley.

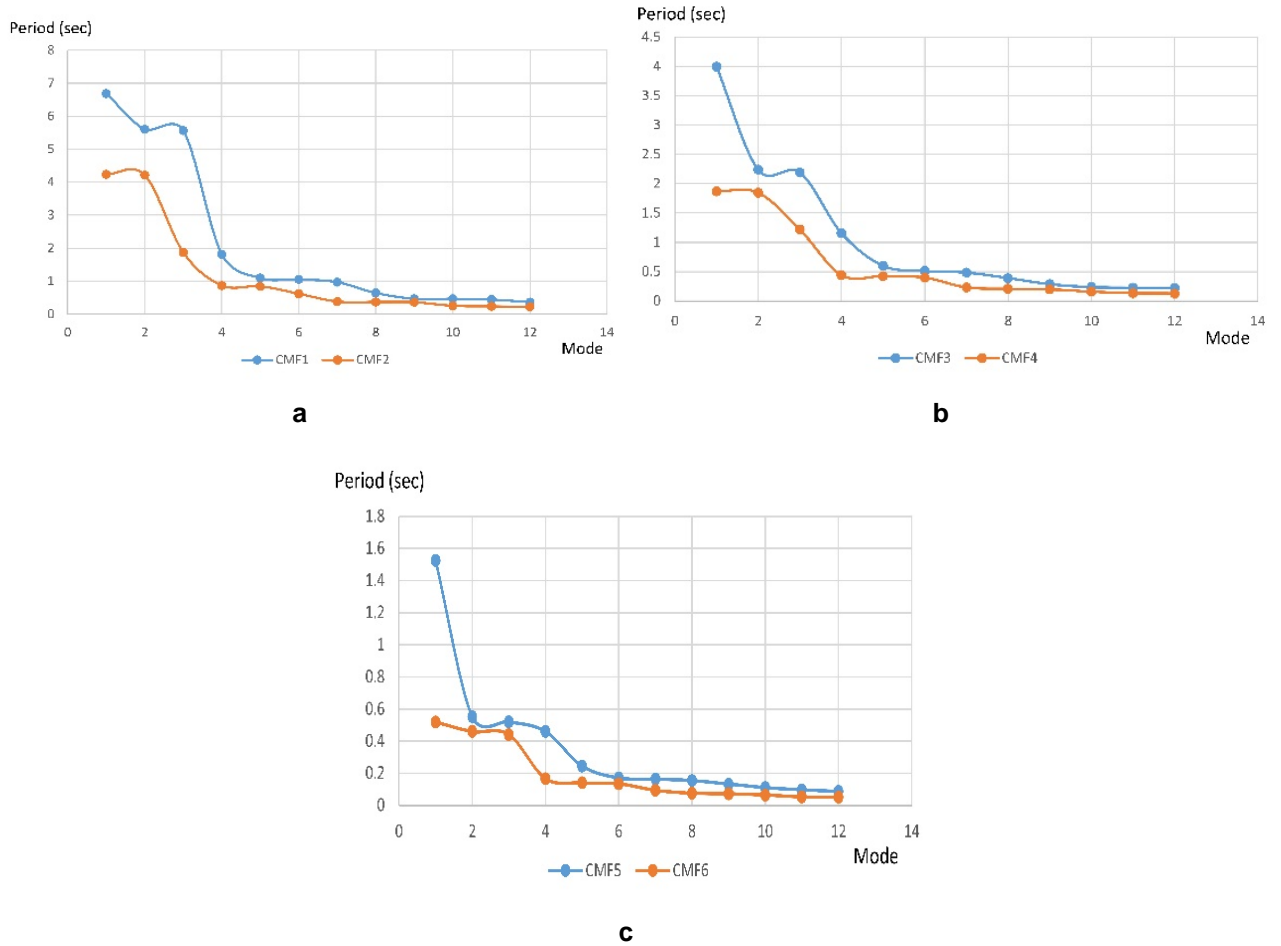


Figure 3. The Period-Mode under EXN (a) CMF1 and CMF2, (b) CMF3 and CMF4, (c) CMF5 and CMF6.

Also, in Table 6 listed the first priods of CMF1, CMF2, CMF3, CMF5 and CMF6, so , as it seen.The end wall reduced periods, effectively.

Table 6. Periods.

Label	T ₁ (sec)
CMF1	6.69
CMF2	4.24
CMF3	3.99
CMF4	1.87
CMF5	1.58
CMF6	0.52

According to Table 6, the end wall effects is observed in the structures in the first mode. On the other hand, as it can be seen, the periods have been decreased in the first mode in CMF2, CMF4, CMF6 apparently. These reductions are 50 %, approximately.

In order to investigate the analytical results, the effects of the torsion on the structures according to the application of the eccentricity ratio in the torsion structure were produced. The effects of this torsion according to ASCE7-2016 code are the conditions and classification for the curvature as follows:

- $\Delta_{max} / \Delta_{avg} \leq 1.2$ regularities torsion in plan
- Control of torsion regularity many irregularities torsion in plan $1.2 < \Delta_{max} / \Delta_{avg} \leq 1.4$
- Severe irregularities torsion in plan $\Delta_{max} / \Delta_{avg} > 1.4$

According to the rules set out in ASCE7-2016 and the output values of the Diaphragm ($\Delta_{max}/\Delta_{avg}$) Drift in CMF1, CMF2, CMF3, CMF4, CMF5 and CMF6 structures, the ratios ($\Delta_{max}/\Delta_{avg}$) are included in Table 7. These values are in accordance with the provisions of the code it is mentioned.

Table 7. Torsional Analytical Results.

Type	Story	Ratio ($\Delta_{max}/\Delta_{avg}$)	Type	Story	Ratio ($\Delta_{max}/\Delta_{avg}$)
CMF ₁ :	Story 1-8	$\Delta_{max} / \Delta_{avg} > 1.4$	CMF ₂ :	Story 1-50	$\Delta_{max} / \Delta_{avg} \leq 1.2$
	Story 9-23	$1.2 < \Delta_{max} / \Delta_{avg} \leq 1.4$			
	Story 22-50	$\Delta_{max} / \Delta_{avg} \leq 1.2$			
	Story 1-20	$\Delta_{max} / \Delta_{avg} > 1.4$			
CMF ₃ :	Story 1-20	$\Delta_{max} / \Delta_{avg} > 1.4$	CMF ₄ :	Story 1-30	$\Delta_{max} / \Delta_{avg} \leq 1.2$
	Story 20-30	$1.2 < \Delta_{max} / \Delta_{avg} \leq 1.4$			
CMF ₅ :	Story 1-10	$\Delta_{max} / \Delta_{avg} > 1.4$	CMF ₆ :	Story 1-10	$\Delta_{max} / \Delta_{avg} \leq 1.2$

As can be seen, in Table 8, eccentricity ratio, in the CMF3 structure, floors 1 through 20 have a severe irregularity torsion and a very irregular torsion 20-30 provided. On the other hand, in CMF4, with the presence of the end wall of the floor 1 to 30 turns into regularity torsion. Also in the CMF1 structure has from 1st to 8th story, the severe irregularity torsion, many irregularity 9 to 23, and regularity torsion 22 to 50, but with the end wall in the CMF2 structure, is tensed from 1st to 50th regular structures. In addition, in the CMF5 indicated severe irregularity at Story 1-10 levels, also, in the CMF6 decreased ratio to 1.2 and it showed regularity torsion.

For comparison and in the form of Fig. 4 (a) Ratio ($\Delta_{max}/\Delta_{avg}$) (based on the relative high in CMF1 torsion, CMF2 structures is plotted, and as it seen, the variations in the Ratio ($\Delta_{max}/\Delta_{avg}$) to the relative height in CMF1 are greater than CMF2. The effect of the presence of the end wall at the CMF2 has been to control the effects of warping and torsion, as well as the end wall.

However, it reduces the variation in the Ratio ($\Delta_{max}/\Delta_{avg}$) at height. In CMF3, CMF4, CMF5, CMF6 is also shown in Fig. 4 (b) and (c) which illustrates the proper function of the end wall in torsion and warping.

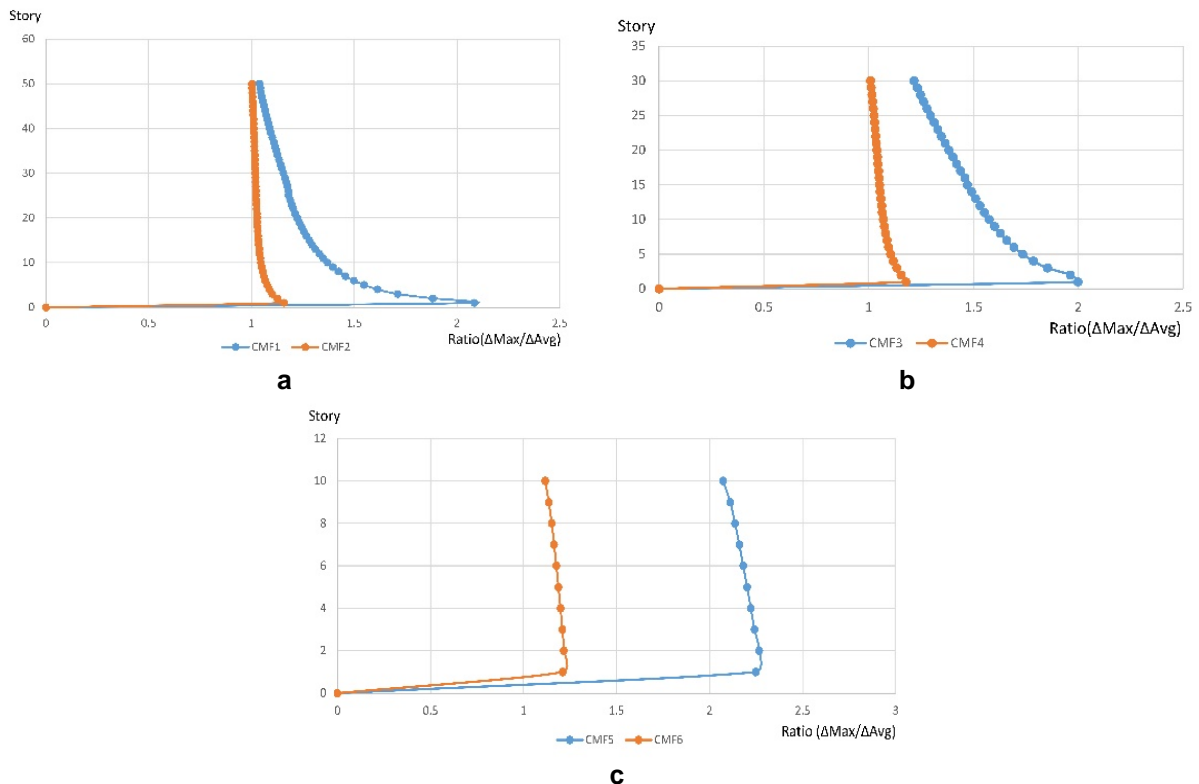


Figure 4. Ratio ($\Delta_{Max} / \Delta_{Avg}$) based on Relative Height (a) CMF1 and CMF2, (b) CMF3 and CMF4, (c) CMF5 and CMF6.

In Fig. 4 (a), (b) and (c), CMF1, CMF3 and CMF5 structures have different the ratios ($\Delta_{max}/\Delta_{avg}$) from low to high levels, but the results of CMF2, CMF4 and CMF6 structures indicate more control on ratios ($\Delta_{max}/\Delta_{avg}$) at levels and it means that the decreasing of torsion and their variations improve remarkable by end walls.

On the other hand, in order to investigate the structure and the state of tensions in the first mode and in the case of torsion in CMF1, CMF3, CMF5 is considered in Fig. 5 (a), (b) and (c), as is shown by the unbalanced and irregular distribution of stresses in Fig. 5, but with the presence of the end wall in Fig. 6, tensions in the first mode have a regular and classified distribution at height.

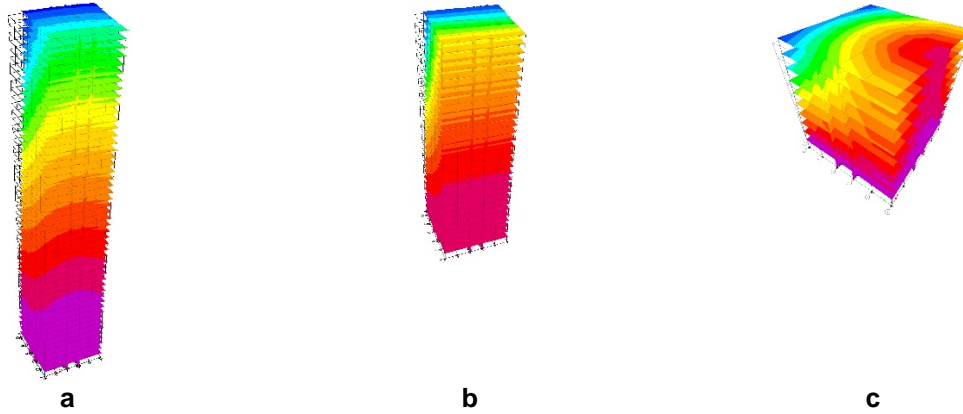


Figure 5. Distribution of structure stress CMF1 (b) CMF3 (c) CMF5.

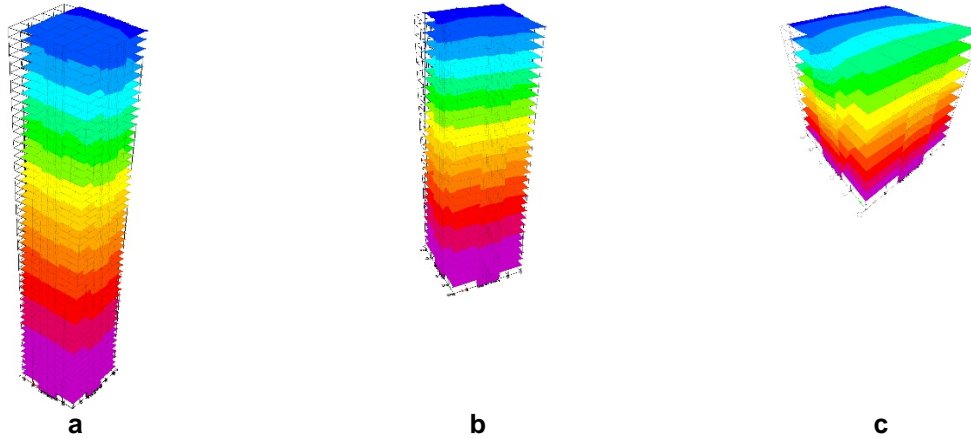


Figure 6. Distribution of structure stress (a) CMF2, (b) CMF4, (c) CMF6.

Also, the Fig. (7) and (8) of the shear wall stresses in CMF1, CMF2, CMF3, CMF4, CMF5 and CMF6 structures, as seen in Fig. 7, are unbalanced and irregular distribution in shear walls in the first mode and in the torsion, and in Fig. 8. Shear walls include the end wall, which distributes regular stress. However, this behavior indicates noticeable by end wall utilization.

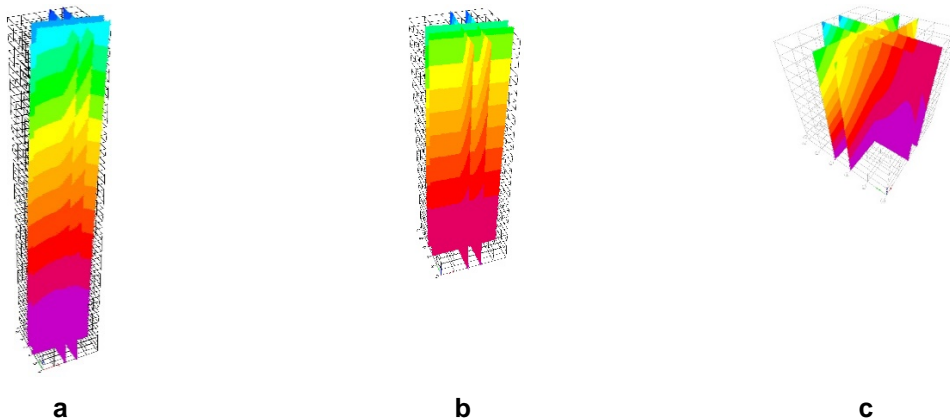


Figure 7. Distribution of Shear Wall Stress CMF1 (b) CMF3 (c) CMF5.

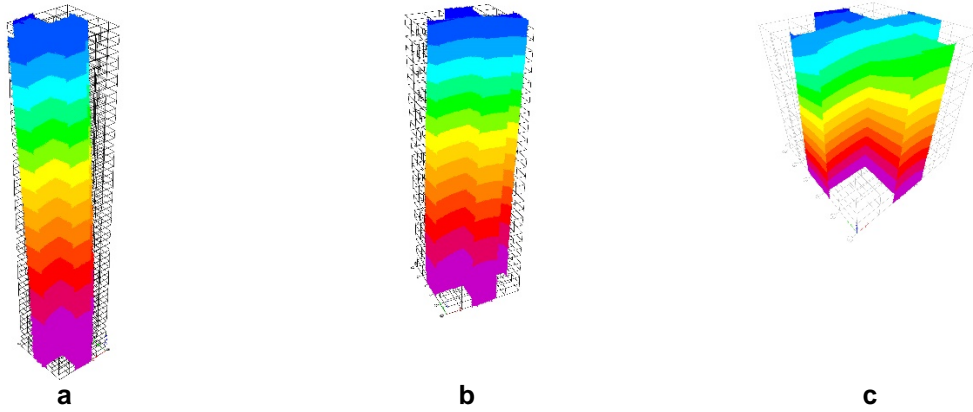


Figure 8. Distribution of Shear Wall Stresses (a) CMF2 (b) CMF4 (c) CMF6.

Also, the classified tensions cause economical design in structures. so, end walls have effective role for structural engineers.

The torsion contour indicated in Fig. (9) and (10), the torsion Contour of structures in CMF1, CMF3 and CMF5 show that high torsion in shear walls and frames, but in CMF2, CMF4 and CMF6 the contour indicates declining torsion by end wall, so, End walls caused better performance at CMF2, CMF4 and CMF6 in comparison with CMF1, CMF3 and CMF5 structures, respectively.

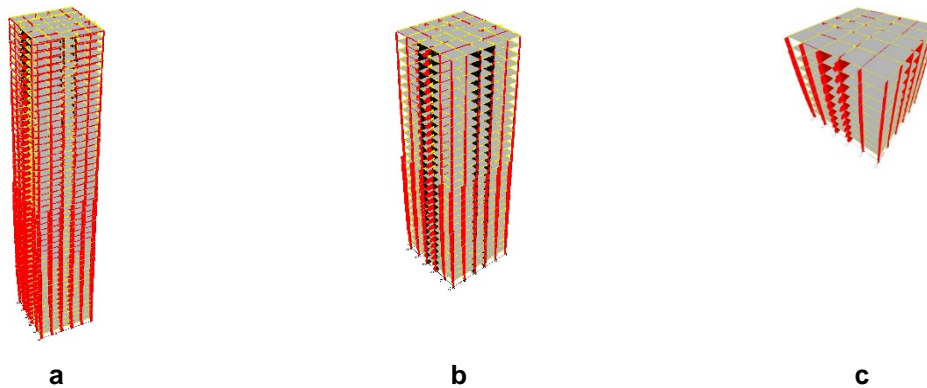


Figure 9. The torsion Contour of structure (a) CMF1 (b) CMF3 (c) CMF5.

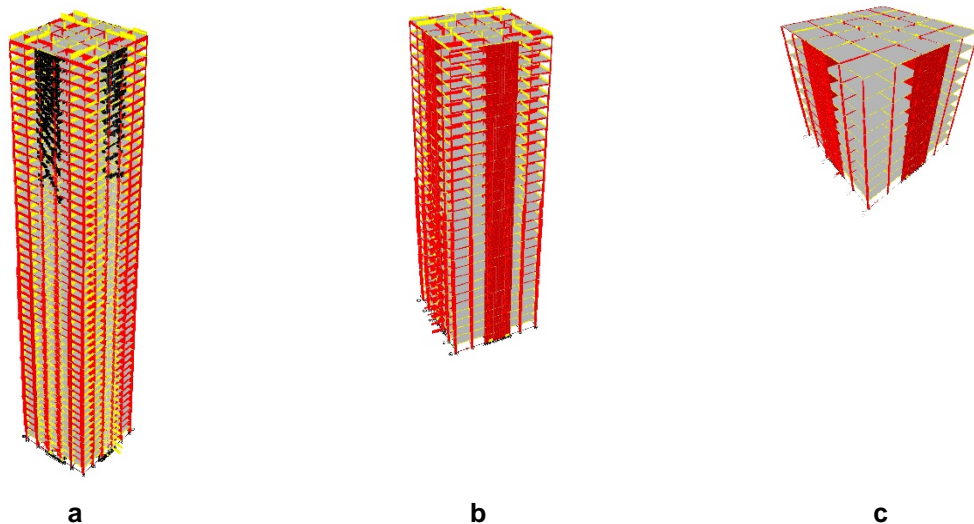


Figure 10. The torsion Contour of structure (a) CMF2 (b) CMF4 (c) CMF6.

As can be seen, the end walls had significant role in all structures type (low-rise, mid-rise and high-rise) such as declining at period, displacement, ratio ($\Delta_{max}/\Delta_{avg}$). For more comparison, floor rotation indicated in Fig. 11 for CMF1, CMF2, CMF3, CMF4, CMF5 and CMF6.

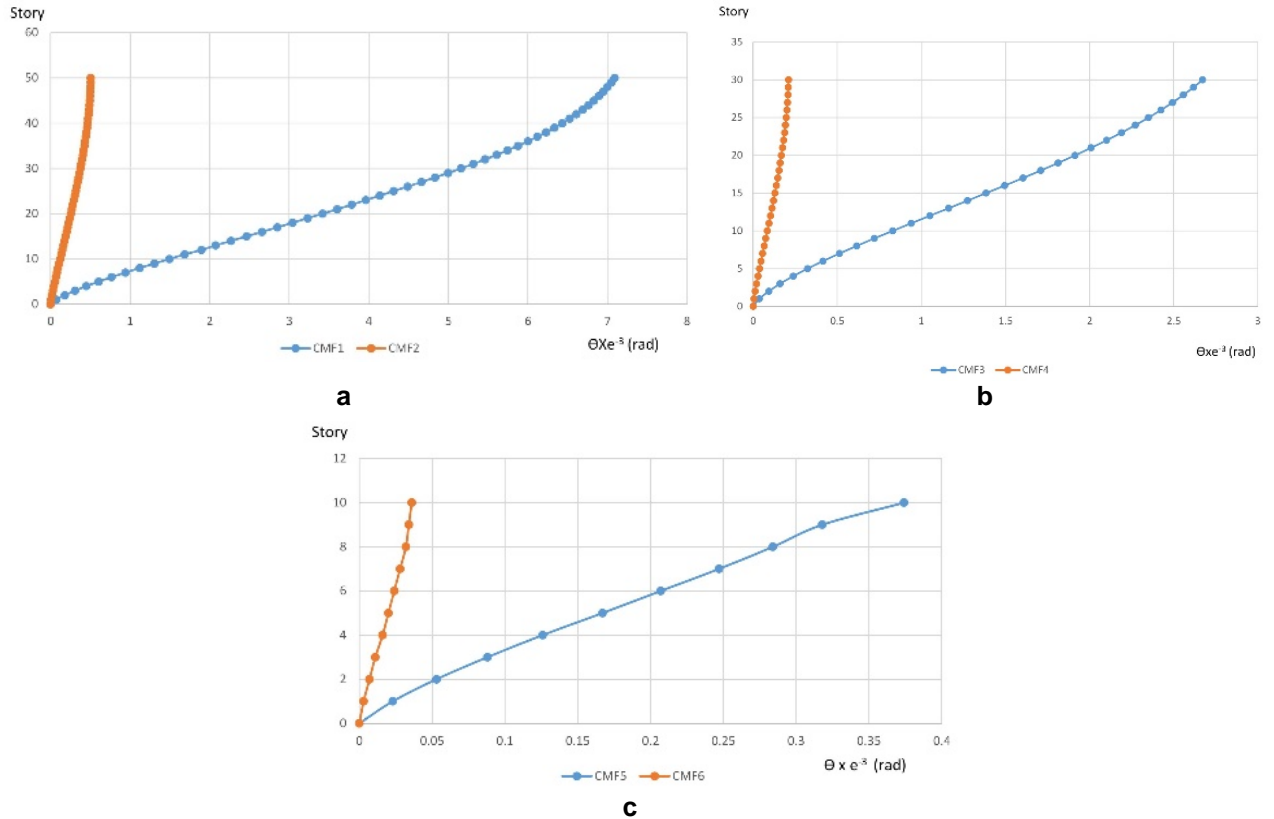


Figure 11. The floor torsion angle-story (a) CMF1 and CMF2, (b) CMF3 and CMF4, (c) CMF5 and CMF6.

Graph illustrates changes in the amounts of torsions in stories at different type of structures.

In other view, the structures without end wall have with softer curved slope rather than structures end wall. This reason means that, the floor torsion declined at CMF2, CMF4 and CMF6 structures. In Fig. 11 (a), the maximum θ are 0.505×10^{-3} (rad) and 7.089×10^{-3} (rad) in CMF1 and CMF2, respectively. So, this obvious difference derived from presence of end walls in CMF2 Also the maximum θ are 0.211×10^{-3} (rad) and 2.672×10^{-3} (rad) in CMF3, CMF4, and 0.036×10^{-3} (rad), 0.374×10^{-3} (rad) in CMF5 and CMF6, respectively. So, the effective role of end walls observes in Fig. 11.

On the other hand, tensions and forces concentrate in opening zone and link beam, so, for more investigation, their values indicated at first level in Fig. 12 and 13.

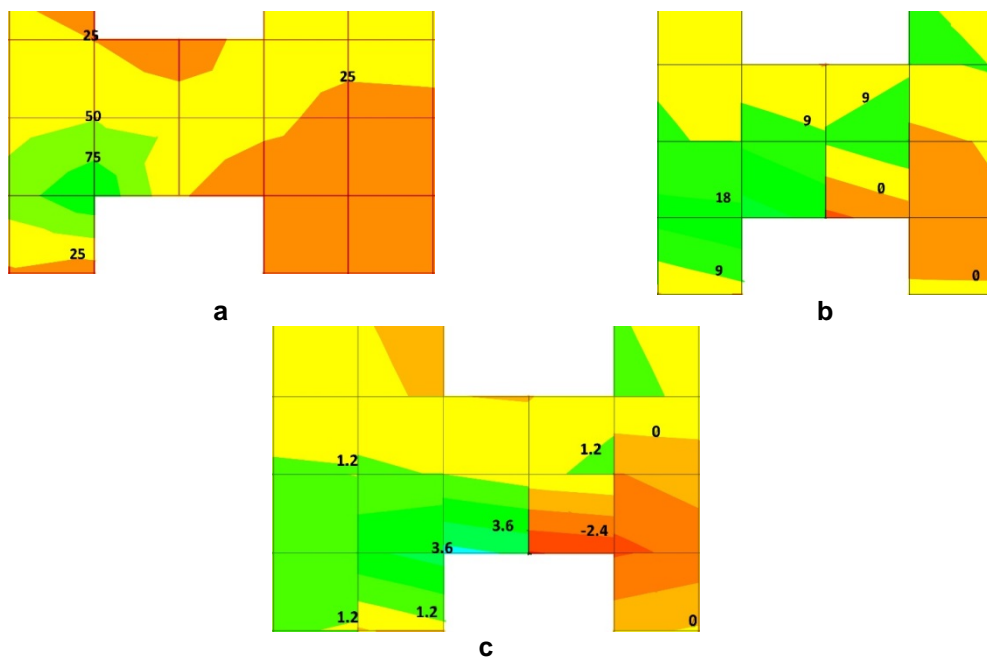


Figure 12. The tension Contour of structure in the opening zone (a) CMF1 (b) CMF2 (c) CMF3.

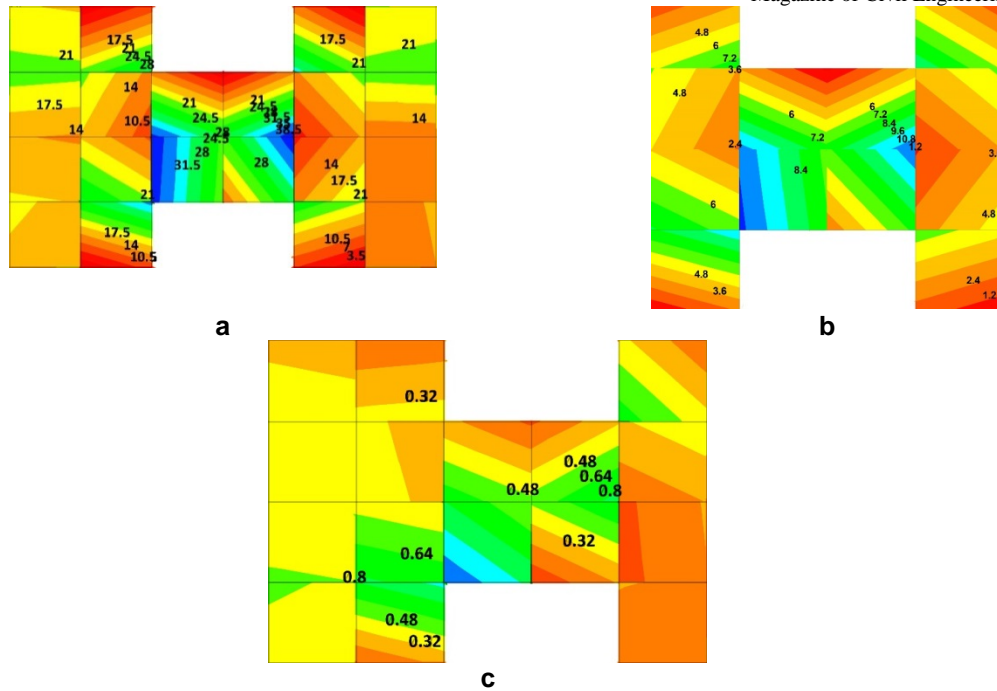


Figure 13. The tension Contour of structure in opening zone (a) CMF2 (b) CMF4 (c) CMF6.

The contour in Fig. 12 (a) express tensions in CMF1, reduction in Fig. 13 (a) is obviously, for example at left the opening zone, tension decreased 50 %, approximately. Also, tension contour in Fig. 13 (b) and 13 (c) is lower than Fig. 13 (b) and 13 (c) dramatically.

However, declining of tensions are remarkable in CMF2, CMF4 and CMF6, it means that the end walls had effective role in the reduction tensions of opening zone.

4. Conclusions

After applying the earthquake force to 10-story, 30-story and 50-story structures with and without end walls and linear static analysis, and investigations carried out on the studied structures, the following results were obtained:

1. Tall buildings with square plan and concrete moment frames under earthquake forces perform better than the same frame without an end wall.
2. Regarding the study of the warping effect on CMF1, CMF2, CMF3, CMF4, CMF5 and CMF6 structures, it was observed that one of the effects of the end wall is the conversion of the torsion mode to the transition mode.
3. In the comparison of CMF1 with CMF2, CMF3 with CMF4 and CMF5 with CMF6 it was concluded that maximum displacement decreases 50 %, approximately.
4. Also, in the comparison of CMF1 with CMF2, CMF3 with CMF4 and CMF5 with CMF6, it was concluded that first period decreases 50 %, roughly.
5. In the comparison of CMF1 with CMF2, CMF3 with CMF4 and CMF5 with CMF6, the periods decreased in different modes by end wall.
6. By attention to the period results in CMF1 with CMF2, CMF3 with CMF4 and CMF5 with CMF6, it was seen, the displacements declined in stories by end wall.
7. The distribution of stress the torsional state in the floors become regular in CMF1, CMF2, CMF3, CMF4 structures with the presence of an end wall.
8. Also, CMF1 is compared with CMF2, CMF3 with CMF4 and CMF5 with CMF6, height where the Ratio ($\Delta_{max}/\Delta_{avg}$) decreases with the presence of the end wall.
9. Due to the fact that CMF1, CMF3, CMF5 in the floors were observed due to the severe irregular torsion of the eccentricity ratio, but with the presence of the end wall in CMF2, CMF4 and CMF6, were change to regularity torsion, and the Ratio ($\Delta_{max}/\Delta_{avg}$) variations reduced in height.
10. The end wall had significant role in opening zone. Approximately, 50 % decreasing of tensions were remarkable in CMF2, CMF4, CMF6.

References

- Leventis, G., Poeppel, A., Principal, S., Leventis, G., Poeppel, A., Principal, S., Syngros, K., Manager, P., International, L. From Supertall to Megatall : Analysis and Design of the Kingdom Tower Piled Raft. 2015.
- Mendis, P. Warping analysis of concrete cores. *Structural Design of Tall Buildings*. 2001. 10 (1). Pp. 43–52. DOI: 10.1002/tal.160
- Meftah, S.A., Tounsi, A., El Abbas, A.B. A simplified approach for seismic calculation of a tall building braced by shear walls and thin-walled open section structures. *Engineering Structures*. 2007. 29 (10). Pp. 2576–2585. DOI: 10.1016/j.engstruct.2006.12.014 URL: <https://linkinghub.elsevier.com/retrieve/pii/S014102960700003X>
- Zhao, Q., Astaneh-Asl, A. Seismic behavior of composite shear wall systems and application of smart structures technology. *International Journal of Steel Structures*. 2007. 7 (7). Pp. 69–75.
- Esmaili, O., Epackachi, S., Samadzad, M., Mirghaderi, S.R. Study of Structural RC Shear Wall System in a 56-Story RC Tall Building. *The 14th World Conference on Earthquake Engineering*. 2008. (June).
- Rahai, A., Hatami, F. Evaluation of composite shear wall behavior under cyclic loadings. *Journal of Constructional Steel Research*. 2009. 65 (7). Pp. 1528–1537. DOI: 10.1016/j.jcsr.2009.03.011
- Mortezaei, A., Kheyroddin, A. Size effects in reinforced concrete flanged shear walls. *International Journal of Civil Engineering*. 2009. 7 (1). Pp. 27–40.
- Bozdogan, K.B., Duygu Ozturk, A.D. Vibration analysis of asymmetric shear wall - Frame structures using the transfer matrix method. *Iranian Journal of Science and Technology – Transactions of Civil Engineering*. 2012. 36 (C1). Pp. 1–12.
- Khatami, S.M., Kheyroddin, A. The effect of flange thickness on the behavior of flanged-section shear walls. *Procedia Engineering*. 2011. 14. Pp. 2994–3000. DOI: 10.1016/j.proeng.2011.07.377 URL: <http://dx.doi.org/10.1016/j.proeng.2011.07.377>
- Emsen, E., Aksogan, O. Static analysis of non-planar coupled shear walls with stepwise changes in geometrical properties using continuous connection method. *Thin-Walled Structures*. 2012. 56. Pp. 21–32. DOI: 10.1016/j.tws.2012.03.006. URL: <https://linkinghub.elsevier.com/retrieve/pii/S0263823112000584>
- Encina, J., de la Llera, J.C. A simplified model for the analysis of free plan buildings using a wide-column model. *Engineering Structures*. 2013. 56. Pp. 738–748. DOI: 10.1016/j.engstruct.2013.05.016 URL: <https://linkinghub.elsevier.com/retrieve/pii/S0141029613002307>
- Bhunia, D., Prakash, V., Pandey, A.D. A Conceptual Design Approach of Coupled Shear Walls. *ISRN Civil Engineering*. 2013. 2013. Pp. 1–28. DOI: 10.1155/2013/161502
- Esmaili, H., Kheyroddin, A., Naderpour, H. Seismic behavior of steel moment resisting frames associated with RC shear walls. *Iranian Journal of Science and Technology – Transactions of Civil Engineering*. 2013. 37 (C+). Pp. 395–407.
- Carpinteri, A., Lacidogna, G., Montrucchio, B., Cammarano, S. The effect of the warping deformation on the structural behaviour of thin-walled open section shear walls. *Thin-Walled Structures*. 2014. 84. Pp. 335–343. DOI: 10.1016/j.tws.2014.07.009
- Hube, M.A., Marihuén, A., de la Llera, J.C., Stojadinovic, B. Seismic behavior of slender reinforced concrete walls. *Engineering Structures*. 2014. 80. Pp. 377–388. DOI: 10.1016/j.engstruct.2014.09.014 URL: <https://linkinghub.elsevier.com/retrieve/pii/S0141029614005513>
- Beiraghi, H., Kheyroddin, A., Kafi, M.A. Forward directivity near-fault and far-fault ground motion effects on the behavior of reinforced concrete wall tall buildings with one and more plastic hinges. *The Structural Design of Tall and Special Buildings*. 2016. 25 (11). Pp. 519–539. DOI: 10.1002/tal.1270 URL: <http://doi.wiley.com/10.1002/tal.1270>
- Kaushik, S., Dasgupta, K. Seismic Damage in Shear Wall-Slab Junction in RC Buildings. *Procedia Engineering*. 2016. 144. Pp. 1332–1339. DOI: 10.1016/j.proeng.2016.05.162 URL: <http://dx.doi.org/10.1016/j.proeng.2016.05.162>
- Chavhan, A.S. Vertical Irregularities in RC Building Controlled By Finding Exact Position of Shear. 2015. Pp. 6614–6630. DOI: 10.15680/IJIRSET.2015.0407195
- Tang, T.O., Su, R.K.L. Gravity-induced shear force in reinforced concrete walls above transfer structures. *Proceedings of the Institution of Civil Engineers: Structures and Buildings*. 2015. 168 (1). Pp. 40–55. DOI:10.1680/stbu.13.00092
- Varjú, G., Prokić, A. The influence of lintel beams and floor slabs on natural frequencies of the tall buildings core – Numerical and experimental studies. *Periodica Polytechnica Civil Engineering*. 2015. 59 (4). Pp. 511–520. DOI:10.3311/PPci.8410
- Beiraghi, H., Kheyroddin, A., Kafi, M.A. Energy dissipation of tall core-wall structures with multi-plastic hinges subjected to forward directivity near-fault and far-fault earthquakes. *The Structural Design of Tall and Special Buildings*. 2016. 25 (15). Pp. 801–820. DOI:10.1002/tal.1284 URL: <http://doi.wiley.com/10.1002/tal.1284>
- Carpinteri, A., Lacidogna, G., Nitti, G. Open and closed shear-walls in high-rise structural systems: Static and dynamic analysis. *Curved and Layered Structures*. 2016. 3 (1). Pp. 154–171. DOI: 10.1515/cls-2016-0013
- Liu, C., Wei, X., Wu, H., Li, Q., Ni, X. Research on shear lag effect of T-shaped short-leg shear wall. *Periodica Polytechnica Civil Engineering*. 2017. 61 (3). Pp. 602–610. DOI: 10.3311/PPci.9491
- Vithal, G.U. Effect of Shear Wall on Sismic Behavior of Unsymmetrical Reinforced Concrete Structure. 2017. IV (X). Pp. 61–81.
- Behrouzi, A.A., Mock, A., Lehman, D., Lowes, L., Kuchma, D. C-SHAPED WALLS SUBJECTED TO UNI- AND BI-DIRECTIONAL LOADING. 2018. (February 2019). Pp. 1–6.
- Welt, T.S., Lehman, D.E., LaFave, J.M. Boundary element detailing in special concrete structural walls. *ACI Structural Journal*. 2018. 115 (3). Pp. 635–647. DOI: 10.14359/51701278
- Abdullah, S.A., Wallace, J.W. Drift capacity of reinforced concrete structural walls with special boundary elements. *ACI Structural Journal*. 2019. 116 (1). Pp. 183–194. DOI:10.14359/51710864
- Nitti, G., Lacidogna, G., Carpinteri, A. Structural Analysis of High-rise Buildings under Horizontal Loads: A Study on the Piedmont Region Headquarters Tower in Turin. *The Open Construction & Building Technology Journal*. 2019. 13 (1). Pp. 81–96. DOI: 10.2174/1874836801913010081
- Smith, B.S., Coull, A. Tall building structures analysis and design 1991.

Contacts:

Mehran Akhavan Salmassi, m.akhavan.s@stu.semnaniau.ac.ir

Ali Kheyroddin, kheyroddin@semnan.ac.ir

Ali Hemmati, ali.hemmati@semnaniau.ac.ir



DOI: 10.18720/MCE.97.8

Behavior of CFRP strengthened columns damaged by thermal shock

R. Al-Rousan*

Jordan University of Science and Technology, Irbid, Jordan

* E-mail: rzalrousan@just.edu.jo

Keywords: reinforced concrete, thermal shock, structural strength, axial strength, fiber reinforced polymer, nonlinear, finite element analysis

Abstract. In the last two decades, using of Carbon Fiber Reinforced Polymers (CFRP) in strengthening of deficient reinforced concrete structural elements has been increased due to their ease of installation, low invasiveness, high corrosion resistance, and high strength to weight ratio. Strengthening damage structures is a relatively new technique. This paper presents a nonlinear finite element analysis (NLFEA) results of reinforced concrete columns confined externally with carbon fiber reinforced polymers (CFRP) subjected to thermal shock impact. After reasonable validation of NLFEA with the experimental test results of companion columns, NLFEA was expanded to provide a parametric study of eighteen columns that correlates the ultimate axial stress of CFRP-confined RC columns to number of CFRP layers and damaged thermal shock. Thermal shock has a significant impact on the behavior of CFRP-confined circular RC columns. The increase in ductility is directly related to a decrease of compressive strength due to thermal shock. Also, the confinement effectiveness in terms of ultimate load was decreased with the increase in concrete compressive strength (undamaged). The influence of the number of CFRP layers on the ductility, energy absorption, and ultimate load improvement percentage is significant. There will be no further significant increase in the ductility and ultimate load of the column after a certain volumetric ratio, while significant increase in its stiffness continues to occur.

1. Introduction

It is inevitable to strengthen and/or retrofit concrete structural elements in order to prevent their potential vulnerability. One common procedure is confining such elements with CFRP wraps, which completely limit the lateral expansion of concrete and delay concrete cover peeling and longitudinal bars buckling. The general influence is clearly an increase in the peak loads of the specimens. Most studies in this area have been focused on column behavior under concentric and eccentric loads [1, 2]. It is necessary to strengthen the deteriorated and damaged reinforced concrete columns due to the overloads from earthquake and environmental conditions. Steel plate jackets and reinforced concrete jackets have been widely used to strengthen the RC columns. However, they have several problems because of their material characteristics, longer construction period due to curing requirement and the enlargement of column size. To solve the above problems, CFRP composites have been used for confinement of concrete since the early 1980's. External confining of concrete with CFRP composites is an efficient repair technique to enhance their strength and ductility due to the extreme high strength to weight ratio, the ease and speed of installation and application, and good corrosion behavior. Issa and Tobaa studied the strength and ductility enhancement in high-strength confined concrete columns. They concluded that the increase in the effective lateral pressure and post-peak ductility of the transverse steel decreases the slope of the descending branch of the stress-strain curve of the confined concrete [3].

Elevated temperatures cause severe damage for reinforced concrete (RC) structures, such as RC beams. RC beams have been reported to loss strength and stiffness with relatively large permanent deformations because of exposure to high temperatures [4]. These harmful effects could be attributed to the deterioration of mechanical characteristics of concrete and steel rebars and the redistribution of stresses within the beam due to the elevated temperatures [4, 5]. Currently, the most commonly used technique to repair the heat-damaged RC beams is using carbon fiber reinforced polymer (CFRP) composites. These sheets are advanced materials that can be easily applied on the structures and characterized by outstanding mechanical and corrosion resistance characteristics. Various studies were performed to investigate the flexural behavior



of RC beams wrapped with CFRP. The results showed that externally bonded carbon FRP (CFRP) sheets and laminates has the ability to enhance the flexural behavior of the beams and recover, to certain limit, the flexural strength of heat-damaged beams. Strengthening level or recovery depends on several factors such as fire resistance [6], elevated temperature [7, 8], fiber type [9–12], analysis type [13–17], energy integrity resistance [18], anchored system [20], heating condition [21, 22], degree of beam's damage and geometry and type of fiber sheet [23], and safety factors for CFRP strengthening of bridges [24].

Reinforcing concrete structures are often subjected to cycles of heating–cooling such as in chimneys, concrete foundations for launching rockets carrying spaceships, concrete near to furnace, clinker silos and nuclear power plants, or those subjected to fire then extinguished using water. Temperature cycles are critical to the stability of concrete structures and require considerations upon design [25, 26]. As well stipulated, the mechanical properties of concrete are preserved for exposure temperatures below 300°C, yet are decreased considerably as temperature exceeds 500 °C. Additional damage results from rapid cooling such as in the case of extinguishing of fire with cool water due to creation of temperature gradient between concrete core and its surface. This results in tensile stresses on the concrete surface that are high enough to crack concrete and this considered as another source of damage results from incompatible expansion and contraction of aggregate and surrounding cement paste. The magnitude of damage is influenced by many factors such as the size of concrete members, the type of cement and aggregate, the concrete moisture content and the predominant environmental factors, Those are represented in heating exposure time and rate, type of cooling, and maximum temperature attained [27]. Different types of materials and techniques were used in strengthening and retrofitting of existing concrete structures such as steel plates bolting, reinforced concrete jackets, pre-stressed external tendons, and most recently FRP composite which has been used on a large scale in different countries. FRP composites have many advantages over conventional methods represented in ease of application, high strength-to-weight ratio, excellent mechanical strength, and good resistance to corrosion, especially that most structures are damaged due to dynamic loads, corrosion of steel, and freeze-thaw cycles [28, 29].

Many reinforced concrete bridges are deteriorating due to problems related to environment and increase in load of trucks. In the last twenty years, considerable attention has been focused on the use of CFRP for structural rehabilitation and strengthening. Therefore, essential issues to produce effective, economical, and successful CFRP strengthening were needed. Also, the impact of CFRP external strengthening on the behavior of deficient reinforced concrete columns damaged by thermal shock must receive miniature consideration. The scientific problem considered in the study is indeed one of the problems in the modern theory of deficient reinforced concrete columns. A lack of literature regarding behavior of deficient columns damaged by thermal shock necessitated conducting the present investigation. In this study, experimental and NLFEA program were carried out to find the improvements in the strength and ductility behavior of reinforced concrete (RC) columns confined externally with CFRP composites. The main parameters studied were number of CFRP layers (Volumetric ratio) and thermal shock impact.

2. Methods

ANSYS V16 software is an effective numerical method and important tool in the analysis of complex structures. The main benefits that NLFEA include: 1) substantial savings in the cost, time, and effort compared with the fabrication and experimental testing of structure elements; 2) allows to change any parameter of interest to evaluate its influence on the structure, such as the concrete compressive strength; 3) allows to see the stress, strain, and displacement values at any location and at any load level. Eighteen full-scale models strengthened using CFRP are developed to carry out different investigated parameters.

2.1. Experimental work review

The validation process of the finite element model is based on the experimental work performed by Issa et al. [30]. CFRP-confined circular RC columns of 750 mm in length and 150 mm in diameter were fabricated and tested to failure. All columns were longitudinally reinforced with 4#3 steel bars ($\rho = 1.56\%$) and laterally reinforced with spiral steel reinforcement, 4.75 mm in diameter, spaced at 75 mm center to center along the entire height of the columns. The spacing of the spirals of 75 mm on center was based on the volumetric spiral reinforcement ratio. The ends of the columns were strengthened with additional two layers of CFRP-sheets for a distance of 125 mm from each end to prevent premature failure at the ends due to stress concentration. The reinforcement details, cross section, and the CFRP confinement configurations of the un-damaged columns are shown in Fig. 1. The CFRP-strengthened columns included columns strengthened with 1 (CS1-UD), 2 (CS2-UD), 3 (CS3-UD), 4 (CS4-UD), and 5 (CS5-UD) layers of CFRP in the transverse direction (Fig. 1). The 28-day cylindrical concrete compressive strength is 55 MPa. The yield stress of the longitudinal and spiral steel reinforcements was 410 MPa. The carbon fiber used was unidirectional in the form of tow sheet, manufactured in wide strips with a tensile strength of 3800 MPa and an elastic modulus of 230 GPa. The specimens were tested in the vertical position under axial compression loading in a special fabricated rigid steel frame. The test setup was designed to simulate pinned-pinned conditions (spherical shape) at both

ends of the columns. The specimens were centered and aligned with the help of lead shims that were laid between the column end and the steel plates to take up possible discrepancies and to ensure an even load distribution.

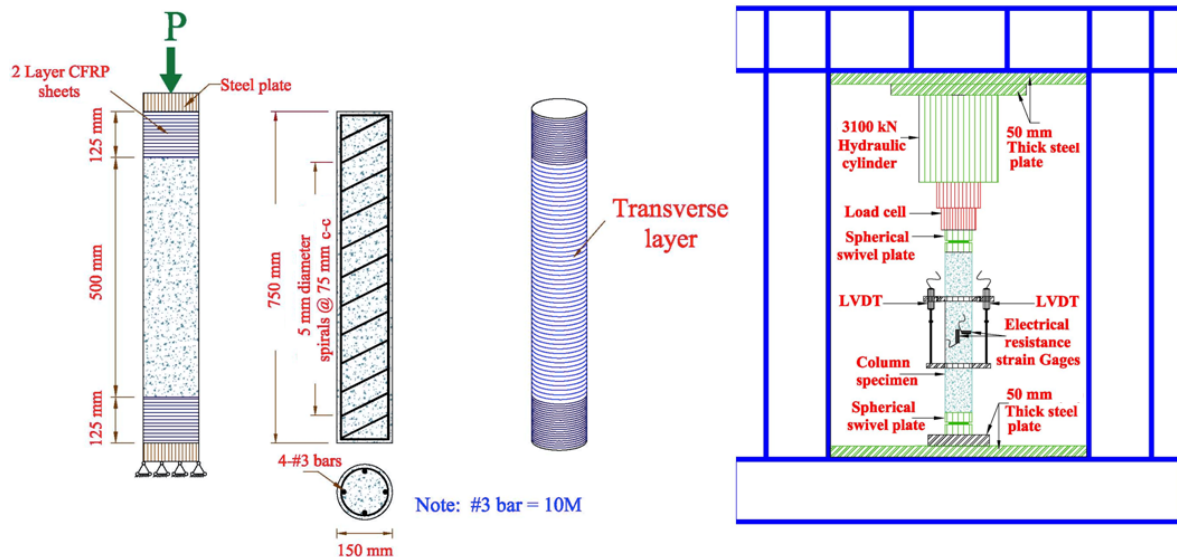


Figure 1. Setup and reinforcement details of the Columns [30].

2.2. Description of non-linear finite element analysis (NLFEA)

Concrete is non-homogenous and brittle material and has different behavior in tension and compression. SOLID 65 element is capable to predict the nonlinear behavior of concrete materials by using a smeared crack approach by ultimate uniaxial tensile and compressive strengths. The average compressive strength of the cylinders before and after being damaged by thermal shock were 55 and 10 MPa, respectively, and the average splitting tensile strength of the cylinders before and after being damaged by thermal shock were 2.9 and 0.7 MPa, respectively [31]. Poisson's ratio of 0.2 and shear transfer coefficient (β_i) of 0.2 for β_i was used in this study. Fig. 2(a) shows the stress-strain relationship for unconfined concrete which describes the post-peak stress-strain behavior.

LINK180 element was used to model the steel reinforcement. The 3-D spar element is a uniaxial tension-compression element with three degrees of freedom at each node with translations in the nodal x, y, and z directions. The element is also capable of plastic deformation. The steel in simulated models was assumed to be an elastic-perfectly plastic material and the same in compression and tension. Poisson's ratio of 0.3 and the yield stress of undamaged and damaged columns were 410 MPa and $0.78 f_y$ [32], respectively, as well as the elastic modulus were 200 GPa and $0.6 E_s$ [32], respectively, were used for the steel reinforcement. Fig. 2 (b) shows the idealized stress-strain relationship. The steel plates were assumed to be linear elastic materials with a Poisson ratio and elastic modulus of 0.3 and 200 GPa, respectively. The CFRP sheet is assumed to be an orthotropic material 0.17 mm thick, tensile strength of 3800 MPa, elastic modulus of 230 GPa, and ultimate tensile strain of 0.0169 as shown in Fig. 2 (c).

The contact area between the concrete and CFRP composite was modeled by a CONTA174 element. In this study, the bond stress-slip model between CFRP plates and damaged concrete by thermal shock proposed by Haddad and Al-Rousan [33] was used as shown in Fig. 3. Full column was simulated to study the behavior of the control reinforced concrete column. By taking advantage of symmetry of the column and loadings, a quarter of the full column was used in the analysis with proper boundary conditions, which reduced the computing time and computer disk space requirements. To simulate the pinned-pinned condition at both ends, one end was modeled as pin support, while only translation in the loading direction and rotation were allowed at the other end (point of load application). A convergence study was carried out to determine the appropriate mesh density. Perfect bonding was assumed between the composite column elements. Fig. 4 shows a typical finite element meshing of all columns. The total load applied was divided into a series of load increments or load steps. Newton-Raphson equilibrium iterations provide convergence at the end of each load increment within tolerance limits equal to 0.001 with load increment of 0.35 kN.

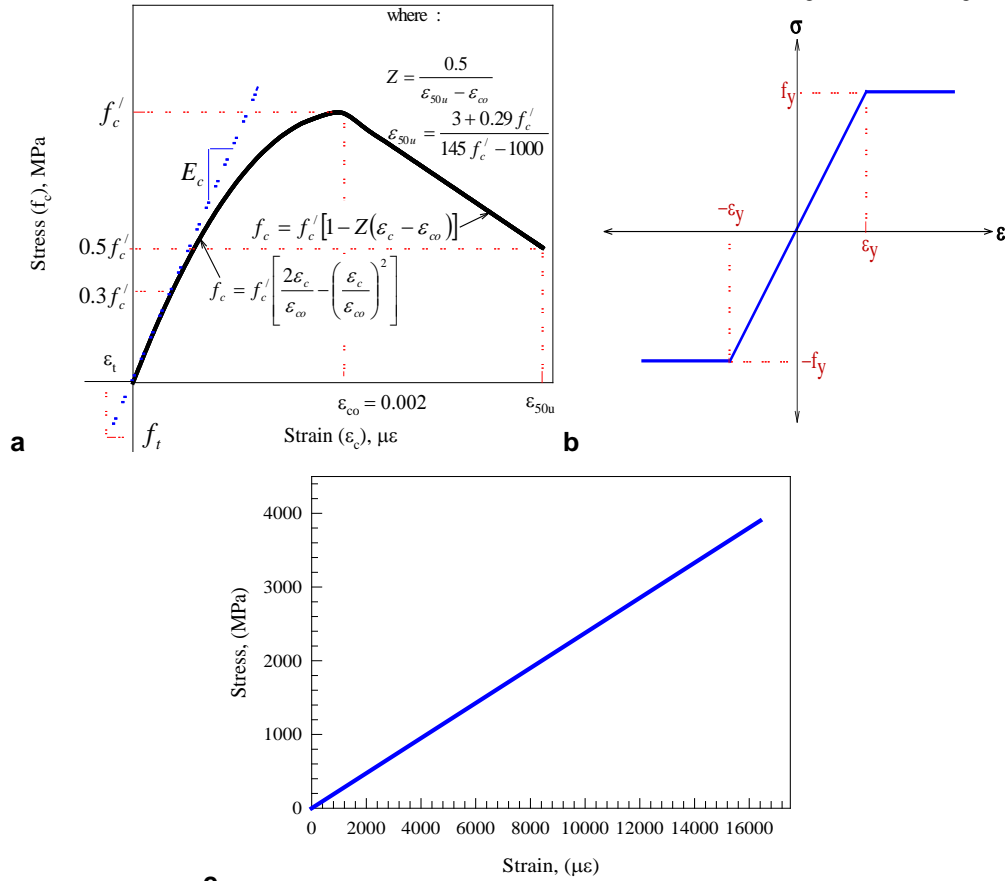


Figure 2. Stress-strain curves for: (a) unconfined concrete [30], (b) steel reinforcement [32], and CFRP composite.

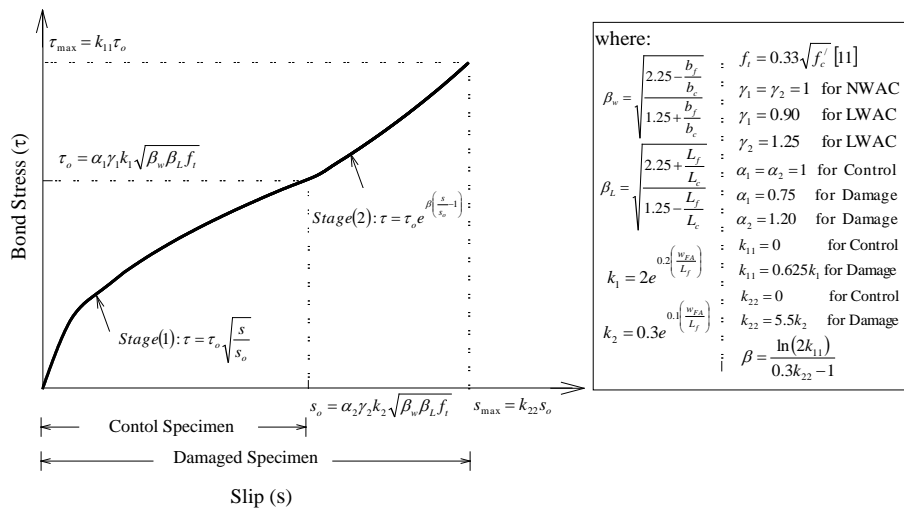


Figure 3. CFRP to concrete bond slip model [33].

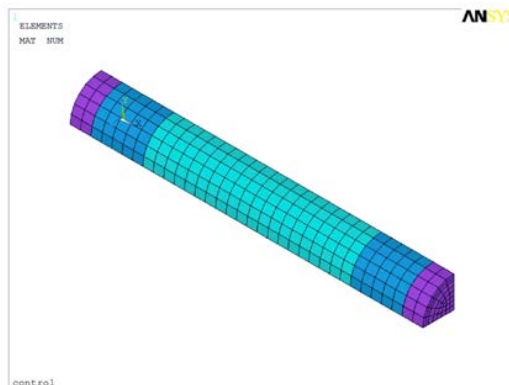


Figure 4. Typical finite element meshing of the Column.

2.3. Investigated Parameters

Table 1 shows configuration of different strengthening techniques, where unlike one un-damaged control column (CC-UD) and one control damaged column (CC-D), and the other sixteen columns were strengthened in shear using CFRP sheets as follows: CS1-UD and CS1-D (undamaged and damaged, respectively) were strengthened with one layer of CFRP (750 mm wide \times 0.17 mm thick). CS2-UD and CS2-D (undamaged and damaged, respectively) were strengthened with two layer of CFRP (750 mm wide \times 0.34 mm thick). CS3-UD and CS3-D (undamaged and damaged, respectively) were strengthened with three layer of CFRP (750 mm wide \times 0.51 mm thick). CS4-UD and CS4-D (undamaged and damaged, respectively) were strengthened with four layer of CFRP (750 mm wide \times 0.68 mm thick). CS5-UD and CS5-D (undamaged and damaged, respectively) were strengthened with five layer of CFRP (750 mm wide \times 0.85 mm thick). CS6-UD and CS6-D (undamaged and damaged, respectively) were strengthened with six layer of CFRP (750 mm wide \times 1.02 mm thick). CS7-UD and CS7-D (undamaged and damaged, respectively) were strengthened with seven layer of CFRP (750 mm wide \times 1.19 mm thick). Finally, CS8-UD and CS8-D (undamaged and damaged, respectively) were strengthened with eight layer of CFRP (750 mm wide \times 1.36 mm thick). A full description of the finite element modeling groups is shown in Table 1.

Table 1. NLFEA results of confined columns with CFRP composites.

Group Number	Number of CFRP layers	Volumetric ratio	Column number	Un-damaged/ Damaged	CFRP strengthening configuration	Ultimate load, kN
1	0	0	CC-UD	Un-damaged	Control column without strengthening	1161
	1	0.00433	CS1-UD		Column strengthened with one layer of CFRP	1628
	2	0.00867	CS2-UD		Column strengthened with two layer of CFRP	2077
	3	0.01300	CS3-UD		Column strengthened with three layer of CFRP	2420
	4	0.01733	CS4-UD		Column strengthened with four layer of CFRP	2700
	5	0.02167	CS5-UD		Column strengthened with five layer of CFRP	2891
	6	0.02600	CS6-UD		Column strengthened with six layer of CFRP	3060
	7	0.03033	CS7-UD		Column strengthened with seven layer of CFRP	3211
	8	0.03467	CS8-UD		Column strengthened with eight layer of CFRP	3336
2	0	0	CC-D	Damaged	Control column without strengthening	422
	1	0.00433	CS1-D		Column strengthened with one layer of CFRP	711
	2	0.00867	CS2-D		Column strengthened with two layer of CFRP	946
	3	0.01300	CS3-D		Column strengthened with three layer of CFRP	1116
	4	0.01733	CS4-D		Column strengthened with four layer of CFRP	1248
	5	0.02167	CS5-D		Column strengthened with five layer of CFRP	1331
	6	0.02600	CS6-D		Column strengthened with six layer of CFRP	1393
	7	0.03033	CS7-D		Column strengthened with seven layer of CFRP	1435
	8	0.03467	CS8-D		Column strengthened with eight layer of CFRP	1461

Note: C: Column, UD: un-damaged, D: Damaged

2.4. Validation Process

The experimental work included the fabrication of fifty-five circular reinforced concrete columns confined externally with various number and configurations of CFRP sheets. The columns were instrumented and tested to failure under pure axial loading. In addition, NLFEA was used to model the structural behavior of these columns. Fig. 5 shows the axial loads versus axial displacement behaviors for the simulated and tested columns. The axial load displacement curves shown in Fig. 5 (a), reveals that there is a significant increase in the ultimate axial load as well as in the ultimate axial displacement when confining the circular columns with CFRP sheets. Fig. 5 (a) also shows that the increase in the ultimate loads and displacements is directly related to an increase in the number of CFRP sheet layers. Also, Fig. 5 (b) shows the axial load versus axial and circumferential strains for the simulated columns.

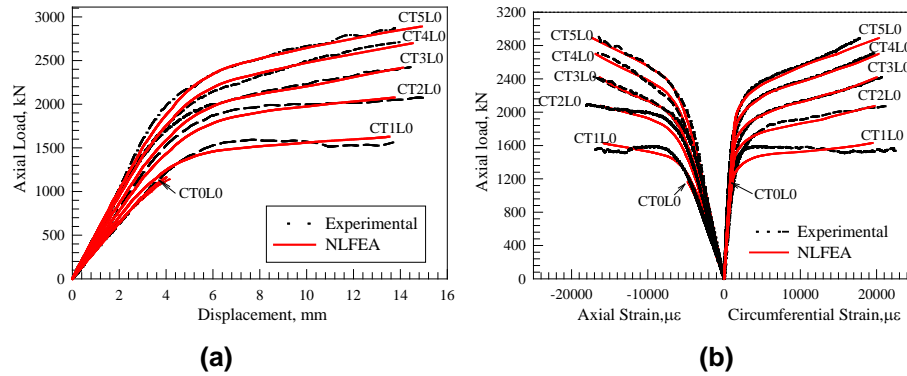


Figure 5. Axial load vs. (a) axial displacement and (b) circumferential strain curves.

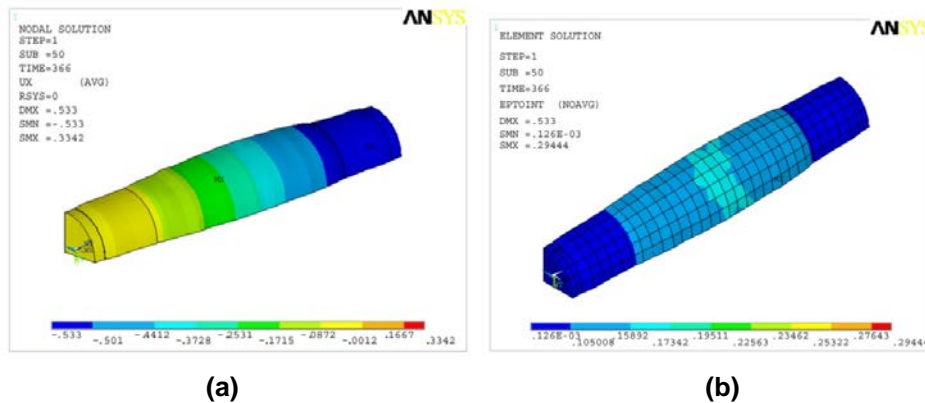


Figure 6. Typical NLFEA contours for (a) control column and (b) column confined with 1 layer of CFRP composites.

The axial load axial strain behavior followed a similar trend as the axial load axial displacement for each specimen. At failure, the circumferential strain readings of the confined columns were greater than 0.017 mm/mm, which is the maximum strain capacity of the carbon fiber. The circumferential strain results coincide with the observed failure mode of the confined columns, the failures did not occur before fracturing of the CFRP sheets. This shows that the effectiveness of the CFRP confinement was good. As a result, there is good agreement between the NLFEA and the experimental test results. The general behaviors of the simulated columns show good agreement with observations and data from the experimental full-scale column tests with an average percentage of less than 5%. Fig. 6 shows a typical NLFEA deformed shape and circumferential strain contours for column confined with 1 layer of CFRP composites. It was suggested to use NLFEA for further research on numerical tests and parametric analysis to provide theoretical understanding for establishing the stress strain curve model.

3. Results and Discussion

3.1. Failure Mode

The typical failure of the NLFEA specimens was initiated by fracture of the CFRP sheets at or near the center of the specimen (Fig. 6). The failure at the extreme edges was not of consequence as the ends were strengthened at these locations. When the load approached the ultimate load, circumferential fracture of the carbon fiber sheets was occurred that leads to a sudden release of energy. The specimen experienced a significant loss in resistance as the CFRP sheets began to fail followed by the fracturing of lateral reinforcement

and buckling of the longitudinal reinforcement. Similarly, failure of the control columns occurred due to the fracturing of the lateral reinforcement followed by buckling of the longitudinal reinforcement.

3.2. Loading behavior stages

The loading behavior of the specimens wrapped with CFRP can be divided into three stages. The first stage A is from zero applied load to $0.65 N_p$ (N_p is the peak load of each wrapped column) as shown in Fig. 7. In this stage, all curves are almost the same. Lateral expansions were very small and the fiber stresses were low (10 % of their ultimate strength). The second Stage B is from $0.65 N_p$ to $0.8 N_p$. At this stage, the steel bars and spirals have yielded. The spirals reached their ultimate strain, the concrete started to have a large expansion, and the fiber begins to be stressed and crushing of the concrete at the end of this stage. After $0.8 N_p$, the third Stage C started with large deformation in the axial and lateral directions and a slow rise in load. The load was carried by the CFRP composite after crushing of the concrete until the fiber fractured.

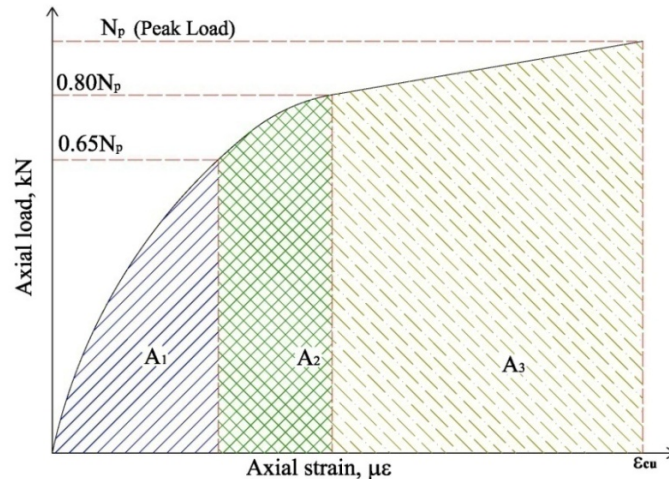


Figure 7. Typical loading behavior stages of the NLFEA columns.

To understand the contribution of each stage, energy absorption (EA) was calculated as the area under the load-displacement curve up to ultimate capacity. The area under the axial load-axial displacement curve was divided into three parts to measure the energy absorption during each stage as shown in Fig. 7. A_1 , which represent the area from zero applied load to $0.65 N_p$ (Stage A), A_2 is the area from $0.65 N_p$ applied load to $0.80 N_p$ (Stage B), and A_3 is the area from $0.80 N_p$ applied load to N_p (Stage C). Fig. 8 shows the normalized energy absorption for all stages with respect to the total energy for damaged and un-damaged columns. Inspection of Fig. 8 reveals that the energy absorption by CFRP composite after crushing of the concrete until the fiber fractures during stage C is about 65–70 % of total energy. Also, the EA only begins decreasing with the number of CFRP layers after seven layers. Until that point, EA increases with increasing number of layers. Stages A and B, which almost have equal absorption energy is about 30–35 % of total energy and increases with an increase in number of layers. Also, the total absorption energy of the composite system has the same trend as Stage C, which reflects the essential occupation of CFRP composite on the behavior of the wrapped column. Inspection of Fig. 8 reveals that the average EA reduction percentage due to thermal shock is 45 %.

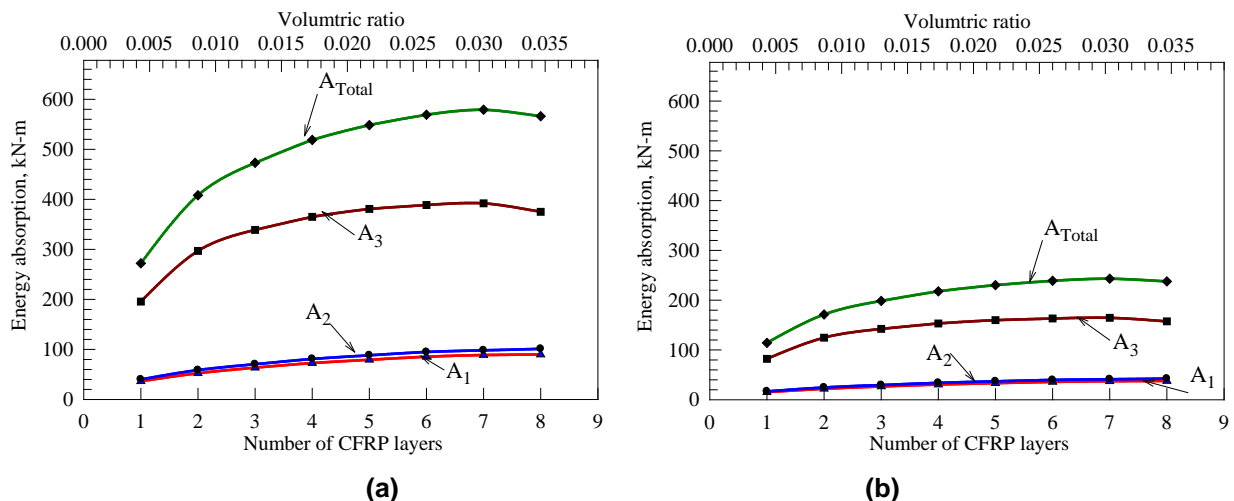


Figure 8. Energy absorption versus number of CFRP layers for (a) Un-damaged and (b) Damaged confined columns.

3.3. Effect of the number of transverse CFRP layers

To determine an enhancement in ductility between the control and CFRP confined columns, the areas under the axial load-axial displacement curves shown in Fig. 5(a) were computed. The energy absorption (EA) is plotted versus CFRP volumetric ratio as shown in Fig. 9. A polynomial relationship was observed with high correlation coefficient of 0.996 and is presented in Fig. 9. Depending on the CFRP volumetric ratio of the circular column and compressive strength of concrete, this relationship can be utilized to calculate the required energy absorption. In addition, the ductility of the RC columns can be calculated as the normalized energy absorption with respect to the energy absorption of control RC column. From this relationship, the energy absorption increases with increasing number of CFRP layers. The percentage of increase in ultimate load (Table 1) with respect to the control column was calculated as shown in Fig. 10. Inspection of Fig. 10 reveals that the rate of strength gain is reduced with increase in CFRP layers. This mean, after a certain volumetric ratio, there would be no further significant increase in the ductility behavior (Fig. 9) and ultimate load (Fig. 10) of the column, while significant increasing in its stiffness continues to occur (Fig. 5(a)). In addition, the increase in stiffness has led to decrease in lateral expansions of fiber stresses (Fig. 5(b)), delays in the spiral and steel yielding, and increases in concrete crushing load.

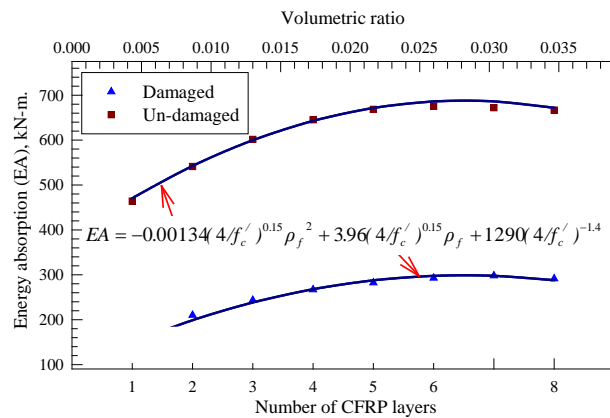


Figure 9. Energy absorption (EA) versus number of CFRP layers.

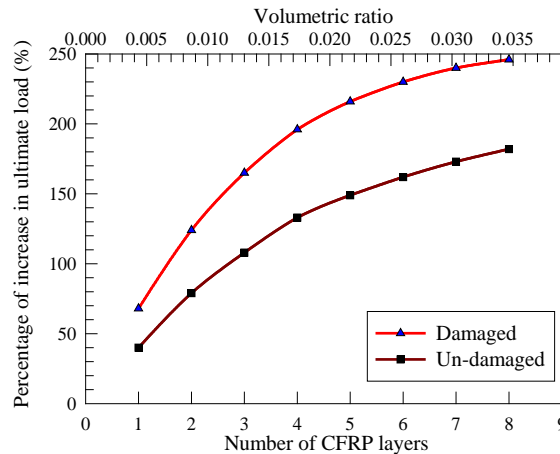


Figure 10. Ultimate load improvement percentages versus number of CFRP layers of confined columns.

3.4. Dilation properties

Fig. 11 shows the average volumetric curves versus the axial stress for NLFEA confined columns with CFRP composites. Inspection of Fig. 11(a) reveals that for un-damaged columns, one to six CFRP layers do not provide adequate confinement pressure to resist the dilation tendency of concrete. Alternatively, for the same column, seven to eight reverse the dilation trend of concrete (Compaction). While, one to three CFRP layers for damaged columns do not provide adequate confinement pressure to resist the dilation tendency of concrete. On the other hand, for the same column strength, four to eight reverse the dilation trend of concrete (Compaction). Therefore, the minimum amount of CFRP for sufficient confinement was four and seven layers of CFRP for damaged and un-damaged columns, respectively. It can be concluded that the number of CFRP layers that provide sufficient confinement to resist the dilation of concrete increased with the decrease of concrete compressive strength due to thermal shock.

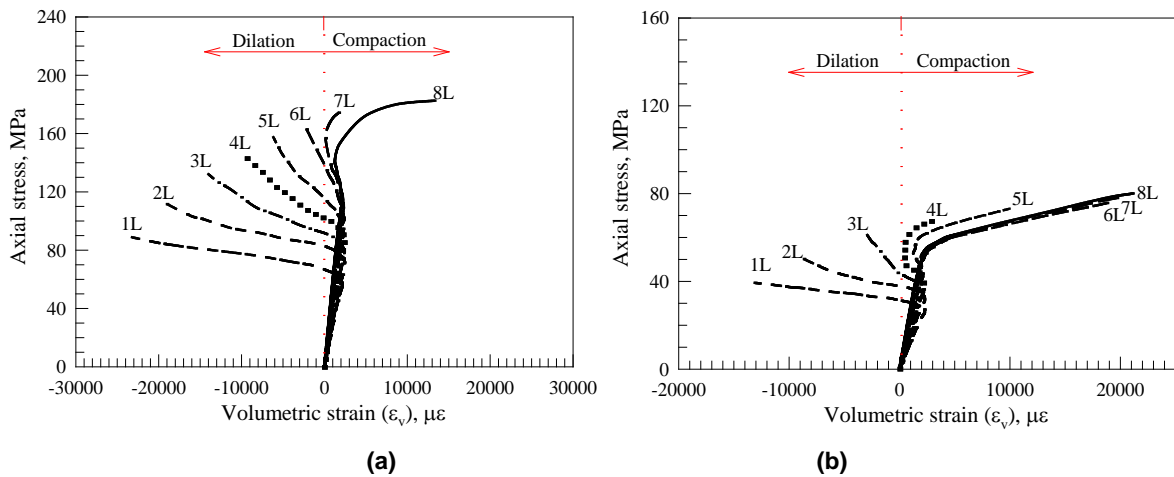


Figure 11. Volumetric strains for (a) Un-damaged and (b) Damaged confined columns.

3.5. Column ductility

The concept of ductility is related to the ability of a structural member to sustain inelastic deformation without substantial decrease in the load carrying capacity. Particularly, when it comes to reinforced concrete columns, ductility is an important issue due to their brittle failure mode. The ductility and energy absorption by CFRP composites are shown in Fig. 12. Inspection of Fig. 12 reveals that the increase in ductility is directly related to the increase in the number of layers of CFRP sheets. Also, Fig. 12 shows that the increase in ductility is directly related to decrease of compressive strength due to thermal shock. This indicated that damaged columns exhibited greater ductility than un-damaged columns. Whereas the ductility behavior (Stabilization of the ductility) of damaged and un-damaged columns decrease after seven and four layers of CFRP sheets, respectively, which can be classified as maximum amount for adequate ductility.

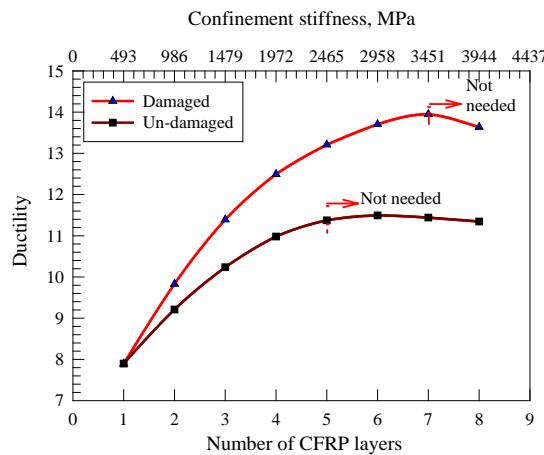


Figure 12. Increase in ductility versus number of CFRP layers.

3.6. Amount of CFRP for sufficient confinement and ductility

Fig. 13 shows the number of CFRP layers required for sufficient ductility and confinement versus concrete compressive strength. Based on the dilation properties and column ductility shown in Fig. 13, the maximum and minimum amount of CFRP were three and seven, respectively, of CFRP for damaged column and seven layers of CFRP for un-damaged columns, respectively. Also, Fig. 13 shows that number of CFRP layers controlled the behavior of the columns with concrete compressive strength less than 29 MPa, which indicated that there are maximum and minimum amount of CFRP to satisfy the ductility and confinement properties. On the other hand, for column with concrete compressive strength more than 29 MPa, the behavior was controlled by concrete compressive strength, which reflected that there is a fixed point for required number of CFRP layers for adequate ductility and confinement properties.

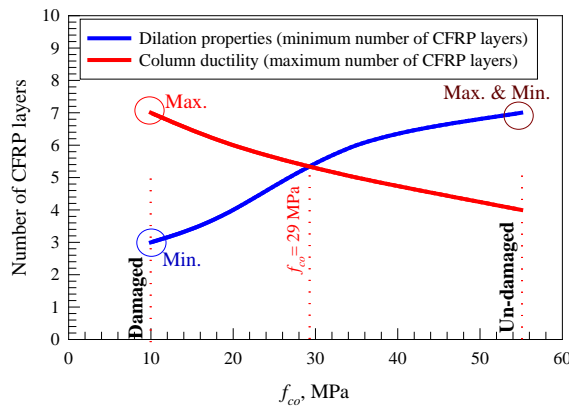


Figure 13. Number of CFRP layers versus unconfined strength of concrete.

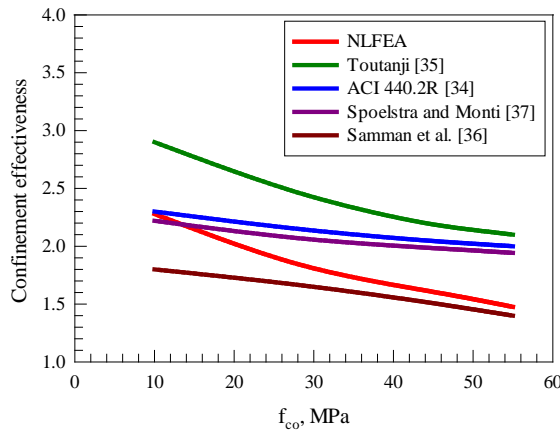


Figure 14. Effect of unconfined strength of concrete on confinement effectiveness.

3.7. Confinement effectiveness

Fig. 14 shows a plot of confinement effectiveness (ultimate load capacity of strengthened column divided by the ultimate load capacity of control column (un-strengthened)) versus the concrete compressive strength for confined column with one layer of CFRP composite. Also, Fig. 14 shows the predicted trends of the confinement effectiveness using ACI 440.2R [34], Toutanji [35], Samman et al. [36] and Spoelstra and Monti [37]. It is evident that as concrete compressive strength increases, confinement effectiveness decreases. The CFRP wrapped damaged columns show the maximum increases in ultimate load capacity. In addition, Fig. 14 shows that the confinement effectiveness of NLFEA columns is in good agreement with ACI 440.2R [34] and Samman et al. [36] damaged and un-damaged, respectively, but Toutanji [35] overestimated the predicted values by NLFEA columns. Fig. 15 shows the effect of concrete compressive strength on the confinement effectiveness or strength enhancement ratio. Inspection of Fig. 15 reveals that confinement effectiveness increased with the decrease of concrete compressive strength of damaged column. Also, Fig. 15 shows that, for relatively damaged, the increase of number of CFRP layers had a significant impact on the confinement effectiveness, which indicated that the ultimate behavior depends only on confinement effectiveness. This effect is insignificant in un-damaged columns, where only marginal increases in confinement effectiveness regardless of the number of layers, which indicated the confinement efficiency does not depend on the confinement level similar to conclusions observed by Issa and Tobaa [3].

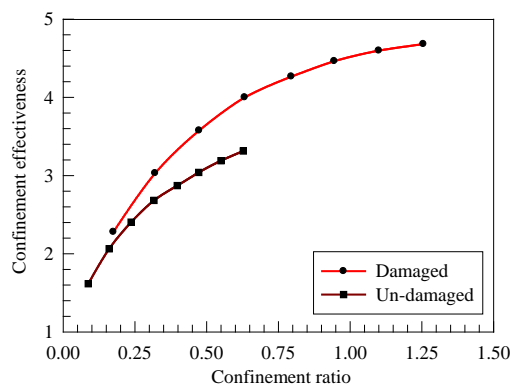


Figure 15. Confinement effectiveness versus confinement ratio.

4. Conclusions

1. The failure mode of the confined RC columns was sudden in the form of CFRP sheet fracture at the mid-height of the specimen followed by the fracturing of the lateral reinforcement and buckling of the longitudinal reinforcement. In the unconfined columns, the failure mode was also sudden due to the fracture of the lateral reinforcement and the outer concrete shell followed by buckling of the longitudinal reinforcement.

2. The axial load versus axial displacement curves of RC circular columns confined with CFRP composites are characterized by three stages. These three stages are the concrete has less expansion and fiber takes little constraining effect (Stage A), the concrete began to have a large expansion and the fiber begins to be stressed and crushing of the concrete at the end of this stage (Stage B), and the load was carried by the CFRP composite after crushing of the concrete until the fiber fractures (Stage C).

3. The influence of the number of CFRP layers on the ductility, energy absorption, and ultimate load improvement percentage is significant. There will be no further significant increase in the ductility and ultimate load of the column after a certain volumetric ratio, while significant increase in its stiffness continues to occur.

4. Thermal shock has a significant impact on the behavior of CFRP-confined circular RC columns. The increase in ductility is directly related to a decrease of compressive strength due to thermal shock. Also, the confinement effectiveness in terms of ultimate load was decreased with the increase in concrete compressive strength (un-damaged).

References

- Mirmiran, A., Shahawy, M., Samaan, M., El-Echary, H. Effect of column parameters on FRP-confined concrete. *J. Compos. Constr.* 1998. 2 (4). Pp. 175–185. DOI: 10.1061/(ASCE)1090-0268(1998)2:4(175)
- Parvin, A., Wang, W. Behavior of FRP jacketed concrete columns under eccentric loading. *J. Compos. Constr.* 2001. 5 (3). Pp. 146–152. DOI: 10.1061/(ASCE)1090-0268(2001)5:3(146)
- Issa, M., Tobaa, H. Strength and ductility enhancement in high-strength confined concrete. *Magazine of Concrete Research.* 1994. 46 (168). Pp. 177-189. DOI: 10.1680/mac.1994.46.168.177
- Kodur, V.K.R., Agrawal, A. An approach for evaluating residual capacity of reinforced concrete beams exposed to fire. *Engineering Structures.* 2016. 110 (1). Pp. 293–306. DOI: 10.1016/j.engstruct.2015.11.047
- Al-Ostaz, A., Irshidat, M., Tenkhoff, B., Ponnappalli, P.S. Deterioration of bond integrity between repair material and concrete due to thermal and mechanical incompatibilities. *Journal of Materials in Civil Engineering.* 2010. 22 (2). Pp. 136–144. DOI: 10.1061/(ASCE)0899-1561(2010)22:2(136)
- Nedviga, E., Beresneva, N., Gravit, M., Blagodatskaya, A. Fire Resistance of Prefabricated Monolithic Reinforced Concrete Slabs of "Marko" Technology. *Adv. Intell. Syst. Comput.* 2018. 692 (1). Pp. 739–749. DOI: 10.1007/978-3-319-70987-1_78
- Hezhev, T.A., Zhurtov, A.V., Tspinov, A.S., Klyuev, S.V. Fire resistant fibre reinforced vermiculite concrete with volcanic application. *Mag. Civ. Eng.* 2018. 80 (1). Pp. 181–194. DOI:10.18720/MCE.80.16
- Goremikins, V., Blesak, L., Novak, J., Wald, F. Experimental investigation on SFRC behaviour under elevated temperature. *J. Struct. Fire Eng.* 2017. 8 (1). Pp. 287–299. DOI: 10.1108/JSFE-05-2017-0034
- Goremikins, V., Blesak, L., Novak, J., Wald, F. To testing of steel fibre reinforced concrete at elevated temperature. *Appl. Struct. Fire Eng.* 2017. DOI: 10.14311/asfe.2015.055
- Blesak, L., Goremikins, V., Wald, F., Sajdlova, T. Constitutive model of steel fibre reinforced concrete subjected to high temperatures. *Acta Polytech.* 2016. 56 (1). Pp. 417–424. DOI: 10.14311/AP.2016.56.0417
- Korsun, V., Vatin, N., Franchi, A., Korsun, A., Crespi, P., Mashtaler, S. The strength and strain of high-strength concrete elements with confinement and steel fiber reinforcement including the conditions of the effect of elevated temperatures. *Procedia Eng.* 2015. 117 (1). Pp. 970–979. DOI: 10.1016/j.proeng.2015.08.192
- Goremikins, V., Blesak, L., Novak, J., Wald, F. Experimental method on investigation of fibre reinforced concrete at elevated temperatures. *Acta Polytech.* 2016. 56 (1). Pp. 258–264. DOI: 10.14311/AP.2016.56.0258
- Selyaev, V.P., Nizina, T.A., Balykov, A.S., Nizin, D.R., Balbalin, A.V. Fractal analysis of deformation curves of fiber-reinforced fine-grained concretes under compression. *PNRPU Mech. Bull.* 2016. 1 (1). Pp. 129-146. DOI: 10.15593/perm.mech/2016.1.09
- Bily, P., Fladr, J., Kohoutkova, A. Finite Element Modelling of a Prestressed Concrete Containment with a Steel Liner. *Proceedings of the Fifteenth International Conference on Civil, Structural and Environmental Engineering Computing.* Civil-Comp Press. 2015. DOI: 10.4203/ccp.108.1
- Bílý, P., Kohoutková, A. Sensitivity analysis of numerical model of prestressed concrete containment. *Nucl. Eng. Des.* 2015. 295 (1). Pp. 204–214. DOI: 10.1016/j.nucengdes.2015.09.027
- Al-Rousan, R. Behavior of two-way slabs subjected to drop-weight. *Magazine of Civil Engineering.* 2019. 90 (6). Pp. 62–71. DOI: 10.18720/MCE.90.6
- Al-Rousan, R. The impact of cable spacing on the behavior of cable-stayed bridges. *Magazine of Civil Engineering.* 2019. 91 (7). Pp. 49–59. DOI: 10.18720/MCE.91.5
- Krishan, A., Rimshin, V., Erofeev, V., Kurbatov, V., Markov, S. The energy integrity resistance to the destruction of the long-term strength concrete. *Procedia Eng.* 2015. 117 (1). Pp. 211–217. DOI: 10.1016/j.proeng.2015.08.143
- Bily, P., Kohoutková, A. Numerical analysis of anchorage between steel liner and prestressed nuclear containment wall. *Proc. 10th fib Int. PhD Symp. Civ. Eng.* 2014. 529–534.
- Korsun, V., Vatin, N., Korsun, A., Nemova, D. Physical-mechanical properties of the modified fine-grained concrete subjected to thermal effects up to 200°S. *Appl. Mech. Mater.* 2014. 633–634. Pp. 1013–1017. DOI: 10.4028/www.scientific.net/AMM.633-634.1013
- Korsun, V., Korsun, A., Volkov, A. Characteristics of mechanical and rheological properties of concrete under heating conditions up to 200°C. *MATEC Web Conf.* 2013. 6 (1). Pp. 07002. DOI: 10.1051/mateconf/20130607002

22. Petkova, D., Donchev, T., Wen, J. Experimental study of the performance of CFRP strengthened small scale beams after heating to high temperatures. *Construction and Building Materials*. 2014. 68 (1). Pp. 55–61. DOI: 10.1016/j.conbuildmat.2014.06.014
23. Ji, G., Li, G., Alaywan, W. A new fire resistant FRP for externally bonded concrete repair. *Construction and Building Materials*. 2013. 42 (1). Pp. 87–96. DOI: 10.1016/j.conbuildmat.2013.01.008
24. Trentin, C., Casas, J.R. Safety factors for CFRP strengthening in bending of reinforced concrete bridges. *Composite Structures*. 2015. 128 (1). Pp. 188–198. DOI: 10.1016/j.compstruct.2015.03.048
25. Ferrari, V.J., de Hanai, J.B., de Souza, R.A. Flexural strengthening of reinforcement concrete beams using high performance fiber reinforcement cement-based composite (HPFRCC) and carbon fiber reinforced polymers (CFRP). *Construction and Building Materials*. 2013. 48 (1). Pp. 485–498. DOI: 10.1016/j.conbuildmat.2013.07.026
26. Attari, N., Amziane, S., Chemrouk, M. Flexural strengthening of concrete beams using CFRP, GFRP and hybrid FRP sheets. *Construction and Building Materials*. 2012. 37 (1). Pp. 746–757. DOI: 10.1016/j.conbuildmat.2012.07.052
27. Kara, I.F., Ashour, A.F., K rog lu, M.A. Flexural behavior of hybrid FRP/steel reinforced concrete beams. *Composite Structures*. 2015. 129(1). Pp. 111–121. DOI: 10.1016/j.compstruct.2015.03.073.
28. Kolchunov, V.I., Dem'yanov, A.I. The modeling method of discrete cracks in reinforced concrete under the torsion with bending. *Magazine of Civil Engineering*. 2018. 81 (5). Pp. 160–173. DOI: 10.18720/MCE.81.16
29. Travush, V.I., Konin, D.V., Krylov, A.S. Strength of reinforced concrete beams of high-performance concrete and fiber reinforced concrete. *Magazine of Civil Engineering*. 2018. No. 77 (1). Pp. 90–100. DOI: 10.18720/MCE.77.8
30. Issa, M.A., Alrousan, R., Issa, M. Experimental and Parametric Study of Columns with CFRP Composites. *Journal of Composites for Construction ASCE*. 2009. 13 (2). Pp. 135–147. DOI: 10.1061/(ASCE)1090-0268(2009)13:2(135)
31. Swesi, A.O. Repair of Shear-Deficient Normal Weight Concrete Beams Damaged by Thermal Shock Using Advanced Composite Materials. Master Thesis. 2011.
32. Zhang, Y.X., Bradford, M.A. Nonlinear analysis of moderately thick reinforced concrete slabs at elevated temperatures using a rectangular layered plate element with Timoshenko beam functions. *Engineering Structures*. 2007. 29(10). Pp. 2751-2761. DOI: 10.1016/j.engstruct.2007.01.016
33. Haddad, R.H., Al-Rousan, R.Z. An anchorage system for CFRP strips bonded to thermally shocked concrete. *International Journal of Adhesion and Adhesives*. 2016. 71(1). Pp. 10–22. DOI: 10.1016/j.ijadhadh.2016.08.003
34. ACI Committee 440. Design and Construction of Externally Bonded FRP Systems for strengthening Concrete Structures. *ACI440.2R-02. 2002. American Concrete Institute, Farmington Hills, Mich.: 45 p. DOI: 10.1061/40753(171)159
35. Toutanji, H. Stress-strain characteristics of concrete columns externally confined with advanced fiber composite sheets. *ACI Materials Journal*. 1999. 96 (3). Pp. 397-404. DOI: 10.14359/639
36. Samaan, M., Mirmiran, A., Shahawy, M. Model of concrete confined by fiber composites. *Journal of Structural Engineering*. 1998. 124(9). Pp. 1025–1031. DOI: 10.1061/(ASCE)0733-9445(1998)124:9(1025)
37. Spoelstra, M., Monti, G. FRP-confined concrete model. *Journal of Composites for Construction*. 1999. 3(3). Pp. 143–150. DOI: 10.1061/(ASCE)1090-0268(1999)3:3(143)

Contacts:

Rajai Al-Rousan, rzalrousan@just.edu.jo



DOI: 10.18720/MCE.97.9

Stress-strain state of fiber cement cladding within curtain wall system

D. Egorov^{a*}, A. Galyamichev^a, E. Gerasimova^b, D. Serdjuks^c

^a Peter the Great St. Petersburg Polytechnic University, St. Petersburg, Russia

^b NIUPC «Mezhregional'nyj institut okonnyh i fasadnyh konstrukcij», St. Petersburg, Russia

^c Riga Technical University, Riga, Latvia

* Email: egorov.dv@edu.spbstu.ru

Keywords: composite materials, cements, fiber reinforced materials, bending strength, facades, finite element method

Abstract. This article presents the experimental methodology and results of laboratory tests and numerical modeling in order to determine the values of bearing capacity and stiffness of fiber cement board (FCB) within a frame of curtain wall system. The performance of a panel as a part of a system is taken into account for evaluation of the stress-strain state of a cladding. An analysis included 2 stages: an experimental study of a full-size fragment of a curtain wall system with fiber cement cladding and its numerical simulation by means of finite element method (FEM). The dependences of the deflection of the panel on a value of uniformly distributed load were obtained, and the experimental results converged with numerical calculation. The maximum values of the uniformly distributed (simulating wind impact) loads acting on the panel under which the panel satisfies the requirements stated by Ultimate and Serviceability Limit States were calculated also. It can be concluded that onset of Ultimate Limit State is characterized by appearance of cracks due to the stresses in the panel exceeding the value of flexural strength in the area of fastening to curtain wall frame. The results demonstrated that the stress-strain state of the cladding depends on the structural scheme of the supporting frame of the curtain wall system and its rigidity, therefore it is recommended to perform tests on the cladding in conjunction with the supporting frame.

1. Introduction

Nowadays curtain wall systems are actively used in construction. Such systems became popular due to the fact that a large number of buildings no longer met the requirements stated by appeared regulatory documents. Renovation of facades by means of traditional methods was significantly less efficient and more expensive. A possibility to install such systems in any weather conditions, which is quite relevant for construction in areas of changeable climate, was an excellent advantage in addition. The curtain wall systems now possess structural importance equivalent to that gained by other structural elements of the building. A certain number of issues related to its application remain to be studied despite the fact that this material was in use since the 1990's. One of them is the development of testing and calculation methods of cladding as part of the curtain wall system, as well as the development of requirements for fastening this cladding to the supporting frame of the system.

Fiber cement board (FCB) is a flat rectangular product made of cellulose fibers, mineral aggregates and cement, with a flat or embossed front surface covered with protective and decorative polymer coating. These panels are used as cladding elements of the external and internal walls (except basement walls) of buildings and structures within curtain wall systems and as opaque elements in glass facades. The advantages and disadvantages of these panels are studied in article as a part of curtain wall systems [1]. Most common sizes of FCB vary in length from 1200 to 3600 mm, in width from 1120 to 1570 mm and a thickness of them is equal to 6, 8, 10, 12, 14 or 16 mm. The panels are fastened to the supporting structure by means of exhaust rivets and self-tapping screws or several types of hidden fixators (e.g., Keil anchors) in most of cases.

Boards with visible fastening by exhaust rivets to the metal supporting frame of curtain wall system were analyzed within this study. One of fastening points is fixed and the rest of them are movable (Fig. 1) in order



to prevent occurrence of stresses due to temperature deformations of the plate and the metal frame. At the moment, in many technical certificates and installation guidelines for curtain wall system with fiber cement cladding, the critical rivet installation step is presumed to be equal to 600 mm, the edge distances in transverse and longitudinal directions are 30 mm and 50–150 mm respectively.

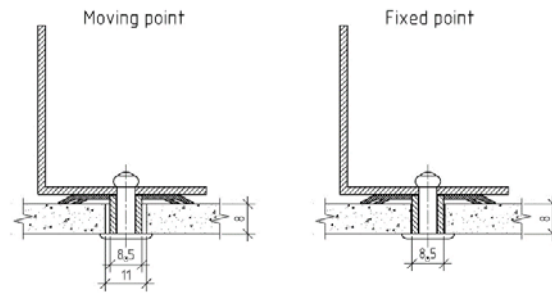


Figure 1. Fastening points of fiber cement board to the supporting frame.

According to their mechanical and deformation characteristics and due to their structure, FCBs are anisotropic material with different characteristics across and along the fibers. The works [2–7] are devoted to the analysis and improvement of the mechanical properties of fiber cement cladding. In [8], the effect of freeze-thaw cycles is considered, and in [9], influence of thermal impact on the properties of the boards is studied. Article [10] presents the results of the tests performed on cement boards with cellulose fibers as a reinforcing material in wet and dry conditions and determines the influence of the moisture rate on blast strength, ductility, bending strengths and other properties of FCBs.

Article [11] presents results of studies on fracture processes in FCBs and the use of non-destructive acoustic emission method and time-frequency analysis for testing FCBs.

In order to design curtain wall system, which fully satisfies the performance requirements during operation, it is necessary to properly calculate its cladding. The calculation should include verification according to both Ultimate Limit State (ULS) and Serviceability Limit State (SLS). Therefore, there is a need in development of a laboratory test and design method for the cladding as part of the curtain wall system, as well as the requirements for its fastening. Similar full-size tests were already performed on glass and thin ceramic panels [12–14]. In [15], elements of filling are taken into account for numerical modeling of translucent facade structures.

Loads and effects acting on the structure remain an important factor, which needs to be taken into account for reliable calculations of curtain wall systems. Loads acting on facade structures in accordance with Limit State Design are described in [16, 17]. Article [18] analyses the procedure of numerical modeling of the cladding panel by FEM. Article [19] verifies the possibility of usage of FCBs as a cladding in lightweight structures. Calculation methods, considering joint performance of structural members, are studied in [20].

The aim of this study was to determine the stress-strain state of fiber cement panels as part of curtain wall system subjected to a uniformly distributed load.

The study was divided into several stages:

1. An experimental study of a full-sized fragment of a curtain wall system with fiber cement cladding.
2. Numerical modeling of the facade fragment by means of FEM realized in SCAD Office software package.
3. Comparison of the results obtained through numerical modeling and experimental study.

The subjects of the study were:

- The value of uniformly distributed load, which leads to the loss of the bearing capacity of FCB under the given conditions of fastening;
- The values of the deflection at the characteristic points of the panels as a result of the action of a uniformly distributed load;
- The character of a panel failure due to limit state occurrence;
- The possibility of usage of FCBs in terms of bearing capacity with a distance between adjacent fastening points more than 600 mm;
- The possibility of usage of FCBs in terms of bearing capacity with a distance from the edge of the panel to the axis of the fastening installation hole equal to 30 mm.

2. Materials and Methods

2.1. Experimental study of FCBs within curtain wall system

The experimental method included a set of the tests on full-size fragments of a curtain wall system with cladding made of FCBs in laboratory conditions. Test bench implied the installation of a fragment in a horizontal position (Fig. 2), and application of the load simulating the most unfavorable type of impact for a given design solution – wind load from leeward side of the building, under which the panel bends with simultaneous separation from the frame of system.

The object of current study was fiber cement panels with thickness of 8 and 10 mm painted on the front surface. The considered panels had geometric dimensions of 3600×1500 mm and were installed as cladding in curtain wall system.

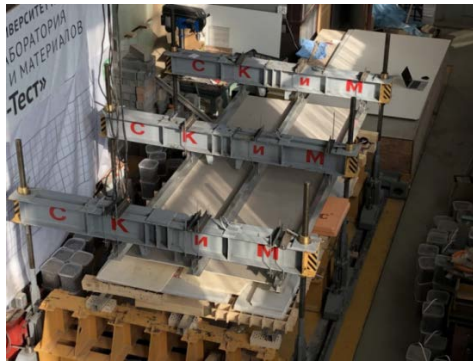


Figure 2. Initial position of the sample on the test bench.

The bearing frame was a system designed for façade cladding by means of sheet panels. The system consisted of a subframe and brackets. Three crossbeams of increased rigidity acted as the supporting base, to which the brackets of the curtain wall system were clamped by an angle profile and threaded rods. The brackets were installed with a step a of 1770 mm and b of 720 mm (Fig. 3), and the subframes were creating two-span continuous scheme, in order to obtain the most general case of curtain wall system. The fixation of the subframe profiles to the brackets was carried out by rivets, the number of which depends on the type of bracket: 8 rivets were used for the bearing bracket, and 4 rivets for the supporting.

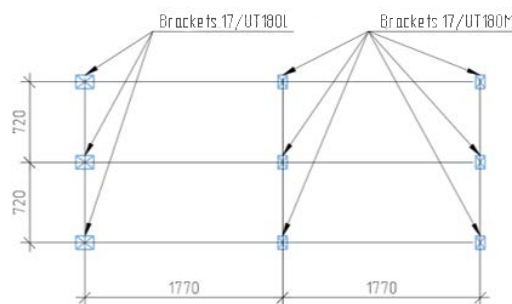


Figure 3. Arrangement of brackets for subframe attachment.



Figure 4. Attachment of brackets to traverses and fixation of the subframe to the brackets.

The FCB was connected to the subframe by rivets installed in pre-drilled holes together with polyamide sleeves. The installation step for fasteners (rivets) in the longitudinal direction (along the larger side) was taken as 708 mm and in the transverse direction as 720 mm, within this study. The distance from the edge of the panel to the axis of the hole for mounting the fastener was equal to 30 mm both in the longitudinal and transverse directions (Fig. 5).

Three dial indicators with an accuracy of 0.01 mm installed at the characteristic points of the structure (Fig. 5) allowed to obtain the values of vertical displacements of the panel. The indicator DI1 was installed at

the point where the maximum vertical displacements of the fiber cement panel were observed, the indicator DI2 showed the joint's displacements of the FCB and the middle subframe profile, and the indicator DI3 tracked the displacements of the edge of the panel together with the subframe profile.

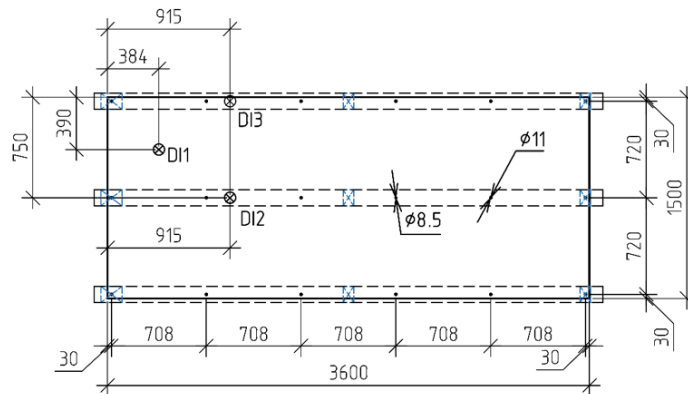


Figure 5. The position of the holes and dial indicators on the test fragment.

Uniformly distributed load was realized through placement of equal loads with weight of 7.5 kg each, located on the surface of the panel in a certain sequence (Fig. 6, 7). Initial load of 22 kg/m³ was applied in order to remove backlash in the mounted structure of the curtain wall system. After that, the load was eliminated and the initial parameters of the dial indicator were recorded for the following calculation of the vertical displacements of the cladding panel. Sequential loading was carried out with simultaneous recording of the deflection values until the panel was fractured or cracks appeared on its outer surface.

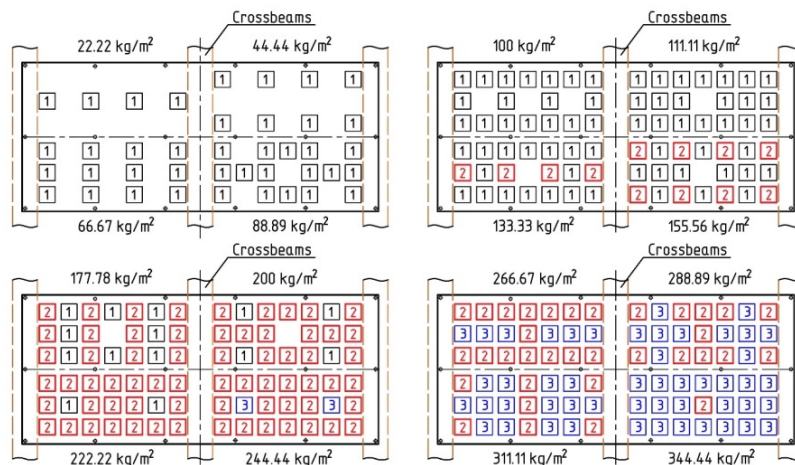


Figure 6. Load distribution on the panel (number indicates the quantity of loads placed one over the other).

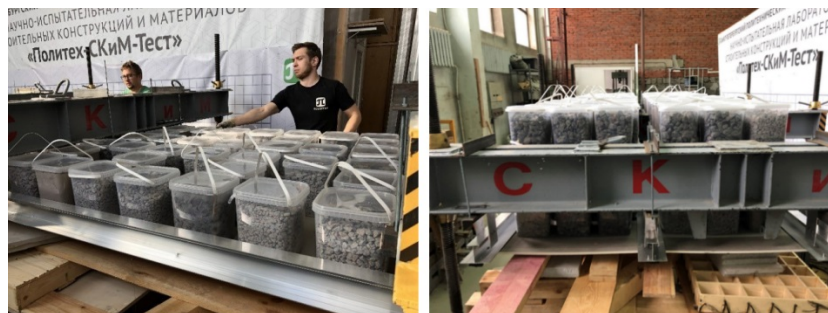


Figure 7. Application of distributed load during the test: left – 100 kg/m²; right – 344.44 kg/m².

2.2. Numerical modeling of FCBs within curtain wall system

Procedure of numerical modeling included the following tasks:

1. Determination of the displacements of the curtain wall system jointly with the cladding panels under the action of uniformly distributed and concentrated load, which was representing uniformly distributed load during the experimental study.

2. Determination of stresses in the cladding panel under the action of uniformly distributed load and verification of the panel in accordance with ULS.

3. Determination the vertical displacements of the cladding panel without taking into account the displacements of the subsystem and verification of the panel in accordance with SLS.

Numerical modeling and static calculation of the cladding jointly with subframe profiles were performed using the finite element method (FEM) implemented in the SCAD Office 21.1 software package.

Metal elements were simulated by one-dimensional finite elements (beams), and the panel was simulated by two-dimensional finite elements (shells). The scheme of the fragment of the curtain wall system is shown in Fig. 8, in which the guide profiles are continuous two-span beam on hinged supports. The hinge support is made along the X and Y axis (in the plane of the facade), and in the Z direction the connection with the finite stiffness is modeled.

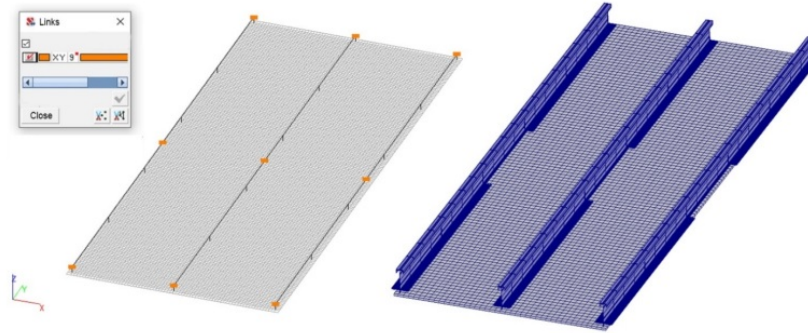


Figure 8. Left - calculation scheme of the curtain wall system, right - calculation model in the SCAD Office.

System stiffness was determined on the base of test results in accordance with the formula:

$$K = \frac{R_z}{f} \quad (1)$$

Where R_z is the support reaction that occurs in the bracket as a result of the load applied during the test (obtained through static calculation in SCAD):

$$R_z = 66.15 \text{ kg}$$

f is a displacement of the central support (obtained through the test with subframe profiles application):

$$f = 0.37 \text{ mm}$$

$$K = \frac{66.15}{0.37} = 178.78 \text{ kg / mm}$$

The panel is fastened to the subframe by hinges, which allow rotation from the plane of the panels and displacement in the plane of the facade (Fig. 9). A fixed fastening point allowed rotation in the plane of the panel and prevented linear displacements in the plane of the facade. Due to the strengthening of the frictional connection between the panel and subframe, jamming in the corresponding direction, which prevented linear and angular displacements, was created at the edge and corner fastening points.

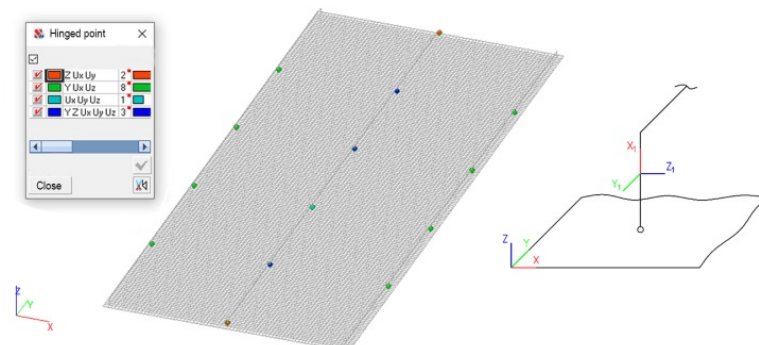


Figure 9. Hinges in the locations of fastening to the subframe profile (local coordinate system).

The reduction of the cross-section of subframe profile and the subsequent calculation of its modified geometric characteristics was performed with consideration of possible local buckling of individual elements subjected to normal compressive stresses.

The geometric characteristics of the cross-section before and after reduction were determined in the SCAD Office 21.1 software package (KONSUL satellite). The initial and final cross-sections are shown in Fig. 10.

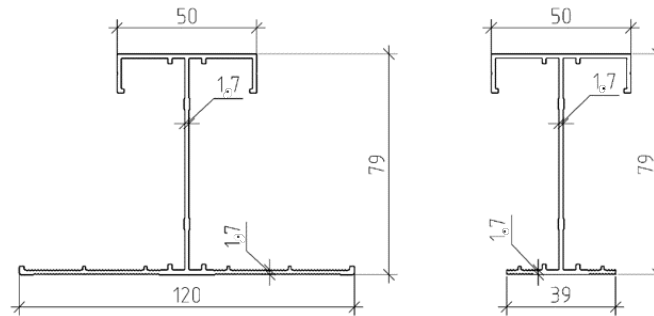


Figure 10. Cross-section of the subframe profile: left – before reduction, right – after reduction of the lower part of cross-section under its compression.

Stiffness characteristics of aluminum subframe profiles: modulus of elasticity is equal to $7.1 \cdot 10^9 \text{ kg/m}^3$; Poisson's ratio is equal to 0.3.

Flexural modulus of FCB:

$$E = 14000 \text{ MPa}$$

Poisson's ratio of FCB:

$$\nu = 0.2$$

Panel's thicknesses:

$$t = 8 \text{ mm}; t = 10 \text{ mm}$$

A set of concentrated loads, which were applied during the test, was simulated as uniformly distributed loads on certain areas corresponding to actual location of single loads (Fig. 11), and their value was determined by the formula:

$$q = \frac{P_{load}}{S} \quad (2)$$

where P_{load} is a load unit weight:

$$P_{load} = 7.5 \text{ kg}$$

S is the area of load unit in contact with panel surface, calculated for assumed FE mesh;

$$S = 0.16 \cdot 0.159 = 0.02544 \text{ m}^2$$

$$q = \frac{7.5}{0.02544} = 294.81 \text{ kg/m}^2$$

Thus, load distribution for each stage of application in numerical model corresponded to actual load application of experimental study.

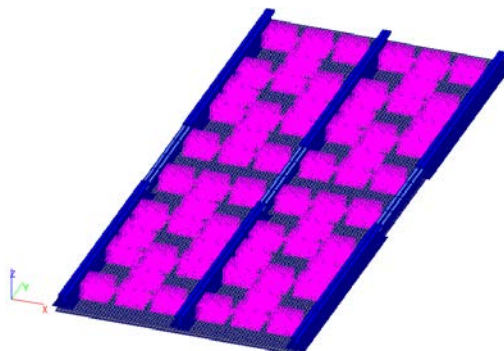


Figure 11. Load application (88.89 kg/m^2) in numerical model.

3. Results and Discussion

3.1. Results of experimental study of FCBs within curtain wall system

Vertical displacements of the panel characteristic points were calculated on the base of dial indicator measurements and displayed in a form of graphs showing dependence of deflections on the applied load (Fig. 12–14).

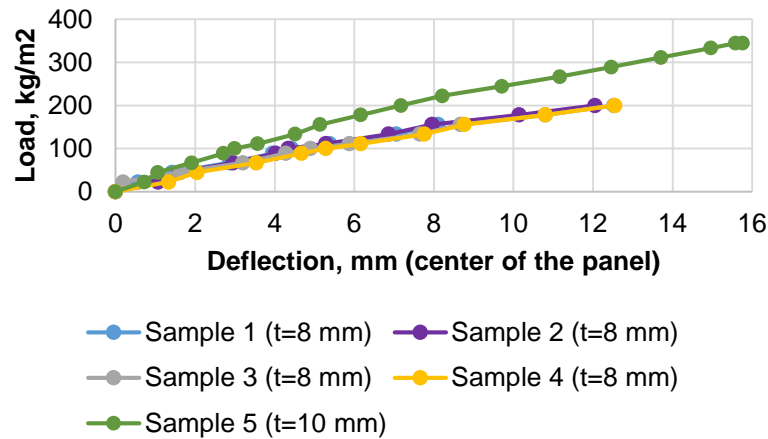


Figure 12. Deflection of the center of the panel under the action of applied load for the panels with the different thicknesses.

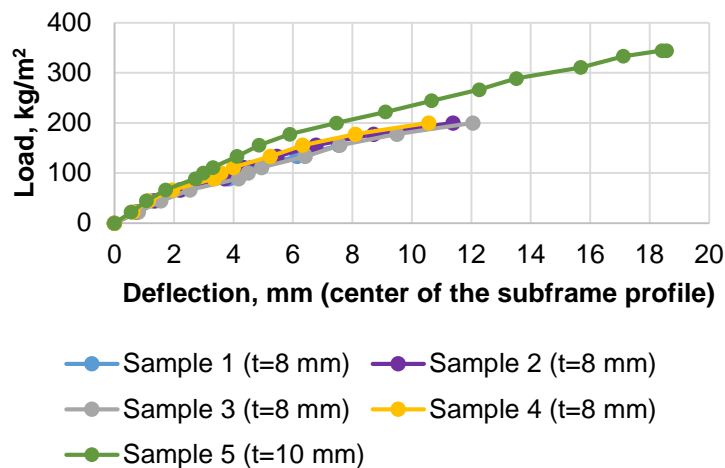


Figure 13. Deflection of the center of the subframe profile under the action of applied load for the panels with the different thicknesses.

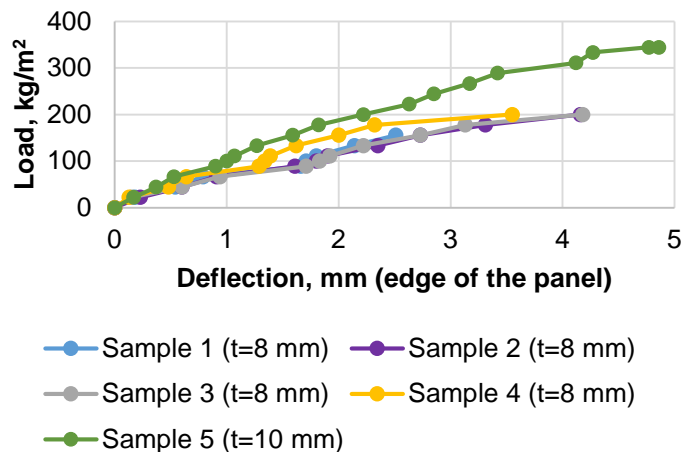


Figure 14. Deflection of the edge of the panel under the action of applied load for the panels with the different thicknesses.

Fracture of the panel was characterized by the formation of a longitudinal crack near the most loaded fastening point (Fig. 15), and the panel was destroyed by bending (Fig. 16) during subsequent loading.



Figure 15. Crack formation: left – sample 1 under the load of 155.56 kg/m²; right – sample 2 under the load of 200 kg/m².



Figure 16. Fracture of the panel: left – sample 3 under the load of 222.22 kg/m²; right – sample 4 under the load of 200 kg/m².

Fig. 17 demonstrates formation and opening of the crack in the corner of the panel under the load of 266.67 kg/m². However, the panel withstood loading up to the value of 344.44 kg/m². (Fig. 18), and fractured along the fibers near the central subframe profile, in the same way as in other tests.



Figure 17. Left – the formation and opening of a crack in sample 5 under the load of 266.67 kg/m²; right – corner fastening point after the panel fracture.



Figure 18. Panel fracture of the sample 5 under the load 344.44 kg/m².

Plastic deformations of the central subframe profile in the area of the fastening point to the central support bracket are shown in Fig. 19. The numerical values of this deformation were measured during subsequent tests and allowed to calculate rigidity of this joint for further implementation in the numerical model.

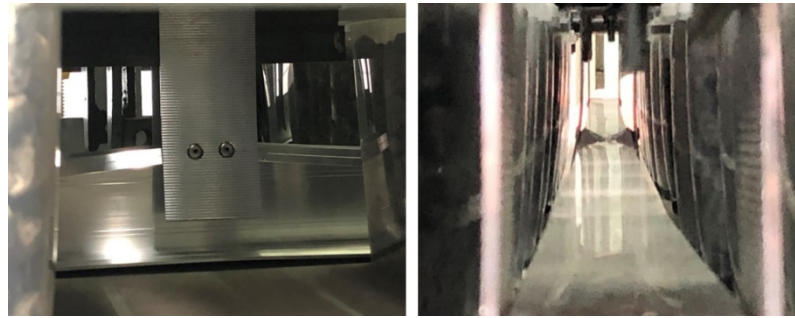


Figure 19. Deformation of the subframe profile in the area of the central bracket under the load of 344.44 kg/m² (sample 5).

3.2. Results of numerical modeling of FCBs within curtain wall system

Vertical displacements of the panel characteristic points were calculated according to results of numerical modeling and displayed in a form of graphs showing dependence of deflections on the applied load (Fig. 20–22).

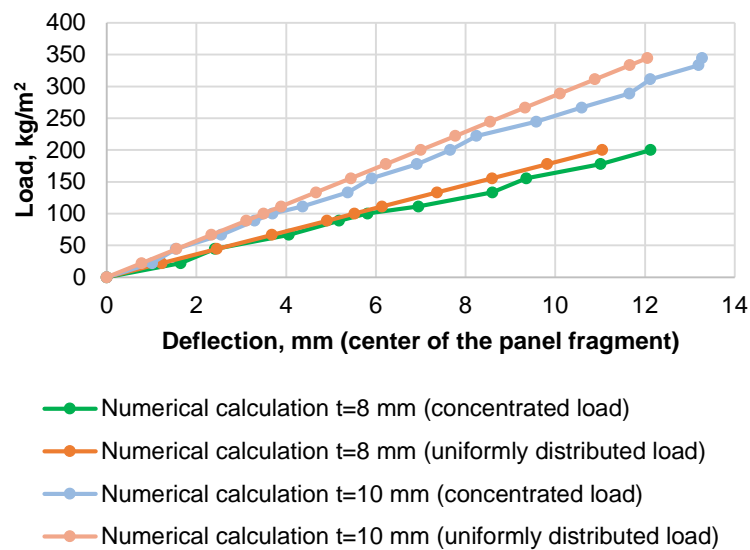


Figure 20. Deflection of the center of the panel fragment for the panels with the different thicknesses.

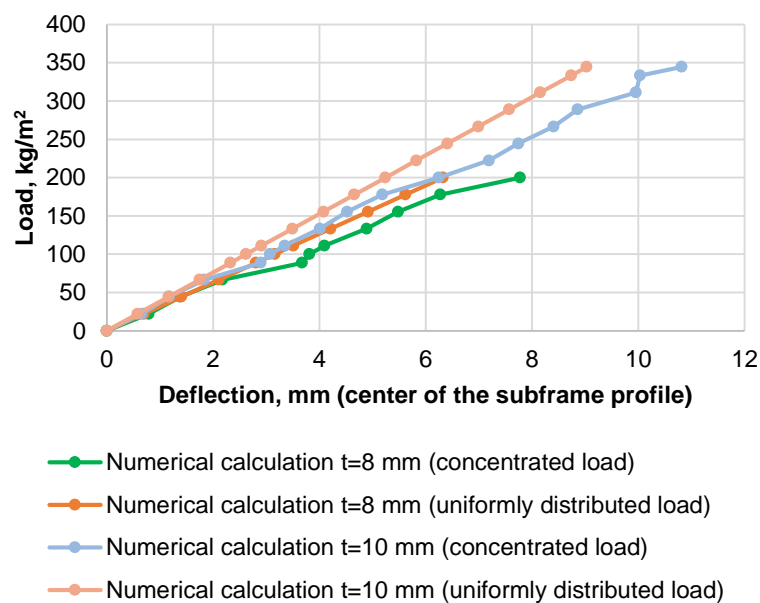


Figure 21. Deflection of the center of the subframe profile for the panels with the different thicknesses.

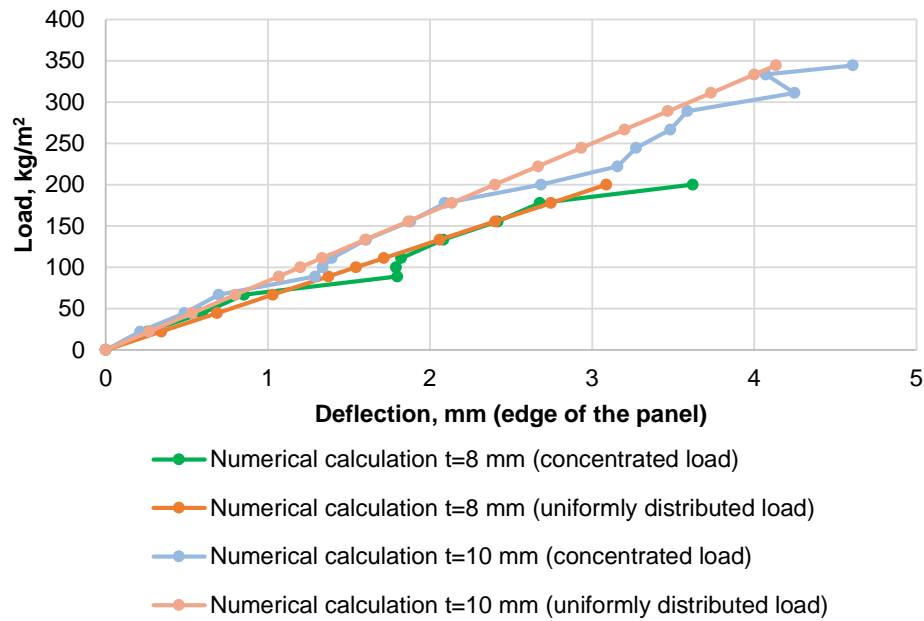


Figure 22. Deflection of the edge of the panel for the panels with the different thicknesses.

3.3. Verification of the cladding in terms of ULS

Major stresses arising in the plate under the action of a uniformly distributed load were calculated for evaluating the panel stress-strain state in accordance with ULS. The character of the stress distribution on the upper surface of the panel is shown in Fig. 23.

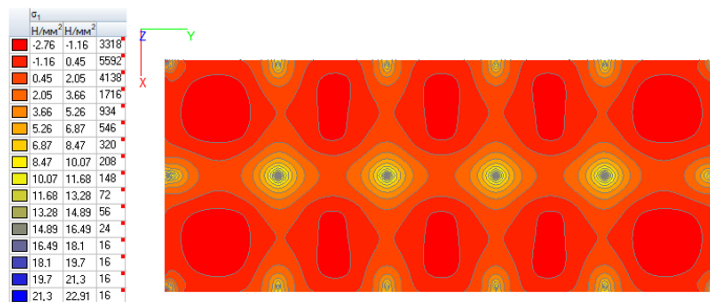


Figure 23. Distribution character of major stresses σ_I in the panel under uniformly distributed load, MPa.

The ULS criteria for FCB is bending strength manufacturer's guideline:

$$R = 26.1 \text{ MPa}$$

Ultimate load acting on the panel and corresponding to the reaching of ULS (Table 1) was calculated according to Fig. 24, by linear interpolation of load and displacement values.

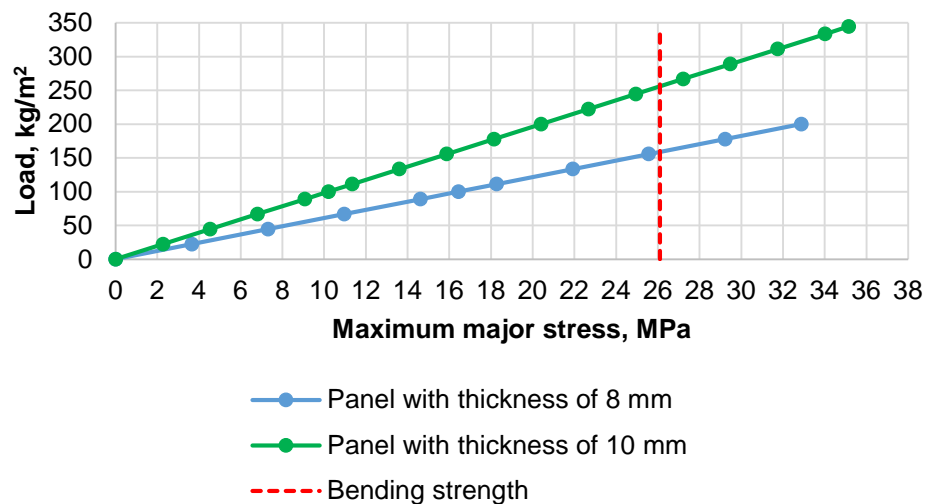


Figure 24. Maximum major stresses in the panel.

Table 1. Maximum allowable load in accordance with ULS requirements.

Panel thickness, mm	Load q_l , kg/m ²
8	158.8
10	255.9

3.4. Verification of the cladding in terms of SLS

The SLS criteria for FCB is its maximum allowable deflection determined in Russian Set of Rules 20.13330.2016 "Loads and actions" and equal to:

$$f_{SLS} = \frac{s}{150} \quad (3)$$

where s is minimum distance between fastening elements of the panel (rivets).

$$f_{SLS} = \frac{708}{150} = 4.72 \text{ mm}$$

In the course of numerical modeling and experimental research, the displacements at characteristic points of the panel within the system were obtained. The final values consisted of joint deflections of the supporting frame and cladding.

For the correct stress-strain state assessment of FCB in accordance with SLS it is necessary to evaluate the deflections of cladding deforming independently. For this purpose, the numerical model of the FCB included cladding apart represented in the form of plate composed of shell finite elements and fixed by hinges at each position of fastening element (rivet) (Fig. 25). At the installation point, linear fixing was made to and from the plane of the facade panel.

Vertical movements of a panel under the action of uniformly distributed load are shown in Fig. 26.

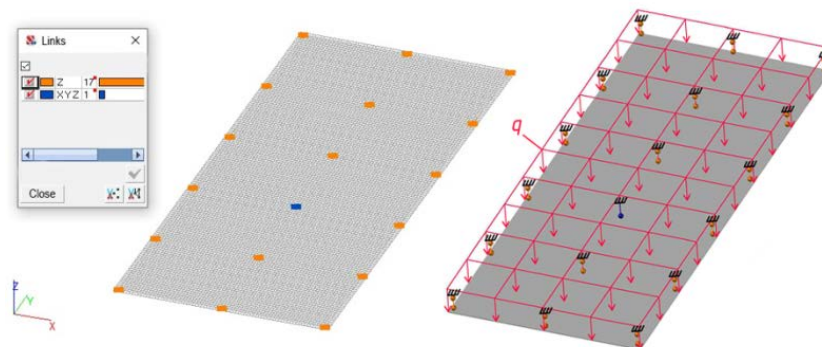


Figure 25. Structural scheme of the panel including fixing points and load application.

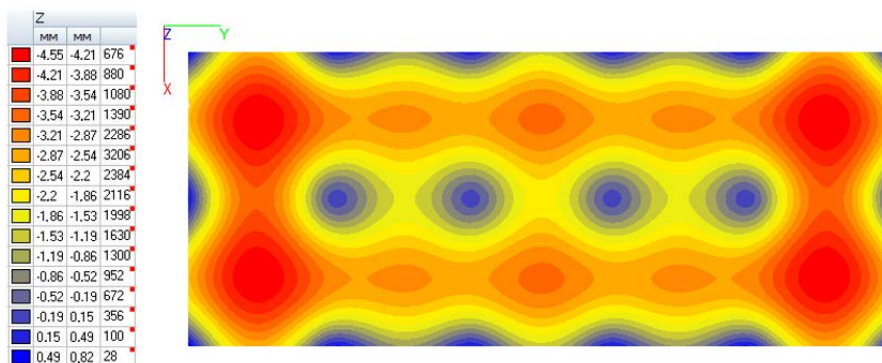


Figure 26. Displacement of the panel ($t = 8$ mm) in z-direction under the action of uniformly distributed load of 88.89 kg/m².

The maximum value of the load acting on the panel, which corresponded to the onset of SLS (Table 2), was calculated on the base of information provided in Fig. 27 by linear interpolation of the load and displacement values.

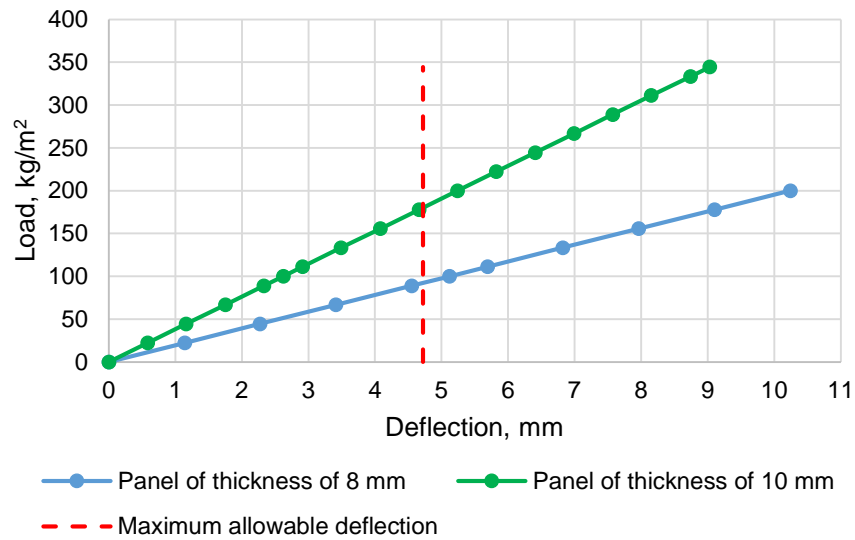


Figure 27. Deflections of the panel obtained through numerical modeling.

For the purpose of correct comparison of the maximum loads at the onset of the SLS and ULS and determination of defining state, a reduced (design) value is introduced for the case of SLS:

$$q_{SLS, SF} = q_{SLS} \cdot \gamma_f \tag{4}$$

where γ_f is safety factor, which is equal to 1.4 for the case of wind load.

Table 2. Maximum allowable load for SLS verification.

Panel thickness, mm	q_{SLS} , kg/m ²	$q_{SLS, SF}$, kg/m ²
8	92.2	129.1
10	181	253.4

3.5. Analysis and Discussion

Maximum vertical displacements of the center of the panel obtained during experimental study and numerical simulation are summarized in Fig. 28 and 29.

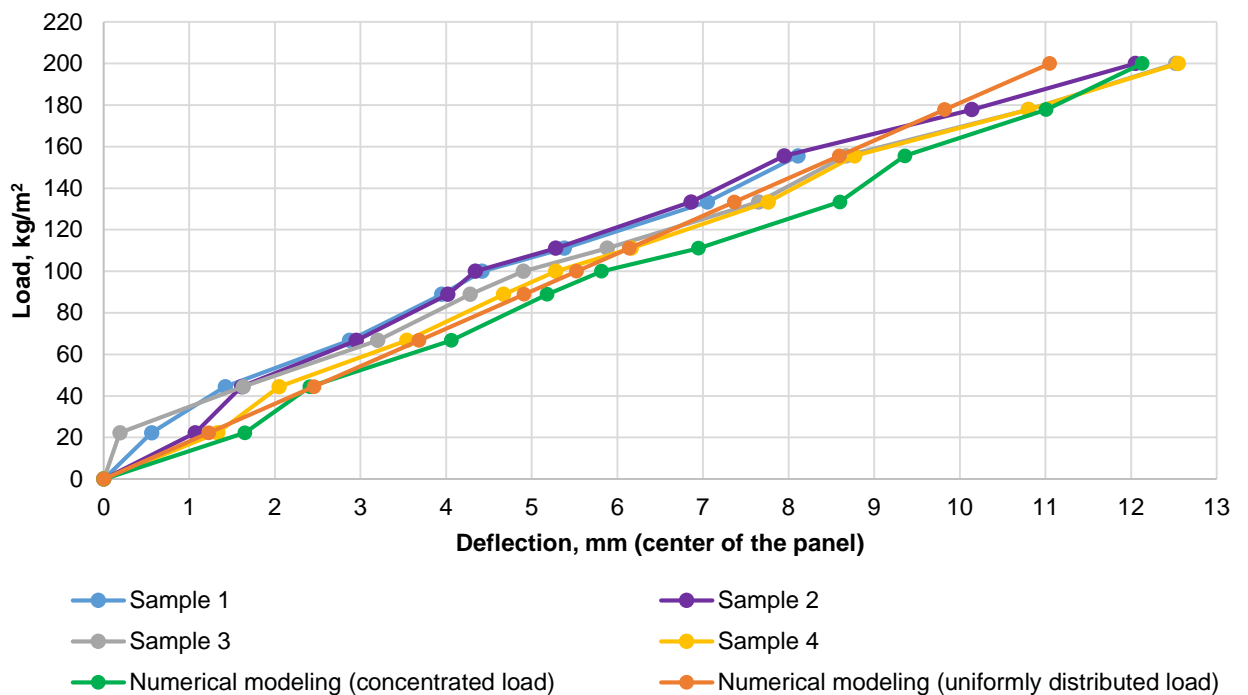


Figure 28. Deflection of the center of the panel (t = 8 mm).

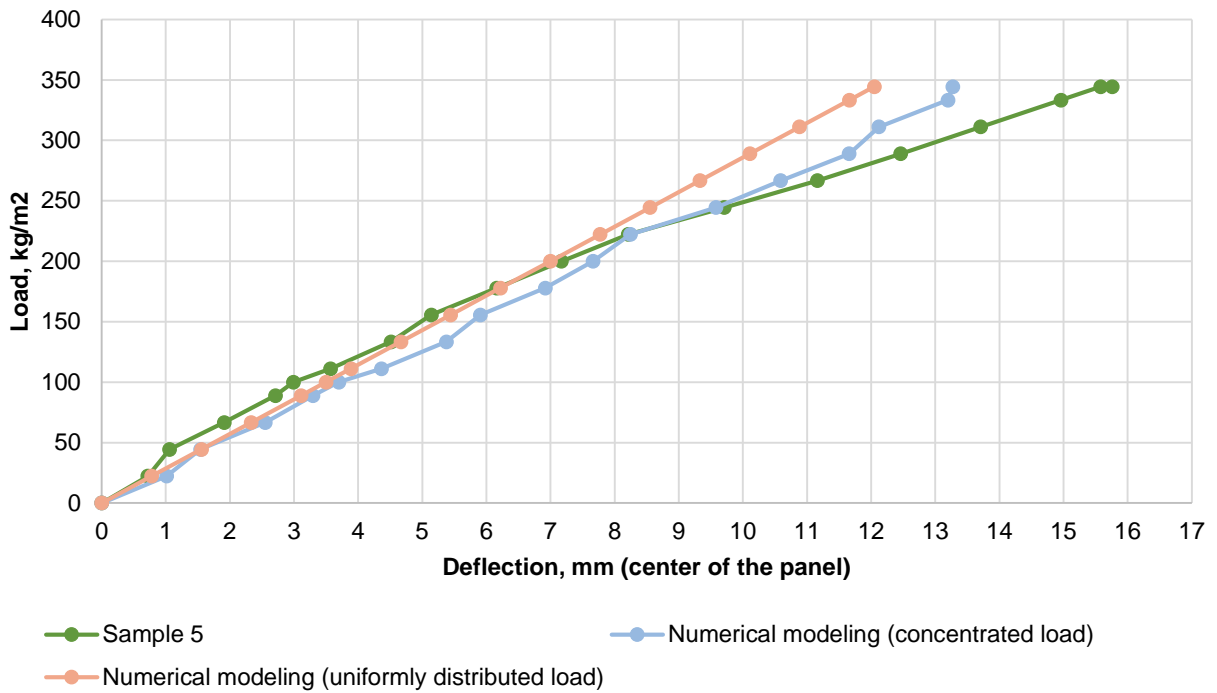


Figure 29. Deflection of the center of the panel (t = 10 mm).

Given that plastic deformations of subframe profile appear and increase near the area of its attachment to the supporting bracket, at certain load values displacements of the panel start to increase sharply (areas of convergence of numerical simulation and experimental research).

The dependence of the movements of the joint between central bracket and subframe profile on the acting load is shown in Fig. 30. When load increases the behavior of this connection changed from elastic to plastic as a result of local plastic deformations of the subframe profile, while in the numerical model it was realized through linear dependence of the displacements on the load by introducing elasto-plastic bonds.

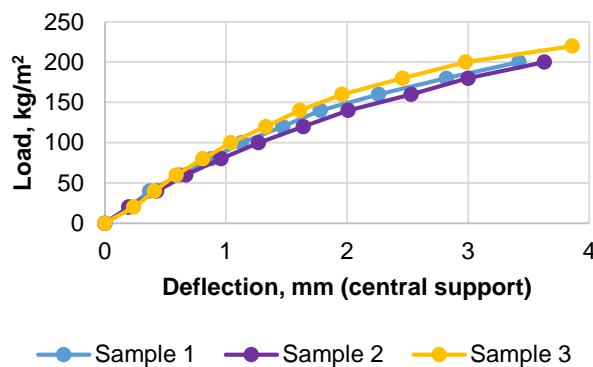


Figure 30. Dependence of the displacement of the joint between central bracket and subframe on the value of load acting on the panel.

According to the results of numerical modeling, loss of bearing capacity of the panel occurred due to the bending of the panel. Similarly, the loss of bearing capacity during the tests occurred due to formation of cracks in the area with the maximum value of bending stresses.

As the numerical modeling provides lower values of the system deflection in comparison with test results, it can be concluded that the design on the base of numerical simulation considered a margin of rigidity and verification of bearing capacity.

The maximum loads corresponding to the onset of ULS and SLS obtained during numerical simulation are shown in Table 3.

Table 3. Values of loads corresponding to the onset of ULS and SLS.

Panel thickness, mm	Maximum value q_{ULS} , kg/m ²	Maximum value $q_{SLS, SF}$, kg/m ²
8	158.8	129.1
10	255.9	253.4

Existing researches, which were found and analyzed by authors within this study, did not have comprehensive information regarding stress-strain state of considered element under consimilar parameters and therefore final results could not be compared, however the design methods and main principles of calculation in accordance with Limit State design remain analogous.

4. Conclusions

FCBs fastened to the metal supporting frame of curtain wall system by exhaust rivets were analyzed within this study. The results obtained through experiments and numerical simulation allow to draw following conclusions:

1. Onset of Serviceability Limit State is critical verification for the design of the investigated type of FCBs.
2. A distance between fastening elements of FCBs equal to 750 mm and an edge distance of 30 mm are acceptable parameters in accordance with requirements arising from Ultimate Limit State design.
3. Onset of Ultimate Limit State is characterized by appearance of cracks due to the stresses in the panel exceeding the value of flexural strength in the area of fastening to curtain wall frame.
4. The profiles of the curtain wall system significantly affect performance of cladding panels and act as stiffening ribs of the FCB.
5. Linear formulation of Finite Element Method with careful consideration of boundary conditions can be used for determination of stress-strain state of FCBs.
6. The numerical calculation method provides a margin in verification of bearing capacity.
7. Accurate assessment of stress-strain state of both the cladding panel and the system as a whole requires calculation and accounting the stiffness of the joint between subframe and supporting bracket.
8. The stress-strain state of the cladding panel depends on the chosen frame of curtain wall system and its rigidity; therefore, cladding panels must be tested as a part of the system.

5. Acknowledgement

The research group would like to thank companies LATONIT and NordFOX for providing the samples of fiber cement boards and curtain wall system respectively.

References

1. Mohr, B.J., El-Ashkar, N.H., Kurtis, K.E. Fiber-cement composites for housing construction: State-of-the-art review. Proceedings of the NSF Housing Research Agenda Workshop. Orlando, 2004. Pp. 112–128.
2. Mukhametrakhimov, R., Lukmanova, L. The Modified Fiber Cement Panels for Civil Construction. *Advances in Intelligent Systems and Computing*. 2018. No. 692. Pp. 852–858. DOI: 10.1007/978-3-319-70987-1_91
3. Lukmanova, L.V., Mukhametrakhimov, R.K., Gilmanshin, I.R. Investigation of mechanical properties of fiber-cement board reinforced with cellulosic fibers. *IOP Conference Series: Materials Science and Engineering*. 2019. 570 (1). DOI: 10.1088/1757-899X/570/1/012113
4. Mukhametrakhimov, R.Kh., Izotov, V.S. Povysheniye fiziko-mekhanicheskikh svoystv i dolgovechnosti fibrotsementnykh plit na osnove tsellyuloznykh volokon [Improvement of physico-mechanical properties and durability of fiber cement boards based on cellulose fibers]. *Izvestiya vuzov. Stroitelstvo*. 2012. No. 9. Pp. 101–107. (rus)
5. Sonphuak, W., Rojanarowan, N. Strength improvement of fibre cement product. *International Journal of Industrial Engineering Computations*. 2013. 4 (4). Pp. 505–516. DOI: 10.5267/j.ijiec.2013.06.004
6. ACI Committee 544. "State-of-the-Art Report on Fiber Reinforced Concrete". American Concrete Institute. 1973. 70 (11). Pp. 729-744.
7. Melcher, J., Karmazinová, M., Pilgr, M. Evaluation of strength characteristics of fibre-cement slab material. *Advanced Materials Research*. 2013. No. 650. Pp. 320–325. DOI: 10.4028/www.scientific.net/AMR.650.320
8. Gorzelańczyk, T., Schabowicz, K. Effect of freeze-thaw cycling on the failure of fibre-cement boards, assessed using acoustic emission method and artificial neural network. *Materials*. 2019. 12 (13). DOI: 10.3390/ma12132181
9. Ranachowski, Z., Ranachowski, P., Debowski, T., Gorzelańczyk, T., Schabowicz, K. Investigation of structural degradation of fiber cement boards due to thermal impact. *Materials*. 2019. 16 (6). DOI: 10.3390/ma12060944
10. Jamshidi, M., Pakravan, H.R., Pacheco-Torgal, F. Assessment of the Durability Performance of Fiber-Cement Sheets. *Journal of Materials in Civil Engineering*. 2013. 25 (6). Pp. 819–823. DOI: 10.1061/(ASCE)MT.1943-5533.0000637
11. Adamczak-Bugno, A., Swit, G., Krampikowska, A. Assessment of Destruction Processes in Fibre-Cement Composites Using the Acoustic Emission Method and Wavelet Analysis. *IOP Conference Series: Materials Science and Engineering*. 2019. 471 (3). DOI: 10.1088/1757-899X/471/3/032042
12. Kondratyeva, N.V. Prochnost i deformativnost konstruktsiy iz listovogo stekla pri poperechnom izgibe ravnomerno raspredelennoy nagruzkoy [Strength and deformability of sheet glass structures under transverse bending by uniformly distributed load]. PhD Thesis. Samara State University of Architecture, Building and Civil Engineering. 2010. 176 p. (rus)
13. Galyamichev, A.V., Alkhimenko, A.I. Design features of facade cassettes from thin ceramics. *Magazine of Civil Engineering*. 2017. 69 (1). Pp. 64–76. DOI: 10.18720/MCE.69.6

14. Schmid, P., Daněk, P., Rozsypalová, I., Holomek, P., Juránek, P. Assessment of the resistance of ventilated facade system by vacuum testing. IOP Conference Series: Materials Science and Engineering. 2019. 549 (1). DOI: 10.1088/1757-899X/549/1/012034
15. Antonov, A.S., Shmelev, G.N., Sabitov, L.S., Kashapov, N.F., Galimullin, I.A. Study of the real work of constructions of translucent facade systems. IOP Conference Series: Materials Science and Engineering. 2019. 570 (1). DOI: 10.1088/1757-899X/570/1/012006
16. Galyamichev, A.V. Spetsifika opredeleniya nagruzok na ograzhdayushchiye konstruksii i yeye vliyaniye na rezultaty ikh staticheskogo rascheta [Specifics of determining loads on building envelopes and its effect on the results of static calculation]. Internet-zhurnal «NAUKOVEDENIE». 2015. 2 (27). (rus). DOI: 10.15862/54TVN215
17. Galyamichev, A.V. Vetrovaya nagruzka i yeye deystviye na fasadnyye konstruksii. Stroitelstvo unikalnykh zdaniy i sooruzheniy [Wind load and its effect on facade structures]. 2017. 9 (60). Pp. 44–57. (rus). DOI: 10.18720/CUBS.60.4
18. Lalin, V.V., Rybakov, V.A. The finite elements for design of building walling made of thin-walled beams. Magazine of Civil Engineering. 2011. 26 (8). Pp. 69–80. (rus). DOI: 10.5862/MCE.26.11
19. Rybakov, V.A., Kozinets, K.G., Vatin, N.I., Velichkin, V.Z., Korsun, V.I. Lightweight steel concrete structures technology with foam fiber-cement sheets. Magazine of Civil Engineering. 2018. 82 (6). Pp. 103–111. DOI: 10.18720/MCE.82.10
20. Ivanova, E., Strakhov, D., Sinyakov, L., Zimin, S. Joint work of steel floor beams and vaults. Construction of Unique Buildings and Structures. 2018. 10 (73). Pp. 7–15. DOI: 10.18720/CUBS.73.1

Contacts:

Denis Egorov, egorov.dv@edu.spbstu.ru

Alexander Galyamichev, gav@spbstu.ru

Ekaterina Gerasimova, katyageras17@gmail.com

Dmitrijs Serdjuks, Dmitrijs.Serdjuks@rtu.lv

© Egorov, D., Galyamichev, A., Gerasimova, E., Serdjuks, D., 2020



DOI: 10.18720/MCE.97.10

The effect of the air duct tightness on the stability of the indoor air parameters

A. Prozuments^a, A. Borodinecs^a, J. Zemitis^a, K.I. Strelets^b

^a Riga Technical University, Riga, Latvia

^b Peter the Great St. Petersburg Polytechnic University, St. Petersburg, Russia

* E-mail: aleksejs.prozuments@rtu.lv

Keywords: air duct tightness, air quality, ventilation, HVAC, energy efficiency

Abstract. The present study aimed to determine the impact of a gradual and lineal increase of the air duct leakage factor on various indoor air stability parameters in ventilation systems across the following scenarios: 1) air leakage effect on the air pressure and volume; 2) air leakage effect on the indoor air parameters when the ductwork passes through an uninsulated and unheated premise. A galvanized steel air duct was used for the air leakage measurement sessions, and orifices were cut in the duct before each subsequent measurement session, thus, consecutively decreasing the air tightness factor of the duct over the measurement sessions. The results indicated that the ductwork air tightness affects the stability of the air parameters such as air temperature, relative humidity and CO₂ concentration, however, up until certain point, the impact was either non-detectable or negligible. The transition in the behavior of the air stability parameters occurred in line with the introduction of orifices 4→5, resulting in perceptible effects on air pressure, volume etc. Although, this factor may be attributed to the errors caused by low instrument sensitivity or by relatively small number and size of the orifices, authors suggest that minor air duct leakage such as presented in this study may result in the disruption of air stability parameters, which in certain instances is critical.

1. Introduction

The goal of the ventilation air ductwork is to transport the fresh air mass to ensure the required indoor air quality parameters in buildings' premises. The efficiency of the air transportation in the duct depends on the three main factors:

1. the cross-sectional shape of the duct (usually round or square ducts);
2. the material the duct is made of (galvanized steel, aluminum zinc, corrugated plastic, fabric etc.);
3. the pressure losses (velocity and friction losses).

However, to ensure that a ventilation system operates properly and maintains the required air parameters, it is of great importance to pay particular attention to the quality of the air ductwork installation and connection. Even minor permanent air leakage from the ductwork may affect the operation of the whole ventilation system and its long term efficiency, if it's not detected or not taken care of. There are number of factors, why leaking air ducts negatively affect the operation of the ventilation system and occupants' well-being.

Reduction of the air tightness in the ducts has a negative effect on the overall operation of the ventilation system, as the ventilation system becomes difficult to operate and control, due to numerous discrepancies between the designed and the actual air volume the system is supposed to transport and deliver.

Also, due to air leakage in the ducts, the fans in the air handling units have to operate at higher loads which leads the system to be inefficient, as the fans have to operate at higher capacity and consume more energy to deliver the same amount of air to the premises. This translates into a significant increase in energy costs [1], [2]. For instance, the energy consumption to run fans in the system with ductwork airtightness class C is up to 30 % higher than that of the class A [3]. As per the case study conducted for a pharmaceutical plant,



where ductwork airtightness is imperative, the associated costs of the excessive air leakage in the ductwork would come out to over 1 million USD over the life cycle of the plant [4].

On the other hand, if the air leakage in the ductwork occurs, and the fans are not equipped with frequency converters (employed mainly in demand controlled ventilation systems such as CAV, DCV and VAV) to operate at higher capacity in order to compensate for the leaked air volume [5], the premises will experience the shortage of fresh air supply, therefore incurring deterioration of the indoor air quality (IAQ) and subsequent health concerns associated with the poor IAQ [6].

In addition, leaking air ducts may cause serious health hazard where maintaining strictly controlled environment is of utmost importance [7], [8]. In improperly installed and/or leaking air duct systems, exhaust air can leak into the supply air, causing unpleasant smells or even exposure to polluted air and poisonous gaseous particles [9], [10]. This applies to healthcare facilities, industrial kitchens, pharmaceutical factories etc.

If an uninsulated and leaking air duct passes through an unheated space, condensation may occur where the air leakage takes place, causing moisture build-up [11], [12] that in the long-term can deteriorate construction materials [13], [14] and induce mold growth that is known to have adverse effects on human's respiratory system [15], [16].

Another issue that stems from poor tightness of the air ductwork is the excessive heat loss [2], [3], [17], which greatly impacts energy consumption for the heat transfer in the ventilation systems' heat exchanger coils [18].

As such, it is critically important to comply with the air duct tightness criteria when it comes to design and, more so, installation of ventilation system ductwork. Furthermore, regular system monitoring serves to detect the occurrence and potential sources of air leakage, and subsequently prevents the excessive energy consumption [19] and poor indoor air quality the building occupants may be exposed to [20].

This study aims to determine the impact of a gradual and lineal increase of the air duct leakage factor on the various parameters in ventilation systems across the following scenarios:

- scenario 1 – effect on the ventilation system operational characteristics (with regards to air pressure and air volume);
- scenario 2 – effect on the indoor climate parameters (when leaking air duct passes through an uninsulated and unheated premise);

The current study contributes to an existing knowledge on the adverse impact of ventilation system air duct leakage on the energy efficiency and indoor air quality (IAQ) however, it also presents a full-scale test approach by looking into two different scenarios and assessing the air leakage impact factor by increasing the leakage degree linearly and in gradual increments.

2. Methods

A galvanized steel air duct of 3.25 m in length and 125 mm in diameter was used for the air leakage measurement sessions, referred to as the "leaking duct". An orifice of 6 mm in diameter was cut in the duct before each subsequent measurement session, thus, consecutively decreasing the air tightness factor of the duct. In total 11 measurements were carried out for each scenario, resulting in 11 orifices at the last measurement session.

Scenario-1

The "leaking air duct" test system was set up in a specially designed test chamber. The air temperature in the test chamber was kept at +22.8 °C and the relative air humidity was kept at 19.7%. Air was blown into the duct by a duct fan. Air pressure differential was measured on the air damper and an air flow rate was measured at the outlet end of the duct during each measurement session.

Scenario-2

The "leaking air duct" was placed into the test chamber which represented a dry, unheated, uninsulated and non-residential premise without active heat loads (such as storage space or auxiliary room). An air stream of RH 50–55 % was blown into the air duct – the relative air humidity, temperature and carbon dioxide concentration (ppm) were measured in the test chamber throughout the session. Based on the results, the effect of the airduct tightness on the indoor climate of the premise it passes through was determined.

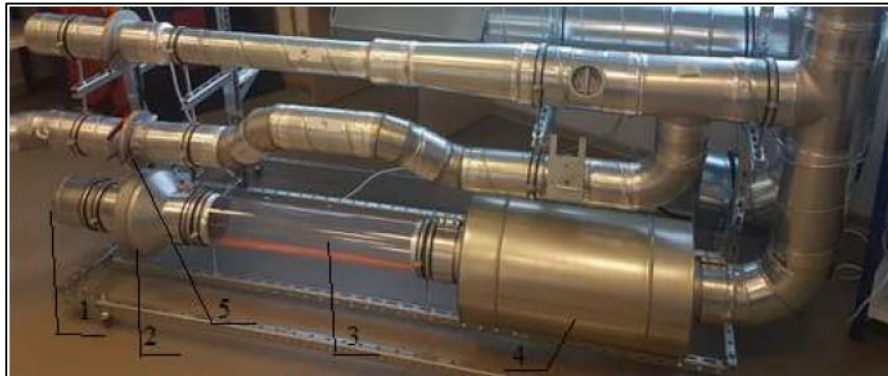
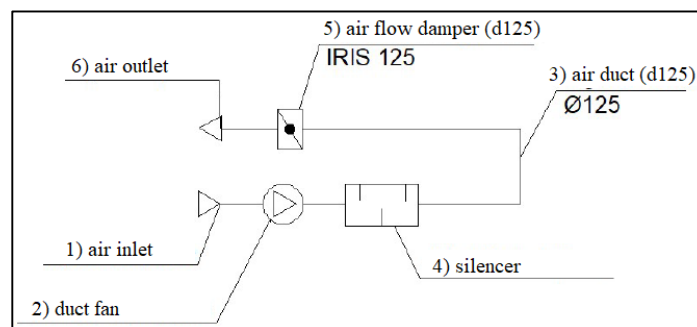
Scenario-1

The aim of scenario-1 was to determine the effect of air duct tightness on the ventilation system's pressure and air volume. For this purpose, a ductwork system shown in Fig. 1 was setup.

Table 1. Parameters of the tested “leaking” air duct.

Length, mm	Diameter, mm	Thickness, mm	Surface area, m ²	Orifice diameter, mm	Number of orifices
3250	125	0.7	1.28	6	1-11 *

* The orifices in the air duct were cut by an increment of 1 orifice for every subsequent measurement, i.e., 1 extra orifice added for each additional measurement, resulting in total of 11 orifices after 11 measurements.

**Figure 1. A ductwork system setup for scenario-1 (see the corresponding legend in Figure 2).****Figure 2. The schematic design of the test setup.**

Scenario-2

In the following scenario, a condition of the leaking air duct passing through an unheated premise was tested, to see how a leaking air duct affects indoor parameters such as air temperature and relative humidity of the premise, if these parameters differ in the both environments (i.e., air duct and the test chamber). To carry out the measurements within the current scenario, the air duct was placed in a test chamber, that represented an unheated, uninsulated and non-residential premise (Fig. 3).

A question to be answered after the completion of the measurements and analysis of the test results: Is there a risk of mold development due to an excessive moisture build up in an unheated premise by an air leakage from a ductwork?

Table 2. Geometric parameters of the test chamber.

Length, m	Width, m	Height, m	Volume, m ³
3.34	2.5	3.0	25.05

**Figure 3. The system setup for scenario-2 (test chamber).**

The procedure of adding orifices in the leaking air duct was similar to the procedure outlined in scenario-1. As such, 11 measurements were conducted. The test chamber air quality parameters before the test run are shown in Table 3.

Table 3. Air quality parameters of the test chamber.

Temperature, °C	Relative humidity, %	CO ₂ concentration
22.8	19.7	877

3. Results and Discussion

Scenario-1

The results for scenario-1 are compiled in Table 4.

Table 4. Results for scenario-1.

Sample #	Number of orifices	Total relative orifice diameter, mm	System pressure, Pa	Air volume, l/s
1	1 x 6 mm	6	155	19
2	2 x 6 mm	12	155	19
3	3 x 6 mm	18	155	19
4	4 x 6 mm	24	155	19
5	5 x 6 mm	30	128	17
6	6 x 6 mm	36	127	17
7	7 x 6 mm	42	125	17
8	8 x 6 mm	48	122	17
9	9 x 6 mm	54	121	17
10	10 x 6 mm	60	119	16
11	11 x 6 mm	66	118	16

The measurement results show that the system's pressure remains constant at 155 Pa until the fifth orifice is introduced in the air duct. At this point the pressure drops down to 128 Pa, and every subsequently added orifice induces further pressure drop, yet, at a very gradual and steady decline rate. The absolute pressure drop throughout the whole measurement section within scenario-1 is 33 Pa, however, the diagram can be divided into three separate segments – first (orifice 1→4) at which the pressure drop is not affected and thus remains constant value; second (orifice 4→5) with a steep pressure drop decrease when the fifth orifice is added; and third (orifice 5→11), throughout which pressure drops gradually in line with subsequent addition of orifices.

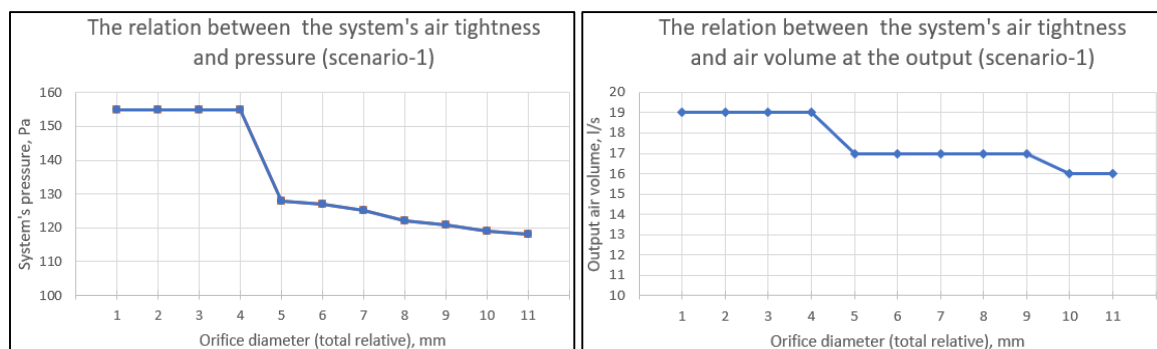


Figure 6. The system's pressure dependence (on the left) and the output air volume dependence (on the right) on the air duct tightness.

A similar pattern is observed with regards to the air volume at the outlet. Air volume remains at 19 l/s, however, once the fifth orifice is introduced, the air volume drops to 17 l/s. Subsequent addition of orifices did not affect the air volume at the provided instrument accuracy (the flowmeter of ± 1.0 l/s accuracy was employed) until the tenth orifice was introduced, that caused a very slight air volume decrease to 16 l/s. As per the results, throughout the whole measurement section (after creation of 11 orifices in the air duct), the absolute air volume decrease was almost negligible ($\Delta q = 3$ l/s).

The results of scenario-1 imply that on a broader scale and in ventilation systems with large ductwork surface area, the air tightness is of critical importance. With compromised air tightness, the end user doesn't

receive the designed air volume (Fig. 6), as the air pressure is not sufficient enough to transport and deliver the required air mass to the end-user.

Insufficient air volume, i.e., insufficient supply of fresh air into the premise causes an increase in carbon dioxide concentration, compromises the indoor air quality and leads to overall deterioration and occupant dissatisfaction with the indoor climate [21].

In case of CAV (constant air volume) systems, the frequency converter will increase fan output to keep the constant air pressure in the system and to ensure the delivery of sufficient amount of air to the end user, however, this results in an increase in energy consumption and thus, lower, system's energy efficiency [22], [23]. Poor ductwork air tightness also affects noise level in the ductwork and at the output terminals [24].

Scenario-2

Scenario-2 was run to determine how a poorly tight air ductwork affects the indoor climate of the premise it passes through. The leaking air duct was installed in an unheated and uninsulated chamber that represents a non-residential premise such as storage space or auxiliary room. Within this scenario the major indoor air quality parameters such as air temperature, relative humidity and carbon dioxide concentration were monitored in the test chamber throughout the 11-sample measurement session. The measurement results for scenario-2 are presented in Table 5.

Table 5. Results for scenario-2.

Sample #	Number of orifices	Total relative orifice diameter, mm	Relative humidity, %	Air temperature, °C	CO ₂ conc., ppm
1	1 x 6 mm	6	19.7	22.8	877
2	2 x 6 mm	12	19.7	22.8	877
3	3 x 6 mm	18	19.7	22.8	877
4	4 x 6 mm	24	19.7	23.0	877
5	5 x 6 mm	30	20.2	23.3	882
6	6 x 6 mm	36	21.0	23.4	1009
7	7 x 6 mm	42	21.2	23.4	1077
8	8 x 6 mm	48	21.7	23.5	1149
9	9 x 6 mm	54	22.2	23.7	1234
10	10 x 6 mm	60	22.6	23.8	1284
11	11 x 6 mm	66	22.9	23.9	1351

stable range

non-stable

Fig. 7 shows that scenario-2 developed a similar pattern to scenario-1 – no change in the air stability parameters until the introduction of the fifth orifice in the air duct. As the air duct tightness is being decreased further (orifice 5→11), the air temperature and relative humidity in the room increase at a steady growth pattern. This again shows that up until the fourth orifice in the air duct, the overall big picture impact on the air tightness is somewhat negligible, while with the introduction of the fifth orifice and onwards (5→11), the air stability parameters are being affected steadily.

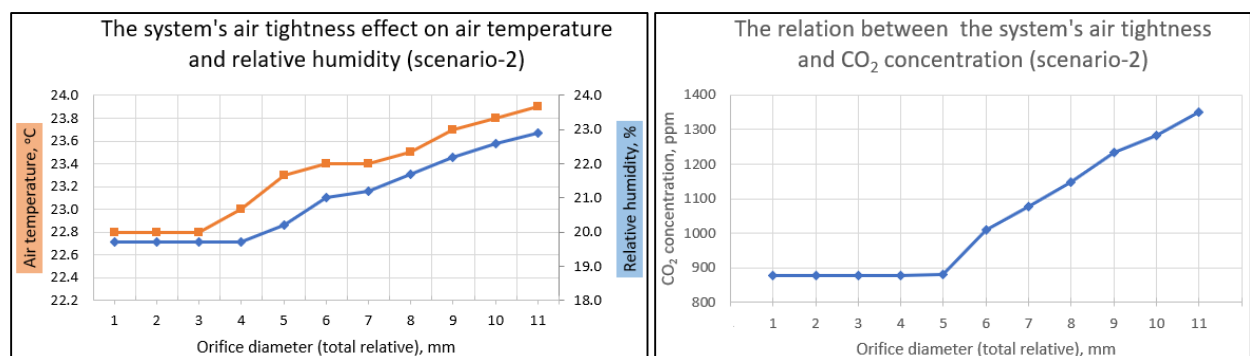


Figure 7. The air temperature and relative humidity dependence on the air duct tightness (on the left); The CO₂ concentration dependence on the air duct tightness (on the right).

The CO₂ concentration (Fig. 7. on the right) in the test chamber can be broken down to three development segments:

1. CO₂ concentration remains constant at 877 ppm throughout the introduction of orifices 1→4;
2. After the fifth orifice (5) is introduced, the CO₂ level rises insignificantly (884 ppm);

3. Throughout the creation of orifices 6→11, the CO₂ concentration increases continuously to reach 1351 ppm at the last sample.

The results show that ductwork air tightness affects the stability of the air parameters such as air temperature, relative humidity and CO₂ concentration, however, up until a certain point, the impact is either non-detectable or negligible. This suggests that a higher accuracy instruments are used in order to obtain a more accurate and detailed dataset. On the other hand, it is highly probable that orifices of 6 mm in size are relatively small to affect the instrument readings regardless of their accuracy or sensitivity, and, thus, there is no detectable effect on the system's operation and behavior, suggesting that some level of air duct leakage is always present and acceptable for that matter, and does not affect the system's operation in the long run [25], [26]. This correlates with a common understanding that no system is perfect and there is always some degree of system malfunction or drawback present. In order to obtain somewhat perceptible readings, either the orifice diameter has to be larger, or the number of orifices has to be higher (as in the current case).

Nevertheless, in the pursuance of the objectives established within the framework of the current study, the accuracy of the carried measurements is reasonably adequate and acceptable to infer broader conclusions relating to impacts on the systems' operating at bigger scale.

4. Conclusions

The study results contribute to the existing knowledge of an adverse effects on the energy efficiency and the IAQ parameters of a poor air duct tightness in ventilation systems. Within the frame of this study indoor air parameters such as air volume, pressure, temperature, relative humidity, CO₂ concentration and mineral-wool particle presence in supplied air stream were measured.

As per scenarios 1 and 2, a certain pattern of a stable and a non-stable range developed with regards to the measured air parameters. Introducing small size orifices of 6 mm in the ductwork did not trigger a detectable response in the indoor air quality parameters throughout the measurement sessions 1→4 (matching the number of orifices cut in the air duct). Perhaps this can be attributed to the lower-tier sensitivity and accuracy of the instruments used to measure air volume and pressure. However, in line with further increasing the number of orifices in the air duct (orifices 5→11), a gradual yet steady change in the indoor air parameters was observed (non-stable range). As per the presumptions, an increased air leakage factor translated in a lower pressure in the system and decreased air volume supplied to the end-user (scenario-1), while also adversely affecting air stability parameters when a leaked duct was placed in a test chamber representing an unheated non-residential premise (scenario-2). The IAQ parameter behavior throughout the creation of orifices 5→11 is rather an expected outcome. On the contrary, the system's unresponsive behavior throughout the introduction of orifices 1→4 is a rather peculiar finding. Authors suggest that the following factors may affect this: 1) low instrument sensitivity, unable to detect such an insignificant change in air pressure and volume; 2) orifices of 6 mm in size do not generate enough air leakage in the duct to cause reasonable fluctuation in air stability parameters up to a certain degree (in this study – up until the introduction of the forth orifice).

The results indicate that the ductwork air tightness affects the stability of the air parameters such as air temperature, relative humidity and CO₂ concentration, however, up until a certain point, the impact is either non-detectable or negligible. This suggests that a higher accuracy instruments have to be used in order to obtain a more accurate and detailed dataset. Also, decreasing the orifice diameter and increasing the number of orifices might present a better picture on how the air stability parameters are affected if an air tightness decrease occurs at very gradual increments across a multitude of measurements.

5. Acknowledgment

This study was supported by European Regional Development Fund project No.1.1.1.1/16/A/048 "Nearly Zero Energy Solutions for Unclassified Buildings".

NATIONAL
DEVELOPMENT
PLAN 2020



EUROPEAN UNION
European Regional
Development Fund

INVESTING IN YOUR FUTURE

References

1. Leprince, V., Carrié, F.R. Impact of ductwork airtightness on fan energy use: Calculation model and test case. *Energy and Buildings*. 2018. 176. Pp. 287–295. DOI: 10.1016/j.enbuild.2018.07.029
2. Soenens, J., Pattijn, P. Feasibility study of ventilation system air-tightness. 32th AIVC Conference. Towards Optimal Airtightness Performance, Brussels, Belgium (2011). 2011. Pp. 51–54.
3. Berthault, S., Boithias, F., Leprince, V. Ductwork airtightness: reliability of measurements and impact on ventilation flowrate and fan energy consumption. 35th Aivc-4 Th Tightvent & 2nd Venticool Conference, 2014. 2014. Pp. 478–487.

4. Dyer, D.F. Case study: effect of excessive duct leakage in a large pharmaceutical plant. 32th AIVC Conference. Towards Optimal Airtightness Performance. 2011. Pp. 55–56.
5. Aydin, C., Ozerdem, B. Air leakage measurement and analysis in duct systems. *Energy and Buildings*. 2006. 38 (3). Pp. 207–213. DOI: 10.1016/j.enbuild.2005.05.010
6. Fernández-Agüera, J., Domínguez-Amarillo, S., Alonso, C., Martín-Consuegra, F. Thermal comfort and indoor air quality in low-income housing in Spain: The influence of airtightness and occupant behaviour. *Energy and Buildings*. 2019. 199. Pp. 102–114. DOI: 10.1016/j.enbuild.2019.06.052
7. Tang, J.W., Li, Y., Eames, I., Chan, P.K.S., Ridgway, G.L. Factors involved in the aerosol transmission of infection and control of ventilation in healthcare premises. 64 (2) 2006.
8. Preusche, R., Böhlmann, S., Ecke, H., Gampe, U. Comparison of data-based methods for monitoring of air leakages into oxyfuel power plants. *International Journal of Greenhouse Gas Control*. 2011. 5 (SUPPL. 1). DOI: 10.1016/j.ijggc.2011.05.024
9. Kim, S., Yang, H. Estimation of leakage rate of air from a fume hood in a radioisotope laboratory using CFD simulations. *Applied Radiation and Isotopes*. 2018. 140. Pp. 300–304. DOI: 10.1016/j.apradiso.2018.07.021
10. Han, O., Li, A., Kosonen, R. Hood performance and capture efficiency of kitchens: A review. 1612019.
11. Moon, H.J., Ryu, S.H., Kim, J.T. The effect of moisture transportation on energy efficiency and IAQ in residential buildings. *Energy and Buildings*. 2014. 75. Pp. 439–446. DOI: 10.1016/j.enbuild.2014.02.039
12. Šadauskienė, J., Šeduikyte, L., Paukštys, V., Banionis, K., Gailius, A. The role of air tightness in assessment of building energy performance: Case study of Lithuania. *Energy for Sustainable Development*. 2016. 32. Pp. 31–39. DOI: 10.1016/j.esd.2016.02.006
13. Kreiger, B.K., Srubar, W. V. Moisture buffering in buildings: A review of experimental and numerical methods. 2022019.
14. Morishita, C., Berger, J., Mendes, N. Weather-based indicators for analysis of moisture risks in buildings. *Science of the Total Environment*. 2020. 709. DOI: 10.1016/j.scitotenv.2019.134850
15. Mendell, M.J., Mirer, A.G., Cheung, K., Tong, M., Douwes, J. Respiratory and allergic health effects of dampness, mold, and dampness-related agents: A review of the epidemiologic evidence. 119 (6) 2011.
16. Hernberg, S., Sripaiboonkij, P., Quansah, R., Jaakkola, J.J.K., Jaakkola, M.S. Indoor molds and lung function in healthy adults. *Respiratory Medicine*. 2014. 108 (5). Pp. 677–684. DOI: 10.1016/j.rmed.2014.03.004
17. Petrichenko, M.R., Nemova, D. V., Kotov, E. V., Tarasova, D.S., Sergeev, V. V. Ventilated facade integrated with the HVAC system for cold climate. *Magazine of Civil Engineering*. 2018. 77 (1). Pp. 47–58. DOI: 10.18720/MCE.77.5
18. Tanyer, A.M., Tavukcuoglu, A., Bekboliev, M. Assessing the airtightness performance of container houses in relation to its effect on energy efficiency. *Building and Environment*. 2018. 134. Pp. 59–73. DOI: 10.1016/j.buildenv.2018.02.026
19. Schibuola, L., Scarpa, M., Tambani, C. Performance optimization of a demand controlled ventilation system by long term monitoring. *Energy and Buildings*. 2018. 169. Pp. 48–57. DOI: 10.1016/j.enbuild.2018.03.059
20. Geikins, A., Borodinecs, A., Daksa, G., Bogdanovics, R., Zajecs, D. Typology of Unclassified Buildings and Specifics of Input Parameters for Energy Audits in Latvia. *IOP Conference Series: Earth and Environmental Science*. 2019. 290 (1). DOI: 10.1088/1755-1315/290/1/012131
21. Hong, T., Kim, J., Lee, M. Integrated task performance score for the building occupants based on the CO₂ concentration and indoor climate factors changes. *Applied Energy*. 2018. 228. Pp. 1707–1713. DOI: 10.1016/j.apenergy.2018.07.063
22. Merema, B., Delwati, M., Sourbron, M., Breesch, H. Demand controlled ventilation (DCV) in school and office buildings: Lessons learnt from case studies. *Energy and Buildings*. 2018. 172. Pp. 349–360. DOI: 10.1016/j.enbuild.2018.04.065
23. Delwati, M., Merema, B., Breesch, H., Helsen, L., Sourbron, M. Impact of demand controlled ventilation on system performance and energy use. *Energy and Buildings*. 2018. 174. Pp. 111–123. DOI: 10.1016/j.enbuild.2018.06.015
24. Liu, Y., Dong, Y., Zhao, L. Comparison of Noise Calculation Methods of Air Conditioning Duct System used in China and USA. *Procedia Engineering*. 2017. 205. Pp. 1592–1599. DOI: 10.1016/j.proeng.2017.10.278
25. Walker, I.S. Distribution system leakage impacts on apartment building ventilation rates. *ASHRAE Transactions*. 1999. 105.
26. Guyot, G., Ferlay, J., Gonze, E., Woloszyn, M., Planet, P., Bello, T. Multizone air leakage measurements and interactions with ventilation flows in low-energy homes. *Building and Environment*. 2016. 107. Pp. 52–63. DOI: 10.1016/j.buildenv.2016.07.014

Contacts:

Aleksejs Prozuments, aleksejs.prozuments@rtu.lv

Anatolijs Borodinecs, anatolijs.borodinecs@rtu.lv

Jurgis Zemitis, jurgis.zemitis@rtu.lv

Kseniya Strelets, kstrelets@mail.ru

© Prozuments, A, Borodinecs, A.B, Zemitis, J., Strelets, K.I., 2020



DOI: 10.18720/MCE.97.11

Assessment of the tornado impact on the Chernobyl new safe confinement

A.V. Perelmuter

Scientific and Production Company «SCAD Soft» Ltd., Kiev, Ukraine

E-mail: anatolyperelmuter@gmail.com

Keywords: design-basis tornado wind speed, Fujita scale, Rankine combined vortex model, nuclear plant

Abstract. All the nuclear facility structures must be analyzed for tornado loads. This analysis was performed when designing the New Safe Confinement over the ruined Chernobyl power unit (NSC ChNPP). The standard methods of tornado analysis could not be applied due to its large size and geometric shape. Therefore, it was necessary to develop new calculation methods. The paper provides detailed information on the performed calculations and describes the conservative assumptions made when there was not enough information. The purpose of this paper is to analyze the gained experience of performing such an analysis of this unique structure, which may be of some interest. The following two complex problems are considered: • establishing the design tornado parameters; • developing an engineering methodology for the tornado analysis. Moreover, questions are formulated that should be clarified when carrying out similar designs.

1. Introduction

The recently completed New Safe Confinement of the Chernobyl Nuclear Power Plant [1, 2] is a large-scale engineering structure with a span of 257 m and a height of 108 m (Fig. 1). This structure was designed in accordance with special technical specifications which required an analysis for the possible tornado impact, and the results had to satisfy both European and national standards.

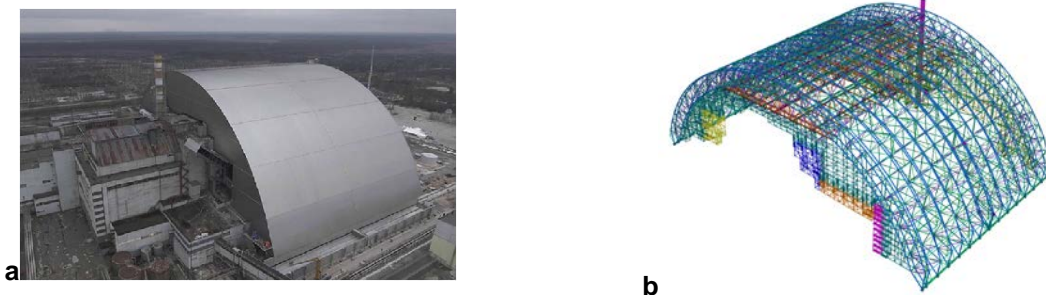


Figure 1. The New Safe Confinement: a – general view, b – design model.

A tornado is characterized by a vortex wind flow [3–6]. Therefore, experimental data gathered from wind tunnels generating straight-line winds could not be applied. Special laboratory wind flow simulators are used to study the tornado effect [7, 8]. However, there are only a few of them and almost all such experimental studies were performed for relatively small buildings not larger than the tornado core (see, for example [9–12]). The results of these studies could not be directly used for the considered large-scale structure as well.

The number of publications on the experience of tornado analysis of larger structures such as [13–21] is extremely small. The design data for these structures could hardly be of any use since they are specific to particular facilities with geometric configurations very different from those of the NSC ChNPP. These structures include main NPP buildings [15, 19, 20], cooling towers [21], lattice transmission towers [16, 17]. More general issues of the tornado analysis methodology considered, for example, in [4, 6, 15, 20], are closely related only to the standard main NPP buildings. Therefore, when performing the analysis for NSC ChNPP, it was necessary to postulate some characteristics of the wind flow making careful conservative decisions.



2. Methods

2.1. Expected tornado class

The safety guide [22] regulating the tornado-induced loads on nuclear facilities uses the Fujita-Pearson scale [23, 24] to classify tornadoes, which is a combination of the Fujita scale for wind speeds and the Pearson scale for path length and width.

The lower limit of Pearson path length L is:

$$L = 1.609 \times 100.5^{(k-1)}, \quad (1)$$

where k is the Fujita-Pearson scale, L is in kilometers.

The path width is the average width of the damage area measured perpendicular to the tornado path. The lower limit of Pearson path width W (in kilometers) is expressed as:

$$W = 1.609 \times 10^{0.5(k-5)}, \quad (2)$$

Unlike [22], the relationships between other tornado parameters and the tornado class were taken not discrete but continuous, as recommended in [13]. The rotational speed V_m , the translational speed of the tornado T and the pressure drop from a normal atmospheric pressure to the center of the tornado vortex Δp_X are defined by the F_k scale of a tornado and the following formulas:

$$V_m = 6.3(k + 2.5)^{1.5} \text{ m/sec}, \quad (3)$$

$$T = 1.575(k + 2.5)^{1.5} \text{ m/sec}, \quad (4)$$

$$\Delta p_m = 0.486(k + 2.5)^3 \text{ GPa}. \quad (5)$$

Recommendations [25] define the annual probability that a point in the local region will experience a wind speed greater than or equal to the winds in the F -scale intensity class k as the joint probability that a tornado passes through this region and its intensity is not lower than F_k :

$$P = P_S (1 - F_k). \quad (6)$$

P_S is defined as the ratio of the damage area S to the product of the survey area A by the period of record T :

$$P_S = \frac{S}{A \cdot T}, \quad (7)$$

and F_k in (6) denotes the integral probability distribution function for tornadoes of various classes, which, by assumption, corresponds to an exponential law. The parameters of this distribution were determined by minimizing the standard deviation of the observed data from the specified theoretical curve.

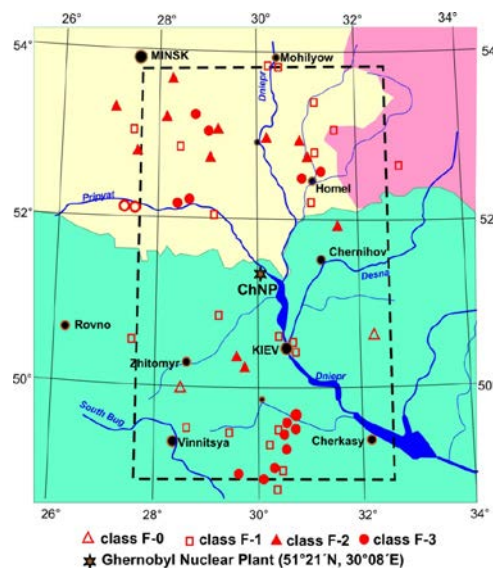


Figure 2. Map of recorded tornadoes.

According to the IAEA safety guide [22] a typical region used to evaluate the design-basis tornado is 3° longitude by 3° latitude, but the initial information for the Chernobyl NPP was taken for the 5°×5° geographic square (Fig. 2). Other geographic squares were considered as well (see Table 1). After analyzing the obtained results (see Table 1), the tornado of class 3 was conservatively selected as a design action. It is characterized by the following data calculated by the formulas (3), (4) and (5): $R_m = 59.0$ m, $T = 20.3$ m/s, $V_m = 81.2$ m/s, $W = 286.1$ m.

Table 1. The effect of the dimensions of the studied area.

Geographic square	2°×2°	3°×3°	4°×4°	5°×5°
Damage area S_0 , km ²	0.000	0.012	0.024	0.037
Damage area S_1 , km ²	0.747	0.996	1.742	2.24
Damage area S_2 , km ²	0.000	4.072	7.329	8.958
Damage area S_3 , km ²	8.183	24.55	73.65	114.567
Total damage area S , km ²	8.93	29.63	82.746	125.80
Probability P_S , 1/year	$6.872 \cdot 10^{-6}$	$8.03 \cdot 10^{-6}$	$1.133 \cdot 10^{-5}$	$9.86 \cdot 10^{-6}$
F -class with probability $P_0 = 1 \cdot 10^{-7}$	3.32	2.79	2.86	2.90
F -class with probability $P_0 = 1 \cdot 10^{-6}$	3.20	2.74	2.83	2.86
F -class with probability $P_0 = 1 \cdot 10^{-5}$	–	–	2.00	–

2.2. Confinement load

The spatial distribution of wind speeds was taken in the form of a Rankine vortex, where the rotational speed is determined by the following formula:

$$V = \frac{r}{R_m} V_m (0 \leq r \leq R_m), \quad V = \frac{R_m}{r} V_m (R_m \leq r < \infty), \quad (8)$$

where V_m is the maximum tangential velocity; R_m is the tornado core radius with the velocity V_m .

The air rarefaction load at a point at the distance r from the tornado axis is calculated by the following formula

$$\Delta p = \frac{\Delta p_m}{2} \left(2 - \frac{r^2}{R_m^2} \right) \quad (0 \leq r \leq R_m), \quad \Delta p = \frac{\Delta p_m}{2} \left(\frac{R_m}{r} \right)^2 \quad (R_m \leq r < \infty). \quad (9)$$

Wind velocity vector \vec{W} is the sum of vectors

$$\vec{W} = \vec{T} + \vec{V}, \quad (10)$$

where the direction of the translational velocity vector \vec{T} is constant for the entire tornado area, and the direction of the rotational velocity vector \vec{V} at each point is perpendicular to the radius r (Fig. 3).

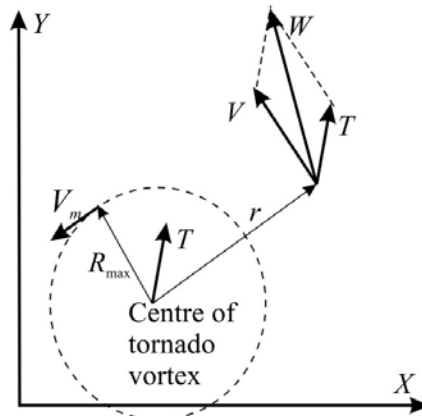


Figure 3. Velocity components.

Wind pressure caused by the wind velocity W is calculated by the following formula:

$$p_w = C\rho W^2 / 2 \quad (11)$$

where $\rho = 1.22 \text{ kg/m}^3$ is the air density.

The most difficult part of the problem is to determine the drag coefficient C , which is used when calculating the velocity component of the load. Design codes and guides mainly provide information for the plane-parallel flow. The coefficients determined during the tests of the confinement model in the wind tunnel were applicable only to parallel flows and could not be used to calculate the tornado vortex effect. Therefore, it was necessary to postulate some characteristics of the wind flow making careful conservative decisions.

Thus, it was proposed to conservatively take C as one. This conservative decision $C = 1.0$ was indirectly based on the results of the tests where the values of C were in the following range (-0.609...-1.075) for different directions of the plane-parallel flow.

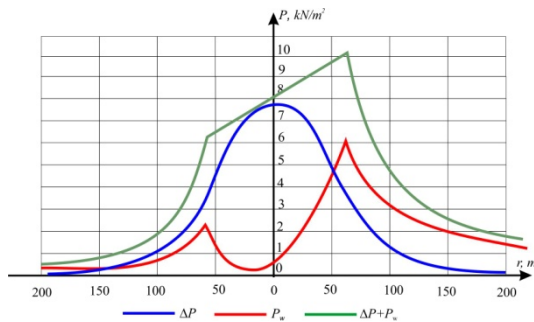


Figure 4. Pressure distribution, line parallel to the tornado direction.

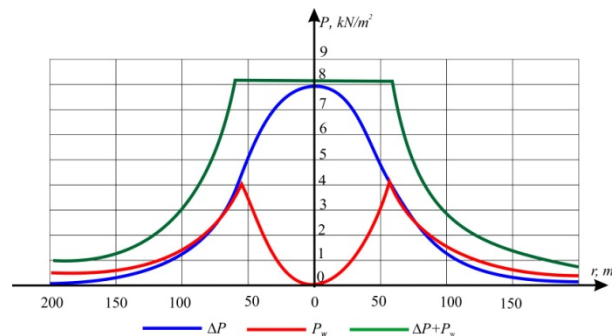


Figure 5. Pressure distribution, line perpendicular to the tornado direction.

Fig. 4 and 5 show the characteristic distribution of pressure along the lines parallel or perpendicular to the tornado direction:

- The red curve reflects the wind velocity pressure with a drag coefficient of 1.0, which corresponds to the main part of the roof.
- The blue curve reflects the pressure drop. This pressure is the same for all NSC enclosing structures.
- The green curve is the sum of two effects and reflects the tornado effects on the main part of the roof.

3. Results and Discussion

3.1. Loading variants

Various tornado scenarios were considered to select load cases unfavorable for the structural members. They differ in the position of the vortex axis and the direction of translational movement. 49 different locations of the tornado axis were considered and four directions of movement were analyzed for each location of the tornado vortex (circles in Fig. 6).

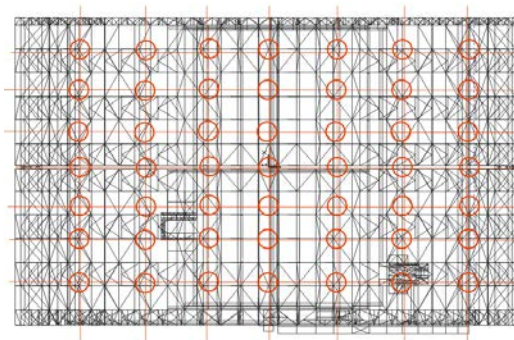


Figure 6. Design locations of the tornado axis.

The peak tornado-induced load reached the value of 10.06 kN/m^2 and was directed upwards, i.e. against the dead load and a number of other loads. However, its unloading effect was greatly reduced due to the uneven distribution over the area, which caused significant forces in the elements of the load-bearing frame.

3.2. Durability check

The analysis for a tornado of class 3 was performed in accordance with the Terms of Reference assuming the integrity of the NSC sheeting:

- the tornado of class 3 was considered only in combination with permanent loads;
- the possibility of limited plastic deformations in the elements of the load-bearing structures was taken into account;
- the possible local overstress in the structural joints which did not lead to the loss of stability of the main load-bearing structures was not taken into account.

The possibility of limited plastic deformations appearance means that under a class 3.0 tornado some arch elements will have residual displacements and the estimation of their influence on the main cranes system work is required. Unfortunately, regulations (both SNiP and Eurocode) don't permit their quantitative calculation.

Anyway, the long-term practice of critical crane industrial buildings using formula (49) from SNiP II-23-81* showed that these concerns are excessive as the field experience demonstrates that the residual deformation measured values don't obstruct the cranes work.

The results of these analyses showed that strength and stability were not provided for many elements of the preliminary NSC design. These elements are shown in red in Fig. 7.

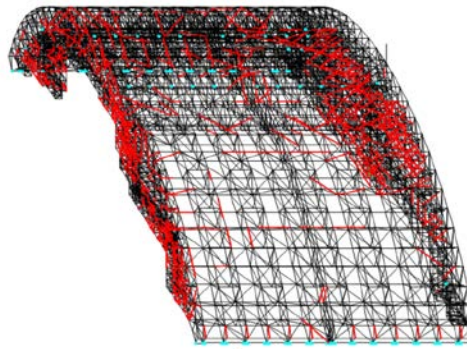


Figure 7. Color indication of the tornado analysis results.

New necessary cross-sections were determined to ensure compliance with the structural load-bearing capacity requirements for the tornado of class 3.0. The additional steel consumption for the new sections amounted to 344.47 tons (2.70 %).

3.3. Loosing contact with foundations

The bearing nodes of the arches are not capable of resisting tension, while the total lift caused by a class 3.0 tornado may achieve 20 thousand tons, the total permanent load weight being about 32 thousand tons. Therefore the hypothesis needs to be verified that some arches may break from the foundation. The hypothesis has been verified using a design model where the arch is supported by unilateral constraints.

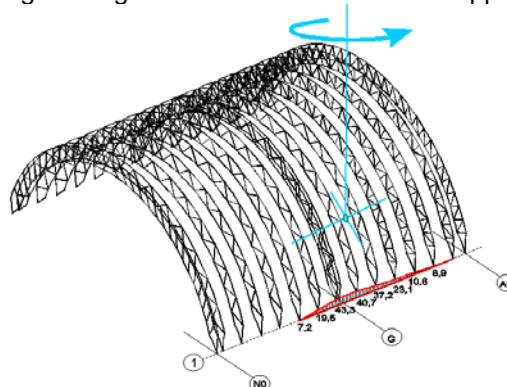


Figure 8. Deformations in unilateral constraints.

The respective nonlinear problem was solved by a step-by-step method in the SCAD environment. The result was refined by iteration for a few tornado load cases. Results of the check for a case which turned out to be worst from the seam opening standpoint are shown in Fig. 8.

As far as the structure of supporting node allows to provide free vertical displacements with dimension up to 50 mm with the purpose to perceive horizontal reaction components, a possibility to be found for raising by 43.3 mm is absolutely safe.

4. Conclusion

The experience of designing the New Safe Confinement has shown that there are a number of unresolved issues related to the methodology for determining the tornado-induced loads on large-span structures of non-standard geometric shapes. In particular, it remains unclear whether a tornado vortex can exist near a vertical wall larger than the tornado core. When designing the NSC ChNPP, we assumed that such a vortex would collapse. Issues related to the drag coefficient, which is used to determine the vortex pressure on the enclosing structures, require clarification and can initiate further studies.

It should also be noted that the methodology for determining the expected tornado class has to be refined. The applied approach, which was based on the IAEA recommendations, does not take into account the local features of the construction site, and therefore can lead to incorrect results.

References

1. Wastiaux, M., Etienne, D. Arche de Tchernobyl: Un ouvrage metallique de duree 100 ans sana maintenance [Online]. URL: <http://afgc.asso.fr/images/stories/visites/GC2011/Session1-7-Wastiaux-Etienne-Tchernobyl.pdf> (reference data 04.02.2020)
2. Boutillon, L., Coulet, D., Waustiaux, M. The Chernobyl new safe confinement: an exemplary contribution by french companies. The French Technology and know-how. Document issued at the 19th IABSE Congress in Stockholm. Sweden September 21–23, 2016. [Online]. URL: <http://www.afgc.asso.fr/images/stories/pub/Stockholm/18-The-Chernobyl-new-safe-confinement-an-exemplary-contribution-by-french-companies.pdf> (reference data 04.02.2020)
3. Solari, G. Wind Science and Engineering. Origins, Developments, Fundamentals and Advancements Springer Nature Switzerland AG, 2019. 944 p. <https://doi.org/10.1007/978-3-030-18815-3>
4. Simiu E., Dong, Hun Yeo. Wind Effects on Structures: Modern Structural Design for Wind, John Wiley & Sons, 2019/ 520 p. DOI: 10.1002/9781119375890
5. Gordeev, V.N., Lantuh-Lyaschenko, A.I., et al. Nagruzki i vozdeystviya na zdaniya i sooruzheniya [Loadings and actions on buildings and constructions]— Moscow: Izd-vo SKAD SOFT, Izd-vo Assotsiatsii stroitelnyih vuzov, DMK Press, 2017. 588 p. (rus)
6. Birbraer, A.N., Roleder, A.J. Extreme actions on structures. Saint Petersburg: Polytrchnic University Publisher House, 2009. 594 p. (rus.)
7. Jischke, M.C., Light, B.D. Laboratory simulation of tornadic wind loads on a rectangular model structure. Journal of Wind Engineering and Industrial Aerodynamics. 1983. Pp. 371–382. DOI.org/10.1016/0167-6105(83)90157-5
8. Sarkar, P., Haan, F., Gallus, Jr.W., et al. Velocity measurements in a laboratory tornado simulator and their comparison with numerical and fullscale data. Technical Memorandum of Public Works Research Institute. 2005. Pp. 197–211. [Online]. URL: <https://www.pwri.go.jp/eng/ujnr/joint/37/paper/42sarkar.pdf> (reference data 04.02.2020).
9. Balaramudu, V. Tornado-induced wind loads on a low-rise building. Retrospective Theses and Dissertations. 2007. <https://lib.dr.iastate.edu/rtd/14860>
10. Case, J., Sarkar, P., Sritharan, S. Effect of low-rise building geometry on tornado-induced loads. Journal of Wind Engineering and Industrial Aerodynamics. 2014. Vol.133, Pp. 124–134. DOI: 10.1016/j.jweia.2014.02.001
11. Zhenqing, L., Takeshi, I. A study of tornado induced mean aerodynamic forces on a gable-roofed building by the large eddy simulations. Journal of Wind Engineering & Industrial Aerodynamics. 2015. Vol. 146. Pp. 39–50. <https://doi.org/10.1016/j.jweia.2015.08.002>
12. Xua, F., Maa, J., Chenb, W.-L., Xiaoa, Y.-Q., Duan, Z.-D. Analysis of load characteristics and responses of low-rise building undertornado. Procedia Engineering. 2017. Vol. 210. Pp. 165–172. <https://doi.org/10.1016/j.proeng.2017.11.062>
13. Wen, J.-K. Dynamic tornado wind loads on tail buildings. Journal of the Structural Division. Proc. ASCE. 1975. — ST1, Pp. 169–182.
14. James, A. Dunlap. Nuclear Power Plant Tornado Design Considerations. Journal of the Power Division. 1971. 97 (2). Pp. 407–417. [Online]. URL: <https://cedb.asce.org/CEDBsearch/record.jsp?dockey=0018118> (reference data 04.02.2020)
15. Barrett, D.J., Agarwal, R., Persinko, D. The effect of a tornado on nuclear power plant structures. Transactions of the 7 international conference on structural mechanics in reactor technology. Vol. D Netherlands: North-Holland, 1983, Pp. 243–249.
16. Ahmad, S., Ansari, Md.E. Response of transmission towers subjected to tornado loads. The Seventh Asia-Pacific Conference on Wind Engineering. 2009. [Online]. URL: https://www.researchgate.net/publication/228790798_Response_of_transmission_towers_subjected_to_tornado_loads/stats (reference data 04.02.2020)
17. Savory, E., Gerard, A.R., Zeinoddini, M., Toy, N., Disney, P. Modeling of Tornado and Microburst Induced Wind Loading and Failure of a Lattice Transmission Tower. Engineering Structures. 2001, Vol.23. Pp. 365–375.
18. Selvam, R.P., Millett, P.C. Computer modeling of tornado forces on buildings. Wind and Structures. 2003, 6(3). 3 Pp. 209–220. DOI: 10.12989/was.2003.6.3.209
19. Kozlov, I.L. Criteria for NPP industrial site flooding by combined impact of tornadoes and earth-quakes in the cooling pond. Eastern-European Journal of Enterprise Technologies. 2015, Vol. 3, No. 6 (75). DOI: <https://doi.org/10.15587/1729-4061.2015.42146>
20. Biswas, J. Tornado Generated Missile Impact to NPP Structures. ASCE Structures Congress 2019. Orlando, Florida. DOI.org/10.1061/9780784482230.031
21. Bazhenov, V.A., Huliar, A.I., Snizhko, N.A., Ovsianikov, O.S. Raschet gradirni AES na vitrovye nagruzki tipa «tornado» poluanaliticheskim metodom konechnyx elementov. [Cooling tower of the atomic power station calculation on wind loadings of type of a tornado a semi-analytical method of finite elements] Opir materialiv i teoriia sporud [Strength of materials and the theory of constructions]. № 71. 2002. Pp. 3–11. (ukr)
22. IEFA Safety Standards Series. Safety Guide 50-SG-S11A. Extreme Meteorological Events in Nuclear Power Plant Siting, Excluding Tropical Cyclones. A Safety Guide, International Atomic Energy Agency: Vienna. 1981. 76 p.
23. Fujita T.T. Tornadoes and downbursts in the context of generalized planetary scales Journal of Atmospheric Sciences, 1981, 38 (6). Pp. 1511–1534.
24. Fujita, T.T., Pearson, A.D. Results of FPP Classification of 1971 and 1972 Tornadoes. Propertis of 8th Conference on Severe Local Storms. 1973. Boston, Massachusetts (1973).
25. Rekomendatsii po otsenke kharakteristik smercha dlya ob'ektov ispol'zovaniya atomnoy energii [Recommendations for assessing the characteristics of a tornado for nuclear facilities. Rukovodstva po bezopasnosti RB-022-01. Gosatomnadzor Rossii. 2002. 69 p.

Contacts:

Anatoly Perelmuter, anatolyperelmuter@gmail.com

© Perelmuter, A.V., 2020



DOI: 10.18720/MCE.97.12

Clinkerless slag-silica binder: hydration process and hardening kinetics (part 2)

G.S Slavcheva^{a*}, O.V. Artamonova^b, M.A. Shvedova^b, M.A. Khan^c

a Voronezh State Technical University, Voronezh, Russia

b Voronezh State University of Architecture and Civil Engineering, Voronezh, Russia

c Karaganda State Technical University, Karaganda, Republic of Kazakhstan

* E-mail: gslavcheva@yandex.ru

Keywords: clinkerless binder, complex nanoadditive, nanosilica, hydration, phase composition, flocculation, hardening, compressive strength

Abstract. In part 1 of the studies, it was shown the results of the implementation of the “top–down” nanotechnological principle to obtain clinkerless binder with a high content of microsilica, activated during grinding what allowed to increase their hydraulic activity. Part 2 of the studies have been implemented in order to ensure the possibility of using of clinkerless slag-silica binder, modified by complex additive of SiO₂ nanoparticles in combination with a plasticizer (“bottom–up” nanotechnological principle), as a hydraulic binder. For nanotechnological activation the solution of nano-additives, synthesized by the sol–gel process, is used. Experimental results of changes phase composition and microstructure of clinkerless slag-silica binder during hydration and structuration processes; flocculation and hardening kinetics are presented. The laser granulometry method, dynamic light scattering and transmission electron microscopy were used to estimate the particle size of original components. XRD – method, scanning electron microscope were used to estimate phase composition and morphology of the clinkerless binder’s hydration product. The flocculation was evaluated by the penetrometric method. The hardening kinetics was evaluated by the mechanical tests after 1, 3, 7, 14, 28 day of curing. As a result, the distinctive features of the main periods of heterogeneous processes of structure formation of the nano-activated clinkerless slag-silica binder are revealed at the different stages of hardening. It was established that the “bottom – up” nanotechnological principle, implemented through the introduction of SiO₂ – nanoparticles into binder paste allows to increase the hydraulic activity of slag due to the catalytic role of nanoparticles and their chemical interaction with slag minerals. As a result, the strength of the of clinkerless slag-silica binder was 35.8 MPa, and it’s setting and hardening rates corresponds to the speed of these processes for Portland cement under normal temperature-humidity conditions.

1. Introduction

Currently, slag-alkaline binders represent a promising alternative to the cement [1–5]. Using industrial waste instead of expensive clinker in the production of slag-alkaline binders significantly reduces the final cost of the products and structures. An important moment when using binders of this type is the activation of the slag in their composition. The activation process is aimed at increasing the reactivity of the slag minerals and hydraulic activity of the binder which allows one to obtain products with high strength and durability [6, 7].

The following methods are known to increase the hydraulic activity of a binder [8]: mechanical grinding, mechanochemical activation of the slag component, the introduction of chemical additives, directional crystallization while lowering the basicity of the dispersed phase and complicating the composition.

The simplest, however, energy-consuming method of activating blast furnace slag is the fine grinding in the presence of activators. This method meets the nanotechnological principle of “top–down” [9]. The results of our research [10] confirmed the effectiveness of such activation of the clinkerless slag-silica binder at the manufacturing stage, as well as the use of the hydraulic potential of nano- and micro-sized particles at the hardening stage. Thus, it was found that the presence of a large amount of silica fume in the ultramicrodispersed state in the clinkerless slag-silica binder allows us to increase the hydraulic activity of the

Slavcheva, G.S, Artamonova, O.V., Shvedova, M.A., Khan, M.A. Clinkerless slag-silica binder: hydration process and hardening kinetics (part 2). Magazine of Civil Engineering. 2020. 97(5). Article No. 9712. DOI: 10.18720/MCE.97.12



This work is licensed under a [CC BY-NC 4.0](https://creativecommons.org/licenses/by-nc/4.0/)

binder and ensure its setting and hardening rate under normal temperature and humidity conditions, comparable to the speed of these processes for Portland cement.

It is known that for the modification of cement systems at present [11–17], not only micro- and ultrafine additives are widely used but also nano-additives that are introduced into cement paste. In a number of works it was established [18–20] that, with the introduction of nano-additives, similar effects are possible not only in cement but also in slag-alkaline clinkerless systems. So, in [18], it was shown that the introduction of 1.5–2 mass. % nano-clay into alkali and geopolymer mortars increases the strength of the resulting composites by 15–24 %, and the addition of nano-sized TiO₂ particles reduces their shrinkage [19]. In [20], nanosilica was used to activate a slag-alkali binder. It was established that its introduction into the system under study contributes to the acceleration of the formation of gel-like hydrosilicates and calcium aluminosilicates, which leads to a quick set of the strength of the slag-alkaline paste. According to the scientific concept that authors formulated earlier [4], this approach to modification corresponds to the “bottom – up” nanotechnological principle. According to author’s studies [18], the most effective for cement systems are complex additives (CND) based on SiO₂ nanoparticles and superplasticizer (SP). SiO₂ nanoparticles play a catalytic role, acting as crystallization centers, and also directly participate in the chemical interaction with cement clinker minerals during cement hydration. At the same time, our studies proved the possibility of accelerating the hydration processes of cement clinker by 20–25 times, as well as increasing the strength of cement composites by 1.5–2 times.

The effectiveness of CND application for cement systems that we established allows us to suggest that its use can also ensure the activation of slag and acceleration of the hydration and hardening processes of the clinkerless binder.

In part 1 of the studies [10] it was shown the results of the implementation of the “top–down” nano technological principle to obtain CSSB1 clinkerless binder, the characteristics of which comply with the physicommechanical characteristics of 32.5 cement according to EN 197-1:2000 “Cement – Part 1: Composition, specifications and conformity criteria for common cements”. The research results presented in this article are an integral part and continuation of the work. The research results discussed in the article examine the possibility and evaluate the effectiveness of nano-technological activation of the slag-alkaline system according to the “bottom-up” principle in comparison with activation according to the “top – down” principle.

The work aimed to assess the possibility of using clinkerless slag-silica binder (CSSB2), modified with a complex nano-sized additive based on SiO₂ (CND), as a hydraulic binder of normal hardening based on comprehensive studies of phase composition, structuration process, and hardening. The research objectives included:

- study of changes in phase composition and CSSB2 microstructure during hydration and structuration processes;
- comparative assessment of flocculation and hardening kinetics of two types of clinkerless binders CSSB1 and CSSB2;
- assessment of the effectiveness of using nanotechnological principles to activate clinkerless binders.

2. Methods¹

The systems shown in Table 1 were investigated. The following raw materials were used to obtain clinkerless slag-silica binder:

- granulated blast-furnace slag from LLP “Arcelor Mittal” plant (Temirtau, Kazakhstan) with a lime factor of 0.75;
- microsilica of MKU-95 grade with a mass fraction of SiO₂ = 96.85 %;
- building lime of an activity of 86.2 %;
- gypsum (gypsum dehydrate);
- powder superplasticizer S-3 based on naphthalenesulfonates,
- superplasticizer of Sika trademark based on polycarboxylic ethers (SP).

¹ The studies were conducted in the laboratory of the Center for Collective Use named after Professor Yu.M. Borisov (Voronezh State Technical University, Russia)

Table 1. Mixture composition.

Systems	Specimen ID	W/C, W/CSSB	Components	Dosage, %	Specific surface area S_u , m ² /kg		
cement +CND	C + CND	0.33	cement CEM I 42.5N	99.79	300		
			CND	NP SiO ₂	0.01	1.42·10 ⁶	
				SP	0.2		
clinkerless slag- silica binder +water	CSSB1 + W	0.30	granulated blast- furnace slag	63	900		
			microsilica	20			
			building lime	14			
			gypsum	1.5			
			S-3	1.5			
clinkerless slag- silica binder + CND	CSSB2 + CND	0.20	granulated blast- furnace slag	63	740		
			microsilica	14			
			building lime	1.5			
			gypsum	NP SiO ₂		0.01	1.42·10 ⁶
				SP		0.2	

For nanotechnological activation of CSSB2, CND solution was used, a detailed sol – gel synthesis of which was described in [17]. The manufacturing conditions and characteristics of CSSB1 are presented in [10]. The CND modified cement system with a SiO₂ nanoparticles dosage of 0.01 % (NP), what was previously studied in detail [18], was taken as a reference.

In preliminary exploratory studies, CND with a dosage of SiO₂ nanoparticles of 0.01 %, 0.05 %, and 0.1 % by weight of the binder was used for nano-modification of the cinder-alkali binder. It was found that slag-alkali systems with nanoparticle dosages of 0.05 % and 0.1 % underwent self-destruction during the removal of samples. Thus, for a clinkerless binder, as well as for cement systems [17], the optimal SiO₂ nanoparticles dosage is 0.01 % by weight of the binder. Therefore, all studies for CSSB2 + CND were conducted with this dosage.

The amount and size of the colloidal nanoparticles SiO₂ synthesized by the sol – gel process were determined using dynamic light scattering (Photocor Complex spectrometer), and transmission electron microscopy (TEM) (Transmission Electron Microscope H-9500, $v_{acs} = 75$ kV).

Operational control of the binder dispersion by its specific surface area was carried out by the method of air permeation on the PSH-8A device. The particle sizes of the microsilica and binder were studied using the laser particle size analyzer ANALYSETTE 22 Nano Tec.

The structuration process, flocculation, and hardening kinetics were studied in the C+CND, CSSB1+W and CSSB2+CND systems. W/C – ratio and W/CSSB – ratio of these systems were different, what were assigned based on the standard normal consistency of fresh pastes.

The phase composition of the clinkerless binder was controlled by the XRD-method (ARL X'TRA diffractometer, CuK α radiation ($\lambda = 1.541788$ Å) after 1, 3, 7, 14, 28 days of hardening under normal temperature and humidity conditions. X-ray decoding and phase identification were carried out using PDWin 4.0 [21].

The morphology of the hardened cement and CSSB paste structure was examined on a JEOL JSM-7001F scanning electron microscope.

After mixing the CSSB with water, the flocculation process of fresh binder paste was controlled in two ways. The setting times were determined on a Vicat-method according to Russian State Standard GOST 30744-2001 "Cements. Methods of testing with using polyfraction standard sand".

The flocculation (setting kinetics) of fresh binder paste was evaluated by the plastic strength index P_{pl} . determined using a universal penetrometer Geopocket S068. To determine the plastic strength, fresh binder paste was placed in a ring with a diameter of 150 mm and a height of 55 mm. The determination of plastic strength was performed by immersing a standard penetrometer plunger (6.4 mm) to a predetermined mark (to a depth of 5 mm). The readings were taken on an internal scale in kgf/cm², the value of plastic strength P_{pl} was determined based on the fact that 1 kgf/cm² = 98.0665 kPa. Tests were carried out from the moment the mixture was prepared until the moment it began to set (determined using a Vicat-method) every 15 minutes. For each test period, 12 measurements were made.

The CSSB hardening kinetics was evaluated by testing samples – cubes 5×5×5 cm in size after 1, 3, 7, 14, 28 days of curing under normal temperature and humidity conditions ($t = 20\text{ }^{\circ}\text{C}$, $\text{RH} = 95 \pm 5\%$). The strength testing was carried out on a universal 4-column floor hydraulic test system INSTRON Sates 1500 HDS. As a result of the tests, the full diagrams “strain σ – displacement Δ ” were obtained. According to the tests, the compressive strength and elastic modulus were determined. To ensure the statistical reliability of the results of physical and mechanical tests, the number of samples in the series was 6 pieces. The intra-series coefficient of variability of the test results was 5–7 %.

3. Results and Discussion

The specific surface area of binders in the CSSB1 + W and CSSB2 + CND systems is $S_u = 900$ and $S_u = 740\text{ m}^2/\text{kg}$, respectively. CSSB2 was ground to a lesser degree of dispersion since its activation is carried out by introducing CND.

According to the methods of transmission microscopy (Fig. 1 a) and dynamic light scattering (Fig. 1 b), (Table 2) the average particle size of SiO_2 is approximately 5–10 nm. Moreover, the CND complex additive based on them is stable for seven days from the moment of synthesis [8]. Microsilica as part of a slag-alkaline binder is an almost mono-dispersed system [5] with an average particle diameter of 15.6 μm .

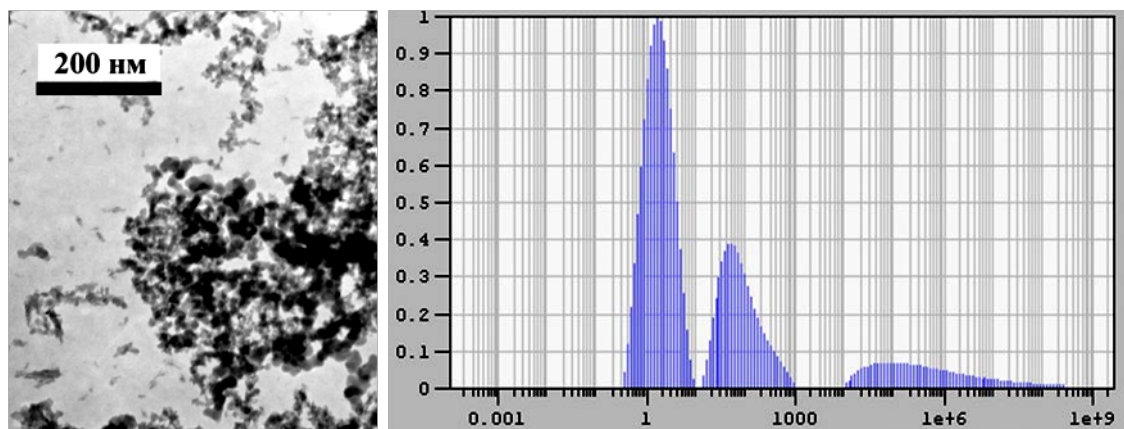


Figure 1. Size and range of SiO_2 - nanoparticles as part of CND after 7 days from the moment of synthesis:

a) micrographs (TEM data); b) particles range (hydrodynamic radius is presented).

Table 2. Sizes of nano- and microparticles.

Name	Data (Analyzette22, PhotocorComplex)	
	ω particles, %	d, μm
Nanosilica	28	0.002
	39.3	0.005
	27.3	0.01
Microsilica	93	15.6
	7	≤ 15.6

In [10], it was shown that the slag we used to obtain clinkerless slag-silica binders is in an amorphized state. In this case, the mellitic phase ($8\text{CaO}\cdot 3\text{Al}_2\text{O}_3\cdot \text{MgO}\cdot 5\text{SiO}_2$) is registered, which in the presence of activators can exhibit binding properties.

The CSSB2+CND system (Fig. 2) is dominated by the phases of highly basic calcium hydrosilicate ($2\text{CaO}\cdot \text{SiO}_2\cdot \text{H}_2\text{O}$) and calcium hydroaluminosilicate ($\text{CaO}\cdot \text{Al}_2\text{O}_3\cdot 2\text{SiO}_2\cdot 4\text{H}_2\text{O}$), which are present in the system throughout the entire hardening time. Also, a small number of tobermorite-like phases ($x\text{CaO}\cdot \text{SiO}_2\cdot z\text{H}_2\text{O}$, $(\text{CaO})_x\cdot \text{SiO}_2\cdot z\text{H}_2\text{O}$) are detected in this system, which appear in the system on the first day of hardening and their number gradually increases over time. In addition, on the first day of hardening, a small amount of the portlandite phase ($\text{Ca}(\text{OH})_2$) is registered in the system, and then the amount of this phase decreases.

X-ray analysis of samples at the age of 28 days of hardening shows that all three systems differ in phase composition (Fig. 3).

In the C+CND system, tobermorite-like phases of the composition $x\text{CaO}\cdot \text{SiO}_2\cdot z\text{H}_2\text{O}$, $(\text{CaO})_x\cdot \text{SiO}_2\cdot z\text{H}_2\text{O}$, as well as the phase of low-basic calcium hydrosilicate $\text{CaO}\cdot \text{SiO}_2\cdot \text{H}_2\text{O}$ are recorded. The amount of these phases increases over time. The phases of ettringite and portlandite are absent in this system [10]. The

CSSB1+W system is characterized by the presence of tobermorite-like phases and highly basic calcium hydrosilicates ($6\text{CaO}\cdot 4\text{SiO}_2\cdot 3\text{H}_2\text{O}$). Also, there is a small number of phases of calcium hydroaluminosilicate with the composition $\text{CaO}\cdot \text{Al}_2\text{O}_3\cdot 2\text{SiO}_2\cdot 2\text{H}_2\text{O}$, ettringite ($3\text{CaO}\cdot \text{Al}_2\text{O}_3\cdot 3\text{CaSO}_4\cdot 31\text{H}_2\text{O}$) and portlandite in this system. In contrast to the above systems, the largest amount of the phase of calcium hydroaluminosilicate ($\text{CaO}\cdot \text{Al}_2\text{O}_3\cdot 2\text{SiO}_2\cdot 4\text{H}_2\text{O}$) is observed for CSSB2 + CND, and small amounts of tobermorite, low-basic calcium hydrosilicates, ettringite are also recorded.

1. It should be noted that in all the samples, diffraction peaks are mixed, which is associated with the multicomponent nature of the systems and the possible formation of crystalline phases of an ultra-dispersed and nano-size scale. The obtained X-ray diffractometric data correlate well with the results of scanning electron microscopy (SEM).

2. According to SEM, the microstructure of the studied systems is also significantly different (Fig. 4). At the microscale level (Fig. 4 a, b) both systems are microheterogeneous with inclusions of pores of various sizes. However, in the CSSB1 + W system, there are more capillary pores (Fig. 4 a), which is naturally associated with a larger W/C value for this system.

3. As it increases, it is observed (Fig. 4 c, d) that the CSSB1+W system has a denser and more uniform structure. At the same time, the structure CSSB2+CND contains inclusions of relatively large slag grains that are not registered in the structure CSSB1+W. This is due to the greater dispersion of CSSB1 ($S_{ii} = 900 \text{ m}^2/\text{kg}$ in comparison with $S_{ii} = 740 \text{ m}^2/\text{kg}$ for CSSB2) and the presence in CSSB1 of a significant amount of microsilica, which provides denser packing of hydration products.

4. The microstructure of hydration products for both systems is mainly represented by lamellar morphology crystallites characteristic of the phases of low-basic calcium hydrosilicates (Fig. 4 e, f, g, h). Particles of hydration products are of various sizes and have a large number of contacts of abutment, coalescence, and intergrowth. Moreover, large needle crystals are observed in the CSSB1+W system, which, according to the X-Ray method data, can be attributed to the ettringite phase (Fig. 4 e, g). A distinctive feature of the CSSB2+CND structure is the presence of large lamellar-prismatic crystals characteristic of calcium hydroaluminosilicate (Fig. 4 f, h).

According to the standard determination of the setting time, the beginning of setting CSSB2+CND is registered after 80 minutes of exposure at a value of $P_{pl} = 412 \text{ kPa}$. In this case, the setting kinetics of the CSSB2+CND system is characterized (Fig. 5) by an intensive increase in plastic strength over the entire flocculation period, in contrast to the CSSB1+W system. For CSSB1+W, an increase in plastic strength is practically not observed for 80 min, the onset of setting was recorded after 150 minutes at $P_{pl} = 387 \text{ kPa}$.

It is established that the form of strain diagrams for the studied systems differs non-substantially. For hardened paste CSSB2+CND (Fig. 6), as well as for CSSB1+W [10], at the age of 1 day, the elasticity area is absent on the diagram and the destruction occurs according to the pseudoplastic type. On the deformation diagrams of CSSB2+CND samples that hardened for 3, 7, 28 days, the elastic area is clearly registered, the length of the descending branch of the diagram is reduced. Thus, as hardening increases, the rigidity increases and the ductility of the system decreases. In both hardened CSSB-pastes at the age of 14 days, a reappearance of the area of plastic deformations was recorded, which corresponds to a temporary decrease in the elastic modulus (Table 3). Despite the similar nature of the destruction, the hardened paste CSSB2+CND is more fragile. With almost the same strength, the elastic modulus values of CSSB2+CND are 1.5–3 times higher than for CSSB1 + W.

Table 3. Hardening kinetics data.

Time, days	1	3	7	14	28
C + CND					
Compressive strength, MPa	64.1	73.0	69.8	83.1	92.7
CSSB1 + W					
Compressive strength, MPa	4.7	14.6	17.1	21.0	37.5
Young's modulus, MPa	340	1390	1536	776	3398
CSSB2 + CND					
Compressive strength, MPa	2.6	12.6	31.9	22.6	35.8
Young's modulus, MPa	177	1690	4112	852	4113

According to the kinetic hardening curve (Fig. 7), the strength increase of CSSB2+CND in the period up to 7 days of hardening is more intense than for CSSB1+W. In the period of 1–7 days, the strength of CSSB2+CND increases 12 times, the strength of CSSB1+W – 4 times. However, for CSSB2+CND, a sharp drop in strength on the 14th day of hardening was recorded. As a result, the strength achieved by the 28th day by both systems has comparable values. Of course, the growth rate and the achieved strength values for

hardened CSSB pastes are significantly lower than for the standard hardened cement paste C+CND. Nanomodification of the cement system allows one to provide 28-day strength normalized for CEM 42.5N already by 1 day of hardening, and the final strength of this system reaches almost 100 MPa. However, the hardening kinetics data results for CSSB pastes suggest that both nanotechnological activation techniques used provide efficient hardening of clinkerless binders without heat treatment, under normal temperature and humidity conditions ($t = 20\text{ }^{\circ}\text{C}$, $\text{RH} = 95 \pm 5\%$).

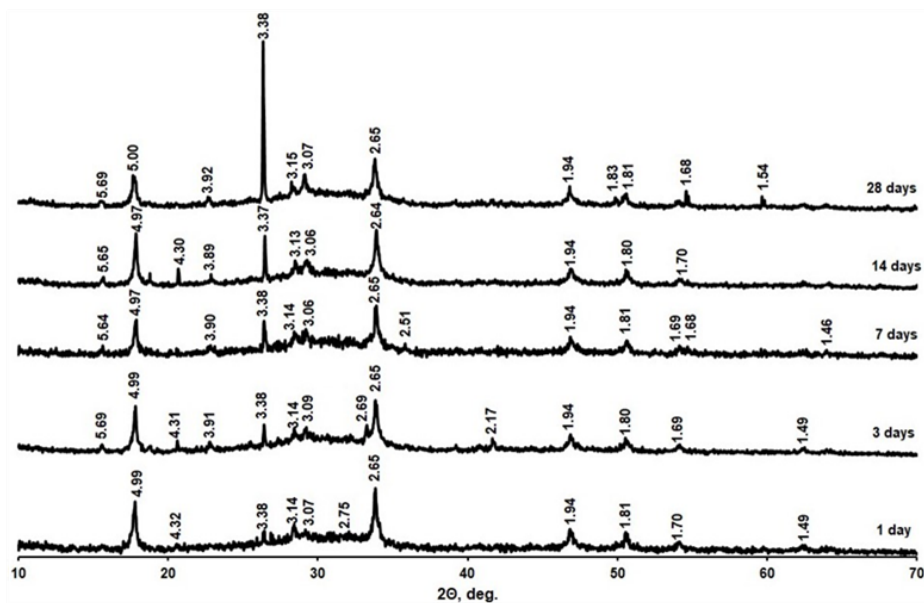


Figure 2. X-Ray Diffraction pattern of hardened paste CSSB2 + CND.

Designations:

$2\text{CaO}\cdot\text{SiO}_2\cdot\text{H}_2\text{O}$ ($d = 3.34, 2.92, 2.25, 1.86, 1.75$);

$\text{CaO}\cdot\text{Al}_2\text{O}_3\cdot 2\text{SiO}_2\cdot 4\text{H}_2\text{O}$ ($4.96, 3.24, 3.14, 2.67, 1.78$,

$x\text{CaO}\cdot\text{SiO}_2\cdot z\text{H}_2\text{O}$ ($d = 3.07, 2.65, 1.83, 1.67, 1.53$);

$(\text{CaO})_x\cdot\text{SiO}_2\cdot z\text{H}_2\text{O}$ ($d = 4.92, 3.34, 3.05, 1.83, 1.67$);

$\text{Ca}(\text{OH})_2$ ($d = 4.93, 3.11, 2.63, 1.93, 1.79$)

$3\text{CaO}\cdot\text{Al}_2\text{O}_3\cdot 3\text{CaSO}_4\cdot 31\text{H}_2\text{O}$ ($d = 4.98, 3.88, 1.90, 1.87, 1.76$)

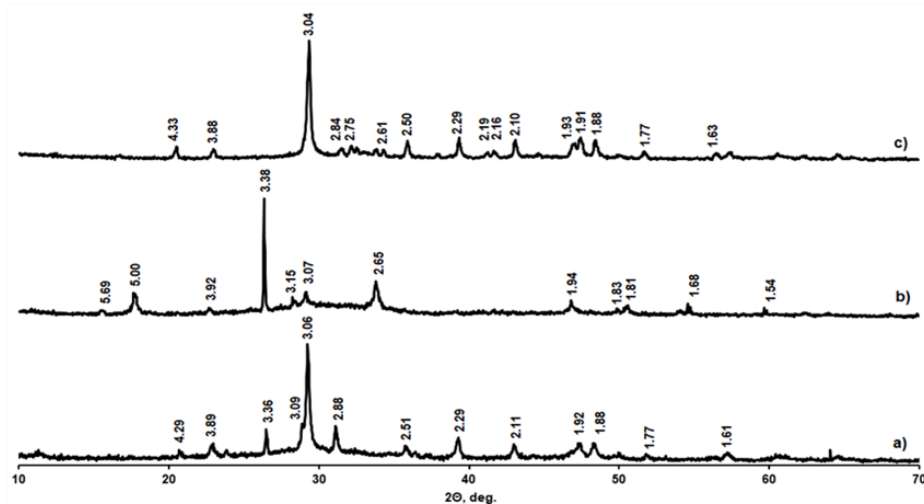


Figure 3. X-Ray Diffraction pattern of hardened system (28 days of hardening):

a) CSSB1 + W, b) CSSB2 + CND, c) C + CND.

Designations:

$6\text{CaO}\cdot 4\text{SiO}_2\cdot 3\text{H}_2\text{O}$ ($d = 4.31, 3.11, 2.26, 1.95, 1.76$);

$2\text{CaO}\cdot\text{SiO}_2\cdot\text{H}_2\text{O}$ ($d = 3.34, 2.92, 2.25, 1.86, 1.75$);

$\text{CaO}\cdot\text{SiO}_2\cdot\text{H}_2\text{O}$ ($d = 3.21, 3.01, 2.78, 2.23, 2.01, 1.77$);

$(\text{CaO})_x\cdot\text{SiO}_2\cdot z\text{H}_2\text{O}$ ($d = 4.92, 3.05, 2.93, 2.80, 1.83$);

$x\text{CaO}\cdot\text{SiO}_2\cdot z\text{H}_2\text{O}$ ($d = 3.07, 2.97, 2.80, 2.28, 1.83$);

$\text{CaO}\cdot\text{Al}_2\text{O}_3\cdot 2\text{SiO}_2\cdot 4\text{H}_2\text{O}$ ($d = 4.91, 4.27, 3.34, 3.19, 2.70$);

$3\text{CaO}\cdot\text{Al}_2\text{O}_3\cdot 3\text{CaSO}_4\cdot 31\text{H}_2\text{O}$ ($d = 4.98, 3.88, 1.90, 1.87, 1.76$)

$\text{Ca}(\text{OH})_2$ ($d = 4.93, 3.11, 2.63, 1.93, 1.79$)

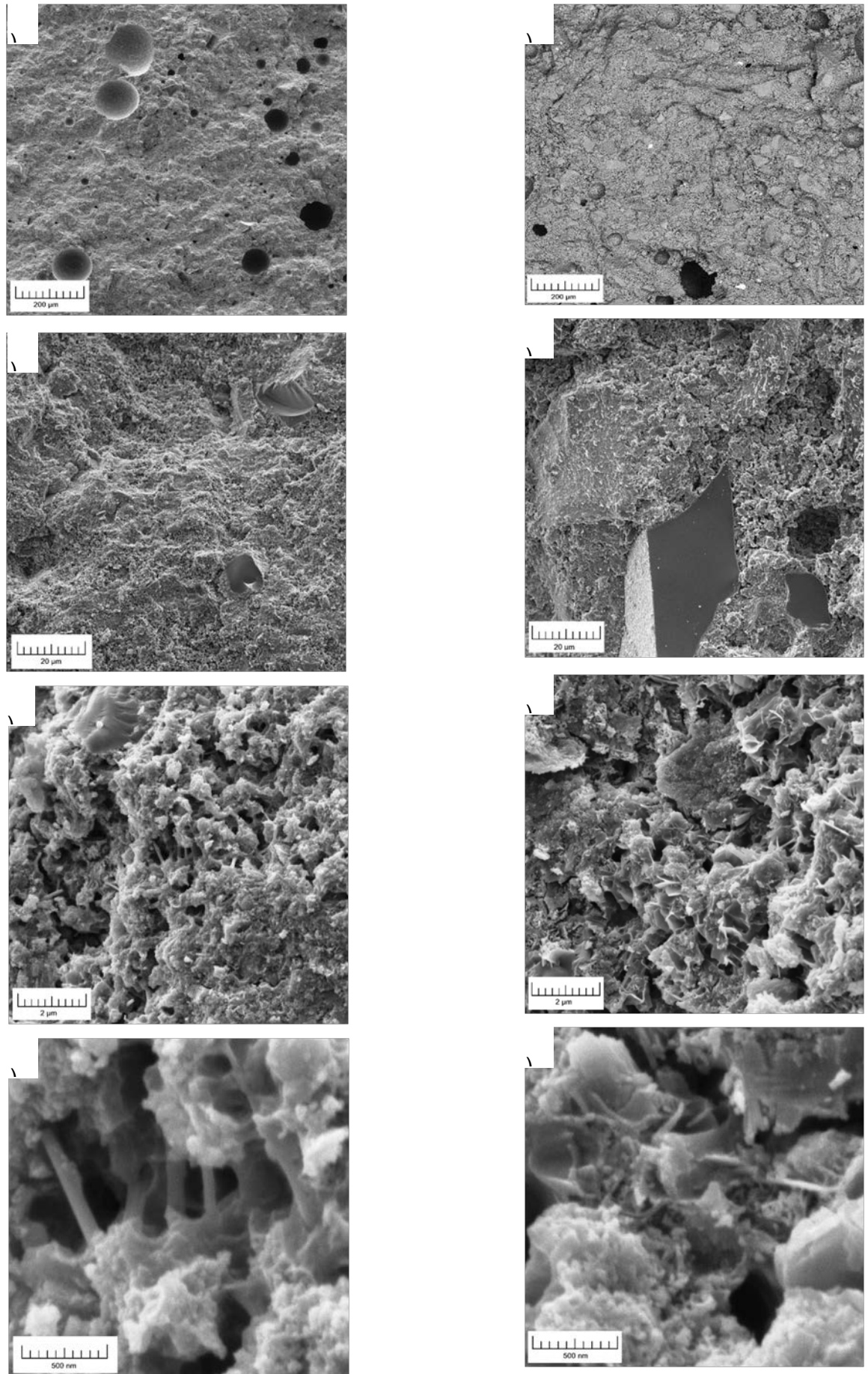


**Figure 4. SEM images of hardened CSSB-pastes:
a, c, e, g) CSSB1 + W; b, d, f, h) CSSB2 + CND.**

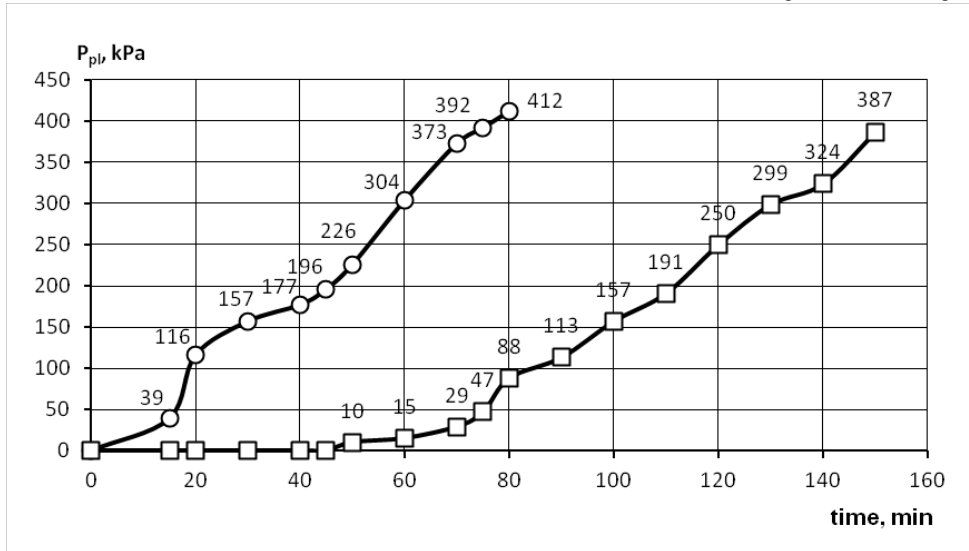


Figure 5. Flocculation kinetics of fresh CSSB-pastes
 Designations: □ – CSSB1 + W; ○ – CSSB2 + CND.

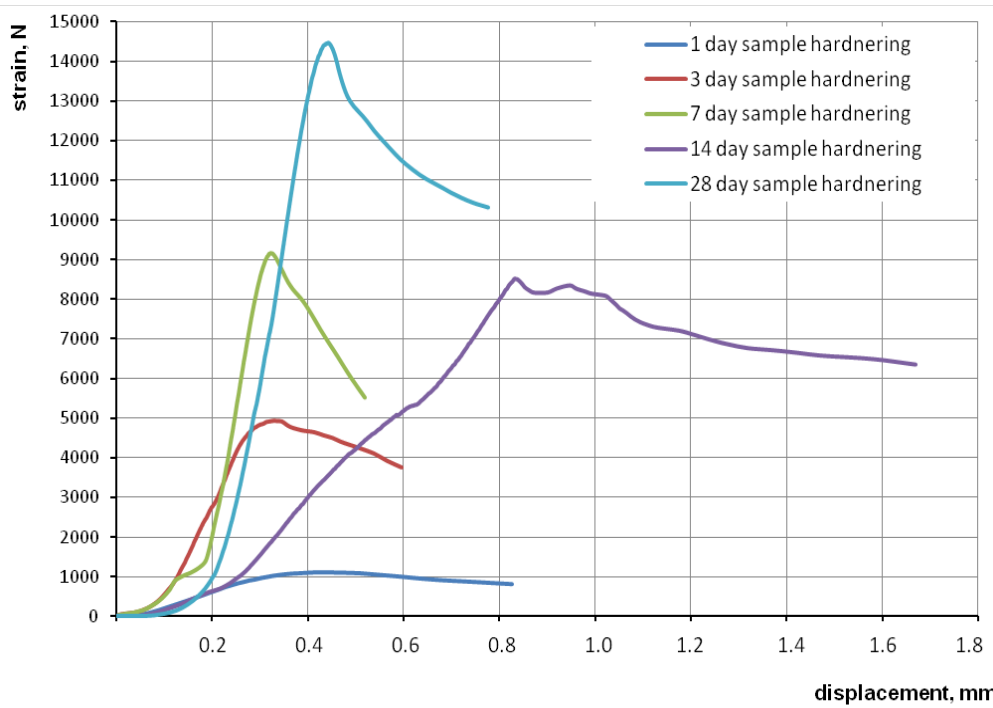


Figure 6. Tested hardened CSSB2 pastes “strain s - displacement Δ” experimental results.

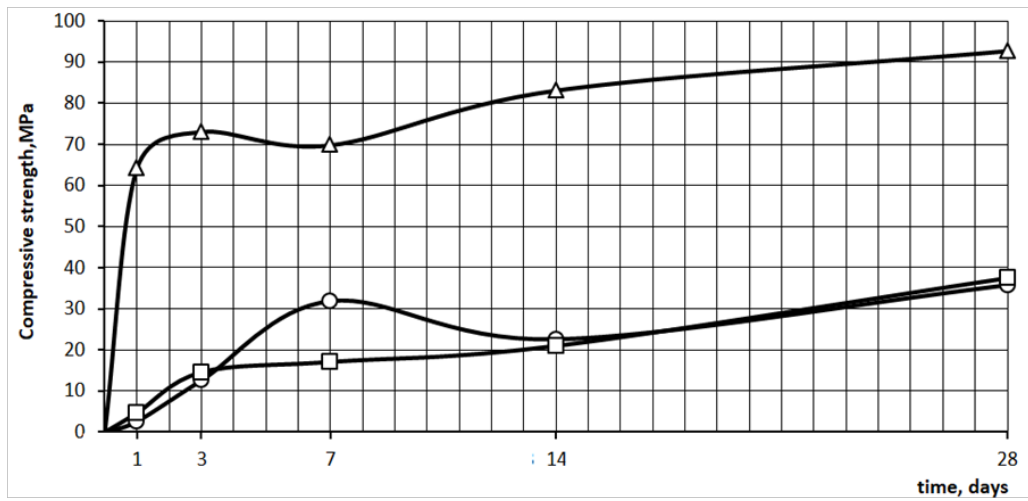


Figure 7. Hardening kinetics of CSSB-pastes and cement paste
 Designations: □ – CSSB1 + W; ○ – CSSB2 + CND; Δ - C + CND.

In [10], it was shown the differences in hydration and hardening of the clinkerless slag-silica binder CSSB1 compared to the traditionally distinguished periods of the hydration of cement systems, namely, the *initial* and *pre-induction*, *induction*, *acceleration*, *deceleration* and *slow interaction*. In the framework of this approach, let us compare the features of hydration processes for all the studied nano-modified systems.

According to the flocculation curve (see Fig. 5) for CSSB1, the set of plastic strength begins after 80 min exposure, which is due to the slow dissolution of the slag grains and the delay in the onset of hydration phases. On the contrary, CSSB2 is characterized by an intensive increase in plastic strength almost from the moment of mixing. This can be attributed to the catalytic role of SiO_2 nanoparticles, which intensify the processes of hydration phase nucleation. As a result, the setting start time for CSSB1 (150 min) corresponds to the standard setting start time range for Portland cement (120-160 min), and for CSSB2 the setting start time is faster (80 min).

For the C + CND nanomodified system, the acceleration period is associated with the formation of a spatial framework in the system as a result of mass crystallization of low-basic tobermorite-like hydrosilicates [4], which determines its high strength already on the 1st day of hardening. On the contrary, for both types of CSSB at this period, highly basic primary calcium hydrosilicates $2\text{CaO}\cdot\text{SiO}_2\cdot\text{H}_2\text{O}$ prevail in the hydration products. They belong to the dendrid-like and amorphous morphological type, which have low strength of crystallization contacts [22]. Therefore, it is logical that, by the first day of hardening, the CSSB1 + W and CSSB2 + CND systems have an abnormal deformation diagram for solids (see Fig. 6), low strength and elastic modulus.

In the period of 1–7 days of hardening for CSSB2 + CND, a more intensive increase in the strength of the system and its elasticity occurs than for CSSB1 + W. The elastic area is clearly defined on the deformation diagrams of both systems, which may be due to the formation of a crystalline framework in hydration products (secondary phases of $6\text{CaO}\cdot 4\text{SiO}_2\cdot 3\text{H}_2\text{O}$ hydrates of fibrous-needle morphology, ettringite crystals, and Aft-phases). A more intensive increase in the strength of CSSB2 + CND may be due to the formation of tobermorite-like phases in it, as they provide the greatest number and strength of contacts per unit volume. In the hydration products of CSSB1 + W, tobermorite-like phases are not registered at this time [10]. The presence of secondary hydrates, a rapid increase in strength allows us to correlate the period of 1 to 7 days with the period of slowdown of the hydration process for both clinkerless systems.

In comparison with clinkerless systems, it is necessary to emphasize that due to nanomodification, the C + CND cement system reaches 70 % of its maximum strength by the 3d day of hardening, the entire subsequent period of its hardening (3–28 days) refers to the stage of slow interaction.

However, further, characteristics of the hardening process of CSSB1 + W and CSSB2 + CND are significantly different. In the period of 3–14 days for CSSB1 + W there is only a slowdown in the set of strength, and for CSSB2 + CND – a decrease in strength by 1.5 times from the value reached by the 7th day.

The strain diagram for both systems on the 14th day of hardening again acquires an anomalous character, characterized by a long plateau of pseudoplastic deformations. This is naturally accompanied by a decrease in the elastic modulus for CSSB1 + W by half, for CSSB2 + CND – by 4 times in relation to its value at the age of 7 days. The change in the elastic-plastic behavior can be associated with the repeated mass formation of primary hydrates $2\text{CaO}\cdot\text{SiO}_2\cdot\text{H}_2\text{O}$, which is especially significant for CSSB2 + CND due to the chemical interaction of SiO_2 nanoparticles with the slag minerals. As a result, the crystallization pressure in the already formed crystalline framework determines a significant decrease in strength.

In the period of 14–28 days, there is an increase in the strength and elasticity of CSSB1 + W and CSSB2 + CND, which can be correlated with the *processes of self-organized structure formation*. In the hardening system CSSB2 + CND, the content of low-basic calcium hydrosilicates, which are represented by crystallites of lamellar morphology, increases (Fig. 4 f, h). CSSB1 + W is characterized by the presence of well-formed ettringite crystals in the structure (Fig. 4 e, g), which provide an increase in the energy of destruction due to microreinforcement of the structure.

It is important to emphasize that during all the hardening periods, the Portlandite $\text{Ca}(\text{OH})_2$ phase is practically absent in the composition of the CSSB1 and CSSB2 hydration products. This indicates that the solution very quickly reaches saturation with HSiO_3^- , SiO_3^{2-} , $\text{H}_2\text{SiO}_4^{2-}$, Al^{3+} , AlO_2^- ions, which bind Ca^{2+} , CaOH^+ cations to hydrated compounds, preventing the crystallization of Portlandite $\text{Ca}(\text{OH})_2$. Also, as part of hydration products of CSSB1 and CSSB2, one of the least active slag phases, the mellitic phase $8\text{CaO}\cdot 3\text{Al}_2\text{O}_3\cdot \text{MgO}\cdot 5\text{SiO}_2$, almost immediately ceases to be registered. On this basis, it can be argued that both obtained binders are characterized by high hydraulic activity. For CSSB1, this is ensured by the good solubility of ultramicrodispersed particles with a diameter of $d \sim 1\text{--}6 \mu\text{m}$ with an amorphized surface. This is the result of mechanochemical activation of CSSB1 during grinding in the presence of S-3 superplasticizer as a complex of surfactants. For CSSB2, hydraulic activity is largely determined by the catalytic role of SiO_2 nanoparticles at the acceleration stage, and their chemical interaction with the slag minerals at the stages of deceleration and slow interaction during hydration.

4. Conclusions

1. The phase composition of hydration products of clinkerless slag-silica binder CSSB2, activated by a complex additive based on SiO₂ nanoparticles, is characterized by the presence of tobermorite phases, low-basic calcium hydrosilicates, ettringite, and a significant content of AFt-phases. At the micro-scale level, the structure of the hardened binder paste is microheterogeneous with inclusions of pores of various sizes and grains of slag. The microstructure of hydration products is mainly represented by lamellar morphology crystallites, which are of different sizes and have a large number of contacts of abutment, coalescence, and intergrowth.

2. The clinkerless binder CSSB1 obtained by mechanochemical activation is characterized by the onset of setting in 150 minutes, a strength of 17.1 MPa at the age of 7 days, 37.5 MPa at 28 days. The clinkerless binder CSSB2, activated by a complex additive based on SiO₂ nanoparticles, is characterized by the onset of setting in 80 minutes, a strength of 31.9 MPa at the age of 7 days, 35.8 MPa at 28 days. The setting and strength indicators of the resulting clinkerless slag-silica binder types meet the physicochemical characteristics of cement grade 32.5 EN 197-1:2000 "Cement – Part 1: Composition, specifications and conformity criteria for common cements".

3. The results of a comprehensive assessment of the characteristics of the two types of clinkerless slag-silica binders and the parameters of their structure formation and hardening made it possible to confirm the effectiveness of using nano technological "bottom – up" principles to activate the hydration and hardening processes. The "top – down" principle, realized through mechanochemical activation of the binder components during grinding, allows one to provide almost 50% content of ultramicrodispersed particles with a diameter of $d \sim 1\text{--}6 \mu\text{m}$ and increase their hydraulic potential. The "bottom – up" principle, implemented through the introduction of SiO₂ nanoparticles into binder paste, allows increasing the hydraulic activity of slag due to the catalytic role of nanoparticles and their chemical interaction with the slag minerals. This made it possible to provide a setting and hardening rate for the obtained clinkerless binders under normal temperature and humidity conditions ($t = 20 \text{ }^\circ\text{C}$, $\text{RH} = 95 \pm 5\%$), comparable with the speed of these processes for Portland cement.

4. The development of research involves the study of the possibilities of producing concrete based on the developed types of clinkerless binders for the production of building products and structures both in factory and in building conditions.

5. Acknowledgement

This research work has been financed by the Russian Foundation for Basic Research (RFBR), Project 19-38-50028.

References

- Sun, J., Zhang, Z., Zhuang, S., et al. Hydration properties and microstructure characteristics of alkali-activated steel slag. *Construction and Building Materials*. 2020. V. 241. Pp. 118141. DOI: <https://doi.org/10.1016/j.conbuildmat.2020.118141>
- Karim, M.R., Hossain, M.M., A Elahi, M.M., et al. Effects of source materials, fineness and curing methods on the strength development of alkali-activated binder. *Journal of Building Engineering*. 2020. V. 29. Pp. 101147. DOI: <https://doi.org/10.1016/j.jobe.2019.101147>
- Rostami, M., Behfarnia, K. The effect of silica fume on durability of alkali activated slag concrete. *Construction and Building Materials*. 2017. V. 134. Pp. 262–268. DOI: <https://doi.org/10.1016/j.conbuildmat.2016.12.072>
- Ramezaniyanpour, A.A., Moeini, M.A. Mechanical and durability properties of alkali activated slag coating mortars containing nanosilica and silica fume. *Construction and Building Materials*. 2018. V. 163. Pp. 611–621. DOI: <https://doi.org/10.1016/j.conbuildmat.2017.12.062>
- Rakhimova, N.R., Rakhimov, R.Z. A review on alkali-activated slag cements incorporated with supplementary materials. *Journal of sustainable Cement-Based Materials*. 2014. V. 3 (1). P. 61. DOI: 10.1080/21650373.2013.876944
- Rakhimova, N.R., Rakhimov, R.Z. Ompozicionnye shlakoshchelochnye vyazhushchie s kremnezemistymi mineral'nymi dobavkami [Composite slag-alkaline binders with silica mineral additives]. *Inorganic materials*. 2012. 9 (48). P. 1083. (rus)
- Rakhimova, N.R., Rakhimov, R.Z. Alkali-activated cements and mortar based on blast furnace slag and redclay brick waste. *Materials and design*. 2015. 8. Pp. 324–331. DOI: 10.1016/j.matdes.2015.06.182
- Bazhenov, Y.M., Zagorodnjuk, L.H., Lesovik, V.S., Yerofeyeva, I.V., Chernysheva, N.V., Sumskoy, D.A. Concerning the role of mineral additives in composite binder content. *International Journal of Pharmacy and Technology*. 2016. 8 (4). Pp. 22649–22661.
- Lesovik, V.S., Alfimova, N.I., Trunov, P.V. Reduction of energy consumption in manufacturing the fine ground cement. *Research Journal of Applied Sciences*. 2014. 9 (11). Pp. 745–748. DOI: 10.3923/rjasci.2014.745.748
- Slavcheva, G.S., Baidzhanov, D.O., Khan, M.A., et al. Clinkerless slag-silica binder: hydration process and hardening kinetics. *Magazine of Civil Engineering*. 2019. 92 (8). Pp. 96–105. DOI: 10.18720/MCE.92.8
- Singh, N.B., Meenu, K., Saxena, S.K. Nanoscience of Cement and Concrete. *Materials Today: Proceedings*. 2017. 4 (4). Pp. 5478–5487. DOI: 10.1016/j.matpr.2017.06.003
- Reches, Y. Nanoparticles as concrete additives: Review and perspectives. *Constructions and Building Materials*. 2018. 175. Pp. 483–495. DOI: <https://doi.org/10.1016/j.conbuildmat.2018.04.214>
- Rai, S., Tiwari, S. Nano Silica in Cement Hydration. *Materials Today: Proceedings*. 2018. 5(3). Pp. 9196–9202. DOI: <https://doi.org/10.1016/j.matpr.2017.10.044>

14. Du, H., Pang, D. High performance cement composites with colloidal nano-silica. *Construction and Building Materials*. 2019. 224. Pp. 317–325. DOI: <https://doi.org/10.1016/j.conbuildmat.2019.07.045>
15. Kong, D., Pan, H., Wang, L., et al. Effect and mechanism of colloidal silica sol on properties and microstructure of the hardened cement-based materials as compared to nano-silica powder with agglomerates in micron-scale. *Cement and Concrete Composites*. 2019. 98. Pp. 137–149. DOI: <https://doi.org/10.1016/j.cemconcomp.2019.02.015>
16. Meng, T., Hong, Y., Wei, H. et al. Effect of nano-SiO₂ with different particle size on the hydration kinetics of cement. *Thermochimica Acta*. 2019. 675. Pp. 127–133. DOI: <https://doi.org/10.1016/j.tca.2019.03.013>
17. Artamonova O.V., Slavcheva G.S., Chernyshov E.M. Effectiveness of combined nanoadditives for cement systems. *Inorganic materials*. 2017. 53 (10). Pp. 1080–1085. DOI: 10.1134/s0020168517100028
18. Assaedi, H., Shaikh, F.U.A., Low, I.M. Effect of nano-clay on mechanical and thermal properties of geopolymer. *Journal of Asian Ceramic Societies*. 2016. 4. Pp. 19–28. DOI: <https://doi.org/10.1016/j.jascer.2015.10.004>
19. Yang, L.Y., Jia, Z.J., Zhang, Y.M., et al. Effects of nano-TiO₂ on strength, shrinkage and microstructure of alkali activated slag pastes. *Cement and Concrete Composites*. 2015. 57. Pp. 1–7. DOI: 10.1016/j.cemconcomp.2014.11.009
20. Wang, J., Du, P., Zhou, Z., et al. Effect of nano-silica on hydration, microstructure of alkali-activated slag. *Construction and Building Materials*. 2019. 220. Pp. 110–118. DOI: <https://doi.org/10.1016/j.conbuildmat.2019.05.158>
21. JCPDS – International Centre for Diffraction Data. © 1987–1995. JCPDS – ICDD. Newtown Square, PA. 19073. USA.
22. Artamonova, O.V., Slavcheva, G.S. Structure of cement systems as objects of nanomodification // *Scientific Herald of the Voronezh State University of Architecture and Civil Engineering*. Construction and Architecture. 2016. No. 1 (29). Pp. 13–26.

Contacts:

Galina Slavcheva, gslavcheva@yandex.ru

Olga Artamonova, ol_artam@rambler.ru

Maria Shvedova, marishwedova@mail.ru

Maxim Khan, han_maks@mail.ru

© Slavcheva, G.S., Artamonova, O.V., Shvedova, M.A., Khan, M.A., 2020



ПОЛИТЕХ
Санкт-Петербургский
политехнический университет
Петра Великого

Инженерно-строительный институт
Центр дополнительных профессиональных программ

195251, г. Санкт-Петербург, Политехническая ул., 29,
тел/факс: 552-94-60, www.stroikursi.spbstu.ru,
stroikursi@mail.ru

Приглашает специалистов проектных и строительных организаций,
не имеющих базового профильного высшего образования
на курсы профессиональной переподготовки (от 500 часов)
по направлению «Строительство» по программам:

П-01 «Промышленное и гражданское строительство»

Программа включает учебные разделы:

- Основы строительного дела
- Инженерное оборудование зданий и сооружений
- Технология и контроль качества строительства
- Основы проектирования зданий и сооружений
- Автоматизация проектных работ с использованием AutoCAD
- Автоматизация сметного дела в строительстве
- Управление строительной организацией
- Управление инвестиционно-строительными проектами. Выполнение функций технического заказчика

П-02 «Экономика и управление в строительстве»

Программа включает учебные разделы:

- Основы строительного дела
- Инженерное оборудование зданий и сооружений
- Технология и контроль качества строительства
- Управление инвестиционно-строительными проектами. Выполнение функций технического заказчика и генерального подрядчика
- Управление строительной организацией
- Экономика и ценообразование в строительстве
- Управление строительной организацией
- Организация, управление и планирование в строительстве
- Автоматизация сметного дела в строительстве

П-03 «Инженерные системы зданий и сооружений»

Программа включает учебные разделы:

- Основы механики жидкости и газа
- Инженерное оборудование зданий и сооружений
- Проектирование, монтаж и эксплуатация систем вентиляции и кондиционирования
- Проектирование, монтаж и эксплуатация систем отопления и теплоснабжения
- Проектирование, монтаж и эксплуатация систем водоснабжения и водоотведения
- Автоматизация проектных работ с использованием AutoCAD
- Электроснабжение и электрооборудование объектов

П-04 «Проектирование и конструирование зданий и сооружений»

Программа включает учебные разделы:

- Основы сопротивления материалов и механики стержневых систем
- Проектирование и расчет оснований и фундаментов зданий и сооружений
- Проектирование и расчет железобетонных конструкций
- Проектирование и расчет металлических конструкций
- Проектирование зданий и сооружений с использованием AutoCAD
- Расчет строительных конструкций с использованием SCAD Office

П-05 «Контроль качества строительства»

Программа включает учебные разделы:

- Основы строительного дела
- Инженерное оборудование зданий и сооружений
- Технология и контроль качества строительства
- Проектирование и расчет железобетонных конструкций
- Проектирование и расчет металлических конструкций
- Обследование строительных конструкций зданий и сооружений
- Выполнение функций технического заказчика и генерального подрядчика

По окончании курса слушателю выдается диплом о профессиональной переподготовке
установленного образца, дающий право на ведение профессиональной деятельности

